

# Automation and Application of fixed-order and matched NLO Simulations

*Automatisierung und Anwendung von NLO Simulationen auf fester Ordnung  
und inklusive matching*

---

## Dissertation

zur Erlangung des Doktorgrades

an der Fakultät für

Mathematik, Informatik und Naturwissenschaften

Fachbereich Physik

der Universität Hamburg

vorgelegt von

**Pascal Stienemeier**

im Jahr

**2022**

in

**Hamburg**



Gutachter:innen der Dissertation:	Dr. Jürgen Reuter Prof. Dr. Gudrid Moortgat-Pick
Zusammensetzung der Prüfungskommission:	Dr. Jürgen Reuter Prof. Dr. Gudrid Moortgat-Pick Dr. Markus Diehl Prof. Dr. Peter Schleper Prof. Dr. Arwen Pearson
Vorsitzende der Prüfungskommission:	Prof. Dr. Arwen Pearson
Vorsitzender des Fach-Promotionsausschusses PHYSIK:	Prof. Dr. Günter H. W. Sigl
Leiter des Fachbereichs PHYSIK:	Prof. Dr. Wolfgang J. Parak
Dekan der MIN Fakultät:	Prof. Dr.-Ing. Norbert Ritter
Datum der Disputation	05.12.2022



## Abstract

Run 3 of the Large Hadron Collider (LHC) has recently begun and heralds an era of unprecedented experimental precision. At the same time, several potential successors, future hadron- but also lepton colliders, advance in design and scheduling. To maximize the gain from the expected huge increase in experimental precision, increased precision of theory predictions is indispensable.

Most theory predictions performed in high-energy physics rely on perturbation theory, in which phenomena are described in a perturbative series. Increasing the precision in this context requires taking more terms up to higher orders in the expansion parameters, i.e., the coupling constants, into account.

Technically, these calculations are implemented in software frameworks called Monte Carlo (MC) event generators. These are tools using numerical methods based on sampling random numbers to compute total cross sections and simulate events. `WHIZARD` is one of the well-established general-purpose MC generators able to simulate events for experiments at hadron- as well as lepton colliders.

In the course of this thesis, we completed the automated computation of terms at next-to-leading order (NLO) in the strong coupling constant of quantum chromodynamics (QCD), using the Frixione–Kunszt–Signer (FKS) subtraction scheme in `WHIZARD`. This includes the extension of the previously existing implementation towards multi-jet final states and hadron collisions featuring emissions from the initial state, generalizing the possibility to simulate events at fixed NLO, and a thorough validation of the implemented NLO QCD corrections by comparison of cross sections computed for a large number of different processes with other MC generators.

Furthermore, we implemented a process-independent version of the POWHEG-matching scheme, which can be used to match partonic events, generated by taking NLO QCD corrections into account, with parton showers, while avoiding to double count any emissions. We apply this matching exemplarily to the standard candle of the LHC, the Drell-Yan process and compare our results with data taken at the Compact Muon Solenoid (CMS) experiment and to top-pair production in association with a jet at a future lepton collider. The former is the first example of matching NLO QCD corrections in `WHIZARD` to a parton shower as well as the first comparison of differential NLO distributions from `WHIZARD` with experimental data.

## Zusammenfassung

Die dritte Datennahme des Large Hadron Colliders (LHC) hat kürzlich begonnen und eine neue Ära des Datenreichtums eingeläutet. Zur selben Zeit schreitet die Entwicklung und Planung möglicher nachfolgender Hadronen- und Leptonenbeschleuniger voran. Um den maximalen Nutzen aus den gewonnenen Daten zu ziehen, ist es unverzichtbar, die Genauigkeit theoretischer Rechnungen in gleicher Weise zu erhöhen.

Theoretische Rechnungen in der Hochenergiephysik basieren in der Regel auf Störungstheorie. Die Genauigkeit solcher Rechnungen zu erhöhen, bedeutet weitere Terme mit höheren Potenzen der Entwicklungsparameter, der Kopplungskonstanten, zu berücksichtigen.

Technisch realisiert sind diese Rechnungen in Monte-Carlo-Ereignisgeneratoren (MC-Generatoren). Diese Programme verwenden numerische Methoden, basierend auf Zufallszahlen, um Wirkungsquerschnitte zu berechnen und Ereignisse zu simulieren. WHIZARD ist einer der etablierten Mehrzweck-MC-Generatoren, der in der Lage ist, Ereignisse in Experimenten sowohl an Hadronen- als auch an Leptonenbeschleunigern zu simulieren.

Im Laufe der vorliegenden Arbeit haben wir die automatisierte Berücksichtigung von Termen zugehörig zur nächstführenden Ordnung in der starken Kopplungskonstanten, basierend auf dem Frixione-Kunst-Signer-Subtraktionsschema, im MC-Generator WHIZARD komplettiert. Dies beinhaltet die Erweiterung der zuvor vorhandenen Implementation auf Endzustände mit mehr als zwei Jets sowie Hadronkollisionen mit Abstrahlungen aus dem Anfangszustand, die Möglichkeit Events zu generieren, die ebenfalls Terme der nächstführenden Ordnung berücksichtigen und eine ausführliche Validierung der Implementation durch den Vergleich von Wirkungsquerschnitten einer großen Bandbreite an Prozessen mit anderen MC-Generatoren. Darüber hinaus haben wir das POWHEG-Matching-Schema prozessunabhängig implementiert. Es kann genutzt werden, um die generierten partonischen Events mit einem Partonshower zu verknüpfen, ohne dabei Abstrahlungen der Korrekturen höherer Ordnung und generiert vom Partonshower doppelt zu zählen. Beispielfähig wenden wir das POWHEG-Matching auf den Drell-Yan-Prozess am LHC an und vergleichen unsere Vorhersagen mit vom CMS-Experiment gemessenen Daten. Dies stellt die erste Anwendung von NLO-Korrekturen in WHIZARD in Verbindung mit einem Partonshower sowie den ersten Vergleich von mit WHIZARD berechneten Vorhersagen, die Korrekturen der nächstführenden Ordnung berücksichtigen, mit gemessenen Daten dar. Um die Prozessunabhängigkeit unserer Implementierung zu unterstreichen, betrachten wir außerdem die Produktion eines Top-Quark-Paares begleitet von einem Jet an einem zukünftigen Leptonenbeschleuniger.

## List of publications

This thesis contributed to the following publications:

- [1] P. Brecht, W. Kilian, J. Reuter, and P. Stienemeier. “NLO Electroweak Corrections to Multi-Boson Processes at a Muon Collider” (Aug. 2022). arXiv: [2208.09438](#)

and proceedings:

- [2] P. Brecht, J. Reuter, and P. Stienemeier. “Automated NLO SM corrections for all colliders”. *41st International Conference on High Energy Physics*. Oct. 2022. arXiv: [2210.07157](#),
- [3] P. Stienemeier et al. “WHIZARD 3.0: Status and News”. *International Workshop on Future Linear Colliders*. Apr. 2021. arXiv: [2104.11141](#),
- [4] J. Reuter et al. “Status of the WHIZARD generator for linear collider”. *International Workshop on Future Linear Colliders*. Feb. 2020. arXiv: [2002.06122](#),
- [5] S. Braß et al. “Precision Monte Carlo simulations with WHIZARD”. *CERN Yellow Reports: Monographs* 3 (2020). Ed. by A. Blondel, J. Gluza, S. Jadach, P. Janot, and T. Riemann, pp. 205–210. DOI: [10.23731/CYRM-2020-003.205](#),
- [6] W. Kilian et al. “New Developments in WHIZARD Version 2.6”. *International Workshop on Future Linear Colliders (LCWS2017) Strasbourg, France, October 23-27, 2017*. 2018. arXiv: [1801.08034](#).

I also contributed to the following publication in preparation to be published soon:

- [7] S. Braß, P. Brecht, J. Reuter, P. Stienemeier, and V. Rothe. “Automation of NLO SM processes in WHIZARD for hadron and lepton collisions”. 2023. in preparation

Furthermore, I contributed to the following publications beyond the scope of this thesis:

- [8] M. Diehl and P. Stienemeier. “Gluons and sea quarks in the proton at low scales”. *Eur. Phys. J. Plus* 135.2 (2020), p. 211. DOI: [10.1140/epjp/s13360-020-00200-6](#). arXiv: [1904.10722](#),
- [9] A. Ballestrero et al. “Precise predictions for same-sign W-boson scattering at the LHC”. *The European Physical Journal C* 78.8 (Aug. 2018), p. 671. ISSN: 1434-6052. DOI: [10.1140/epjc/s10052-018-6136-y](#). arXiv: [1803.07943](#),
- [10] C. F. Anders et al. “Vector boson scattering: Recent experimental and theory developments”. *Rev. Phys.* 3 (2018), pp. 44–63. DOI: [10.1016/j.revip.2018.11.001](#). arXiv: [1801.04203](#).

An up to date version of my list of publications can also be found online  .

# Contents

<b>1</b>	<b>Introduction</b>	<b>1</b>
<b>I</b>	<b>Part 1 – Automation of NLO corrections: fixed order and beyond</b>	<b>8</b>
<b>2</b>	<b>The Frixione-Kunszt-Signer subtraction scheme</b>	<b>9</b>
2.1	NLO computations and subtraction schemes . . . . .	9
2.1.1	Counting coupling constants . . . . .	9
2.1.2	Contributions to the cross section at next-to-leading order . . . . .	10
2.1.3	Subtraction schemes . . . . .	10
2.2	Notation . . . . .	11
2.3	The singular regions . . . . .	12
2.3.1	The FKS pairs . . . . .	12
2.3.2	Parametrization of the radiation phase-space . . . . .	15
2.3.3	The $S$ functions . . . . .	17
2.4	The real phase-space construction . . . . .	19
2.4.1	Radiation off a massless final-state emitter . . . . .	20
2.4.2	Radiation off a massive final-state emitter . . . . .	25
2.4.3	Radiation off a massless initial-state emitter . . . . .	28
2.5	The Born contribution . . . . .	31
2.6	The real contribution and subtraction terms . . . . .	32
2.6.1	Final-state subtraction terms . . . . .	33
2.6.2	Initial-state subtraction terms . . . . .	37
2.6.3	Partitioning the real contribution . . . . .	40
2.7	The virtual contribution and integrated subtraction terms . . . . .	42
2.7.1	The DGLAP remnant contribution . . . . .	43
2.8	Fixed next-to-leading order differential distributions . . . . .	44
2.8.1	Fixed next-to-leading order histogramming . . . . .	47
<b>3</b>	<b>The POWHEG matching scheme</b>	<b>50</b>
3.1	Parton showers and the Sudakov form factor . . . . .	50
3.2	Improving the parton shower – merging and matching . . . . .	52
3.2.1	Merging . . . . .	52
3.2.2	Matching . . . . .	53
3.3	POWHEG matching – the concept . . . . .	55
3.4	Prerequisites . . . . .	57
3.4.1	Generation of the underlying Born configuration and event weights . . . . .	57
3.5	The generation of radiation – the veto procedure . . . . .	58
3.5.1	The veto procedure in general . . . . .	58
3.5.2	Dividing and conquering the Sudakov form factor . . . . .	61
3.5.3	The upper bounding function . . . . .	63
3.5.4	Normalizing the upper bounding function – the POWHEG grid . . . . .	66
3.5.5	The POWHEG veto procedure – the massless FSR case . . . . .	69
3.5.6	The POWHEG veto procedure – massless recoil systems . . . . .	72

3.5.7	The POWHEG veto procedure – the massless ISR case . . . . .	75
3.5.8	The POWHEG veto procedure – the massive FSR case . . . . .	79
3.5.9	The POWHEG veto steps – summary . . . . .	81
3.6	Refinements and optimizations . . . . .	84
3.6.1	Performance optimizations in the Sudakov factorization . . . . .	84
3.6.2	Optimizations of the Sudakov competition in the highest-bid algorithm . . . . .	85
3.6.3	Born zeroes . . . . .	85
3.6.4	The POWHEG damping factor . . . . .	86
3.6.5	Scale choice for the events . . . . .	86
3.6.6	Improving the NLL accuracy of $\alpha_S$ . . . . .	87
3.6.7	Color flow of POWHEG events . . . . .	88
3.6.8	Resonance history insertion . . . . .	89
3.6.9	Reducing the number of negative weights . . . . .	90
<b>4</b>	<b>The Monte Carlo event generator WHIZARD</b>	<b>92</b>
4.1	The Monte Carlo event generator WHIZARD at NLO QCD . . . . .	92
4.2	Parton shower, merging and matching in WHIZARD . . . . .	95
<b>II</b>	<b>Part 2 – Applications of fixed-order and matched Simulations</b>	<b>96</b>
<b>5</b>	<b>Validation of fNLO cross sections</b>	<b>97</b>
5.1	Consistency checks . . . . .	97
5.2	Comparison of fixed-order cross sections at NLO QCD . . . . .	100
5.2.1	Process setup . . . . .	100
5.2.2	Results for the cross sections . . . . .	101
5.3	Validation of the real partition . . . . .	107
<b>6</b>	<b>Applications of POWHEG matching</b>	<b>108</b>
6.1	The Drell-Yan process compared to the POWHEG-BOX . . . . .	108
6.1.1	Process setup and event selection . . . . .	109
6.1.2	Total cross sections . . . . .	110
6.1.3	POWHEG events . . . . .	112
6.1.4	Effects of the parton shower . . . . .	119
6.2	The Drell-Yan process compared to data . . . . .	122
6.2.1	Process setup and event selection . . . . .	122
6.2.2	Cross sections . . . . .	123
6.2.3	Differential distributions . . . . .	124
6.3	Predictions for $e^+e^- \rightarrow t\bar{t}j$ measurements . . . . .	128
6.3.1	Process setup and event selection . . . . .	128
6.3.2	Total cross sections . . . . .	129
6.3.3	Differential distributions . . . . .	130
6.4	Corollary . . . . .	135
<b>7</b>	<b>Conclusion and outlook</b>	<b>137</b>

---

<b>Appendix</b>	<b>141</b>
<b>A The Altarelli-Parisi splitting functions</b>	<b>142</b>
A.1 The spin-dependent case . . . . .	142
A.2 The spin-averaged case . . . . .	142
<b>B Basic random number sampling methods</b>	<b>144</b>
B.1 Basic definitions . . . . .	144
B.2 Inverse Transform Sampling (ITS) . . . . .	144
B.3 Rejection Sampling (RS) . . . . .	145
<b>C Technical supplements to the POWHEG veto procedure</b>	<b>146</b>
C.1 Evolution of the transverse momentum . . . . .	146
C.2 Veto and survival rates . . . . .	147
<b>D Generating POWHEG events with WHIZARD</b>	<b>149</b>
D.1 Steering WHIZARD - The SINDARIN file . . . . .	149
D.2 Using Rivet . . . . .	152
<b>References</b>	<b>153</b>
<b>List of figures</b>	<b>x</b>
<b>List of tables</b>	<b>xi</b>
<b>List of acronyms</b>	<b>xii</b>
<b>Acknowledgements</b>	<b>xiii</b>

# 1 Introduction

The success story of higher-order corrections in perturbative quantum field theories begins with the hydrogen atom, probably the most favorite toy of physicists during the last century.

## The history of the hydrogen atom

Soon after Sir J. J. Thomson discovered the electron in 1897 [11] and came up with the plum pudding model of the atom in 1904, describing it as "negatively electrified corpuscles enclosed in a sphere of uniform positive electrification" [12], this idea was proven incorrect by his student Ernest Rutherford, who discovered the atomic nucleus in his gold foil experiment in 1911 [13], inspiring him to describe the atom as a central positive charge surrounded by negatively charged electrons, coining the Rutherford model of the atom. Two years later, Niels Bohr enhanced his model to the (Rutherford-)Bohr model of the atomic nucleus [14, 15], which explains the discrete energy levels of the electrons around the nucleus by assuming them moving on quasi-classical circular radiationless trajectories. It was the first model of the atom able to explain the Rydberg formula for the atomic line spectrum, which was experimentally already known for 25 years [16], by spontaneous quantum jumps between the discrete energy levels yielding emission energies of

$$\Delta E = R_E \left( \frac{1}{n_f^2} - \frac{1}{n_i^2} \right) \quad (1.1)$$

where  $R_E$  is given by  $hc$  times<sup>1</sup> the Rydberg constant and  $n_i$  and  $n_f$  are the principal quantum numbers of the initial and final energy levels, respectively. However, it was noticed that the energy levels were only accurately described up to  $\mathcal{O}(10^{-5})$ , and the model also failed to predict the spectra of larger atoms. Also, it could not explain the relative intensities of the spectral lines and why some spectral lines were observed very close to each other.

These shortcomings could be overcome by enhancements to the Bohr model of the atom suggested by Arnold Sommerfeld [17] in 1916. He introduced two additional degrees of freedom to the electron movement, allowing elliptic trajectories, which could later be mapped to the electron orbital angular momentum, with the quantum number  $\ell$ , and its projection on the  $z$  axis, with the quantum number  $m_\ell$ , as well as the *fine structure constant*  $\alpha$  as the velocity ratio of the electron in the first orbit in units of the speed of light, which later became known as the electromagnetic coupling constant. While in the Bohr picture, all states with the same  $n$  had the same energy, this degeneracy was lifted by Sommerfeld's description accounting for the angular momentum. This is displayed on the left hand side (LHS) of fig. 1.1. Despite its success in adequately describing a variety of experimental results, it could not treat all systems and exhibited some mathematical inconsistencies.

In the development of modern quantum mechanics, another, regarding most results empirically equivalent, description of the hydrogen atom arose from the Schrödinger equation postulated in 1925 and published one year later by Erwin Schrödinger [18]. It describes the time evolution of the wave function of quantum mechanical systems. For the hydrogen atom, this equation factorizes into radial, angular and spin part, making it analytically solvable. Its solutions are the energy eigenstates of the electrons, the *orbitals*, expressed using spherical harmonics characterized by four quantum numbers, including the spin.

Schrödinger's description of the hydrogen atom did not include any relativistic effects. Although it was possible to enhance Schrödinger's description with relativistic corrections, the first fully relativistic quantum mechanical description was achieved by Paul Dirac in 1928 [19]. The analytical solution of the Dirac equation for the hydrogen atom once more improved the accuracy of the prediction for the energy levels. The fully

---

<sup>1</sup>This factor is  $2\pi$  in natural units.

relativistic quantum mechanical description of the hydrogen atom is often called the *fine structure* of the hydrogen atom.

In the Dirac picture, states with the same quantum numbers  $n$  and  $j$ , such as the two states  $2S_{1/2}$  and  $2P_{1/2}$ , have the same energy level. However, the Lamb-Retherford experiment [20] from 1947 showed that transitions between the two states can be stimulated with radio frequencies, implying that the two states indeed have different energies. This energy splitting is displayed on the right hand side (RHS) of fig. 1.1.

The Lamb shift was explained in the same year by Hans Bethe [21]. Bethe described the Lamb shift by interactions of the hydrogen electron with virtual photons. In his calculation, he encountered divergences due to the unconstrained photon energy, which he solved by renormalizing the electron mass. In a perturbative interpretation, the Lamb shift can be seen as the first higher-order correction to the quantum mechanical approach marking the beginning of modern quantum field theory (QFT), especially quantum electrodynamics (QED).

Further corrections to the energy levels of the hydrogen atom arise from the multipole interactions of the atomic nucleus with the electrons. These effects are summarized as the hydrogen *hyperfine structure*.

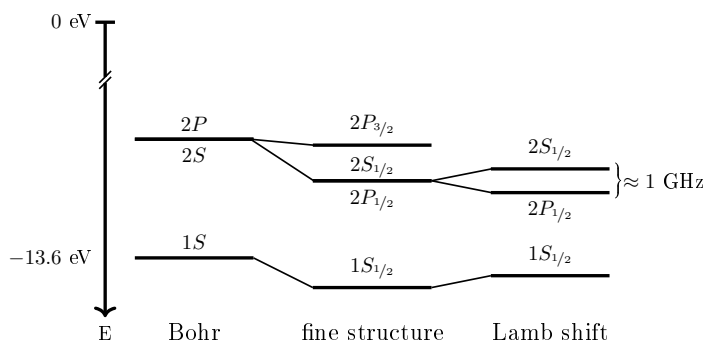


Fig. 1.1: Fine structure and Lamb shift of the hydrogen atom's energy levels.

The second huge success of modern QFT was achieved just one year later by Julian Schwinger [22] when he calculated the electron magnetic moment. It was predicted by Dirac's theory to exactly equal 2 until Schwinger computed the first-order correction based on local Green's functions, further developing the renormalization theory. His results were almost immediately confirmed experimentally by Polykarp Kusch and Henry Foley [23]. Today, the electron magnetic moment is known and experimentally confirmed up to 12 digits, being probably the most precisely known and measured fundamental quantity in all of physics.

### The Standard Model of particle physics

In the coming decades, many bright minds continued to develop the mathematical groundwork of renormalization theory and QFT, which finally allowed the formulation of the Standard Model of particle physics (SM). The Standard Model is a QFT describing the particles, fields and interactions of three of the known four fundamental forces of nature.

The electromagnetism is described by QED, which governs the interactions of all electrically charged particles, including the charged leptons (electrons, muons and taus), and photons. It is unified with the weak force in the electroweak (EW) theory, additionally describing the interactions of neutrinos and heavy bosons such as the  $W$ , the  $Z$  and the Higgs boson.

The theory of QCD governs the interactions of all color-charged particles, such as the three generations of quarks and the gluon. The fundamental particles of the Standard Model are organized in generations I-III as depicted in fig. 1.2.

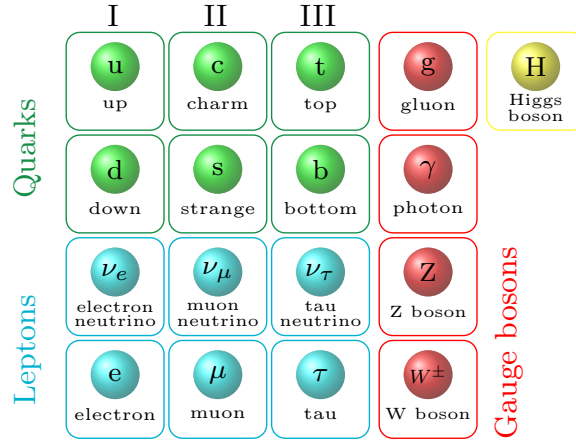


Fig. 1.2: Particle content of the Standard Model of particle physics. Quarks are displayed in green, leptons in turquoise, gauge bosons in red and the scalar Higgs boson in yellow. Provided by ref. [24].

For decades, the SM was very successful in predicting and describing many of these interactions and particles even long before they were discovered. The latest success was the discovery of the Higgs boson a decade ago [25, 26], 48 years after its prediction [27–29].

To identify possible shortcomings of the SM, the precision of both, predictions and measurements, has to increase. Run 3 of the LHC has recently begun and will be followed by the High-Luminosity LHC (HL-LHC) [30]. During its runtime, each upgrade will yield more data for hadron-hadron collisions than ever collected before. In the future, high precision lepton collider experiments such as the International Linear Collider (ILC) [31, 32], the Compact Linear Collider (CLIC) [33], the Future Circular Collider (FCC) [34, 35] or the Circular Electron Positron Collider (CEPC) [36] are foreseen and will allow to test the SM at unmatched precision. These high-precision experiments would be useless if most of the analyses were limited by theoretical uncertainties [37].

### Higher order calculations

The majority of theoretical calculations in the SM are performed in a perturbative approach. Cross sections and observables are expanded in powers of the strong coupling constant,  $\alpha_S$ , and the electromagnetic coupling  $\alpha$ . The first non-zero term in the perturbative series is the leading order (LO) term. In general, it is of the order  $\mathcal{O}(\alpha_S^n \alpha^m)$ . Subleading terms are at higher order in either  $\alpha_S$  or  $\alpha$  or both. We refer to the term of the order  $\mathcal{O}(\alpha_S^{n+1} \alpha^m)$  as the NLO QCD term, while the term of order  $\mathcal{O}(\alpha_S^n \alpha^{m+1})$  is referred to as the NLO EW term. Further terms are part of the next-to-next-to-leading order (NNLO) correction and so on. At hadron colliders, the NLO QCD correction is the most dominant one as  $\alpha \ll \alpha_S$ , while the NLO EW correction is comparable to the NNLO QCD correction with a few exceptions. At lepton colliders, the EW corrections often exceed the QCD corrections due to the EW nature of the processes studied.

Feynman diagrams have turned out to be an incredibly useful, illustrative and mathematically rigorous tool to describe this perturbative expansion. In these diagrams, particles are depicted by different types of lines, their interaction by vertices. Each three-particle vertex is proportional to one of the coupling constants. Thus, in terms of Feynman diagrams, higher orders generally feature more vertices caused by loops and additional radiation. The LHS of fig. 1.3a shows the LO Feynman diagram for dijet production at a lepton collider,  $e^+e^- \rightarrow jj$ . It represents the mathematical terms for the LO *matrix element*. As the cross section

is computed from *squared* matrix elements  $|\mathcal{M}|^2$ , the RHS of fig. 1.3a is also shown and represents the complex conjugate.

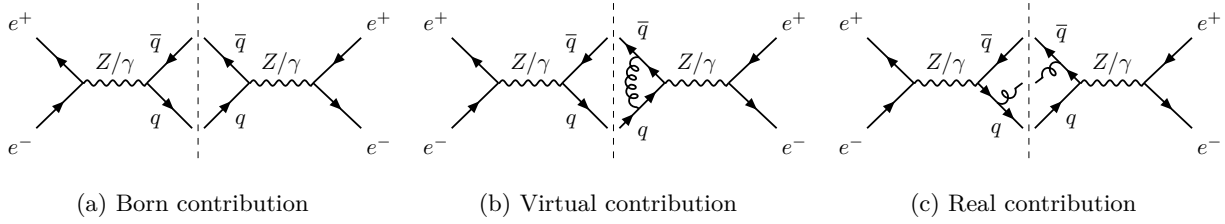


Fig. 1.3: Diagrammatic representation of the NLO QCD contributions to dijet production at a lepton collider,  $e^+e^- \rightarrow jj$ . Created for ref. [38].

In an NLO calculation, the leading term is the *Born* contribution. It is diagrammatically equivalent to the LO contribution with the subtle difference that, when computing the Born term, we take the NLO values for parameters such as widths and parton distribution functions (PDFs), which are accurate to NLO, so the Born contribution does not necessarily agree numerically with the LO contribution.

The other two diagrams, fig. 1.3c and 1.3b depict the two types of NLO corrections, here for NLO QCD. To see which terms we need to compute to get the NLO matrix element, we square the infinite series of the matrix elements, keeping all terms up to order  $\mathcal{O}(\alpha_S^{n+1})$ . This results in

$$|\mathcal{M}_{\text{NLO}}|^2 = |\mathcal{M}_{\text{NLO}}^{\text{B}}|^2 + 2\text{Re}[\mathcal{M}_{\text{NLO}}^{\text{B}}\mathcal{M}_{\text{NLO}}^{\text{V},*}] + |\mathcal{M}_{\text{NLO}}^{\text{R}}|^2 \quad . \quad (1.2)$$

In this way, we find that also loop matrix elements become relevant, as displayed in fig. 1.3b. We refer to this contribution as the *virtual* contribution as it features a virtual particle in a loop; in the case of fig. 1.3b, the gluon. The third type of contributing diagrams are *real* diagrams, shown for  $e^+e^- \rightarrow jj$  in fig. 1.3c. Real corrections include additional radiated particles.

In a naive computation, both types of corrections are infinite. The virtual contribution includes integrals over unconstrained loop momenta, which diverge for infinitely large as well as for infinitesimally small momenta. In the first case, we call them *ultraviolet (UV) divergences* and in the second case *infrared (IR) divergences*. The UV type of divergences is precisely the same type of problem that Bethe encountered when calculating the Lamb shift. The solution is analog, too. In any renormalizable QFT, such as the SM, these divergences are cured by renormalizing fields, couplings and masses. This comes at the price of introducing the dependence on an artificial energy scale  $\mu_R$ , the *renormalization scale*. If all orders of coupling constants were summed up, the dependence on  $\mu_R$  would vanish entirely. For any finite number of terms, however, it remains. Typically, variations of such scales like  $\mu_R$  by a factor of order 2 are used to estimate the theoretical uncertainties from higher-order corrections beyond the considered fixed order. The IR divergences cannot be remedied by renormalization. They are present in both the virtual and the real contribution and are best visualized for the real emission.

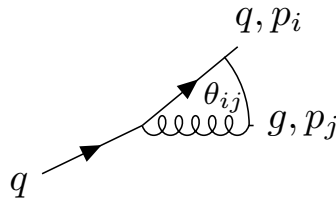


Fig. 1.4: Feynman diagram of a quark radiating a gluon. The resulting momenta are  $p_i$  and  $p_j$ . All Feynman diagrams in this thesis are created with TikZ-Feynman [39].

A real emission of, e.g., a gluon as depicted in fig. 1.4 adds an additional leg to the Born diagram as well as an additional propagator from the original leg. For a particle  $i$  radiating a massless particle  $j$ , the propagator before the emission will make the squared matrix element proportional to

$$\frac{1}{(p_i + p_j)^2 - m_i^2} = \frac{1}{2E_i E_j (1 - \beta_i \cos(\theta_{ij}))} \quad \text{with velocity} \quad \beta_i = \frac{|\vec{p}_i|}{E_i} = \sqrt{1 - \frac{m_i^2}{E_i^2}} . \quad (1.3)$$

From this propagator alone, we can identify the two types of IR divergences<sup>2</sup>. On the one hand, they include *soft* divergences if  $E_j \rightarrow 0$ , due to the emission of a particle with infinitesimal energy<sup>3</sup>, and on the other hand they appear for particles  $j$  radiated *collinear* in the same direction as their mother particle  $i$ , i.e.,  $\theta_{ij} \rightarrow 0$  if the emitter is massless too, implying  $\beta_i = 1$ .

There are multiple ways to deal with IR divergences. One could introduce small but non-zero mass parameters, but this would unnecessarily increase the complexity of the calculation and, in some cases, even violate gauge invariance, one of the mathematical principles underlying QFT. The most common strategy in analytic calculations is *dimensional regularization* [40]. However, as this approach works in non-integer dimensions, it is hardly portable to numerical computations.

The most successful numerical approach is based on the observation that the IR divergences of the real emissions turn out to precisely cancel out the IR divergences of the virtual diagrams. This fact was first observed by Felix Bloch and Arnold Nordsieck [41] for pure QED and almost 30 years later simultaneously generalized by Tōichirō Kinoshita [42] and Tsung–Dao Lee and Michael Nauenberg [43] to the Kinoshita–Lee–Nauenberg (KLN) theorem. It states that higher-order amplitudes in a theory of massless fields are finite, order by order, given that degenerate states are summed over. This is the case if all calculated observables are defined in an *IR-safe* way, meaning that they are unchanged by additional soft or collinear emissions.

The KLN theorem is the underlying basis of subtraction schemes, which are methods allowing the automated numerical calculation of higher-order cross sections. There are different subtraction schemes, but the general idea for all of them is the same. They introduce a subtraction term  $\mathcal{S}$  to the real contribution rendering the integral over the difference of both finite. This subtraction term is then integrated over the radiation degrees of freedom and added to the virtual contribution, rendering also this integral finite so that

$$\sigma^{\text{NLO}} = \underbrace{\sigma^{\mathcal{B}} + \int_{n+1} (d\sigma^{\mathcal{R}} - d\sigma^{\mathcal{S}})}_{\text{finite by construction}} + \underbrace{\int_n \left( d\sigma^{\mathcal{V}} + \int_{\text{rad}} d\sigma^{\mathcal{S}} \right)}_{\text{finite by KLN}} . \quad (1.4)$$

There is some freedom in the construction of the subtraction term as long as it cancels out the divergences. From this freedom, different subtraction schemes arose. One such scheme, the FKS subtraction scheme, has been implemented in the course of this thesis and its predecessors. We will discuss its mathematical structure in sec. 2 and show its validation and some applications in sec. 5.

## Monte Carlo Generators

Both LO, and higher-order calculations, are made available to other physicists in the form of MC generators, numerical computer programs predicting integrated cross sections and simulating events from high energetic interactions, governed by perturbative QFT up to the subsequent parton shower. Fig. 1.5 colorfully illustrates the different parts of the event simulation on the example of a deep inelastic collision of two hadrons. In

<sup>2</sup>Other authors might exclude the collinear divergences from the term "IR divergences". Some authors refer to them as "mass singularities" instead.

<sup>3</sup>This is the pedagogical explanation. In fact, as the phase-space volume also decreases with the energy of the radiated particle, both effects could potentially cancel out. We will discuss soft divergences more thoroughly in sec. 2.6.

this figure, the two incoming hadrons are depicted by the two largest light green ellipses on a horizontal line. Two of their constituents enter the most energetic, i.e., the *hard interaction*, depicted by a red circular blob in the center, possibly after emitting lower energetic initial-state radiation (ISR). Two other partons may perform a *secondary interaction*, less energetic than the first one but still contributing to the overall energy deposits as the *underlying event*. Those partons not involved in any of the hard interactions form the *beam remnants*, depicted by the small light blue ellipses. At the end of all the hard interactions, the *parton shower* simulates further less energetic emissions of gluons and quarks, shown in red, as well as photons, shown in yellow, until at some scale, the emerged partons *hadronize* to semi-stable hadrons. These hadrons decay, producing sprays of particles coined *jets*.

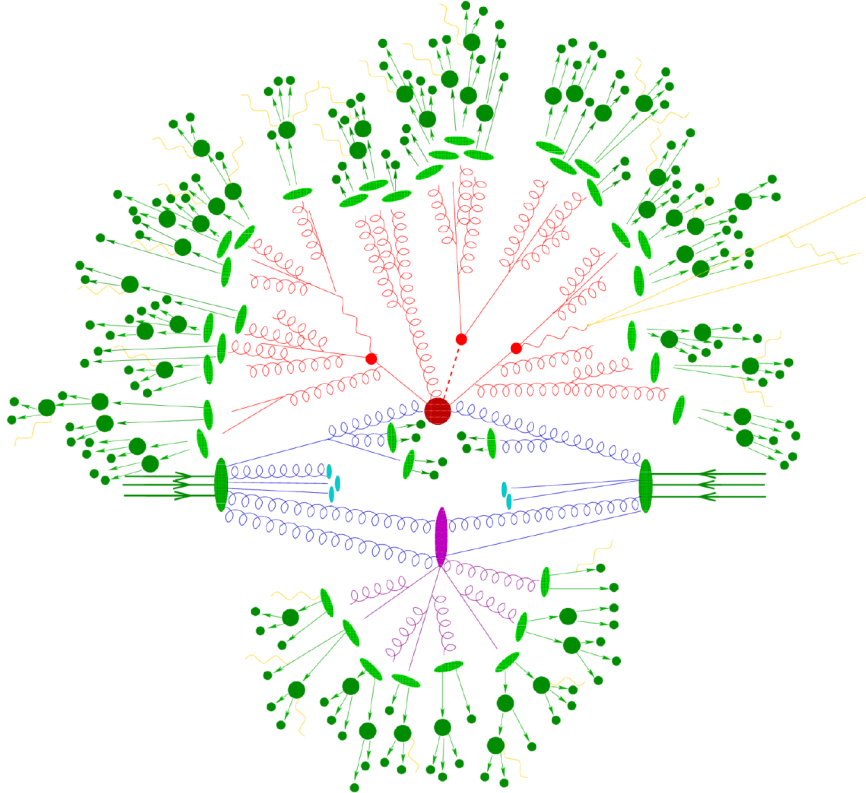


Fig. 1.5: Schematic of a hadron-hadron collision indicating different parts of the simulation by color. The hard interaction is depicted as the red blob in the center. Also shown in red, surrounding the red blob, is the parton shower. The light green ellipses indicate the parton-to-hadron transition, followed by hadron decays displayed in darker green and photon radiation in yellow. The purple ellipse and the attached gluons show a potential secondary interaction, the underlying event. On a horizontal line with the incoming hadrons, also beam remnants can be seen. This picture was taken from ref. [44].

The MC programs employed to simulate these parts are just as multifaceted as the underlying physics. MC generators such as `MadGraph5_aMC@NLO` [45], or short `MG5_aMC`, the `POWHEG-BOX` [46–48], `Sherpa` [49, 50] and `WHIZARD` [51] focus on simulating the *hard* interaction. They receive matrix elements from in- or external matrix element generators and perform a numerical phase-space integration based on MC strategies to compute the total cross section of a process. Afterwards, or sometimes also during this integration, they generate *partonic events*, i.e., collections of particle flavors, colors and momenta, which can be written to disk to directly be analyzed or processed further.

The parton shower then acts on these partonic events. It performs a cascade of subsequent soft or collinear splittings on the hard partons until they hadronize to semi-stable hadrons, which then further decay down

to long-lived or stable particles. Although most MC programs are able to simulate both the partonic events as well as some parton shower, most have special expertise in one of the two areas. We call the latter Shower Monte Carlos (SMCs) to differentiate the two. The two most commonly employed SMCs are PYTHIA [52] and HERWIG [53].

In any experiment, most of the long-lived or stable particles will finally end up being detected in one of the many layers of modern particle detectors. For the simulated predictions to be meaningful, also this interaction has to be simulated. Often, they also involve MC strategies, but we refer to them as *detector simulations*. In this thesis, only the first two kinds of MC generators will be relevant and we will put a strong focus on the MC generators for the hard process.

There are two complementary approaches considering these MC programs. On the one hand, there are many programs written specifically to simulate some specific process or a subclass of processes. These are typically less flexible and harder to use but allow spearhead calculations of the highest-order precisions. On the other hand, there are *general purpose* MCs; programs whose intention is to be able to simulate a large variety of diverse kinds of processes, often also for diverse collider setups. These programs are frequently developed over multiple decades, growing parallel to the large-scale experiments at which they are employed as workhorses for signal and background processes alike. Being able to simulate different kinds of processes with the same tools comes with the advantage of significantly increased useability and comparability of different analyses required for large-scale experiments. WHIZARD and also MG5\_aMC belong to this class of MC generators. In sec. 4, we will further elaborate on the technical details of the former, WHIZARD.

Realistic studies require the simulation of the hard process performed by one of the MC generators as well as the parton shower and hadronization, which are taken care of by one of the SMCs programs. In a LO simulation, both tools can be implemented rather independently and a clear interface such as the Les Houches Interface for User Processes (LHIUP) [54, 55] can be defined to manage the communication between the two programs. If the parton shower is to be applied to an NLO calculation, however, the two procedures have to be more intertwined, as both the real radiation in the NLO description of the hard process and the parton shower, add additional emissions to the process. In a naive implementation, both programs would simulate emissions of the same energy scales, spoiling the accuracy by generating too much radiation. In order to avoid this, *parton-shower-matching schemes*, algorithms to avoid this *double counting*, have been invented and are widely employed. We will discuss one such matching scheme, the POWHEG matching [46, 47, 56] scheme, in great detail in sec. 3 and show applications of it in sec. 6.

Part I

Part 1 – Automation of NLO corrections:  
fixed order and beyond

## 2 The Frixione-Kunszt-Signer subtraction scheme

After a general introduction to NLO computations and subtraction schemes, this section will focus on the technical details of the FKS subtraction scheme as implemented in the MC event generator WHIZARD.

### 2.1 NLO computations and subtraction schemes

#### 2.1.1 Counting coupling constants

First, we should clarify which terms we aim to compute. Even when computing LO cross sections, there may be several contributions. Considering for example, the process  $u\bar{u} \rightarrow u\bar{u}$ , there are three contributions, i.e.  $u\bar{u} \rightarrow g \rightarrow u\bar{u}$  at order  $\mathcal{O}(\alpha_S^2 \alpha^0)$ ,  $u\bar{u} \rightarrow \gamma/Z \rightarrow u\bar{u}$  at order  $\mathcal{O}(\alpha_S^0 \alpha^2)$  and their interference at order  $\mathcal{O}(\alpha_S^1 \alpha^1)$ .

In general, the orders contributing to the total LO cross section reach from the highest order in the strong coupling  $\mathcal{O}(\alpha_S^N \alpha^m)$  to the highest order in the EW coupling  $\mathcal{O}(\alpha_S^n \alpha^M)$ , where  $N \geq n, M \geq m$  with a constant total power of couplings  $N + m = n + M$ . This series of contributions consists of alternating dominant terms and subleading interference terms. Especially at the LHC, the size of the dominant terms typically decreases in this order.

Each of these contributions may receive NLO corrections of each type, NLO QCD and NLO EW. This results in a scheme of possible contributions as shown in fig. 2.1.

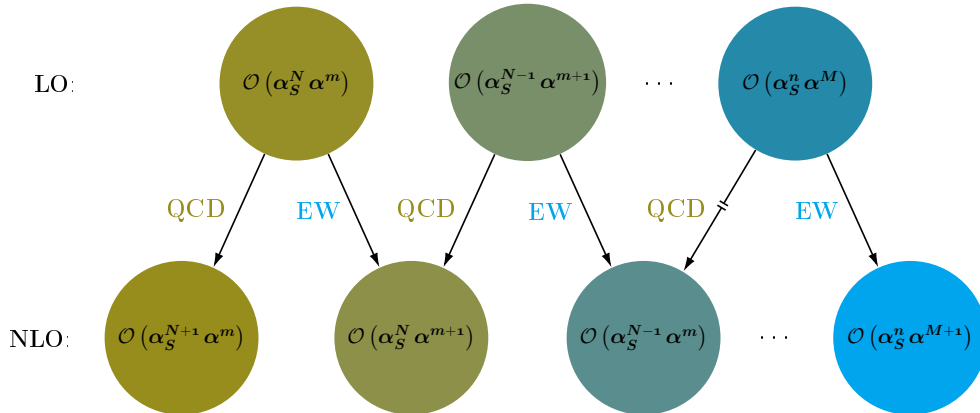


Fig. 2.1: Contributions to the total mixed QCD-EW NLO cross section. The LO contributions consist of an alternating series of dominant Born terms and subleading interference terms. Each LO term may receive QCD (olive) and EW (light blue) corrections connecting it to two different NLO terms. The leftmost lower blob represents the pure QCD correction; the rightmost lower blob the pure EW correction. All inner terms receive mixed corrections from a dominant and an adjacent subleading Born term.

As we can see, the majority of NLO terms is made up of both NLO QCD as well as NLO EW corrections to different LO terms. To ensure a full cancellation of all the divergences, it is crucial to consider both types of corrections simultaneously. Thus, we refer to this type of corrections as *mixed corrections*.

There are two terms, however, for which mixed corrections are not required. It is the QCD correction to the LO term of the highest order in  $\alpha_S$  and the EW correction to the LO term of the highest order in  $\alpha$ . These are the *pure* NLO QCD and the *pure* NLO EW terms, respectively.

Throughout this thesis, we will mostly focus on the pure QCD contribution to the total NLO cross section. It is usually the dominant one as  $\alpha_S \gg \alpha$ . However, many results, especially the phase-space construction, will be entirely applicable for NLO EW and mixed corrections as well.

### 2.1.2 Contributions to the cross section at next-to-leading order

In NLO computations, we aim to compute the first-order correction to the LO cross section. The LO cross section is given by the integral of the squared LO matrix element

$$\sigma^{\text{LO}} = \int |\mathcal{M}^{(0)}|^2 d\Phi_n \quad . \quad (2.1)$$

To obtain this simple relation, we absorb the flux factor and the  $\delta$  distribution forcing four-momentum conservation in the phase-space measure  $d\Phi_n$ .

As aforementioned in the introduction, sec. 1, the NLO cross section receives contributions<sup>4</sup> from squared Born matrix elements,  $\mathcal{B}$ , squared real matrix elements,  $\mathcal{R}$ , and squared virtual matrix elements,  $\mathcal{V}$ ,

$$\sigma^{\text{NLO}} = \int \mathcal{B}(\Phi_n) d\Phi_n + \int \mathcal{R}(\Phi_{n+1}) d\Phi_{n+1} + \int \mathcal{V}(\Phi_n) d\Phi_n \quad . \quad (2.2)$$

We then construct a subtraction term,  $\mathcal{S}$ , for the real contribution such that by virtue of the KLN theorem, all contributions are separately finite.

$$\sigma^{\text{NLO}} = \int \mathcal{B}(\Phi_n) d\Phi_n + \underbrace{\int (\mathcal{R}(\Phi_{n+1}) - \mathcal{S}(\Phi_{n+1})) d\Phi_{n+1}}_{\text{finite by construction}} + \underbrace{\int \left( \mathcal{V}(\Phi_n) + \left( \int_{\text{rad}} \mathcal{S}(\Phi_{n+1}) d\Phi_{\text{rad}} \right) d\Phi_n \right)}_{\text{finite by KLN}} \quad (2.3)$$

This is equivalent to but more detailed than eq. (1.4). There is some freedom in the choice of the subtraction term, which can be used to formulate different subtraction schemes.

### 2.1.3 Subtraction schemes

The common idea of most subtraction schemes is to subdivide the real phase space into *singular regions* such that the divergences in each of these regions are simple enough to construct subtraction terms for each of the singular regions separately.

Most subtraction schemes can be assigned to one of two classes. The first are the dipole-based subtraction mechanisms, the most common one being Catani-Seymour (CS) subtraction [57, 58] but also antenna subtraction [59–61] belongs to this class. The general idea of dipole subtraction schemes is to organize the singular regions of the real phase space into *dipoles*, consisting of two partons originating from a splitting and a *spectator*, such that each dipole corresponds to one of the  $n + 1$  particle states that are degenerate with a given  $n$  particle Born state. They then construct a subtraction term in each region according to a universal factorization formula. Summarized, this means that CS subtraction performs a  $3 \rightarrow 2$  mapping from the real to the Born phase space to organize the singular regions.

This is fundamentally different in the FKS subtraction scheme. It was initially applied to three-jet production at a hadron collider [62] and further generalized two years later [63]. Instead, the FKS subtraction builds on a given Born configuration constructing the singular regions of the real phase space by parametrizing just the two particles resulting from the splitting. This corresponds to a  $1 \rightarrow 2$  mapping from the Born to the real phase space.

Because of the reduced number of particles characterizing a divergent phase-space region in FKS compared to CS, there are, in general, less FKS subtraction terms to be computed, giving the FKS subtraction a better performance scaling for processes with many potential emitters [64]. In the FKS approach, the

<sup>4</sup>In sec. 2.7.1, we will encounter a fourth contribution connected to PDFs, the *DGLAP remnant*. For now, we consider it to be part of the virtual term.

singular regions are distinct and independent, making it straightforwardly parallelizable. However, the Born to real mapping of FKS requires the real phase space to be parametrized in the same coordinates as the subtraction terms, which is a disadvantage compared to the CS approach working with any generic phase-space parametrization.

In terms of event generation, the CS subtraction is better compatible with dipole-based showers because of the structural similarities in the shower and the subtraction prescription. On the other hand, in the FKS approach, the fixed Born momentum configuration simplifies the organization of subtraction terms in generated fixed next-to-leading order (fNLO) events. It is also better suited for matching schemes like MC@NLO [45, 56] or POWHEG [46, 47] matching for the fact that both matching algorithms also operate on the identified singular regions which are in a one-to-one correspondence with IR singularities, which, in turn, are at the core of the shower mechanism.

A third, less often applied subtraction scheme is the Nagy-Soper subtraction scheme [65, 66]. It is based on splitting functions in an improved parton shower [67–69], promising to facilitate the matching to parton showers. It scales comparable to FKS while keeping the phase-space parametrization general. However, this comes at the cost of more complex expressions for the integrated subtraction terms. It has not been implemented in a general purpose MC generator so far.

The CS subtraction mechanism has been implemented in `Sherpa` [70] while the FKS subtraction was preferred for `MG5_aMC` [64] and the `POWHEG-BOX` [47, 48]. In `WHIZARD`, the FKS subtraction scheme has been implemented in full generality over the course of several doctoral theses [71–73] and the present work. Its implementation as well as application to a variety of processes at NLO QCD and NLO EW is also discussed in detail in ref. [7]. For this reason, it is the FKS subtraction scheme as implemented in `WHIZARD`, which we will focus on in this section, beginning with some general notational remarks and the phase-space construction.

## 2.2 Notation

We will first clarify the notation used in this thesis. It is mostly adapted from refs. [47, 64, 73]. Throughout this thesis, we use natural units such that

$$\hbar = c = 1 \quad . \quad (2.4)$$

Furthermore, we choose the metric signature  $(+, -, -, -)$ , so that the square of a four-momentum is given by

$$p^2 = (p^0)^2 - p_x^2 - p_y^2 - p_z^2 = E^2 - (\vec{p})^2 = m^2 \quad , \quad (2.5)$$

where  $p^0 = E$  is its energy,  $\vec{p}$  its three-momentum and  $m$  its mass.

Computing NLO corrections to scattering processes, all momenta will belong to one of two phase spaces. The *Born phase space* of the underlying  $2 \rightarrow n$  process is given by

$$\bar{\Phi}_n = \{\bar{k}_\oplus, \bar{k}_\ominus, \bar{k}_3, \dots, \bar{k}_{n+2}\} \quad , \quad (2.6)$$

where the indices  $\oplus$  and  $\ominus$  denote the initial-state momenta parallel and anti-parallel to the beam axis along the positive  $z$  direction. The final-state particles are numbered from 3 onwards to implicitly leave  $\bar{k}_1 \equiv \bar{k}_\oplus$  and  $\bar{k}_2 \equiv \bar{k}_\ominus$  for the two initial-state particles. Here, we used barred momenta to stress their connection to the Born phase space. In some occasions, we will instead decorate quantities of the Born process with an index  $\mathcal{B}$ .

The *real phase space* has to include one more four-momentum for the radiated particle. Also, the emission

may boost the remaining particles, so we need a different set of four-momenta for the real phase space. We denote it as

$$\Phi_{n+1} = \{k_{\oplus}, k_{\ominus}, k_3, \dots, k_{n+2}, k_{n+3}\} \quad , \quad (2.7)$$

omitting the bars this time. If we want to stress that a quantity belongs to the real phase space, we may use an index  $\mathcal{R}$ .

The described physics will be invariant under a reordering of the final-state particles. We can thus always assume that the radiated momentum is given by the last one in the list, i.e.,  $k_{n+3}$ . For final-state splittings, we often assume that  $k_{n+2}$  is the emitter's momentum after the real splitting.

We require both sets of four-momenta to fulfill energy-momentum conservation, i.e.,

$$\bar{k}_{\oplus} + \bar{k}_{\ominus} = \sum_{i=3}^{n+2} \bar{k}_i \quad \text{and} \quad k_{\oplus} + k_{\ominus} = \sum_{i=3}^{n+3} k_i \quad . \quad (2.8)$$

This momentum conservation is expressed by the  $\delta$  distribution in the  $n$ -body phase-space element

$$d\Phi_n(\bar{k}_{\oplus}, \bar{k}_{\ominus}, \bar{k}_3, \dots, \bar{k}_{n+2}) = (2\pi)^4 \delta^4 \left( \bar{k}_{\oplus} + \bar{k}_{\ominus} - \sum_{i=3}^{n+2} \bar{k}_i \right) \prod_{i=3}^{n+2} \frac{d^3 \bar{k}_i}{(2\pi)^3 2\bar{k}_i^0} \quad , \quad (2.9)$$

in which we will additionally absorb a factor of  $dx_{\mathcal{B},\oplus} dx_{\mathcal{B},\ominus}$  if emissions from the initial state are possible. If this is the case, we need to distinguish up to three different center-of-mass energies. The hadronic center-of-mass energy is the largest one. It will be denoted by  $S = (K_{\oplus} + K_{\ominus})^2$  where  $K_{\oplus}$  and  $K_{\ominus}$  are the four-momenta of the incoming hadrons beams. The partonic center-of-mass energy of the Born process will be given by

$$s_{\mathcal{B}} = (\bar{k}_{\oplus} + \bar{k}_{\ominus})^2 = x_{\mathcal{B},\oplus} x_{\mathcal{B},\ominus} S \quad , \quad (2.10)$$

where  $x_{\mathcal{B},\oplus}$  are the energy fractions of the partons relative to the protons, i.e. the Bjorken- $x$ , so that

$$\bar{k}_{\oplus} = x_{\mathcal{B},\oplus} K_{\oplus} \quad . \quad (2.11)$$

In case of an emission from the initial state, it is different from the partonic center-of-mass energy of the real process, which is given by

$$s_{\mathcal{R}} = (k_{\oplus} + k_{\ominus})^2 = x_{\mathcal{R},\oplus} x_{\mathcal{R},\ominus} S \quad \text{where} \quad k_{\oplus} = x_{\mathcal{R},\oplus} K_{\oplus} \quad . \quad (2.12)$$

In general, it is  $s_{\mathcal{R}} \geq s_{\mathcal{B}}$ , which may be interpreted such that in FKS, the energy for the radiation is "borrowed" from the incoming hadron instead of from the Born system. In the case of equality, we may simply denote them as  $s$ . We will derive the exact relation in sec. 2.4.3.

## 2.3 The singular regions

As mentioned in sec. 2.1.3, the FKS subtraction mechanism follows a divide and conquer principle by identifying and organizing divergent phase-space regions into singular regions or *alpha regions (ALRs)*, in such a way that in each ALR there is no more than a single pair of particles, whose momenta constitute a soft, a collinear or both types of IR divergences. We call such a pair of partons an *FKS pair*.

### 2.3.1 The FKS pairs

Focusing on QCD corrections, there will be three types of FKS pairs [72, 73]:

$(q, g)$  A(n anti)quark emitting a gluon produces a soft singularity for vanishing gluon energy and/or a collinear singularity if the gluon is emitted collinear to a massless (anti)quark.

$(\bar{q}, q)$  Two massless quarks resulting from a  $g \rightarrow q\bar{q}$  splitting may give rise to a collinear singularity.

$(g, g)$  Two gluons resulting from a  $g \rightarrow gg$  splitting are possibly both collinear and soft divergent.

These pairs are exemplary for a final-state splitting when computing NLO QCD corrections. The FKS pairs for initial-state splittings and for EW corrections follow the same rules as described in this section.

The pairs are ordered so that the second particle is always massless. If possible, it is the gluon. The mirrored pairs, e.g.,  $(g, q)$ , give rise to the same divergences but would also describe the same process as their counterparts. We thus do not need to take them into account explicitly.

To identify these FKS pairs, we need to introduce a notation describing the flavors present in the process. We will label the Born flavor structure with

$$f_{\mathcal{B}} = \{f_{\mathcal{B}}^1, f_{\mathcal{B}}^2, \dots\} \quad (2.13)$$

and equivalently, the real flavor structure  $f_{\mathcal{R}}$ . We will assume an ordering of the flavors in each flavor structure. Similar to refs. [64, 72, 73], we define

- $n_I$  := number of initial-state particles,
- $n_{\emptyset}$  := number of non-strongly interacting final-state particles,
- $n_F$  := index of the first strongly interacting particle,
- $n_H$  := number of strongly-interacting massive final-state particles,
- $n_L$  := number of strongly-interacting massless final-state particles,
- $n_S$  := total number of strongly-interacting particles,

where more specifically,  $n_F$  takes the values 1, 2, 3 for hadron-hadron, lepton-hadron and lepton-lepton collisions, respectively.

Using these definitions, we can impose an ordering of the flavor structures so that each flavor structure contains

1. the initial-state partons  $\{f^i \mid 1 \leq i \leq n_I\}$  followed by
2. all the non-QCD particles  $\{f^i \mid n_I + 1 \leq i \leq n_I + n_{\emptyset}\}$ ,
3. the heavy final-state partons  $\{f^i \mid n_I + n_{\emptyset} + 1 \leq i \leq n_I + n_{\emptyset} + n_H\}$  and
4. lastly the light, i.e. massless, final-state partons  $\{f^i \mid n_I + n_{\emptyset} + n_H + 1 \leq i \leq n_I + n_{\emptyset} + n_H + n_L\}$ .

Additionally, we sort the particles within each group so that particles and antiparticles appear pair-wise with antiparticles first.

On the ordered real flavor structures, we can now formally define the set of FKS pairs as

$$\begin{aligned} \mathcal{P}_{\text{FKS}}(f_{\mathcal{R}}) := & \left\{ (i, j) \mid n_F \leq i \leq n_I \text{ (ISR)} \quad \text{or} \quad n_I + n_{\emptyset} < i < n_I + n_{\emptyset} + n_H + n_L \text{ (FSR)}, \right. \\ & n_I + n_{\emptyset} + n_H + 1 \leq j \leq n_I + n_{\emptyset} + n_H + n_L, \quad j > i, \\ & \left. \mathbb{J}(\Phi_{n+1}) \mathcal{R}(\Phi_{n+1}, f_{\mathcal{R}}) \rightarrow \infty \text{ if } E_j \rightarrow 0 \text{ and/or } \vec{k}_i \parallel \vec{k}_j \right\}. \end{aligned} \quad (2.14)$$

In each FKS pair, we call particle  $i$  the *emitter* and  $j$  the *radiated* particle. The FKS pairs as defined by eq. (2.14) make sure that the *radiated* particle is always massless,  $f_{\mathcal{R}}^j$  comes after  $f_{\mathcal{R}}^i$  in the flavor structure

and we do not double count the symmetric pairs,  $(i, j)$  and  $(j, i)$ .

In eq. (2.14) we have also silently introduced the *Jet measurement function*  $\mathbb{J}$ . It is present to ensure the finiteness of the Born-like partonic short distance cross section. This is necessary as the FKS subtraction mechanism will only deal with phase-space divergences arising from the real splitting. The most common method to restrict the  $n$ -body phase space to IR finite regions only, is to apply an IR safe jet-clustering algorithm and require at least  $n_L$  well-defined reconstructed jets. We will further elaborate on this condition when discussing the Born contribution in sec. 2.5.

At this point, we want to emphasize that the indices in the FKS pair always refer to the real flavor structure  $f_{\mathcal{R}}$ , which contains the *external* legs of the process. This means that the FKS pairs describing flavor-changing splittings depicted in fig. 2.2a and fig. 2.2b will be  $(g, \bar{q})$  and  $(\bar{q}, q)$  respectively. In this case, the "emitter" will somewhat unintuitively have a different flavor than the splitting particle that was part of the Born flavor structure.



Fig. 2.2: Exemplary flavor-changing splittings.

As a practical example of the labeling defined in this section, tab. 1 shows all the ALRs for the process  $e^+e^- \rightarrow jjj$  as generated by WHIZARD. Restricted to just two light quark flavors, this process has only two different Born flavor structures  $f_{\mathcal{B}}$  labeled by  $i_{\mathcal{B}}$ . With three light QCD particles in the Born process, there are three possible final-state emitters 3, 4 and 5. Each emitter may radiate a gluon. Additionally, the Born gluon may split into one of both allowed flavors. This makes 5 different singular regions per underlying Born flavor structure; 10 singular regions in total.

For example, in ALR 1, a gluon present in the Born process splits into two quarks matching the flavor of the two existing quarks. The matrix element will be invariant under a reordering of the final-state particles. We thus need to take into account all possible  $(q, \bar{q})$  pairs in  $\mathcal{P}_{\text{FKS}}$ .

Considering ALRs 2 – 4, we see that we keep apart these three ALRs although they have the same flavor structures. The only difference is the associated emitter. The reason is that different emitters will lead to different real phase-space points (PSPs) even for the same set of Born momenta, as we will see in sec. 2.3.2. On the other hand, regions sharing the same emitter index will also share the same phase-space parametrization.

Also regions 5 and 6 are instructive. A gluon splitting connects the Born and the real process in both regions. Although only a single gluon is present in the Born flavor structure, two  $(q, \bar{q})$  FKS pairs must be considered. The reason is again that the real matrix element does not know about any specific emitter and will thus diverge if either pair of same-flavored quarks become collinear to each other. Due to the different ordering of the flavors in the real flavor structure, both ALRs are assigned the same emitter ID  $\mathbf{em}$ , which, however, refers to different quark flavors.

Taking into account all relevant FKS pairs is crucial for a subdivision of the real phase space in such a way

that only a single soft and/or collinear divergence remains in each region and no specific region of the phase space is double counted by the phase-space integration. This includes correctly defining all the FKS pairs, especially also taking into account FKS pairs not fitting the same but a different ALR's underlying Born flavor structure as in ALR 5 and 6 in tab. 1.

$\alpha_r$	$f_{\mathcal{R}}$	$i_{\mathcal{R}}$	em	mul	$\mathcal{P}_{\text{FKS}}$	$f_{\mathcal{B}}$	$i_{\mathcal{B}}$
1	[11,-11,-2,2,-2, 2]	1	5	4	{(3, 4), (3, 6), (4, 5), (5, 6)}	[11,-11,-2,2,21]	1
2	[11,-11,-2,2,21,21]	2	3	2	{(3, 5), (3, 6), (4, 5), (4, 6), (5, 6)}	[11,-11,-2,2,21]	1
3	[11,-11,-2,2,21,21]	2	4	2	{(3, 5), (3, 6), (4, 5), (4, 6), (5, 6)}	[11,-11,-2,2,21]	1
4	[11,-11,-2,2,21,21]	2	5	1	{(3, 5), (3, 6), (4, 5), (4, 6), (5, 6)}	[11,-11,-2,2,21]	1
5	[11,-11,-2,2,-1, 1]	3	5	1	{(3, 4), (5, 6)}	[11,-11,-2,2,21]	1
6	[11,-11,-1,1,-2, 2]	4	5	1	{(3, 4), (5, 6)}	[11,-11,-1,1,21]	2
7	[11,-11,-1,1,-1, 1]	5	5	4	{(3, 4), (3, 6), (4, 5), (5, 6)}	[11,-11,-1,1,21]	2
8	[11,-11,-1,1,21,21]	6	3	2	{(3, 5), (3, 6), (4, 5), (4, 6), (5, 6)}	[11,-11,-1,1,21]	2
9	[11,-11,-1,1,21,21]	6	4	2	{(3, 5), (3, 6), (4, 5), (4, 6), (5, 6)}	[11,-11,-1,1,21]	2
10	[11,-11,-1,1,21,21]	6	5	1	{(3, 5), (3, 6), (4, 5), (4, 6), (5, 6)}	[11,-11,-1,1,21]	2

Tab. 1: FKS table for the process  $e^+e^- \rightarrow jjj$  restricted to  $j \in \{d, \bar{d}, u, \bar{u}, g\}$ . The index  $\alpha_r$  labels the ALRs,  $f_{\mathcal{B}}$  and  $f_{\mathcal{R}}$  are the Born and the real flavor structure given in terms of PDG IDs [74] labeled by  $i_{\mathcal{B}}$  and  $i_{\mathcal{R}}$ , respectively.  $\mathcal{P}_{\text{FKS}}$  denotes the ALRs set of possible FKS pairs. The index **em** refers to the real flavor structure defining the emitter relevant in this ALR, while **mul** is a multiplicity factor counting the number of equivalent and thus omitted regions.

### 2.3.2 Parametrization of the radiation phase-space

The subtraction of divergences in the FKS scheme will be implemented individually per ALR. To construct subtraction terms, we need a mapping between the  $n$ -body Born phase space  $\bar{\Phi}_n$  and the  $n+1$ -body real phase space  $\Phi_{n+1}$ . One characteristic of the FKS scheme is the Born-to-real mapping, meaning that the real phase space will be constructed based on a Born phase space and a generated *radiation phase space*  $\Phi_{\text{rad}}$  in a factorized approach such that

$$d\Phi_{n+1}^{(\alpha_r)} = d\bar{\Phi}_n d\Phi_{\text{rad}}^{(\alpha_r)} \quad (2.15)$$

in each ALR labeled by  $\alpha_r$ . We will discuss this phase-space construction in the following subsections.

The inverse mapping from the real phase space to the Born phase space is straightforward. Given the real flavor structure, the FKS pair and the real kinematics, i.e., the set of real momenta, we can map the real phase space to the *underlying Born* phase space by replacing the FKS pair with a single particle. In the case of a singular region with a soft divergence, we can simply delete the particle becoming soft. In the case of a singular region with a collinear divergence and final-state radiation (FSR), the substituting particle will carry the sum of the FKS pair's momenta. For collinear divergences in ISR, we remove both the radiated parton and the emitter so that only the momentum fraction of the parton after the radiation remains [64, 73]. In all three cases, momentum conservation is ensured.

After determining the set of momenta, the inserted particle's flavor can be determined from the existing vertices. With a subsequent relabeling of the momenta according to the procedure described close to eq. (2.13), we can determine  $d\bar{\Phi}_n$ . This mapping is unique given the real kinematics, flavors and the FKS pair. The same is not true for the opposite mapping, as the real phase space features three degrees of freedom more than the underlying Born phase space.

We parametrize the radiation phase space in the three *FKS variables*  $(\xi, y, \phi)$  such that

$$d\Phi_{\text{rad}}^{(\alpha_r)} = \mathcal{J}^{(\alpha_r)}(\xi, y, \phi) d\xi dy d\phi \quad , \quad (2.16)$$

where  $\mathcal{J}$  is the Jacobian (determinant) for this parametrization. We will deduce it for three different cases in sec. 2.4. If not explicitly specified by their indices, they always refer to the FKS pair  $(i, j)$  in  $\mathcal{P}_{\text{FKS}}$  where  $i$  coincides with the ALR's emitter, i.e.

$$\xi \equiv \xi_j \quad , \quad y \equiv \begin{cases} y_{ij} & \text{for FSR} \\ y_j & \text{for ISR} \end{cases} \quad \text{and} \quad \phi \equiv \phi_j \quad . \quad (2.17)$$

They parametrize

- the energy of the radiated particle

$$\xi := \frac{2E_j}{\sqrt{s_{\mathcal{R}}}} \quad (2.18)$$

rescaled to half the available total energy  $\frac{\sqrt{s_{\mathcal{R}}}}{2}$ . For FSR off a massless emitter, it is limited by the total energy of the emitting particle before the splitting such that

$$0 < \xi < \xi_{\text{max}} := \frac{2\bar{k}_i^{-0}}{\sqrt{s_{\mathcal{R}}}} \leq 1 \quad . \quad (2.19)$$

where we find  $\xi_{\text{max}} = 1$  only if the recoil system is massless, as in, e.g.,  $e^+e^- \rightarrow q\bar{q}$ .

The upper energy limit will be more complicated for massive emitters and ISR. We will derive them explicitly in secs. 2.4.2 and 2.4.3.

- the polar separation of the radiated particle with respect to the emitter direction after the emission, in case of FSR, or the beam axis in positive  $z$  direction, in case of ISR, in form of a cosine such that

$$(-1, 1) \ni y := \begin{cases} \cos(\theta_{i,j}) & = \frac{\bar{k}_i \cdot \bar{k}_j}{|\bar{k}_i| |\bar{k}_j|} & \text{for FSR} \\ \cos(\theta_{\oplus,j}) & = \frac{\bar{k}_{\oplus} \cdot \bar{k}_j}{|\bar{k}_{\oplus}| |\bar{k}_j|} & \text{for ISR} \end{cases} \quad . \quad (2.20)$$

This implies that for ISR, the sampled phase-space points will be independent of the emitter reducing the number of different PSPs to compute. Again, we refer the derivation for massive emitters to sec. 2.4.2.

- the azimuthal angle between the radiated particle and the same reference direction as in the definition of  $y$

$$\phi \in (0, 2\pi) \quad . \quad (2.21)$$

Although it is one of the three FKS parameters,  $\phi$  will not play an important role, as for incoming beams along the  $z$  axis, we can always assume  $\phi = 0$  and rotate the phase-space point by an angle  $\phi$  at the end. The divergence structure instead manifests in  $\xi$  and  $y$ . For  $\xi \rightarrow 0$ , the energy of the radiation vanishes, resulting in a soft divergence, while for  $y \rightarrow 1$  the angle between the emitter and the radiated particle vanishes, leading to a collinear divergence. For ISR, we additionally have to take into account that both initial-state partons are separated by exactly  $180^\circ$  in the polar angle<sup>5</sup>. This implies that an emission anti-collinear to

<sup>5</sup>In reality, initial-state partons may have intrinsic transverse momentum, violating this statement. In simulations, however, this effect is only added at a later stage, often by the SMC.

one initial-state parton is collinear to the other. We thus have to take into account both collinear limits,  $y \rightarrow \pm 1$  for emissions from the initial state to describe all collinear divergences.

Technically, we use the same set of FKS parameters  $(\xi, y, \phi)$  for all ALRs. Due to the fact that the meaning of  $y$  depends on the emitter direction, this set of parameters does not refer to geometrically identical PSPs for every single set of parameters. However, as the MC integration covers the whole fiducial phase space, they are merely mirrored mappings of the same total real phase space so that in the end, the terms of all ALRs will be integrated over the same total real phase space<sup>6</sup>.

### 2.3.3 The $S$ functions

#### General requirements

At this point, we have introduced particle labels to identify pairs of particles responsible for divergent regions of the real phase space. We also chose a parametrization so that a region is collinear divergent if  $y \rightarrow \pm 1$  and soft divergent if  $\xi \rightarrow 0$ . Consequently, the next step in the FKS approach is to define a set of functions able to subdivide the real phase space in such a way that in each ALR, a single collinear and/or soft divergent region remains. In the FKS literature [47, 62, 64, 72, 73], they are in general called  $S$  functions,  $S_{ij}^{\alpha_r}$ .

The  $S$  functions will be weights between 0 and 1 defined for each FKS pair  $(i, j) \in \mathcal{P}_{\text{FKS}}^{\alpha_r}$  in each ALR across the entire phase space reducing the contributions from PSPs in which a pair other than  $(i, j)$  become soft or collinear. Effectively, we can absorb these weights into the real matrix element

$$\mathcal{R}_{ij} := S_{ij}^{\alpha_r} \mathcal{R} \quad , \quad (2.22)$$

where  $i$  is the emitter of the ALR  $\alpha_r$  allowing to directly integrate the product of both over the phase space. For ease of notation, we keep the dependence of  $S$  and  $\mathcal{R}$  on  $f_{\mathcal{R}}$  and  $\Phi_{n+1}$  implicit.

There is some freedom in the choice of the  $S$  functions. In the original FKS publication [62] they were defined as a product of Heaviside step functions so that  $S_{ij}^{\alpha_r} \in \{0, 1\}$ , effectively slicing the phase space into disjunct regions. It was later recognized [75] that smooth functions improve the numerical behavior.

There are some general conditions these functions must fulfill. Following ref. [47], we obviously require that the  $S$  functions are a partition of unity<sup>7</sup>,

$$\sum_{(i,j) \in \mathcal{P}_{\text{FKS}}^{\alpha_r}} \mathcal{R}_{ij} = \mathcal{R} \quad \implies \quad \sum_{(i,j) \in \mathcal{P}_{\text{FKS}}^{\alpha_r}} S_{ij}^{\alpha_r} = 1 \quad (2.23)$$

at each PSP in  $\Phi_{n+1}$ .

Also, only a single divergence should remain in each ALR. We achieve this by requiring that they vanish in regions where any other FKS pair becomes collinear or soft, i.e.

$$\lim_{\vec{k}_k \parallel \vec{k}_l} S_{ij}^{\alpha_r} = 0 \quad \forall \mathcal{P}_{\text{FKS}}^{\alpha_r} \ni (k, l) \neq (i, j) \quad \text{and} \quad m_{f_{\mathcal{R}}}^i = 0 \quad (2.24)$$

$$\text{as well as} \quad \lim_{E_k \rightarrow 0} S_{ij}^{\alpha_r} = 0 \quad \forall k \notin \{i, j\} \mid f_{\mathcal{R}}^k \in \{g, \gamma\} \wedge \exists (l, k) \in \mathcal{P}_{\text{FKS}}^{\alpha_r} \quad (2.25)$$

<sup>6</sup>This is true if we consider pure NLO QCD or NLO EW corrections. When computing mixed corrections, however, some ALRs will feature the radiation of a QCD parton while others will feature photon radiation. In this case, if jet clustering as well as photon recombination (c.f. sec. 2.5) are applied, even the total phase spaces may be different.

<sup>7</sup>It is important here that the  $S$  functions sum up to unity if summed over  $(i, j)$  in a single fixed ALR  $\alpha_r$ , not if summed over all ALRs as different ALRs are not always evaluated at the same real PSPs as mentioned earlier. We will come back to this in sec. 5.1.

taking values between 0 and 1 anywhere else.

On the other hand, in regions where the particles  $i$  and  $j$  become collinear, we require

$$\lim_{\vec{k}_i \parallel \vec{k}_j} S_{ij}^{\alpha_r} = h_{ij} := \begin{cases} \frac{2E_i}{E_i + E_j} & \forall (i, j) \in \mathcal{P}_{\text{FKS}}^{\alpha_r} \mid (f_{\mathcal{R}}^i, f_{\mathcal{R}}^j) = (g, g) \text{ if } n_I < i, j \\ 1 & \text{else} \end{cases} . \quad (2.26)$$

We need to special case  $(f_{\mathcal{R}}^i, f_{\mathcal{R}}^j) = (g, g)$  as in these regions, also a soft *emitter* would give rise to a divergence. We already desymmetrized  $\mathcal{P}_{\text{FKS}}$  in eq. (2.27) to avoid counting this region twice. To these regions, we apply the so-called *double FSR factor* [48]  $h_{ij}$ . This removes the divergence for a soft gluon at position  $i$  compensating the left out half of the phase space by a factor of 2 for the rest.

In regions where the particles  $i$  and  $j$  become soft, we require

$$\lim_{E_j \rightarrow 0} S_{ij}^{\alpha_r} = c_{ij} \quad \forall \mathcal{P}_{\text{FKS}}^{\alpha_r} \ni (i, j) \mid f_{\mathcal{R}}^j \in \{g, \gamma\} \quad , \quad (2.27)$$

where the  $c_{ij} \in \mathbb{R}$  are constrained by

$$0 < c_{ij} \leq 1 \quad \text{and} \quad \sum_{(i,j) \in \mathcal{P}_{\text{FKS}}^{\alpha_r}} c_{ij} = 1 \quad . \quad (2.28)$$

It is not always  $c_{ij} \equiv 1$  because a single radiated soft gluon may constitute a soft divergent FKS pair with more than a single emitter.

### Explicit choice of $S$ functions

Explicitly, we implemented  $S$  functions recommended by refs. [47, 64] as

$$S_{ij}^{\alpha_r} := \frac{h_{ij}}{\mathcal{D} d_{ij}} \quad (2.29)$$

with normalization

$$\mathcal{D} := \sum_{(k,l) \in \mathcal{P}_{\text{FKS}}} \frac{h_{kl}}{d_{kl}} \quad (2.30)$$

and phase-space weights for FSR

$$d_{ij} := 2k_i \cdot k_j \frac{E_i E_j}{(E_i + E_j)^2} \underset{m_j \rightarrow 0}{\overset{m_i \rightarrow 0}{=}} 2 \left( \frac{E_i E_j}{E_i + E_j} \right)^2 (1 - y) \quad (2.31)$$

such that

$$d_{ij} = 0 \quad \text{iff} \quad E_i = 0 \quad \vee \quad E_j = 0 \quad \vee \quad \vec{k}_i \parallel \vec{k}_j \quad . \quad (2.32)$$

This choice fulfills all conditions imposed in the previous subsection. Additionally, if the radiated particle becomes soft, the  $d_{ij}$  correspond to the square of the transverse momentum  $k_T$ . A phase-space subdivision based on  $k_T$  will prove to be beneficial for implementing a  $k_T$ -based matching to a  $k_T$ -ordered parton shower [47] like the POWHEG-matching algorithm which we will discuss in sec. 3.

To describe ISR, we do not have to consider vanishing emitter energies. Therefore, we can assume  $E_i \gg E_j$  to define

$$d_{ij} := 2E_j^2 (1 + (-1)^i y_j) \quad \text{for} \quad i \in \{1, 2\} \quad . \quad (2.33)$$

We remember from the definition of  $y$  in eq. (2.20) that  $y$  is independent of the emitter in case of ISR which means that the same PSPs are sampled in regions with emitter 1 and emitter 2. So if there are two ALRs with emitter 1 and emitter 2 and the same flavor structures, it is possible to merge both regions into a single one which we will assign emitter 0 to remember that they have been merged. Specifically, this is possible if a gluon is radiated and both initial-state partons are color charged or if a photon is radiated and both initial-state partons are electrically charged. For the ALRs with emitter 0, we define

$$d_{0j} := \frac{1}{\frac{1}{d_{1j}} + \frac{1}{d_{2j}}} = E_j^2(1 - y_j^2) \quad . \quad (2.34)$$

### The $S$ functions in the soft limit

The  $S$  functions we have defined so far may become ill-defined in the soft limit. We can see this by rewriting the reciprocal of eq. (2.29) to

$$\left(S_{ij}^{\alpha_r}\right)^{-1} = \mathcal{D} \frac{d_{ij}}{h_{ij}} = 1 + \sum_{\substack{k | (k,j) \in \mathcal{P}_{\text{FKS}} \\ k \neq i}} \frac{d_{ij} h_{kj}}{d_{kj} h_{ij}} + \sum_{\substack{(k,l) \in \mathcal{P}_{\text{FKS}} \\ l \neq j}} \frac{d_{ij} h_{kl}}{d_{kl} h_{ij}} \quad (2.35)$$

and examining the second term. It contains the ratio of phase-space weights for different emitters radiating the same particle at position  $j$ . In the soft limit,  $E_j \rightarrow 0$ , the ratio of the  $h$  factors becomes constant and both  $d_{ij}$  and  $d_{kj}$  approach zero. However, computing the limit analytically using eq. (2.31) for FSR we find

$$\lim_{E_j \rightarrow 0} \frac{d_{ij}}{d_{kl}} = \lim_{E_j \rightarrow 0} \frac{2(k_i \cdot \hat{k}_j) E_i E_j^2 (E_k + E_j)^2}{2(k_k \cdot \hat{k}_j) E_k E_j^2 (E_i + E_j)^2} = \frac{2(k_i \cdot \hat{k}_j) E_k}{2(k_k \cdot \hat{k}_j) E_i} \quad . \quad (2.36)$$

Here we split  $k_j = E_j \hat{k}_j$  such that  $\hat{k}_j$  is a unit vector in the direction of the radiated particle, which, according to our definition of  $\mathcal{P}_{\text{FKS}}$  in eq. (2.14), is massless. So we can instead define

$$d_{ij}^{\text{soft}} := \frac{2 k_i \cdot \hat{k}_j}{E_i} \quad (2.37)$$

for the soft limit without altering the ratio in eq. (2.29). Moreover, a soft emission also leaves the emitter momentum unchanged. We can thus implement eq. (2.37) using the Born momenta  $\bar{k}_i$ .

We can derive a similarly simplified form of the phase-space weights in the case of ISR by using  $d_{ij}$  as defined in eq. (2.33) and eq. (2.34) instead of eq. (2.31). In this case, we arrive at

$$\begin{aligned} d_{ij}^{\text{soft}} &:= 2(1 + (-1)^i y_j) \quad \text{for } i \in \{1, 2\} \\ d_{0j}^{\text{soft}} &:= 1 - y_j^2 \quad \text{for } i = 0 \quad . \end{aligned} \quad (2.38)$$

## 2.4 The real phase-space construction

In sec. 2.3.2, we stated that we construct the real  $(n+1)$ -body phase space in a factorized approach according to eq. (2.15). However, we still need to derive the explicit construction.

In this discussion, we will assume the Born phase space  $\bar{\Phi}_n$  to be given as a regular  $n$ -body phase space by the MC event generator. The remaining task is to construct the radiation phase-space element  $d\Phi_{\text{rad}}$  given by eq. (2.16) in such a way that the divergent regions are explicit. Having already defined the FKS parameters  $(\xi, y, \phi)$  for the simple cases, we have to determine the Jacobian for this phase-space parametrization.

We divide three different cases

1. massless FSR emitters,
2. massive FSR emitters,
3. massless ISR emitters.

The fourth possibility, massive ISR emitters, may be relevant when describing, e.g., muon colliders [1]. In this thesis, the initial-state partons will always be massless. We refer to ref. [76] for the construction of the phase space in this case.

For the derivations, we follow ref. [47] in both cases of massless emitters. The case of massive emitters in the final state has been derived in ref. [77] on the example of NLO EW corrections to single- $W$  production but is applicable to general NLO corrections as the phase-space construction is independent of the flavor structures. This also implies that the discussion here will cover the kinematic constructions to compute NLO EW corrections as well. In the framework of the WHIZARD MC generator, all three cases have also been mentioned in refs. [72, 73] and are reviewed in detail in ref. [7].

We will discuss the phase-space generation for a fixed generic ALR. As before, the radiated particle is the last in the real flavor structure. Furthermore, to simplify the notation, especially when summing up momenta throughout this subsection, we assume, without loss of generality, that the emitter is directly before the radiated particle in the ordering, such that for FSR the momenta of the emitter and the radiated particle are given by  $k_{n+2}$  and  $k_{n+3}$  respectively.

### 2.4.1 Radiation off a massless final-state emitter

We will start by sampling the FKS variables, then construct the real phase space and afterwards compute the Jacobian determining  $d\Phi_{\text{rad}}$ .

#### Sampling the FKS variables

The radiation phase space has three degrees of freedom that we choose to parametrize using  $(\xi, y, \phi)$  in sec. 2.2. However, the actual MC integration will always cover the unit hypercube, so we first need to determine the FKS variables  $(\xi, y, \phi)$  from the underlying sampled random numbers  $r_\xi, r_y, r_\phi \in (0, 1)$ , respectively.

We determine  $\xi$  using a rescaled

$$\tilde{\xi} := \xi/\xi_{\text{max}} = \xi_{\text{min}} + r_\xi(1 - \xi_{\text{min}}) \quad \Longrightarrow \quad \mathcal{J}_\xi = \xi_{\text{max}}(1 - \xi_{\text{min}}) \quad , \quad (2.39)$$

where  $\xi_{\text{max}}$  is the upper bound given by eq. (2.19) and  $\xi_{\text{min}}$  is the lower bound. We typically choose a tiny but non-zero value for  $\xi_{\text{min}}$  just to prevent numerical instabilities. It can be adjusted with the parameter `fks_xi_min`. Its default value is  $\xi_{\text{min}} = 10^{-7}$ .

$y$  is sampled using

$$y = 1 - 2r_y \quad \text{followed by} \quad y \leftarrow \frac{3}{2} \left( y - \frac{y^3}{3} \right) \quad \Longrightarrow \quad \mathcal{J}_y = 3(1 - y^2) \quad . \quad (2.40)$$

Here, the reassignment of  $y$  performs an importance sampling favoring (anti-)collinear values.

Finally,  $\phi$  is trivially sampled according to

$$\phi = 2\pi r_\phi \quad \Longrightarrow \quad \mathcal{J}_\phi = 2\pi \quad . \quad (2.41)$$

This variable transformation in total requires an additional Jacobian factor

$$\mathcal{J}_{\text{rand}} = \mathcal{J}_\xi \mathcal{J}_y \mathcal{J}_\phi \quad (2.42)$$

to be taken into account.

Having sampled the FKS variables, we can continue to construct the phase space.

### Phase-space construction

Continuing the discussion we started in sec. 2.2, we notice that for FSR, the initial-state momenta are unaffected by the additional radiation,

$$x_{\mathcal{R},\oplus} = x_{\mathcal{B},\oplus} \quad \implies \quad k_{\oplus} = \bar{k}_{\oplus} \quad , \quad (2.43)$$

so that the center-of-mass (CM) frame will be the same in both systems allowing us to work in this frame. Extending eq. (2.8) we require four-momentum conservation between the Born and the real particle set such that

$$q := \bar{k}_{\oplus} + \bar{k}_{\ominus} = \sum_{i=3}^{n+2} \bar{k}_i = k_{\oplus} + k_{\ominus} = \sum_{i=3}^{n+3} k_i \quad , \quad (2.44)$$

where we also defined  $q$  as the system's four-momentum, which in the CM frame explicitly reads

$$q^0 = \sqrt{s} \quad \text{and} \quad \vec{q} = \vec{0} \quad . \quad (2.45)$$

For the subsequent discussion, dividing the momenta into two sets will prove helpful. We will refer to the momenta  $\{k_{n+2}, k_{n+3}\}$  as the *emitter-radiated system* while the remaining momenta  $\{k_3, \dots, k_{n+1}\}$  form the *recoil system*. In the construction of the  $(n+1)$ -body phase space, we impose a conservation of the recoil system's invariant mass,

$$M_{\text{rec}}^2 := k_{\text{rec}}^2 := \left( \sum_{i=3}^{n+1} k_i \right)^2 = \left( \sum_{i=3}^{n+1} \bar{k}_i \right)^2 =: \bar{k}_{\text{rec}}^2 \quad . \quad (2.46)$$

Imposing the same invariant mass implies that the two sets of recoiling momenta are related by a Lorentz-boost  $\Lambda$  along the common recoil direction, i.e., the direction of the emitter before radiation in the Born system, in such a way that the difference between the initial-state momenta and the recoiling system is light-like, i.e.

$$(q - \Lambda k_{\text{rec}})^2 = 0 \quad . \quad (2.47)$$

For a generic Lorentz boost, this implies the condition

$$q^0 - \gamma k_{\text{rec}}^0 - \gamma\beta |\vec{k}_{\text{rec}}| \stackrel{!}{=} \gamma\beta k_{\text{rec}}^0 + \gamma |\vec{k}_{\text{rec}}| \quad (2.48)$$

which we can solve for  $q^0$ , square and rearrange again to find that the boost velocity is given by

$$\beta = \frac{q^2 - (k_{\text{rec}}^0 + |\vec{k}_{\text{rec}}|)^2}{q^2 + (k_{\text{rec}}^0 + |\vec{k}_{\text{rec}}|)^2} \quad . \quad (2.49)$$

Defining the four-momentum for the emitter-radiated system

$$k := k_{n+2} + k_{n+3} = q - k_{\text{rec}} \quad \text{so that} \quad \vec{k} = -\vec{k}_{\text{rec}} \quad , \quad (2.50)$$

we find that

$$k^2 \geq 0 \quad \Longrightarrow \quad k^0 \geq |\vec{k}| = |\vec{k}_{\text{rec}}| \quad . \quad (2.51)$$

Together with  $q^0 = k^0 + k_{\text{rec}}^0$  from eq. (2.44), we conclude that  $\beta$  is positive and smaller than 1, so this boost always exists.

Using the boost, we can explicitly formulate the relations

$$\bar{k}_i = \Lambda k_i \quad \forall i \in \{3, \dots, n+1\} \quad (2.52)$$

$$\text{and } \bar{k}_{n+2} = q - \Lambda k_{\text{rec}} \quad (2.53)$$

between the sets of Born and real momenta such that by construction, the momentum conservation imposed in eq. (2.44) holds.

From our definition of  $\xi$ , eq. (2.18), we can quickly determine the radiated energy to be given by

$$E_{n+3} = |\vec{k}_{n+3}| = \xi \frac{\sqrt{s}}{2} \quad . \quad (2.54)$$

To determine the energy of the emitter in the real phase space, we reformulate the energy-momentum conservation from eq. (2.44) to

$$q^0 = E_{\text{rec}} + E_{n+2} + E_{n+3} = \sqrt{|\vec{k}|^2 + M_{\text{rec}}^2} + |\vec{k}_{n+2}| + |\vec{k}_{n+3}| \quad , \quad (2.55)$$

where we used the definition in eq. (2.50) from which we also get

$$|\vec{k}|^2 = |\vec{k}_{n+2}|^2 + |\vec{k}_{n+3}|^2 + 2|\vec{k}_{n+2}||\vec{k}_{n+3}|y \quad (2.56)$$

using the definition of  $y$  (c.f. eq. (2.20)). From eqs. (2.46), (2.47) and (2.53) we find for the recoil mass

$$M_{\text{rec}}^2 = k_{\text{rec}}^2 = (\Lambda k_{\text{rec}})^2 = (q - \bar{k}_{n+2})^2 \quad . \quad (2.57)$$

Together with the condition that the radiated energy is less than the emitter energy before the emission, which we can derive from eq. (2.57),

$$E_{n+3} \leq |\vec{k}_{n+2}| = \frac{q^2 - M_{\text{rec}}^2}{2q^0} \quad , \quad (2.58)$$

we find only one solution for the emitter energy:

$$\boxed{E_{n+2} = |\vec{k}_{n+2}| = \frac{q^2 - M_{\text{rec}}^2 - 2q^0|\vec{k}_{n+3}|}{2(q^0 - |\vec{k}_{n+3}|(1-y))}} \quad . \quad (2.59)$$

From eq. (2.58) and eq. (2.57) we can also derive the upper limit

$$\xi \leq \frac{q^2 - M_{\text{rec}}^2}{q^2} = \frac{2\bar{k}_{n+2}^{-0}}{q^0} = \xi_{\text{max}} \quad (2.60)$$

which we already stated in eq. (2.19).

After that, we construct the angles and thus the vectors  $\vec{k}_{n+2}$  and  $\vec{k}_{n+3}$  such that their sum  $\vec{k} = \vec{k}_{n+2} + \vec{k}_{n+3}$  is parallel to the emitter direction before the emission,  $\vec{k}_{n+2}$ , and the azimuth between  $\vec{k}_{n+3}$  and  $\vec{k}$  is  $\phi$ .

Together, they determine the four-momentum  $k$  according to eq. (2.50) which also allows us to compute  $k_{\text{rec}}$ . Using  $k_{\text{rec}}$  we can compute the boost velocity  $\beta$  by eq. (2.49). This, in turn, makes it possible to compute all real momenta of the recoil system's constituents by inverting eq. (2.52). This concludes the phase-space parametrization up to the Jacobians.

### Determining the Jacobian

In order to express the radiation phase space in terms of the FKS variables, we need to determine the Jacobian of this transformation. We start with the  $(n+1)$ -body phase-space element in analogy to eq. (2.9),

$$\begin{aligned} d\Phi_{n+1} &= (2\pi)^4 \delta^4 \left( q - \sum_{i=3}^{n+3} k_i \right) \prod_{i=3}^{n+3} \frac{d^3 k_i}{2E_i (2\pi)^3} \\ &= (2\pi)^4 \delta^4 \left( q - k - \sum_{i=3}^{n+1} k_i \right) \frac{d^3 k_{n+3}}{2E_{n+3} (2\pi)^3} \frac{d^3 k}{2E_{n+2} (2\pi)^3} \prod_{i=3}^{n+1} \frac{d^3 k_i}{2E_i (2\pi)^3} \quad , \end{aligned} \quad (2.61)$$

using  $k$  instead of  $k_{n+2}$  as integration variable. We now want to determine the Jacobian  $\mathcal{J}$  according to eq. (2.15) and eq. (2.16), i.e., such that

$$d\Phi_{n+1} = \left[ \mathcal{J}(\xi, y, \phi) d\xi dy d\phi \right] \left[ (2\pi)^4 \delta^4 \left( q - \sum_{i=3}^{n+2} \bar{k}_i \right) \prod_{i=3}^{n+2} \frac{d^3 \bar{k}_i}{2\bar{E}_i (2\pi)^3} \right] \quad , \quad (2.62)$$

repeating eq. (2.9), by equating these two expressions.

Now, we make a few observations:

- By construction,  $\vec{k}$  is parallel to  $\vec{\bar{k}}_{n+2}$  which implies

$$d^3 k = d\Omega_2 |\vec{k}|^2 d|\vec{k}| \quad \text{and} \quad d^3 \bar{k}_{n+2} = d\Omega_2 |\vec{\bar{k}}_{n+2}|^2 d|\vec{\bar{k}}_{n+2}| \quad (2.63)$$

allowing us to cancel the solid angle measures  $d\Omega_2$ .

- The first  $n-1$  momenta are connected by just a Lorentz boost (c.f. eq. (2.52)). Furthermore, using eq. (2.53) we find  $q - \bar{k}_{n+2} = \Lambda(q - k)$  so these terms are also connected by just a boost. Now the phase-space elements and four-dimensional delta distributions in eqs. (2.61) and (2.62) are Lorentz invariant implying

$$(2\pi)^4 \delta^4 \left( q - k - \sum_{i=3}^{n+1} k_i \right) \prod_{i=3}^{n+1} \frac{d^3 k_i}{2E_i (2\pi)^3} = (2\pi)^4 \delta^4 \left( q - \bar{k}_{n+2} - \sum_{i=3}^{n+1} \bar{k}_i \right) \prod_{i=3}^{n+1} \frac{d^3 \bar{k}_i}{2\bar{E}_i (2\pi)^3} \quad . \quad (2.64)$$

- Using the definition of the FKS variables, the phase-space measure for spherical coordinates and  $\frac{d|\vec{k}_{n+3}|}{d\xi} = \frac{q^0}{2}$  we can infer

$$\frac{d^3 k_{n+3}}{2E_{n+3} (2\pi)^3} = \frac{q^2}{(4\pi)^3} \xi d\xi d\cos(\psi) d\phi \quad , \quad (2.65)$$

where we defined  $\psi$  as the angle between  $\vec{k}_{n+3}$  and  $\vec{k}$  or, equivalently,  $\vec{\bar{k}}_n$ .

Putting the above three points together, we find that the Jacobian has to fulfill

$$\frac{q^2}{(4\pi)^3} \xi d\cos(\psi) \frac{|\vec{k}|^2 d|\vec{k}|}{E_{n+2}} = \mathcal{J} |\vec{\bar{k}}_{n+2}| dy d|\vec{\bar{k}}_{n+2}| \quad . \quad (2.66)$$

To solve this further we thus have to express  $(y, |\vec{k}_{n+2}|)$  in terms of  $(\cos(\psi), |\vec{k}|)$  for a fixed value of  $\xi$ . We can achieve this by squaring  $\vec{k}_{n+2}$  and  $\vec{k}$  (c.f. eq. (2.56)), remembering the upper limit of the radiated energy, eq. (2.58), and expanding  $M_{\text{rec}}^2 = (q - k_{n+2} - k_{n+3})^2$  to get the relations

$$\begin{aligned} \vec{k}_{n+2}^2 &= \vec{k}^2 + \vec{k}_{n+3}^2 - 2|\vec{k}| |\vec{k}_{n+3}| \cos(\psi) \quad , & y &= \frac{|\vec{k}|^2 - |\vec{k}_{n+2}|^2 - |\vec{k}_{n+3}|^2}{2 |\vec{k}_{n+2}| |\vec{k}_{n+3}|} \quad , \\ |\vec{k}_{n+2}| &= \frac{q^2 - M_{\text{rec}}^2}{2q^0} & \text{and} & \quad M_{\text{rec}}^2 = (q^0 - |\vec{k}_{n+3}| - |\vec{k}_{n+2}|)^2 - \vec{k}^2 \quad . \end{aligned} \quad (2.67)$$

Using these to compute the partial derivatives, we can compute the determinant

$$\det \begin{pmatrix} \frac{\partial |\vec{k}_{n+2}|}{\partial |\vec{k}|} & \frac{\partial y}{\partial |\vec{k}|} \\ \frac{\partial |\vec{k}_{n+2}|}{\partial \cos(\psi)} & \frac{\partial y}{\partial \cos(\psi)} \end{pmatrix} = \frac{|\vec{k}|^2}{|\vec{k}_{n+2}|^3} \left( |\vec{k}_{n+2}| - \frac{\kappa^2}{2q^0} \right) \quad . \quad (2.68)$$

We define

$$\kappa^2 := 2|\vec{k}_{n+2}| |\vec{k}_{n+3}| (1 - y) \quad (2.69)$$

to finally conclude from eq. (2.66)

$$\boxed{\mathcal{J} = \frac{q^2 \xi}{(4\pi)^3} \frac{|\vec{k}_{n+2}|^2}{|\vec{k}_{n+2}|} \left( |\vec{k}_{n+2}| - \frac{\kappa^2}{2q^0} \right)^{-1}} \quad \text{so that} \quad d\Phi_{\text{rad}} = \mathcal{J} d\xi dy d\phi \quad . \quad (2.70)$$

### The Jacobian in the soft limit

We will also need the Jacobian in the limit of a soft or a collinear emission, so we will quickly derive it here. In the soft limit, no energy is radiated so that

$$|\vec{k}_{n+3}| = E_{n+3} \rightarrow 0 \implies \kappa \rightarrow 0 \quad \text{and} \quad |\vec{k}_{n+2}| \rightarrow |\vec{k}_{n+2}| \quad . \quad (2.71)$$

This leads to

$$\mathcal{J}_{\text{soft}} = \frac{q^2 \xi}{(4\pi)^3} \quad . \quad (2.72)$$

### The Jacobian in the collinear limit

In the collinear limit, we find similarly

$$y \rightarrow 1 \implies \kappa \rightarrow 0 \quad \text{and} \quad \lim_{y \rightarrow 1} |\vec{k}_{n+2}| = \frac{q^2 - M_{\text{rec}}^2}{q^0} - |\vec{k}_{n+3}| = |\vec{k}_{n+2}| - \xi \frac{q^2}{2} \quad , \quad (2.73)$$

so that the Jacobian is given by

$$\mathcal{J}_{\text{coll}} = \frac{q^2 \xi}{(4\pi)^3} \left( 1 - \frac{q^0 \xi}{2\vec{k}_{n+2}} \right) \quad . \quad (2.74)$$

### Example: The Jacobian for $e^+e^- \rightarrow q\bar{q}$

Exemplary, we also want to discuss the specific form of the Jacobian for a  $2 \rightarrow 2$  process such as  $e^+e^- \rightarrow q\bar{q}$ . In such a process, both particles are back-to-back and take an equal share of the available energy. As one particle recoils against the other, the recoil system will be massless, i.e.,  $M_{\text{rec}} = 0$ . So we find, based on

eqs. (2.58), (2.18) and eq. (2.59)

$$|\vec{k}_{n+2}| = \frac{q^0}{2} \quad , \quad |\vec{k}_{n+3}| = \frac{q^0}{2} \xi \quad (2.75)$$

$$|\vec{k}_{n+2}| = \frac{q^2 - M_{\text{rec}}^2 - 2q^0 |\vec{k}_{n+3}|}{2q^0 - 2|\vec{k}_{n+3}|(1-y)} = \frac{q^0}{2} \frac{1-\xi}{1-\frac{\xi}{2}(1-y)} \quad . \quad (2.76)$$

With these, the Jacobian given by eq. (2.70) simplifies to

$$\mathcal{J} = \frac{q^2}{(4\pi)^3} \frac{\xi(1-\xi)}{\left[1 - \frac{\xi}{2}(1-y)\right]^2} \quad . \quad (2.77)$$

### 2.4.2 Radiation off a massive final-state emitter

#### Sampling the FKS variables

In the case of a massive emitter, we will sample  $\phi$  as usual and  $\xi$  as in the massless case according to eq. (2.39). However, we choose to parametrize  $y$  according to

$$y = \frac{1}{\beta_{\text{em}}} \left( 1 - (1 + \beta_{\text{em}}) \exp \left[ r_y \log \left[ \frac{1 - \beta_{\text{em}}}{1 + \beta_{\text{em}}} \right] \right] \right) \quad \text{with} \quad \beta_{\text{em}} = \sqrt{1 - \frac{m^2}{E_{n+2}^2}} \quad (2.78)$$

so that we will use

$$\mathcal{J}_y = \frac{1 - \beta_{\text{em}} y}{\beta_{\text{em}}} \log \left[ \frac{1 + \beta_{\text{em}}}{1 - \beta_{\text{em}}} \right] \quad (2.79)$$

as the Jacobian factor instead of the one given in eq. (2.40).

#### Phase-space construction

To a large extent, the phase-space construction for the emission of a massless particle from a massive emitter is equivalent to the massless case we just discussed in sec. 2.4.1. However, due to the emitter with mass  $m > 0$ , the kinematic bounds and the construction of the emitter momentum after the emission,  $k_{n+2}$ , have to be adjusted.

We will again work in the CM frame of both systems and define the recoil system according to eq. (2.46). Thus, we find

$$\begin{aligned} M_{\text{rec}}^2 = [q - \bar{k}_{n+2}]^2 &= q^2 + \bar{k}_{n+2}^2 - 2q^0 \bar{E}_{n+2} & \Leftrightarrow & \quad \bar{E}_{n+2} = \frac{q^2 + m^2 - M_{\text{rec}}^2}{2q^0} \\ m^2 = [q - \bar{k}_{\text{rec}}]^2 &= q^2 + \bar{k}_{\text{rec}}^2 - 2q^0 \bar{E}_{\text{rec}} & \Leftrightarrow & \quad \bar{E}_{\text{rec}} = \frac{q^2 - m^2 + M_{\text{rec}}^2}{2q^0} \end{aligned} \quad (2.80)$$

for the energies of the emitter and the recoil system in the Born phase space, respectively.

The construction of the four-momenta in the emitter-radiated system  $\{k_{n+2}, k_{n+3}\}$  is more involved. It is based on the observation [77] that the energies  $E_{n+2}$ ,  $E_{n+3}$  and  $E_{\text{rec}}$  fill a convex Dalitz domain [78, 79]. It is thus possible to choose the parametrization

$$E_{n+2} = \bar{E}_{n+2} - z E_{n+3} \quad , \quad (2.81)$$

where  $z$  is the slope of the Dalitz plot.

For each value of  $z$ , there is a maximum value of  $E_{n+3}$  such that the point lies within the Dalitz domain.

All points fulfilling

$$|\vec{k}_{n+3}| \pm |\vec{k}_{n+2}| \pm |\vec{k}_{\text{rec}}| = 0 \quad (2.82)$$

for at least one combination of signs are at the domain's boundary. We can now isolate  $|\vec{k}_{\text{rec}}|$ , square, isolate  $2|\vec{k}_{n+3}||\vec{k}_{n+2}|$  and square again to get rid of the ambiguous signs and arrive at

$$\left(|\vec{k}_{n+3}|^2 + |\vec{k}_{n+2}|^2 - |\vec{k}_{\text{rec}}|^2\right)^2 = 4|\vec{k}_{n+3}|^2|\vec{k}_{n+2}|^2 \quad . \quad (2.83)$$

Using eqs. (2.80), (2.81) as well as

$$\vec{k}_{n+2}^2 = E_{n+2}^2 - m^2 \quad \text{and} \quad \vec{k}_{\text{rec}}^2 = (q^0 - E_{n+2} - E_{n+3})^2 - M_{\text{rec}}^2 \quad (2.84)$$

we can transform eq. (2.83) equation into

$$4|\vec{k}_{n+3}|^2 \left( 2|\vec{k}_{n+3}|q^0z(1-z) + q^2z^2 - 2q^0z\bar{E}_{\text{rec}} + M_{\text{rec}}^2 \right) = 0 \quad . \quad (2.85)$$

Solving this quadratic equation for  $|\vec{k}_{n+3}| = E_{n+3}$  yields the boundaries of the radiated energy

$$0 \leq E_{n+3} \leq \frac{2q^0|\vec{k}_{\text{rec}}|z - q^2z^2 - M_{\text{rec}}^2}{2q^0z(1-z)} \quad , \quad (2.86)$$

from which we can immediately determine the maximum of  $\xi$  to be given by

$$\boxed{\xi_{\text{max}} = \frac{2q^0|\vec{k}_{\text{rec}}|z - q^2z^2 - M_{\text{rec}}^2}{q^2z(1-z)}} \quad . \quad (2.87)$$

There are two values of  $z$  for which the allowed maximum of the radiated energy vanishes

$$z_{1/2} := \frac{\bar{k}_{\text{rec}}^0 \pm \sqrt{\bar{E}_{\text{rec}}^2 - M_{\text{rec}}^2}}{q^0} \quad . \quad (2.88)$$

These are the boundaries of the allowed  $z$  values so that  $z \in [z_2, z_1]$ . We can use this to parametrize  $z$  using  $y$  according to

$$z = z_2 - (z_2 - z_1) \frac{1+y}{2} \quad (2.89)$$

so that we can use  $z$  instead of  $y$  as third FKS variable to parametrize the radiation phase space  $\Phi_{\text{rad}}$ .

With eqs. (2.81), (2.87) and (2.89), we have all the ingredients to compute the momenta of the emitter-radiated system from given values of  $(\xi, y, \phi)$  using an angular construction similar to the massless case.

Finally, we can determine the momenta of the recoil system  $k_3, \dots, k_{n+1}$  via boosting the Born momenta  $\bar{k}_3, \dots, \bar{k}_{n+1}$  parallel to  $-\vec{k}_{\text{rec}} = \vec{k}$  as in eq. (2.52) using an inverse boost  $\Lambda^{-1}(\beta)$  with [72]

$$\beta = \frac{1 - \alpha^2}{1 + \alpha^2} \quad \text{with} \quad \alpha = \frac{E_{\text{rec}} + |\vec{k}_{\text{rec}}|}{E_{\text{rec}} - |\vec{k}_{\text{rec}}|} \quad (2.90)$$

concluding this phase-space construction up to the Jacobian.

### Determining the Jacobian

To determine the Jacobian, we will again compare the full phase-space element of the  $(n+1)$ -body phase

space with one factorized as  $(n \otimes 1)$ -body phase space

$$d\Phi_{n+1} = \tilde{\mathcal{J}} dE_{n+3} dE_{n+2} d\phi d\bar{\Phi}_n \quad (2.91)$$

similar to eqs. (2.61) and (2.62) for the massless case. We will factorize both phase spaces further by separating the phase space of the recoil system. For the real phase space, the remainder is a 3-body phase space with the emitter, the radiated particle and the recoil system  $d\Phi_{\text{rec}}$  such that

$$d\Phi_{n+1} = d\Phi_3 d\Phi_{\text{rec}} \quad \text{with}$$

$$d\Phi_3 = \frac{dM_{\text{rec}}^2}{2\pi} \frac{d^3 k_{n+3}}{2E_{n+3}} \frac{d^3 k_{n+2}}{(2\pi)^3} \frac{d^3 k_{\text{rec}}}{2E_{\text{rec}} (2\pi)^3} (2\pi)^4 \delta^4(q - k_{n+3} - k_{n+2} - k_{\text{rec}}) \quad . \quad (2.92)$$

In the Born phase space, just a 2-body phase space of  $\bar{k}_{n+2}$  and  $k_{\text{rec}}$  remains such that we can write

$$d\bar{\Phi}_n = \frac{dM_{\text{rec}}^2}{2\pi} \frac{d^3 \bar{k}_{n+2}}{2\bar{E}_{n+2} (2\pi)^3} \frac{d^3 \bar{k}_{\text{rec}}}{2\bar{E}_{\text{rec}} (2\pi)^3} (2\pi)^4 \delta^4(q - \bar{k}_{n+2} - \bar{k}_{\text{rec}}) d\bar{\Phi}_{\text{rec}} \quad . \quad (2.93)$$

We again make a few observations:

- The two recoil phase spaces  $\Phi_{\text{rec}}$  and  $\bar{\Phi}_{\text{rec}}$  are connected by a Lorentz boost such that their phase-space elements are identical and can be canceled on both sides.
- We can simplify the real 3-body phase-space element by integrating out the recoil momentum  $d^3 k_{\text{rec}}$  and then using the Dalitz variables  $E_{n+3}$  and  $E_{n+2}$  to find

$$d\Phi_3 = \frac{d^3 k_{n+3}}{2E_{n+3} (2\pi)^3} \frac{d^3 k_{n+2}}{2E_{n+2} (2\pi)^3} (2\pi) \delta((q - k_{n+3} - k_{n+2})^2 - M_{\text{rec}}^2)$$

$$= \frac{d\Omega_{n+1}}{4(2\pi)^6} k_{n+3} k_{n+2} dE_{n+3} dE_{n+2} d\cos(\theta) d\phi (2\pi) \delta((q - k_{n+2} - k_{n+2})^2 - M_{\text{rec}}^2) \quad (2.94)$$

In the next step, we can rewrite the argument of the  $\delta$  distribution according to

$$(q - k_{n+3} - k_{n+2})^2 - M_{\text{rec}}^2 = q^2 + m^2 - M_{\text{rec}}^2 - 2q^0(E_{n+3} + E_{n+2}) + 2E_{n+3}E_{n+2} + 2\cos(\theta)k_{n+3}k_{n+2} \quad (2.95)$$

to execute the polar integral, which yields

$$d\Phi_3 = \frac{d\Omega_{n+3}}{8(2\pi)^5} dE_{n+3} dE_{n+2} d\phi = \frac{d\Omega}{8(2\pi)^5} dE_{n+3} dE_{n+2} d\phi \quad , \quad (2.96)$$

where we chose to denote just  $\Omega$  as the angular orientation can be chosen relative to any of the three bodies.

- Repeating the analogous steps, we can also get rid of the  $\delta$  distribution in the Born phase-space element finding

$$\frac{d^3 \bar{k}_{n+2}}{2\bar{E}_{n+2} (2\pi)^3} \frac{d^3 \bar{k}_{\text{rec}}}{2\bar{E}_{\text{rec}} (2\pi)^3} (2\pi)^4 \delta^4(q - \bar{k}_{n+2} - \bar{k}_{\text{rec}}) = \frac{d^3 \bar{k}_{n+2}}{2\bar{E}_{n+2} (2\pi)^3} 2\pi \delta((q - \bar{k}_{n+2})^2 - M_{\text{rec}}^2) = \frac{d\Omega}{8(2\pi)^2} \frac{2|\vec{k}_{n+2}|}{q^0} \quad .$$

We can use these observations to simplify the phase-space elements of eq. (2.92) and (2.93). Plugging them together into eq. (2.91) and canceling all the common factors, we find that the Jacobian has to fulfill

$$\frac{1}{(2\pi)^3} = \tilde{\mathcal{J}} \frac{2|\vec{k}_{n+2}|}{q^0} \quad (2.97)$$

so that we can conclude

$$\tilde{\mathcal{J}} = \frac{q^0}{(2\pi)^3} \frac{1}{2|\vec{k}_{n+2}|} \quad \text{with} \quad d\Phi_{\text{rad}} = \tilde{\mathcal{J}} dE_{n+3} dE_{n+2} d\phi \quad . \quad (2.98)$$

We now perform one more transformation to the actual FKS variables in the massive case using eqs. (2.18) and (2.81) for the derivatives of  $E_{n+3}$  and  $E_{n+2}$ , respectively, to finally determine the Jacobian

$$\boxed{\mathcal{J} = \frac{q^2}{(2\pi)^3} \frac{E_{n+3}}{4|\vec{k}_{n+2}|}} \quad \text{with} \quad d\Phi_{\text{rad}} = \mathcal{J} d\xi dz d\phi \quad . \quad (2.99)$$

### 2.4.3 Radiation off a massless initial-state emitter

#### Phase-space construction

For initial-state emissions, we always assume here that the emitter is massless. We can thus use the same formulae to sample the FKS variables  $(\xi, y, \phi)$  that we used in the case of FSR emissions off a massless emitter in sec. 2.4.1.

The phase-space construction, however, has some notable differences. Most notably, as already mentioned in sec. 2.2, the CM of the Born and the real momenta will differ. Consequently, the center-of-mass energies of the Born and the real system will be different, i.e.,  $s_{\mathcal{R}} \geq s_{\mathcal{B}}$ . We choose to work in the real CM frame, such that  $(x_{\mathcal{R},\oplus} K_{\oplus} + x_{\mathcal{R},\ominus} K_{\ominus}) = (\sqrt{s}, \vec{0})$ .

Following ref. [47], we parametrize the radiated momentum as

$$k_{n+3} = \frac{\sqrt{s_{\mathcal{R}}}}{2} \xi \left( 1, \sin(\theta) \sin(\phi), \sin(\theta) \cos(\phi), \cos(\theta) \right) \quad . \quad (2.100)$$

with  $y = \cos(\theta)$  as usual in the case of a massless emitter.

We use  $k_{n+3}$  to define

$$k_{\text{tot}} := \sum_{i=3}^{n+2} k_i = x_{\mathcal{R},\oplus} K_{\oplus} + x_{\mathcal{R},\ominus} K_{\ominus} - k_{n+3} \quad (2.101)$$

as the total momentum available after the initial-state radiation.

For the Born system, we can similarly define the total momentum of the partonic system

$$\bar{k}_{\text{tot}} := \sum_{i=3}^{n+2} \bar{k}_i = x_{\mathcal{B},\oplus} K_{\oplus} + x_{\mathcal{B},\ominus} K_{\ominus} \quad . \quad (2.102)$$

Next, we want to determine the boost that connects both systems. We define it in such a way that both  $k_{\text{tot}}$  and  $\bar{k}_{\text{tot}}$  have the same invariant mass and rapidity. This is achieved by concatenating three different boosts. The first boost,  $\Lambda_L$ , boosts into a system with zero longitudinal momentum, i.e., such that the rapidity of

both  $\Lambda_L \bar{k}_{\text{tot}}$  and  $\Lambda_L k_{\text{tot}}$  vanishes. This is achieved with a boost velocity of [72]

$$\vec{\beta}_L = \frac{\vec{k}_{\text{tot}}}{k_{\text{tot}}^0} = \frac{\vec{k}_{\oplus} + \vec{k}_{\ominus}}{k_{\oplus}^0 + k_{\ominus}^0} . \quad (2.103)$$

Secondly, we apply a transversal boost  $\Lambda_T$  such that the transversal momentum of the system  $\Lambda_T \Lambda_L k_{\text{tot}}$  vanishes. The boost velocity, in this case, is given by [72]

$$\beta_T = \frac{1}{\sqrt{1 + \frac{s_{\mathcal{B}}}{k_{T,n+3}^2}}} . \quad (2.104)$$

Finally, we restore the original rapidity by applying the inverse longitudinal boost  $\Lambda_L^{-1}$ . Summarizing, the two systems are connected by the boosts

$$\bar{k}_{\text{tot}} = \Lambda_L^{-1} \Lambda_T \Lambda_L k_{\text{tot}} , \quad (2.105)$$

which implies that we can construct the remaining  $(n-1)$  real momenta using the inverse operation

$$k_i = \Lambda_L^{-1} \Lambda_T^{-1} \Lambda_L \bar{k}_i \quad \text{for } i \in \{3, \dots, n+2\} . \quad (2.106)$$

Based on the above construction, we can also determine the relation of the Bjorken- $x$  values of both systems. First of all, we observe that the invariant mass of  $k_{\text{tot}}$  is given by

$$k_{\text{tot}}^2 = (x_{\mathcal{R},\oplus} K_{\oplus} + x_{\mathcal{R},\ominus} K_{\ominus})^2 + k_{n+3}^2 - 2k_{n+3} \cdot (x_{\mathcal{R},\oplus} K_{\oplus} + x_{\mathcal{R},\ominus} K_{\ominus}) = s_{\mathcal{R}} + 0 - 2\sqrt{s_{\mathcal{R}}} \frac{\sqrt{s_{\mathcal{R}}}}{2} = s_{\mathcal{R}}(1-\xi) \quad (2.107)$$

and for its rapidity, we find

$$y(k_{\text{tot}}) = \frac{1}{2} \ln \left[ \frac{k_{\text{tot}}^0 + k_{\text{tot}}^z}{k_{\text{tot}}^0 - k_{\text{tot}}^z} \right] = \ln \left[ \sqrt{\frac{2 - \xi(1+y)}{2 - \xi(1-y)}} \right] \quad (2.108)$$

using eqs. (2.100) and (2.101) in the last step.

We also find for the CM energies of both systems

$$s_{\mathcal{R}} = (x_{\mathcal{R},\oplus} K_{\oplus} + x_{\mathcal{R},\ominus} K_{\ominus})^2 = 2x_{\mathcal{R},\oplus} x_{\mathcal{R},\ominus} (K_{\oplus} K_{\ominus}) \quad (2.109)$$

$$s_{\mathcal{B}} = (x_{\mathcal{B},\oplus} K_{\oplus} + x_{\mathcal{B},\ominus} K_{\ominus})^2 = 2x_{\mathcal{B},\oplus} x_{\mathcal{B},\ominus} (K_{\oplus} K_{\ominus}) = s_{\mathcal{R}}(1-\xi) , \quad (2.110)$$

where we used eq. (2.107) and the fact that  $k_{\text{tot}}$  and  $\bar{k}_{\text{tot}}$  have the same invariant mass in the last step. By division, we get

$$\frac{x_{\mathcal{B},\oplus}}{x_{\mathcal{R},\oplus}} = \frac{x_{\mathcal{R},\ominus}}{x_{\mathcal{B},\ominus}} (1-\xi) . \quad (2.111)$$

Furthermore, we notice that the incoming hadrons are light-like so that in the rest frame of the incoming partons,

$$K_{\oplus}^0 = \pm K_{\oplus}^z \quad \implies \quad x_{\mathcal{R},\oplus} K_{\oplus}^0 = x_{\mathcal{R},\ominus} K_{\ominus}^0 . \quad (2.112)$$

Also, the fact that by definition,  $k_{\text{tot}}$  has the same rapidity as  $(x_{\mathcal{B},\oplus} K_{\oplus} + x_{\mathcal{B},\ominus} K_{\ominus})$  together with eq. (2.108) implies

$$\frac{x_{\mathcal{B},\oplus} K_{\oplus}^0}{x_{\mathcal{B},\ominus} K_{\ominus}^0} = \frac{2 - \xi(1+y)}{2 - \xi(1-y)} = \frac{x_{\mathcal{B},\oplus} x_{\mathcal{R},\ominus}}{x_{\mathcal{R},\oplus} x_{\mathcal{B},\ominus}} \quad (2.113)$$

so that, together with eq. (2.111), we can find the relations

$$x_{\mathcal{R},\oplus} = \frac{x_{\mathcal{B},\oplus}}{\sqrt{1-\xi}} \sqrt{\frac{2-\xi(1\mp y)}{2-\xi(1\pm y)}} \quad . \quad (2.114)$$

$\xi$  must not take values such that any  $x_{\mathcal{R},\oplus}$  exceeds unity. This condition allows us to derive the maximum value,  $\xi_{\max}$ , that  $\xi$  may take for ISR.

We can square and rearrange eq. (2.114) to find

$$1 \stackrel{!}{\geq} x_{\mathcal{R},\oplus}^2 = \frac{x_{\mathcal{B},\oplus}^2 (1+y) + (1-\xi)(1-y)}{1-\xi(1-y) + (1-\xi)(1-y)} \quad (2.115)$$

which we can again rearrange to

$$0 \stackrel{!}{\geq} (1-\xi)^2 + (1-\xi) \frac{(1-y)(1-x_{\mathcal{B},\oplus}^2)}{1+y} - x_{\mathcal{B},\oplus}^2 \quad , \quad (2.116)$$

an equation quadratic in  $(1-\xi)$ . With the condition  $\xi \leq 1$  we find the only solution

$$(1-\xi) = \frac{2(1+y)x_{\mathcal{B},\oplus}^2}{(1-y)(1-x_{\mathcal{B},\oplus}^2) + \sqrt{(1+x_{\mathcal{B},\oplus}^2)^2(1-y)^2 + 16yx_{\mathcal{B},\oplus}^2}} \quad . \quad (2.117)$$

We can get the analog solution for  $x_{\mathcal{B},\ominus}$  by  $y \rightarrow -y$ . In this way, we determined that

$$\xi_{\max} = 1 - \max \left\{ \frac{2(1+y)x_{\mathcal{B},\oplus}^2}{(1-y)(1-x_{\mathcal{B},\oplus}^2) + \sqrt{(1+x_{\mathcal{B},\oplus}^2)^2(1-y)^2 + 16yx_{\mathcal{B},\oplus}^2}}, \frac{2(1-y)x_{\mathcal{B},\ominus}^2}{(1+y)(1-x_{\mathcal{B},\ominus}^2) + \sqrt{(1+x_{\mathcal{B},\ominus}^2)^2(1+y)^2 - 16yx_{\mathcal{B},\ominus}^2}} \right\} \quad (2.118)$$

is the maximum value that  $\xi$  may take.

### Determining the Jacobian

Determining the Jacobian for the parametrization of  $\Phi_{\text{rad}}$  with  $(\xi, y, \phi)$  will be straightforward in this case.

- From the definition of  $k_{n+3}$ , eq. (2.100), we can immediately derive

$$\frac{d^3 k_{n+3}}{2E_{n+3} (2\pi)^3} = \frac{s_{\mathcal{R}}}{(4\pi)^3} \xi d\xi dy d\phi \quad . \quad (2.119)$$

- Next, from eq. (2.114) we can compute

$$dx_{\mathcal{R},\oplus} dx_{\mathcal{R},\ominus} = \frac{dx_{\mathcal{B},\oplus} dx_{\mathcal{B},\ominus}}{1-\xi} \quad . \quad (2.120)$$

Using both observations and the Lorentz invariance of the integration measure, we can rewrite the  $(n+1)$ -body phase-space element as

$$\begin{aligned}
d\Phi_{\text{rad}} &= dx_{\mathcal{R},\oplus} dx_{\mathcal{R},\ominus} (2\pi)^4 \delta^4 \left( x_{\mathcal{R},\oplus} K_{\oplus} + x_{\mathcal{R},\ominus} K_{\ominus} - \sum_{i=3}^{n+3} k_i \right) \prod_{i=3}^{n+3} \frac{d^3 k_i}{2E_i (2\pi)^3} \\
&= dx_{\mathcal{B},\oplus} dx_{\mathcal{B},\ominus} \frac{s_{\mathcal{R}}}{(4\pi)^3} \frac{\xi}{1-\xi} d\xi dy d\phi (2\pi)^4 \delta^4 \left( x_{\mathcal{R},\oplus} K_{\oplus} + x_{\mathcal{R},\ominus} K_{\ominus} - k_{n+3} - \sum_{i=3}^{n+2} k_i \right) \prod_{i=3}^{n+2} \frac{d^3 k_i}{2E_i (2\pi)^3} \\
&= dx_{\mathcal{B},\oplus} dx_{\mathcal{B},\ominus} \frac{s_{\mathcal{R}}}{(4\pi)^3} \frac{\xi}{1-\xi} d\xi dy d\phi (2\pi)^4 \delta^4 \left( x_{\mathcal{B},\oplus} K_{\oplus} + x_{\mathcal{B},\ominus} K_{\ominus} - \sum_{i=3}^{n+2} \bar{k}_i \right) \prod_{i=3}^{n+2} \frac{d^3 \bar{k}_i}{2\bar{E}_i (2\pi)^3} \\
&= \frac{s_{\mathcal{R}}}{(4\pi)^3} \frac{\xi}{1-\xi} d\xi dy d\phi d\bar{\Phi}_n
\end{aligned} \tag{2.121}$$

We can immediately read off the Jacobian

$$\boxed{\mathcal{J} = \frac{s_{\mathcal{R}}}{(4\pi)^3} \frac{\xi}{1-\xi}} \quad \text{with} \quad d\Phi_{\text{rad}} = \mathcal{J} d\xi dy d\phi \quad . \tag{2.122}$$

Having this final piece, we concluded the construction of the  $(n+1)$ -body phase space from the Born  $n$ -body phase space for all relevant types of emitters.

## 2.5 The Born contribution

Having the recipes for generating the phase spaces at hand, we will turn our attention to the integrands, i.e., the matrix elements and subtraction terms, next. As explained in sec. 2.1.2, we will compute the total NLO cross section as the sum of separate contributions. Typically the largest contribution to the cross section comes from the Born term.

Computing the Born contribution to the cross section is almost as straightforward as computing a LO cross section, a problem already solved in all modern MC generators. In contrast to the computation of the LO cross section, however, we use input parameters such as particle widths and also PDFs with (at least) NLO accuracy for the Born term.

In general, also the Born configuration may be divergent in some degenerate regions of the phase space. This is especially the case for processes featuring light partons (leptons and photons included) in the final state. These divergences will *not* be treated by the subtraction mechanism, so they have to be taken care of in advance.

Just as in a LO computation, these regions are excluded by imposing kinematic constraints on the final-state momenta of the partons known as *cuts*. Similar to ref. [64], we will denote this condition symbolically via the *jet measurement function*  $\mathbb{J}(\Phi_n)$  which we already used in sec. 2.3. This condition is always implicitly present, but we will write it explicitly only when relevant.

Obviously, we have to apply the same cuts to all components of the NLO cross section to compute a physically meaningful quantity. To avoid spoiling the subtraction mechanism, the imposed cuts have to be IR safe, i.e., not affected by soft or collinear radiation. Usually, this condition is met by requiring  $n_L^{\mathcal{B}}$  or  $n_L^{\mathcal{R}} = n_L^{\mathcal{B}} + 1$  jets reconstructed with an IR-safe jet algorithm [80] and/or photon recombination of radiated photons.

For the NLO cross section to be finite, it is in general *not* sufficient to just require a finite Born cross section and a suitable subtraction mechanism. The kinematic conditions rendering the Born cross section finite also need to be *radiation proof*, as the subtraction will only remedy divergences related to the radiated particle. One of the simplest examples is given by the process  $pp \rightarrow e^+e^-$  computed at NLO QCD with massless

electrons and the condition that  $p_T > 20 \text{ GeV}$  holds for each of the leptons. In the Born phase space, the leptons are back-to-back, so no collinear divergence is possible. Hard initial-state radiation, however, may boost the  $e^+e^-$  system, so that a collinear divergence of both non-QCD particles becomes problematic. Requiring  $n_L^{\mathcal{B}} = 0$  or  $n_L^{\mathcal{R}} = 1$  reconstructed jets is indeed not sufficient.

Given an adequate jet measurement function  $\mathbb{J}$ , we can formulate the Born contribution in more detail than before as

$$\sigma^{\mathcal{B}}(f_{\mathcal{B}}) = \int \frac{\mathbb{J}(\Phi_n)}{\mathcal{N}(f_{\mathcal{B}})} \mathcal{B}(\Phi_n) d\Phi_n \quad , \quad (2.123)$$

also making explicit a symmetry factor  $\mathcal{N}(f_{\mathcal{B}})$  to account for identical particles in the final state.

## 2.6 The real contribution and subtraction terms

From the perspective of the MC integration, computing the real contribution is probably the most demanding part of the NLO calculation. On the one hand, due to the factorized construction of the phase space, which we already discussed and on the other hand, because it is this part of the computation which requires the meticulous construction of subtraction terms to yield a finite result.

As discussed in sec. 2.3, we divide the real phase space into singular regions, ALRs, such that we can use eq. (2.23) to write

$$\begin{aligned} \sigma^{\mathcal{R}}(f_{\mathcal{R}}) &= \int \frac{\mathbb{J}(\Phi_{n+1})}{\mathcal{N}(f_{\mathcal{R}})} \mathcal{R}(f_{\mathcal{R}}) d\Phi_{n+1} \\ &= \sum_{\alpha_r \in \mathcal{P}_{\text{FKS}}} \int \frac{\mathbb{J}(\Phi_{n+1})}{\mathcal{N}(f_{\mathcal{R}})} \mathcal{R}_{\alpha_r}(f_{\mathcal{R}}) d\Phi_{\text{rad}}^{(\alpha_r)} d\bar{\Phi}_n \quad . \end{aligned} \quad (2.124)$$

We explicitly included the jet measurement function  $\mathbb{J}$  and the symmetry factor  $\mathcal{N}(f_{\mathcal{R}})$  just as for the Born contribution in eq. (2.123). Eq. (2.124) describes the *non-subtracted* real cross section as we left out the subtraction term  $\mathcal{S}$  compared to eq. (2.3). We will dedicate this subsection to the real contribution and the construction of these subtraction terms, following the procedure described in refs. [47, 73] and also ref. [64]. In this discussion, we will representatively concentrate on one single ALR.

In order to construct the subtraction terms, we first make the divergences in eq. (2.124) explicit by using dimensional regularization in  $d = 4 - 2\epsilon$  dimensions. We can use the FKS variables  $(\xi, y)$  we defined in sec. 2.3.2 to rewrite the phase-space element as [47, 62]

$$d\Phi_{n+1} = \underbrace{(2\pi)^d \delta^d \left( k_{\oplus} + k_{\ominus} - \sum_{l=3}^{n+3} k_l \right) \left[ \prod_{\substack{l=3 \\ l \neq j}}^{n+3} \frac{d^{d-1} k_l}{(2\pi)^{d-1} 2E_l} \right]}_{d\bar{\Phi}_n} \underbrace{\left( \frac{s^{1-\epsilon}}{(4\pi)^{d-1}} \xi^{1-2\epsilon} (1-y^2)^{-\epsilon} d\xi dy d\Omega_{d-2} \right)}_{d\Phi_{\text{rad}}^{(\alpha_r)}} \quad , \quad (2.125)$$

where the indices  $i$  and  $j$  are reserved for the emitter and the radiated particle, as usual. For  $y$  and  $d\Omega$ , they are  $y_i$  and  $d\Omega_i$  for ISR and  $y_{ij}$  and  $d\Omega_{ij}$  for FSR. In both cases, the azimuthal integral yields the area of a  $(d-3)$ -dimensional sphere

$$\int d\Omega_{d-2} = \frac{2\pi^{1-\epsilon}}{\Gamma(1-\epsilon)} \quad . \quad (2.126)$$

In the first part, we will focus on the subtraction terms for final-state radiation, returning to the subtraction terms for initial-state radiation in sec. 2.6.2.

### 2.6.1 Final-state subtraction terms

Due to divergent propagators in the matrix element, final-state divergences will occur for  $\xi \rightarrow 0$  or  $y \rightarrow 1$ . We can use this knowledge to define the finite *regularized* squared real amplitude

$$\tilde{\mathcal{R}}_{\alpha_r}(\xi, y) := \xi^2(1-y) \mathcal{R}_{\alpha_r} \quad \text{such that} \quad \mathcal{R}_{\alpha_r} = \frac{1}{\xi^2} \frac{1}{1-y} \tilde{\mathcal{R}}_{\alpha_r}(\xi, y) \quad . \quad (2.127)$$

Here, both factors come from the propagator. The factor  $1/\xi$  enters squared in the squared amplitude while one factor of  $(1-y)$  is canceled by the sum over the radiated polarization states [7].

Together with eq. (2.125) we find that we can express the integral over the radiation phase space as

$$\int \mathcal{R}_{\alpha_r}(f\mathcal{R}) d\Phi_{\text{rad}}^{(\alpha_r)} = \frac{s^{1-\epsilon}}{(4\pi)^{d-1}} \int_0^{\xi_{\text{max}}} \frac{1}{\xi^{1+2\epsilon}} \int_{-1}^1 \frac{1}{(1+y)^\epsilon(1-y)^{1+\epsilon}} \int \tilde{\mathcal{R}}_{\alpha_r}(\xi, y) d\Omega_{d-2} dy d\xi \quad . \quad (2.128)$$

Now that the divergences are isolated, we can deal with them in terms of *modified plus distributions*. They are defined such that they regularize the appearing divergent terms:

$$\int_0^{\xi_{\text{max}}} \left( \frac{1}{\xi} \right)_{\xi_{\text{cut}}} f(\xi, y) d\xi = \int_0^{\xi_{\text{max}}} \frac{f(\xi, y) - f(0, y)\Theta(\xi_{\text{cut}} - \xi)}{\xi} d\xi \quad (2.129)$$

$$\int_0^{\xi_{\text{max}}} \left( \frac{\log(\xi)}{\xi} \right)_{\xi_{\text{cut}}} f(\xi, y) d\xi = \int_0^{\xi_{\text{max}}} \frac{f(\xi, y) - f(0, y)\Theta(\xi_{\text{cut}} - \xi)}{\xi} \log(\xi) d\xi \quad (2.130)$$

$$\int_{-1}^1 \left( \frac{1}{1 \mp y} \right)_{\delta_{O/I}} f(\xi, y) dy = \int_{-1}^1 \frac{f(\xi, y) - f(\xi, \pm 1)\Theta(\pm y - 1 + \delta_{O/I})}{1 \mp y} dy \quad . \quad (2.131)$$

Here, we introduced three parameters  $\xi_{\text{cut}}$ ,  $\delta_I$  and  $\delta_O$ . While  $\xi_{\text{cut}}$  allows to shift the soft contribution between the subtracted real and the integrated subtraction terms (c.f. eq. (2.3)),  $\delta_O$  does the same for the collinear contributions to the FSR subtraction terms. We also used the opportunity to introduce  $\delta_I$ , the analogon to  $\delta_O$  for ISR. They can be chosen in the ranges  $0 < \xi_{\text{cut}} \leq 1$  and  $0 < \delta_{O/I} \leq 2$ , but the total summed result should be independent of the explicit choice. By default, we choose  $\xi_{\text{cut}} = 1$  and  $\delta_{O/I} = 2$  restoring the unmodified plus distributions bar the integration ranges, i.e.

$$\left( \frac{1}{\xi} \right)_{\xi_{\text{cut}}=1} = \left( \frac{1}{\xi} \right)_+ \quad \text{and} \quad \left( \frac{1}{1 \mp y} \right)_{\delta_{O/I}=2} = \left( \frac{1}{1 \mp y} \right)_+ \quad . \quad (2.132)$$

We can use these plus distributions and a Laurent expansion of the integrands to rewrite the divergent parts of eq. (2.128) as

$$\frac{1}{\xi^{1+2\epsilon}} = -\frac{\xi_{\text{cut}}^{-2\epsilon}}{2\epsilon} \delta(\xi) + \left( \frac{1}{\xi} \right)_{\xi_{\text{cut}}} - 2\epsilon \left( \frac{\log(\xi)}{\xi} \right)_{\xi_{\text{cut}}} + \mathcal{O}(\epsilon^2) \quad \text{and} \quad (2.133)$$

$$\frac{1}{(1-y)^{1+\epsilon}} = -\frac{\delta_O^{-\epsilon}}{\epsilon} \delta(1-y) + \left( \frac{1}{1-y} \right)_{\delta_O} - \epsilon \left( \frac{\log(1-y)}{1-y} \right)_{\delta_O} + \mathcal{O}(\epsilon^2) \quad . \quad (2.134)$$

With these insights we can continue from eq. (2.128) to find

$$\begin{aligned}
\int \mathcal{R}_{\alpha_r}(f_{\mathcal{R}}) d\Phi_{\text{rad}}^{(\alpha_r)} &= \frac{s^{1-\epsilon}}{(4\pi)^{d-1}} \left[ \int \frac{\xi^{-2\epsilon} (2\delta_O)^{-\epsilon}}{2\epsilon^2} \tilde{\mathcal{R}}_{\alpha_r}(0, 1) d\Omega_{d-2} \right. \\
&\quad - \int \int_{-1}^1 (1+y)^{-\epsilon} \frac{\xi_{\text{cut}}^{-2\epsilon}}{2\epsilon} \left[ \left( \frac{1}{1-y} \right)_{\delta_O} - \epsilon \left( \frac{\log(1-y)}{1-y} \right)_{\delta_O} \right] \tilde{\mathcal{R}}_{\alpha_r}(0, y) dy d\Omega_{d-2} \\
&\quad - \int \int_0^{\xi_{\text{max}}} \frac{(2\delta_O)^{-\epsilon}}{\epsilon} \left[ \left( \frac{1}{\xi} \right)_{\xi_{\text{cut}}} - 2\epsilon \left( \frac{\log(\xi)}{\xi} \right)_{\xi_{\text{cut}}} \right] \tilde{\mathcal{R}}_{\alpha_r}(\xi, 1) d\xi d\Omega_{d-2} \left. \right] \\
&\quad + \int \int_0^{\xi_{\text{max}}} \int_{-1}^1 \left( \frac{1}{\xi} \right)_{\xi_{\text{cut}}} \left( \frac{1}{1-y} \right)_{\delta_O} \frac{\mathcal{J}^{(\alpha_r)}}{\xi} \tilde{\mathcal{R}}(\xi, y) dy d\xi d\phi + \mathcal{O}(\epsilon) \\
&\equiv I_{sc, \alpha_r}^{\text{FSR}} + I_{s+, \alpha_r}^{\text{FSR}} + I_{+c, \alpha_r}^{\text{FSR}} + I_{++, \alpha_r}^{\text{FSR}} + \mathcal{O}(\epsilon) \tag{2.135}
\end{aligned}$$

where we get a factor of  $2^{-\epsilon}$  in the first and third row due to  $\delta(1-y)$  acting on  $(1+y)^{-\epsilon}$ .

We also labeled the remaining integrals in the last step using 's' and 'c' for soft and collinear divergent terms, respectively, and + for the part regularized by the plus distributions. We can see that the first three terms of eq. (2.135) are soft-collinear, soft and collinear divergent, respectively. These terms are guaranteed by the KLN theorem to cancel with corresponding terms in the one-loop virtual amplitude and thus can be used to construct the integrated subtraction terms for the virtual contribution. We will return to them in sec. 2.7.

For the real contribution, we will focus on the last integral,  $I_{++, \alpha_r}^{\text{FSR}}$ . It is a finite contribution to the real cross section, so we can safely compute it in  $d = 4$  dimensions, i.e., with  $\epsilon = 0$ . In this case, the angular measure  $d\Omega_{d-2}$  reduces to  $d\phi$ . We have also already derived the Jacobians for four dimensions in sec. 2.4. They already include a factor of  $\xi$  which is also present in eq. (2.125). Thus, we can include the Jacobian factor in the real squared matrix element by defining

$$\hat{\mathcal{R}}_{\alpha_r}(\xi, y) := \frac{\mathcal{J}^{(\alpha_r)}(\xi, y, \phi)}{\xi} \tilde{\mathcal{R}}_{\alpha_r}(\xi, y) \tag{2.136}$$

taking out one factor of  $\xi$ .

Using this definition and the modified plus distributions, we can again split the remaining finite part according to

$$\begin{aligned}
I_{++, \alpha} &= \int_0^{2\pi} d\phi \int_0^{\xi_{\text{max}}} \frac{d\xi}{\xi} \int_{-1}^1 \frac{dy}{1-y} \left[ \hat{\mathcal{R}}_{\alpha_r}(\xi, y) \right. \\
&\quad \left. - \hat{\mathcal{R}}_{\alpha_r}(0, y) \Theta(\xi_{\text{cut}} - \xi) - \hat{\mathcal{R}}_{\alpha_r}(\xi, 1) \Theta(y - 1 + \delta_O) + \hat{\mathcal{R}}_{\alpha_r}(0, 1) \Theta(\xi_{\text{cut}} - \xi) \Theta(y - 1 + \delta_O) \right] . \tag{2.137}
\end{aligned}$$

This is the master formula for the real-emission subtraction terms. It states that the finite real matrix element is obtained by subtracting the soft and collinear limits,  $\hat{\mathcal{R}}_{\alpha_r}(\xi, 1)$  and  $\hat{\mathcal{R}}_{\alpha_r}(0, y)$  and adding the soft-collinear limit to compensate subtracting this limit with each of the other two terms once, similar to eq. (2.135). Although this is not surprising, only the parametrization using  $\xi$  and  $y$  ensures that the divergences are separated consistently.

We can now proceed to separately construct the subtraction terms,  $\tilde{\mathcal{R}}_{\alpha_r}(\xi, 1)$  for the collinear,  $\tilde{\mathcal{R}}_{\alpha_r}(0, y)$  for the soft and  $\tilde{\mathcal{R}}_{\alpha_r}(0, 1)$  for the soft-collinear limit, respectively. In every divergent limit, the real configuration becomes degenerate, i.e., Born-like. We use this fact to construct the counterterms: we approximate the

limit of the squared real matrix element as the squared Born matrix element times a kinematic factor. The construction of the counterterms is explained in refs. [48, 73]. We will summarize the results in the following.

### The collinear counterterms

In the collinear limit, we can write

$$\bar{k}_i^\mu = \frac{k_j^\mu}{z} + k_\perp^\mu - \frac{\eta^\mu z k_\perp^2}{2(1-z)k_j \cdot \eta} \quad , \quad (2.138)$$

parametrizing the momentum of the Born emitter using the energy fraction

$$z := \frac{E_{\text{rad}}}{E_{\text{em}}} = \frac{\xi\sqrt{s}}{2E_{\text{em}}} \quad \Leftrightarrow \quad 1-z = \frac{E_{\text{em}}}{E_{\text{em}}} \quad . \quad (2.139)$$

$k_\perp$  is defined such that it is transverse to the collinear FKS pair  $(i, j)$  and satisfies  $k_\perp \cdot k_j = 0$  and an additional vector  $\eta$  is defined such that  $k_\perp \cdot \eta = 0$  and  $\eta^2 = 0$ . This construction preserves the emitter as a light-like vector  $k_i^2 = (\bar{k}_i^\mu - k_j^\mu)^2 = 0$ , which we assume here, as there are no collinear divergent regions with massive emitters.

The construction of the collinear counterterms is then based on the observation that the squared real amplitude can be factorized as a splitting function times the Born amplitude, i.e.

$$\mathcal{R}_{\alpha_r}^{f_B^i \rightarrow f_R^i f_R^j} \simeq \frac{8\pi\alpha_S}{\bar{k}_i^2} \hat{P}_{f_B^i \rightarrow f_R^i f_R^j}^\lambda(z, k_\perp) \mathcal{B}_\lambda^{(i)} \quad , \quad (2.140)$$

where the splitting functions  $\hat{P}_{f_B^i \rightarrow f_R^i f_R^j}^\lambda(z, k_\perp)$  are QCD splitting functions derived by Altarelli and Parisi [81]. Here, we used their spin-dependent form in  $d = 4$  dimensions with  $\lambda$  representing either two spinor or two vector indices and  $\epsilon = 0$ . We refer to app. A.1 for their formal definition. The Born matrix element in eq. (2.140) is the *spin-correlated squared Born matrix element* obtained by leaving the spin indices of the emitting particle uncontracted, which is non-trivial only for gluonic emitters.

In this setup, we can derive the *regularized real collinear counterterms* for each of the final-state splittings depicted in fig. 2.3 as [73]

$$\tilde{\mathcal{R}}_{\alpha_r}^{q \rightarrow qg}(\xi, 1) = \tilde{\mathcal{R}}_{\alpha_r}^{\bar{q} \rightarrow \bar{q}g}(\xi, 1) = S_{ij}^{\alpha_r} \frac{16\pi\alpha_S C_F}{s(1-z)} \left[ 1 + (1-z)^2 \right] \mathcal{B} \quad (2.141)$$

$$\tilde{\mathcal{R}}_{\alpha_r}^{g \rightarrow q\bar{q}}(\xi, 1) = S_{ij}^{\alpha_r} \frac{16\pi\alpha_S T_F}{s(1-z)} \left[ -zg^{\mu\nu} - 4z^2(1-z) \frac{k_\perp^\mu k_\perp^\nu}{k_\perp^2} \right] \mathcal{B}_{\mu\nu} \quad (2.142)$$

$$\tilde{\mathcal{R}}_{\alpha_r}^{g \rightarrow gg}(\xi, 1) = S_{ij}^{\alpha_r} \frac{16\pi\alpha_S C_A}{s(1-z)} \left[ -2 \left( \frac{z^2}{1-z} + (1-z) \right) g^{\mu\nu} + 4z^2(1-z) \frac{k_\perp^\mu k_\perp^\nu}{k_\perp^2} \right] \mathcal{B}_{\mu\nu} \quad (2.143)$$

where the constants  $C_F = 4/3$ ,  $T_F = 1/2$  and  $C_A = 3$  are the usual  $SU(3)$  constants. The counterterms are evaluated in the collinear kinematic limit. In this limit, only the  $S$  function in eq. (2.143) is non-trivial (c.f. eq. (2.26)) while in the other cases, they reduce to 1 and are included for uniformity.

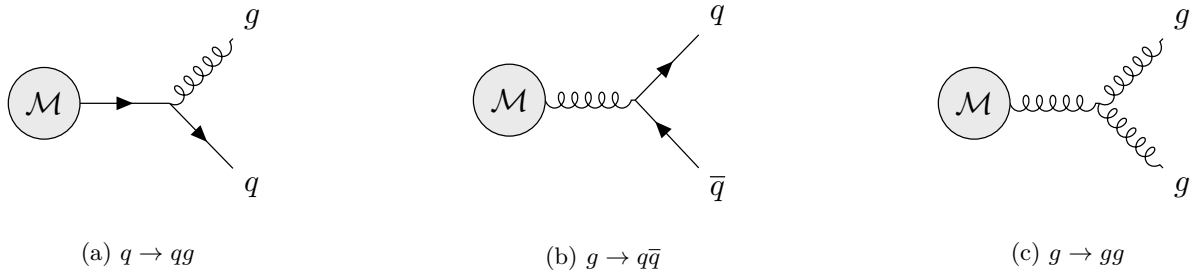


Fig. 2.3: Diagrams of all possible FSR QCD splittings.

### The soft-collinear counterterms

The soft-collinear limit is characterized by  $y \rightarrow 1$  and  $z \rightarrow 0$ . It is sufficient not to consider the mirror soft singularity  $1 - z \rightarrow 0$  since we desymmetrized  $\mathcal{P}_{\text{FKS}}$  and introduced the double FSR factor in eq. (2.26). This limit is still collinear, so the discussion of the collinear counterterms still applies. In fact, we can take the limit  $z \rightarrow 0$  in eqs. (2.141-2.143) and use the relation

$$g^{\mu\nu} \mathcal{B}_{\mu\nu} = -\mathcal{B} \quad (2.144)$$

to find

$$\tilde{\mathcal{R}}_{\alpha_r}^{q \rightarrow gg}(0, 1) = \tilde{\mathcal{R}}_{\alpha_r}^{\bar{q} \rightarrow \bar{q}g}(0, 1) = S_{ij}^{\alpha_r} \frac{32\pi\alpha_S C_F}{s} \mathcal{B} \quad \text{and} \quad \tilde{\mathcal{R}}_{\alpha_r}^{g \rightarrow gg}(0, 1) = S_{ij}^{\alpha_r} \frac{32\pi\alpha_S C_A}{s} \mathcal{B} \quad (2.145)$$

while  $\tilde{\mathcal{R}}_{\alpha_r}^{g \rightarrow q\bar{q}}(0, 1)$  vanishes as the splitting  $g \rightarrow q\bar{q}$  is not soft divergent. We see that also all the terms involving spin-correlations vanish as in the soft-collinear limit, there is no kinematic freedom left. Technically, we do not use eq. (2.145) but instead use eqs. (2.141) and (2.143) implemented in a soft-finite way.

### The soft counterterms

The soft counterterms will also only be relevant for gluon emissions. In the soft but not collinear limit, the gluon still takes away no momentum from the emitter, so there are no spin interactions. However, the gluon still carries a color charge. Moreover, the soft gluon has a large wavelength leading to non-local color-correlations [82] with the whole system of external colored partons. These can be described by expressing the real matrix element in the *eikonal approximation* [83, 84] summing over all external momenta and color charges<sup>8</sup>,

$$\mathcal{M}_{\alpha_r}^{n+1}(\Phi_{n+1}) \simeq \epsilon_{s_j, \mu}^*(k_j) \frac{g_s}{E_j} \left( \sum_{k=1}^{n+2} \hat{T}_{c_k, c'_k}^a \frac{\bar{k}_k^\mu}{\bar{k}_k \cdot \hat{k}_j} \right) \mathcal{M}^n(\bar{\Phi}_n) \quad (2.146)$$

where  $\epsilon_{s_j, \mu}^*(k_j)$  denotes the gluon polarization vector with spin  $s_j$ , we introduced  $\hat{k}_j$  such that  $k_j = E_j \cdot \hat{k}_j$  for the radiated massless particle and we used the fact that in the soft limit, the Born and real momenta are equivalent  $k_k = \bar{k}_k \forall k \in \{3, \dots, n+2\}$ .

We can now square eq. (2.146), sum over final-state spins and colors to derive the regularized real soft counterterms [48, 73]

$$\tilde{\mathcal{R}}_{\alpha_r}(0, y) = \delta_{gf_{\mathcal{R}}} S_{ij}^{\alpha_r} \frac{16\pi\alpha_S}{s} (1-y) \left[ \sum_{k>l}^{n+2} \frac{2\bar{k}_k \cdot \bar{k}_l}{(\bar{k}_k \cdot \hat{k}_j)(\bar{k}_l \cdot \hat{k}_j)} \mathcal{B}_{kl} - \sum_{k=1}^{n+2} \frac{\bar{k}_k^2}{(\bar{k}_k \cdot \hat{k}_j)^2} C(f_B^k) \mathcal{B} \right] . \quad (2.147)$$

<sup>8</sup>Colorless particles in the sum will drop out because of their vanishing color operator.

Here,  $\mathcal{B}_{kl}$  denotes the *color-correlated squared Born matrix element*  $\mathcal{B}_{kl} = -|\mathcal{M}_{kl}^n|^2$ . It is symmetric and obeys

$$\sum_{k \neq l}^{n+2} \mathcal{B}_{kl} = C(f_{\mathcal{B}}^l) \mathcal{B} \quad (2.148)$$

where  $C(f_{\mathcal{B}}^l)$  are the Casimir constants for the flavor  $f_{\mathcal{B}}^l$ . We used these conditions to split off the second term in the brackets of eq. (2.147) from the first.

Finally, we remind ourselves that for the  $S$  functions appearing in the soft counterterms, we have to use the  $S$  functions in the soft limit, taking into account the findings in sec. 2.3.3.

In the counterterms derived so far, we have explicitly not included the symmetry factor for identical final-state particles. Although we use the Born matrix elements to construct the counterterms, it is important that the counterterms are equipped with the *real* symmetry factor  $\mathcal{N}(f_{\mathcal{R}})$  for the  $(n+1)$ -body final state for the counterterms to match the divergent real terms.

The counterterms also have to be multiplied by the appropriate jet measurement function  $\mathbb{J}$ , i.e., they must obey the phase-space cuts. Contrary to the symmetry factor, however, their jet measurement function is evaluated using the underlying Born kinematics as the real kinematic degenerates in any divergent limit. Moreover, we need to add the same term to the real component that we subtract from the virtual component for the subtraction approach to be valid. If different jet measurement functions were applied to the subtraction terms in both contributions, the result would depend on details of the subtraction scheme, e.g., the explicit values of  $\delta_I$  and  $\delta_O$ .

### 2.6.2 Initial-state subtraction terms

So far, we have only treated emissions from the final-state partons. However, emissions from the initial-state partons also exhibit a divergent structure and thus require careful construction of subtraction terms.

Contrary to FSR, the initial state real and virtual divergences do not entirely cancel each other and instead leave uncanceled initial state collinear divergences. These remaining divergences are only properly canceled by also taking renormalized NLO PDFs into account, which themselves contain collinear divergences in the NLO PDF evolution kernels. This is explained, e.g., in ref. [73].

Fortunately, we can derive the subtraction terms for both the initial-state emissions in the partonic cross section as well as the PDF divergences analogous to our derivation of the final-state subtraction terms in sec. 2.6.1. We start by defining the regularized squared real amplitude in this case as

$$\tilde{\mathcal{R}}_{\alpha_r}(\xi, y) := \xi^2(1-y^2) \mathcal{R}_{\alpha_r} \quad \text{such that} \quad \mathcal{R}_{\alpha_r} = \frac{1}{\xi^2} \frac{1}{1-y^2} \tilde{\mathcal{R}}_{\alpha_r}(\xi, y) \quad , \quad (2.149)$$

where this time, we account for divergent regions for both,  $y \rightarrow +1$  and  $y \rightarrow -1$ . Following the steps we took in sec. 2.6.1, we use the expansion for the  $y$ -dependent factor

$$\begin{aligned} \frac{1}{(1-y^2)^{1+\epsilon}} &= -\frac{(2\delta_I)^{-\epsilon}}{2\epsilon} \left[ \delta(1-y) + \delta(1+y) \right] \\ &+ \frac{1}{2} \left[ \left( \frac{1}{1-y} \right)_{\delta_I} + \left( \frac{1}{1+y} \right)_{\delta_I} - \epsilon \left( \frac{\log(1-y)}{1-y} \right)_{\delta_I} - \epsilon \left( \frac{\log(1+y)}{1+y} \right)_{\delta_I} \right] + \mathcal{O}(\epsilon^2) \end{aligned} \quad (2.150)$$

and eq. (2.133) for the  $\xi$ -dependent factor to find

$$\begin{aligned}
\int \mathcal{R}_{\alpha_r}(f\mathcal{R}) d\Phi_{\text{rad}}^{(\alpha_r)} &= \frac{s_{\mathcal{R}}^{1-\epsilon}}{(4\pi)^{d-1}} \left[ \int \frac{\xi_{\text{cut}}^{-2\epsilon} (2\delta_I)^{-\epsilon}}{4\epsilon^2} \left[ \tilde{\mathcal{R}}_{\alpha_r}(0, 1) + \tilde{\mathcal{R}}_{\alpha_r}(0, -1) \right] d\Omega_{d-2} \right. \\
&\quad - \int \int_{-1}^1 \frac{\xi_{\text{cut}}^{-2\epsilon}}{4\epsilon} \left[ \left( \frac{1}{1-y} \right)_{\delta_I} - \epsilon \left( \frac{\log(1-y)}{1-y} \right)_{\delta_I} + \left( \frac{1}{1+y} \right)_{\delta_I} - \epsilon \left( \frac{\log(1+y)}{1+y} \right)_{\delta_I} \right] \tilde{\mathcal{R}}_{\alpha_r}(0, y) dy d\Omega_{d-2} \\
&\quad - \int \int_0^{\xi_{\text{max}}} \frac{(2\delta_I)^{-\epsilon}}{2\epsilon} \left[ \left( \frac{1}{\xi} \right)_{\xi_{\text{cut}}} - 2\epsilon \left( \frac{\log(\xi)}{\xi} \right)_{\xi_{\text{cut}}} \right] \left[ \tilde{\mathcal{R}}_{\alpha_r}(\xi, 1) + \tilde{\mathcal{R}}_{\alpha_r}(\xi, -1) \right] d\xi d\Omega_{d-2} \left. \right] \\
&\quad + \int \int_0^{\xi_{\text{max}}} \int_{-1}^1 \left( \frac{1}{\xi} \right)_{\xi_{\text{cut}}} \frac{1}{2} \left[ \left( \frac{1}{1-y} \right)_{\delta_I} + \left( \frac{1}{1+y} \right)_{\delta_I} \right] \frac{\mathcal{J}^{(\alpha_r)}}{\xi} \tilde{\mathcal{R}}_{\alpha_r}(\xi, y) dy d\xi d\phi + \mathcal{O}(\epsilon) \\
&\equiv I_{sc, \alpha_r}^{\text{ISR}} + I_{s+, \alpha_r}^{\text{ISR}} + I_{+c, \alpha_r}^{\text{ISR}} + I_{++, \alpha_r}^{\text{ISR}} + \mathcal{O}(\epsilon) \quad . \quad (2.151)
\end{aligned}$$

We see a number of additional terms arising compared to eq. (2.135). The first two terms are soft divergent and will subtract similar terms of the virtual contribution. The third term  $I_{+c, \alpha_r}^{\text{ISR}}$  is collinear divergent and will cancel with virtual terms and the divergences of the NLO PDFs. We will discuss these cancellations in sec. 2.7.1. The last term  $I_{++, \alpha_r}^{\text{ISR}}$  is finite in  $\epsilon$  so we took the limit  $\epsilon \rightarrow 0$  and used eq. (2.119) to reintroduce the Jacobian  $\mathcal{J}^{(\alpha)}$ . It is the analogon to eq. (2.137) featuring additional (soft-)collinear counterterms for  $y \rightarrow -1$  which we will review in the remainder of this section.

### The collinear counterterms

Before explicitly constructing the subtraction terms, we have to elaborate on the kinematic structure of the initial-state splittings, especially the collinear ones. Fig. 2.4 depicts all possible initial-state splittings diagrammatically. We notice that, compared to fig. 2.3, there is one more splitting type depicted for the fact that for initial-state splittings, the partons not connected to the rest of the matrix element are not interchangeable. We denote the different initial-state splittings using the backwards-evolution interpretation. If we consider, e.g., fig. 2.4b, the splitting describing the transformation from the Born to the real matrix element is the splitting of a gluon into quarks instead of a quark radiating a gluon. Thus we write  $qq \leftarrow g$ , in general,  $f_{\mathcal{R}}^i f_{\mathcal{R}}^j \leftarrow f_{\mathcal{B}}^i$  in such a way that the real external particles are on the LHS and the Born particles are on the RHS to stress the fact that we are describing an initial-state splitting. Doing this, we keep the convention of writing the radiated particle last on the LHS and using the external particle flavors, which results in notations such as  $g\bar{q} \leftarrow q$  for the splitting depicted in fig. 2.4c which at first glance may seem unintuitive.

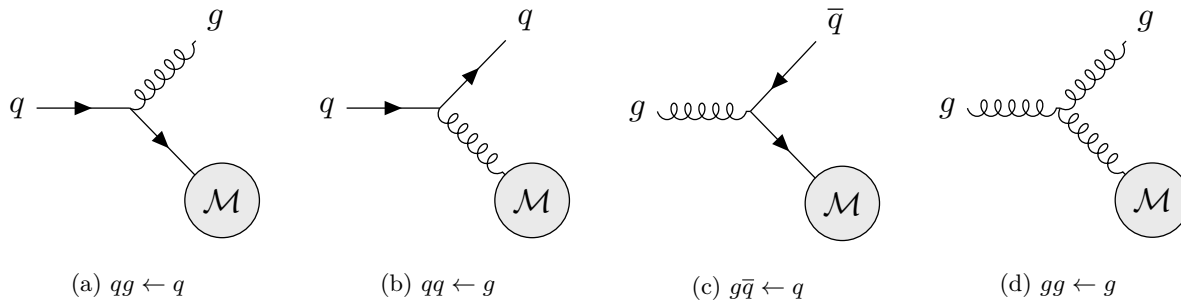


Fig. 2.4: Diagrams of all possible ISR QCD splittings. The notation is explained in the text.

As in the case of FSR, we compute the collinear counterterms in the strictly collinear limit. In the case of ISR, this means that the radiated parton is strictly collinear to either of the beams. Contrary to FSR, the collinear ISR configuration is left with an additional degree of freedom, the energy of the radiated parton, linearly parametrized by  $z$  such that

$$\bar{k}_i^\mu = zk_i^\mu + k_\perp^\mu + \frac{\eta^\mu k_\perp^2}{2(1-z)k_i \cdot \eta} \quad (2.152)$$

where we defined  $k_\perp$  and  $\eta$  analogous to eq. (2.138).

We also find that in the collinear limit, the relation  $z = 1 - \xi$  connects both parameters. Using this, the collinear phase space directly follows as the collinear case of the discussion in sec. 2.4.3.

With this definition, we can derive the collinear counterterms again as a product of splitting functions and Born amplitudes. For the *regularized real collinear counterterms* we find [48, 73]

$$\tilde{\mathcal{R}}_{\alpha_r}^{g\bar{q}^{\leftarrow}q}(\xi, \pm 1) = \tilde{\mathcal{R}}_{\alpha_r}^{gq^{\leftarrow}\bar{q}}(\xi, \pm 1) = \frac{8\pi\alpha_S T_F}{E_{\text{em}}^2} (1-z)[z^2 + (1-z)^2] \mathcal{B} \quad (2.153)$$

$$\tilde{\mathcal{R}}_{\alpha_r}^{qg^{\leftarrow}q}(\xi, \pm 1) = \tilde{\mathcal{R}}_{\alpha_r}^{\bar{q}g^{\leftarrow}\bar{q}}(\xi, \pm 1) = \frac{8\pi\alpha_S C_F}{E_{\text{em}}^2} (1+z)^2 \mathcal{B} \quad (2.154)$$

$$\tilde{\mathcal{R}}_{\alpha_r}^{qg^{\leftarrow}g}(\xi, \pm 1) = \frac{8\pi\alpha_S C_F}{E_{\text{em}}^2} \left[ -z(1-z)g^{\mu\nu} + 4\frac{(1-z)^2}{z} \frac{k_\perp^\mu k_\perp^\nu}{k_\perp^2} \right] \mathcal{B}_{\mu\nu} \quad (2.155)$$

$$\tilde{\mathcal{R}}_{\alpha_r}^{gg^{\leftarrow}g}(\xi, \pm 1) = \frac{8\pi\alpha_S C_A}{E_{\text{em}}^2} \left[ -2(z+z(1-z)^2)g^{\mu\nu} + 4\frac{(1-z)^2}{z} \frac{k_\perp^\mu k_\perp^\nu}{k_\perp^2} \right] \mathcal{B}_{\mu\nu} \quad (2.156)$$

for all ISR QCD splittings. We did not include any explicit  $S$  function in eq. (2.153f) as they are equivalent to unity in all cases.

Finally, we note again that in the Born amplitudes, we have to use the real symmetry factor  $\mathcal{N}(f_{\mathcal{R}})$ . Moreover, we have to use the real PDFs with the rescaled  $x_{\mathcal{R},\oplus} = \frac{x_{\mathcal{B},\oplus}}{z}$ , which is the collinear limit of eq. (2.114) and also the PDF with the real flavor  $f_{\mathcal{R}}^i$  for the emitting parton which is different than the Born flavor for the splittings depicted in figs. 2.4b and 2.4c.

### The soft-collinear counterterms

Just as for the FSR case, the ISR soft-collinear counterterms simply follow from eqs. (2.153-2.156) with  $z = 1 \Leftrightarrow \xi = 0$  which can directly be applied as the regularized counterterms are already formulated in a soft finite way.

### The soft counterterms

Only the splittings featuring an additional gluon in the final-state feature soft divergences, i.e. the ones shown in fig. 2.4a and 2.4d. The emission of a soft gluon neither changes the emitter momentum nor the flavor, so the real and Born PDFs will coincide in this case. The eikonal approximation also holds for ISR so the subtraction terms are equivalent to the ones given in eq. (2.147) with the replacements  $(1-y) \rightarrow (1-y^2)$  in the equations and using the soft  $S$  functions whose  $d_{ij}^{\text{soft}}$  are given in eq. (2.38).

### 2.6.3 Partitioning the real contribution

#### The general idea

In sec. 2.3, we have identified all regions in which the real contribution diverges. These insights can be used to split off a finite piece of the real contribution dividing the real contribution into a singular, diverging part and a finite part without any singularities so that the finite part can be handled almost like an ordinary LO contribution. This was first mentioned in ref. [46] and first implemented in the course of ref. [85].

This partition is performed per ALR so that

$$\mathcal{R}^{\alpha_r} = \mathcal{R}_{\text{sin}}^{\alpha_r} + \mathcal{R}_{\text{fin}}^{\alpha_r} \quad . \quad (2.157)$$

In general, the partition may be achieved by defining a function  $F(\Phi_{n+1})$  taking values between 0 and 1 and assigning

$$\mathcal{R}_{\text{sin}}^{\alpha_r} = \mathcal{R}^{\alpha_r} F(\Phi_{n+1}) \quad (2.158)$$

$$\mathcal{R}_{\text{fin}}^{\alpha_r} = \mathcal{R}^{\alpha_r} [1 - F(\Phi_{n+1})] \quad (2.159)$$

with the condition that  $F \rightarrow 1$  in the phase-space region, which is singular in the given ALR. For the whole FKS subtraction mechanism, it is then sufficient to take the singular real contribution  $\mathcal{R}_{\text{sin}}^{\alpha_r}$  into account, while the finite real contribution  $\mathcal{R}_{\text{fin}}^{\alpha_r}$  can be integrated separately. This contribution is finite across the whole phase space, so it does not require any subtraction terms, ALRs or  $S$  functions to be integrable and no counterevents to generate finite differential distributions. We will see in sec. 2.8 that both are in general necessary for event generation at fixed NLO.

The events representing the finite contribution will have  $(n+1)$ -body kinematics, and the associated weights will be positive definite, implying that also unweighted event generation would be possible for this component. However, as this is not possible for the events associated with the singular contribution, this is rarely useful. The real singular contribution will be integrated including the subtraction terms across the entire phase space, so the associated cross section will often be negative. Events for the singular contribution will be generated just as in the case without any real partition, which we will discuss in detail in sec. 2.8.

In the end, the results from both contributions need to be additively merged in order to restore the fNLO accuracy. While the cross sections can simply be summed, the event samples can be merged, assuring that the sum of weights for each contribution is proportional to their respective cross section. It is equivalently possible to directly generate a mixed event sample by deciding on an event-by-event basis whether an event based on the finite or the singular contribution should be generated so that the probability for an event based on the finite contribution is given by

$$\frac{\mathcal{R}_{\text{fin}}^{\alpha_r}(\Phi_{n+1})}{\mathcal{R}_{\text{fin}}^{\alpha_r}(\Phi_{n+1}) + \mathcal{R}_{\text{sin}}^{\alpha_r}(\Phi_{n+1})} \quad . \quad (2.160)$$

While the former approach is the default procedure in **WHIZARD**, the latter is realized in the **POWHEG-BOX**. The restoration of the fNLO accuracy refers to the computation of NLO cross sections as well as the simulation of fNLO events which will, in the end, be independent of the explicit choice of the real-partition function. When generating events to be matched to a parton shower, however, we will treat the singular real contribution significantly different from the finite real contribution so that the details of the choice for  $F$  will impact the predictions.

### Choices for the real-partition function

Different realizations of the real-partition function  $F(\Phi_{n+1})$  are possible.

In WHIZARD, the default definition is given by [71]

$$F(\Phi_{n+1}) = \begin{cases} 1 & \text{if } \exists (i, j) \in \mathcal{P}_{\text{FKS}} \text{ with } \sqrt{(p_i + p_j)^2} < m_i + m_j + h_F \\ 0 & \text{else} \end{cases} . \quad (2.161)$$

By definition of the FKS pairs,  $m_j = 0$ . If also the second member of the pair is massless, eq. (2.161) simplifies to

$$F(\Phi_{n+1}) = \begin{cases} 1 & \text{if } \exists (i, j) \in \mathcal{P}_{\text{FKS}} \text{ with } 2E_i E_j (1 - \cos(\theta_{ij})) < h_F^2 \\ 0 & \text{else} \end{cases} . \quad (2.162)$$

Here,  $h_F$  is the real-partition scale determining which PSPs we consider close enough to a divergence and thus belonging to the real singular. It can be used to estimate the theoretical uncertainty of this procedure.  $\mathcal{P}_{\text{FKS}}$  refers to the collection of FKS pairs given by eq. (2.14). It is initially collected across all ALRs so that the finite contribution does not require knowledge about the ALRs.

The motivation for the functional form of  $F$  is simple. As soon as at least one FKS pair falls below the threshold given by  $h_F$ , it is possible for soft or collinear singularities to arise, so the real contribution may not be finite, and we set  $F(\Phi_{n+1}) = 1$ .

It is also possible to base the real-partition function not directly upon the kinematics but on a direct comparison of the squared real matrix element with its soft or collinear limit, which we determined in the previous subsection. The default choice in the POWHEG-BOX [48] is

$$F(\Phi_{n+1}) = 1 - \theta(\mathcal{R}^{\alpha_r} - n \cdot \mathcal{R}_{\text{soft}}^{\alpha_r}) \theta(\mathcal{R}^{\alpha_r} - n \cdot \mathcal{R}_{\text{coll}}^{\alpha_r}) \quad (2.163)$$

such that  $F$  is zero if the real squared amplitude (excluding PDFs) is larger than  $n$  times its soft or collinear approximation, meaning that the real amplitude will be treated as finite far off the singular phase-space regions. The default choice is  $n = 5$ . This decision is made for each ALR and each PSP individually so that for the decision itself, knowledge about the ALRs is necessary.

While we previously only discussed partition functions making a clear cut between finite and singular contributions, it is also possible to use a smooth function for this separation. A possible choice suggested in ref. [86] is to set

$$F = \frac{Z}{Z + H} \quad \text{with} \quad Z = \mathcal{B} \frac{k_T^2}{\mathcal{B}_{\text{max}}} \quad \text{and} \quad H = k_T^2. \quad (2.164)$$

where  $\mathcal{B}_{\text{max}}$  is an upper bound for the Born cross section so that  $Z$  vanishes like the Born cross section and  $H$  serves as hardness scale. In this case, the singular contribution  $\mathcal{R}_{\text{sin}}$  vanishes like the Born contribution  $\mathcal{B}$ , keeping the ratio  $\mathcal{R}/\mathcal{B}$  finite. We will understand in sec. 3, esp. sec. 3.6.3f, that this behavior is beneficial for the POWHEG approach of matching NLO events to a parton shower.

It would be an interesting future project to compare the different approaches performance-wise for the integration and their impact on the predictions of matched differential observables.

### A particular example

While it is always possible to use the aforementioned partition of the real matrix element, there are some cases where the benefit of this approach is most evident. One particular example is given by the real

correction to the process  $e^+e^- \rightarrow t\bar{t}j$ . The partonic final state of the Born process consists of two top quarks and a gluon. The real correction receives contributions where the gluon splits into two light quarks, i.e. from matrix elements  $\mathcal{M}_{e^+e^- \rightarrow t\bar{t}q\bar{q}}$ .

Fig. 2.5 shows the contributing diagrams. Fig. 2.5a depicts the typical contribution where the gluon splits into light quarks giving rise to collinear divergences. The contribution depicted in fig. 2.5b, however, is finite because here, the collinear divergence is regularized by the top mass. This process corresponds to a different underlying Born process than  $e^+e^- \rightarrow t\bar{t}j$ , but in a full gauge invariant calculation, all contributing diagrams have to be summed up.

The consequence is a very poor convergence of the integration in the ALRs with a  $g \rightarrow q\bar{q}$  splitting, as we will see in sec. 6.3 because we still have to apply the counterterms in these ALRs to remedy the divergence caused by diagrams such as fig. 2.5a. As also mentioned in ref. [72], the partition of the real matrix element discussed here solves this problem by splitting off the finite part of the matrix element into its own contribution, greatly improving the performance of this kind of processes.

Other affected processes include  $pp \rightarrow t\bar{t}j$ , which has the same problem, although suppressed by more ALRs featuring gluon radiation instead of a gluon splitting and  $e^+e^- \rightarrow b\bar{b}j$ , where the same effect is present but suppressed by the much smaller  $b$  mass as well as  $e^+e^- \rightarrow t\bar{t}\gamma$  at NLO EW.

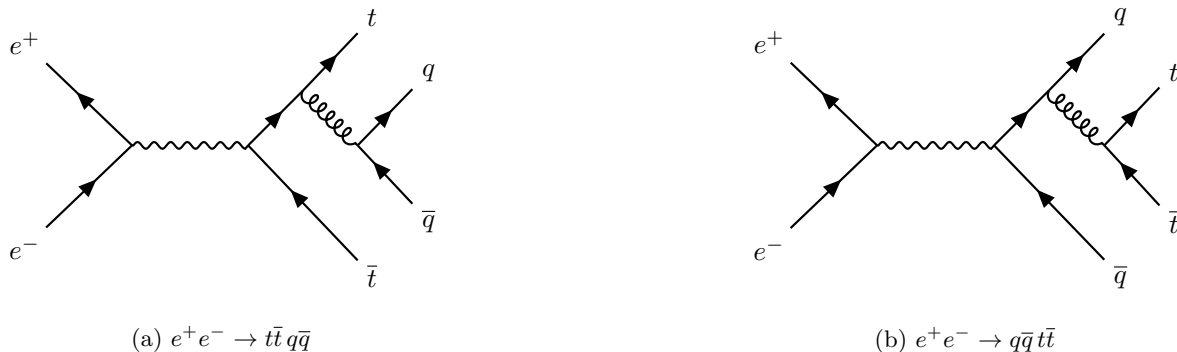


Fig. 2.5: Exemplary Feynman diagrams for the real correction to the process  $e^+e^- \rightarrow t\bar{t}j$ . Only (a) fits the underlying Born process  $e^+e^- \rightarrow t\bar{t}j$ , but corrections from (b) are also required for gauge invariance.

## 2.7 The virtual contribution and integrated subtraction terms

In this section, we want to discuss the virtual contribution to the total NLO cross section. As stated earlier, the virtual contribution is, in general, UV as well as IR divergent. While we can treat the UV divergences using renormalization, we rely on the KLN theorem for the cancellation of IR divergences between the real and the virtual contribution. Specifically, this cancellation implies that we can construct the subtraction terms for the virtual contribution by integrating the divergent parts of the real contribution over the radiation phase space and adding them with opposite signs according to eq. (2.3). For this reason, we will refer to them as the *integrated subtraction terms*.

The computation of the *bare*, i.e., the divergent, virtual contribution involves the solution of loop integrals, which is usually performed by dedicated tools known as *one-loop providers (OLPs)*. The solution is usually provided via coefficients of the Laurent expansion in the form

$$\mathcal{V} = \frac{1}{\epsilon^2} \mathcal{V}^{(2)} + \frac{1}{\epsilon} \mathcal{V}^{(1)} + \mathcal{V}^{(0)} + \mathcal{O}(\epsilon) \quad . \quad (2.165)$$

Here, the first term includes soft-collinear IR poles while the second term accounts for soft *or* collinear IR poles.  $\mathcal{V}$  is assumed to be UV finite by renormalization.

In the previous section, specifically eq. (2.135) for FSR and eq. (2.151) for ISR, we already derived the divergent parts of the real contribution. By performing the integrals  $I_{sc,\alpha_r}^{FSR}$ ,  $I_{s+,\alpha_r}^{FSR}$ ,  $I_{+c,\alpha_r}^{FSR}$  and summing over all ALRs, we can derive the counterterms canceling all  $\epsilon$  poles in eq. (2.165) from FSR and also the remaining finite contributions from the subtraction terms.

When computing the soft and soft-collinear integrals  $I_{s+,\alpha_r} + I_{sc,\alpha_r}$ , we will again encounter color-correlations and integrands of the form  $\frac{k_k \cdot k_l}{(k_k \cdot k)(k_l \cdot k)}$  similar to eq. (2.147) which are called *eikonal factors*  $\mathcal{E}_{kl,\rho}^{(m_k,m_l)}$ . Their explicit form depends on the masses of the particles  $k$  and  $l$  and we will also get separate factors for each pole in  $\epsilon$  denoted by the index  $\rho \in \{0, -1, -2\}$ . We will not go into the details of the computation of the eikonal factors here. The eikonal factors for the massless case can be found in refs. [62] and [48], while the massive cases are given in refs. [64] and [48].

The collinear limit is derived in, e.g., ref. [87] and ref. [88]. When computing  $I_{+c,\alpha_r}^{FSR}$ , the angular integral will average the involved splitting functions (c.f. sec. A.2) and the spin-correlated squared matrix elements  $\mathcal{B}_{\mu\nu}$ , so that it can be written as a prefactor  $\mathcal{Q}_i$  times the squared Born matrix element  $\mathcal{B}$ .

With these considerations, we can write the finite *subtracted virtual squared amplitude* in the form

$$\mathcal{V}(\Phi_n, f_{\mathcal{B}}) = \frac{\alpha_S}{2\pi} \sum_{k,l} \mathcal{E}_{kl,0}^{(m_k,m_l)} \mathcal{B}_{kl}(\Phi_n, f_{\mathcal{B}}) + \frac{\alpha_S}{2\pi} \sum_i \mathcal{Q}_i \mathcal{B}(\Phi_n, f_{\mathcal{B}}) + \mathcal{V}^{(0)}(\Phi_n, f_{\mathcal{B}}) \quad , \quad (2.166)$$

where we assume a factor of  $\frac{\alpha_S}{2\pi}$  to be included in  $\mathcal{V}^{(0)}(\Phi_n, f_{\mathcal{B}})$ . Eventually, the *subtracted virtual contribution* to the total cross section results from

$$d\sigma^{\mathcal{V}}(f_{\mathcal{B}}) = \int \frac{\mathbb{J}(\Phi_n)}{\mathcal{N}(f_{\mathcal{B}})} \mathcal{V}(\Phi_n, f_{\mathcal{B}}) d\Phi_n \quad . \quad (2.167)$$

### 2.7.1 The DGLAP remnant contribution and integrated subtraction terms

In the discussion of the virtual counterterms, we have explicitly excluded the ISR counterterms. The soft and soft-collinear counterterms  $I_{s+,\alpha_r}^{ISR}$  and  $I_{sc,\alpha_r}^{ISR}$  can be treated just as the FSR terms canceling almost all soft divergences.

The counterterms for the initial state collinear divergences,  $I_{+c,\alpha_r}^{ISR}$ , require a separate treatment as the initial state collinear divergences do not cancel with the virtual contribution alone but also require a proper treatment of collinear divergent terms arising from the NLO PDF evolution.

The finite remainders of this cancellation can be integrated separately, so they can be treated as their own NLO component. This component is Born-like in nature like the virtual component but kinematically has one additional degree of freedom describing the energy share of the initial-state splitting in the collinear limit. For this reason, it is coined as either the *Dokshitzer–Gribov–Lipatov–Altarelli–Parisi (DGLAP) remnant* component to stress the relevance of the PDF evolution [81, 89, 90] or *degenerate (n + 1)-body contribution* [64] from the kinematical point of view.

Starting from eq. (2.151), we can solve the angular integral in  $I_{+c,\alpha_r}^{ISR}$  and again average the splitting functions and the spin-correlated squared matrix elements  $\mathcal{B}_{\mu\nu}$ . Additional terms will emerge from the  $\epsilon$  expansion of the spin-averaged splitting functions  $\langle \hat{P}_{f_{\mathcal{R}}^i f_{\mathcal{R}}^j \leftarrow f_{\mathcal{B}}^i} \rangle(\xi, \epsilon)$  in  $d = 4 - 2\epsilon$  dimensions and taking into account the divergent PDF terms. For the details of this calculation, we refer to refs. [62] and [73]. In the end, the regularized sum of  $I_{+c,\alpha_r}^{ISR}$  and the collinear PDF counterterms can be split into a finite and a remaining

divergent part

$$\mathcal{G}_{\alpha_r}^{(\text{in},\oplus)}(\bar{\Phi}_n, \xi) = \mathcal{G}_{\alpha_r, \text{fin}}^{(\text{in},\oplus)}(\bar{\Phi}_n, \xi) + \mathcal{G}_{\alpha_r, \text{div}}^{(\text{in},\oplus)}(\bar{\Phi}_n, \xi) \quad (2.168)$$

where the finite part is given by

$$\begin{aligned} \mathcal{G}_{\alpha_r, \text{fin}}^{(\text{in},\oplus)}(\bar{\Phi}_n, \xi) = & \frac{\alpha_S}{2\pi} \left( \bar{P}_{f_{\mathcal{R}}^i f_{\mathcal{R}}^j \leftarrow f_{\mathcal{B}}^i}(\xi) \left[ \left( \frac{1}{\xi} \right)_{\xi_{\text{cut}}} \log \left[ \frac{s\delta_I}{2\mu^2} \right] + 2 \left( \frac{\log(\xi)}{\xi} \right)_{\xi_{\text{cut}}} \right] \right. \\ & \left. - \bar{P}_{f_{\mathcal{R}}^i f_{\mathcal{R}}^j \leftarrow f_{\mathcal{B}}^i}^{(1)}(\xi) \left( \frac{1}{\xi} \right)_{\xi_{\text{cut}}} \right) \mathcal{B}(\bar{\Phi}_n^{(\alpha_r)}, f_{\mathcal{B}}) \end{aligned} \quad (2.169)$$

using the definition

$$\xi(\hat{P})(\xi, \epsilon) =: \bar{P}(\xi, \epsilon) = \bar{P}^{(0)}(\xi) + \epsilon \bar{P}^{(1)}(\xi) + \mathcal{O}(\epsilon^2) \quad (2.170)$$

inspired by ref. [64] for the expansion of the splitting functions in  $\epsilon$ .

The remaining divergent part  $\mathcal{G}_{\alpha_r, \text{div}}^{(\text{in},\oplus)}(\bar{\Phi}_n, \xi)$  still has a pole in  $\epsilon$  left which will cancel the remaining soft divergence of the initial-state virtual terms but is of no further concern here.

We used the index  $\alpha_r$  in eq. (2.169) to stress the fact that the DGLAP remnant contribution can be computed per ALR. In practice, we compute this contribution per ALR, summing up the contributions of all real flavor structures  $f_{\mathcal{R}}$  for each underlying Born flavor structure  $f_{\mathcal{B}}$  such that

$$\mathcal{G}_{\text{fin}}^{(\text{in},\oplus)}(\bar{\Phi}_n, \xi, f_{\mathcal{B}}) = \sum_{\alpha_r | f_{\mathcal{B}}} \mathcal{G}_{\alpha_r, \text{fin}}^{(\text{in},\oplus)}(\bar{\Phi}_n, \xi) \quad (2.171)$$

is the integrand for the DGLAP remnant contribution. This is finally computed according to

$$\sigma^{\mathcal{G}}(f_{\mathcal{B}}) = \int \frac{\mathbb{J}(\bar{\Phi}_n, \xi)}{\mathcal{N}(f_{\mathcal{B}})} \mathcal{G}_{\text{fin}}^{(\text{in},\oplus)}(\bar{\Phi}_n, \xi, f_{\mathcal{B}}) d\xi d\bar{\Phi}_n \quad , \quad (2.172)$$

again taking jet measurement function  $\mathbb{J}$  and the symmetry factor for identical particles  $\mathcal{N}$  into account. While we sum up the contributions for all individual Born flavor structures in the computation of the total cross section, we need the results for specific Born flavor structures to generate fixed-order events.

This concludes the discussion of all NLO contributions to the total cross section.

## 2.8 Fixed next-to-leading order differential distributions

So far, we have discussed all contributions to the NLO total cross section. However, MC *event generators* have received their name not just by computing cross sections, so we want to dedicate the remainder of this section to the simulation of events with NLO accuracy.

Strictly speaking, what we call "*events*" in this context should not be considered equivalent to any event that will occur under realistic experimental conditions. It should rather be understood as a simulated collection of particles with flavor, spin and charge associated with momenta and a weight, such that these objects produce histograms similar to histograms produced by actual measured events if processed through an event analysis and adding their weights in each bin. To stress this distinction, they are sometimes referred to as "four-vectors with weights".

Different accuracies can be incorporated at the level of these events. In this section, we will focus on *fixed-order NLO events*, i.e., events that include the complete differential NLO information allowing to compute differential cross sections with NLO accuracy but no effects beyond that. This implies that they will only include up to a single emission, i.e., the real emission. They will not take into account additional soft or collinear emissions and subsequent hadronization. They are thus called *partonic* events.

Events beyond the parton level take into account further emissions simulated by SMCs. Having multiple emissions simulated by parton showers while retaining NLO accuracy for the first emission requires a proper *matching* of both approaches. We will discuss the matching of NLO events to parton showers in great detail in sec. 3 while focusing on fixed-order NLO events as implemented in the MC generator WHIZARD [73, 91] in this section.

To generate events at fixed NLO, we need to consider all components relevant for the computation of the NLO cross section also for the event generation. There are two ways to achieve this. It is possible to generate the events for each component separately, summing up the predictions for the differential observables in the end or in a single run for all components combined. Generating them all simultaneously is more user-friendly for further processing. However, the separate generation allows to generate more real events than events for other components, which is often useful as the real phase space is usually more complex to describe.

In the separate simulation of all components, simulating the events for the Born, the virtual and possibly also the DGLAP remnant component is straightforward. For each of them, we generate a Born-like kinematic configuration  $d\Phi_n$  with an associated weight based on the corresponding squared matrix element  $\mathcal{B}, \mathcal{V}$  or  $\mathcal{G}$  respectively, i.e., the integrands of eqs. (2.123), (2.167) or (2.172).

For the real events however, we need to ensure that the FKS subtraction mechanism also works on the level of generated events. To achieve this, we need to generate subtraction events with negative weights associated with an  $n$ -particle configuration and real events with an  $n + 1$  particle configuration correlatedly. For this, we introduce the notion of an *event group*. An event group consists of multiple *subevents* forming a set of correlated momentum configurations associated with individual weights<sup>9</sup>. One may consider the sum of all subevents in an event group as a single "NLO event" rather than each subevent on its own.

Each event group will consist of one collective *counterevent* accounting for the subtraction term with a Born-like momentum configuration and an associated weight  $-\mathcal{d}\sigma^S$  followed by a number of real subevents with  $n + 1$  particle momenta and a weight  $\mathcal{d}\sigma^R$  based on the non-subtracted real contribution each.

As we have discussed in sec. 2.3, often multiple ALRs share the same Born process. We compute a single subtraction term for all real flavor structures sharing the same Born flavor structure. Consequently, we need to generate multiple subevents with real kinematics, i.e., with one additional radiated particle, for each Born-like event generated. All these subevents will share the same underlying Born phase space  $d\Phi_n$  but will have different radiation kinematics  $d\Phi_{\text{rad}}$  to account for all the real terms whose subtraction terms are included in the Born-like subevent.

The real-like subevents will also have different flavor structures if the Born process allows a flavor-changing initial-state splitting or features a final-state gluon. We randomly determine each subevent's flavor structure with probability proportional to that flavor structure's portion of the total squared matrix element at each PSP.

We generate as many real subevents as there are distinct real phase spaces whose number is given by  $N_{\text{phs}}$ . As all real subevents share the same Born kinematic, two phase spaces are equivalent if they have the same emitter and share the same resonances, which we will discuss in sec. 3.6.8. In all other cases, they are distinct. This implies that  $N_{\text{phs}}$  is equal to the number of emitters for processes with a single resonance history. Hence, in order to produce a histogram with the statistics of  $N_{\text{events}}$  NLO events, we need to generate and analyze in total up to  $4N_{\text{events}}$  Born-like and  $N_{\text{phs}} \cdot N_{\text{events}}$  real-like momentum configurations associated with weights.

If all components are treated separately, special attention must be paid to normalizing the generated events properly. For the total histogram filled with these fNLO events to be correctly normalized to the total NLO

<sup>9</sup>Technically, subevents in the same event group share the same event ID e.g., in the HepMC event format.

cross section, each component individually has to be normalized to its respective cross section. While this is trivial for the Born, virtual and DGLAP remnant subevents, the real subevents must be normalized together with the counterevents.

The nature of the event groups consisting of subevents with individual but correlated, indefinite weights makes generating unweighted events impossible and forces the subevents to have non-uniform weights so that it is only possible to generate *weighted* fNLO events.

The performance and usability can be improved by using the combined NLO integration mode (c.f. sec. 4.1), which will generate events for all components combined. In the combined mode, the sum of the weights of all components with Born-like kinematics

$$d\sigma^{\mathcal{B}}(\Phi_n, f_{\mathcal{B}}) + d\sigma^{\mathcal{V}}(\Phi_n, f_{\mathcal{B}}) + d\sigma^{\mathcal{G}}(\Phi_n, f_{\mathcal{B}}) - \sum_{\alpha_r | f_{\mathcal{B}}} d\sigma^{\mathcal{S}\alpha}(\Phi_n, \Phi_{\text{rad}}^{(\alpha_r)}, f_{\mathcal{B}})$$

is assigned to a single Born-like subevent. Again, the sum over  $\alpha_r$  runs over all alpha regions sharing the same Born process. It is not necessary to have a distinct kinematic configuration for each of these components<sup>10</sup>.

One may wonder why the counterevents share the kinematics with the Born subevents, although they depend on the radiation phase-space variables, and when computing the total cross section, the subtraction term is part of the subtracted real component. Intuitively, this is the case as the counterterms are computed in the soft and/or the collinear limit. An infinitely soft or an infinitely collinear particle will, by definition of IR- and collinear-safe observables never influence any such observable and thus does not need to be explicitly included in the event.

We can also understand this at the level of histograms. Let us consider events with at least  $N$  clustered jets for a general process  $e^+e^- \rightarrow X + N\text{jet}$  at fNLO parton level. Fig. 2.6 shows a figurative histogram of the number of jets in these events separated by components. With appropriate jet clustering and energy requirement for the jets, this is a well-defined observable. It is clear that, at fNLO, all events with  $N + 1$  clustered jets have to be real-like subevents featuring real radiation. For the real events, it is also possible that two final-state partons are clustered into a single jet, so the real events also contribute to the  $N$ -jet bin. If we require at least  $N$  clustered jets, it is also clear that the Born and the virtual component contribute with their total cross sections to the  $N$ -jet bin. The same holds for the counterevents with negative weights. As discussed around eq. (2.129), it is possible to use parameters like  $\delta_O$  and  $\xi_{\text{cut}}$  to shift contributions of the collinear or soft phase-space regions between the real-subtracted component and the integrated subtraction terms. Now, if the counterevents and the virtual subevents had different kinematics, it would be possible that both contribute to different bins. In this case, individual bins would depend on the choices of  $\delta_O$  and  $\xi_{\text{cut}}$ . As all observables are supposed to be independent of these parameters, this would be inconsistent, and thus, the counterevents always have to have the same kinematics as the virtual subevents.

<sup>10</sup>All Born-like components share the same final-state momenta. However, the initial-state momenta for the DGLAP remnant component and the initial-state flavor for the subtraction component may differ from the Born component. In the combined event generation mode, these two minor points are neglected. The properties of the initial state should not have any effect on the resulting histograms.

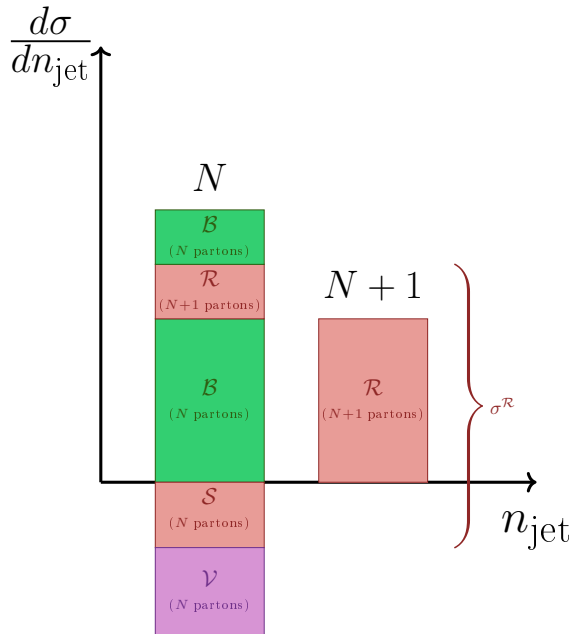


Fig. 2.6: Contributions from all components to a figurative histogram showing the number of clustered jets for a process like  $e^+e^- \rightarrow N\text{jet}$ . The real cross section contributes in three different ways: First of all, it contributes via the weights of all events with  $N + 1$  clustered jets and it contributes to the  $N$ -jet bin if two partons out of the  $N + 1$  partons are clustered into the same jet. Additionally, the counterevent weights (labeled  $\mathcal{S}$ ) are part of the total real cross section  $\sigma^{\mathcal{R}}$ . They also contribute to the  $N$ -jet bin just as the Born ( $\mathcal{B}$ ) and the ( $\mathcal{V}$ ) contribution.

### 2.8.1 Fixed next-to-leading order histogramming

After generating an event sample, it can be analyzed using tools like `ROOT` [92] or `Rivet` [93, 94], computing algorithmically defined kinematical observables for each event, while summing up the weights of all events in small predefined ranges for each observable, i.e., in bins, producing differential distributions visualized as histograms. Analyzing the generated fNLO event groups is not a trivial task, as care must be taken to preserve the cancellation between the different NLO terms without spoiling the statistical treatment of uncertainties when filling the subevents into binned histograms.

When filling histograms, the cancellation between the Born-like counterevents and the real-like subevents needs to be ensured *per bin*, as otherwise, the large and positive weights of especially the real subevents featuring soft or collinear radiation would pile up to unphysically large values in some bins, while the large and negative weights of the counterevents would sum up to large and even negative values in other bins. To some extent, this can be achieved by constructing IR-safe observables as discussed in sec. 2.5 so that by definition, the soft and collinear real-like subevents end up in the same bins as the counterevents of said event group. However, at the level of binned histograms, there are still some caveats, of which we will discuss a few here on the simple example of two-jet production at a lepton collider, i.e., the partonic process  $e^+e^- \rightarrow jj$ . But the same holds for  $pp \rightarrow jj$  and many other processes.

Fig. 2.7a shows the differential distribution of the energy of the hardest jet, i.e., the jet with the highest transverse momentum. Although all jets have been reconstructed using an IR-safe jet-clustering algorithm, we clearly see that something is wrong: the LO events gather in the bin including  $E_{j_1} = \sqrt{s}/2 = 250 \text{ GeV}$  as each of the two jets in these events has an equal energy share. In contrast, the fNLO distribution shows a

large positive peak slightly below 250 GeV followed by a large negative dip right after.

The reason is simple: each of the two jets in the Born-like subevents has, like in the LO events, an energy of  $\sqrt{s}/2 = 250$  GeV so that all Born-like subevents including all counterevents end up in this one bin. Although per construction of the jets, some real-like subevents featuring a very soft or collinear emission will also end up in this bin, the sum of all negative counterevent weights outweighs the sum of all other event weights. The real-like subevents solely populate all other bins, and especially in the bin right below 250 GeV, they feature increasingly large weights towards the upper bin edge. This explains the overshooting of the Born distribution in the central region as well as the huge statistical uncertainties of the most pronounced bin. The same problem described here for the jet energy also affects other observables, such as obviously the jet momentum, but also, e.g., the thrust of the event. Apart from the careful definition of all observables and manually choosing bin edges such that the positive and negative weights in each bin always sum up to a positive value, a more general approach to solving this issue, characterized as *misbinning effects*, is to apply some *weight smearing* across several neighboring bins when filling the histograms, as implemented in Rivet 3 [94]. If summed over all bins, these effects vanish so that the total cross section does not suffer from these artifacts.

As a second example of a common mistake when dealing with fNLO events, fig. 2.7b shows the rapidity distribution of the hardest jet in the same setting as before. We can clearly see the huge uncertainties of the fNLO distribution, and by taking a closer look, we also see that the LO distribution is unexpectedly asymmetric. The same distribution for the second hardest jet is exactly mirrored in comparison to fig. 2.7b. For this reason, it is omitted here. The problem is that the "hardest" jet is defined by its transverse momentum, which is ambiguous for all Born-like events. For the LO events, this ambiguity is solved by preferring the jet in the positive direction of the beam axis, explaining the asymmetry of the LO distribution. Consequently, if the jet which is determined to be the hardest in the Born-like counterevents happens to be the emitter in the real-like subevents, the emission will decrease its energy so that the "hardest jet" in the real-like subevents of the same event group will not be the same jet as before. For the fNLO distribution, this forces the real-like subevents with positive weights predominantly on the LHS of the distribution explaining the huge bin values and uncertainties while the counterevents lead to a negative distribution on the RHS. Of course, this misfeature could be remedied in this case by just considering the absolute value  $|y_{j_1}|$  shown in fig. 2.7d as both jets of the Born-like events are exactly  $180^\circ$  apart from each other.

Finally, fig. 2.7c shows the transverse momentum of the third hardest jet, i.e., the real emission. This histogram is entirely populated by the real-like subevents and does not include any counterevents. In a sense, histogramming an observable explicitly depending on the real radiation is like imposing a cut on the real radiation, which is illegal in the subtraction formalism. For this reason, the leftmost bin is not well-defined. It includes arbitrarily soft emissions without any counterterms<sup>11</sup>. To avoid numerical instabilities of matrix elements in exactly these regions of very soft real emissions, we impose a technical cut of  $\xi > \xi_{\min} := 10^{-7}$  (c.f. eq. (2.39)) on all generated events, and also when computing the cross section. This technical cut does not affect any reasonably defined NLO observable. Without this cut, the leftmost bin would exhibit an unregulated IR divergence. If not properly excluded from the analysis, these soft emission events also disturb angular distributions not sensitive to the jet energy. Beyond fixed-order, this would also not pose a problem as soft real radiation gets lost in all the additional emissions from the parton shower. Furthermore, the entire distribution arises only from the real correction, i.e., it constitutes the LO-accurate description of the  $(n + 1)$ -jet process  $e^+e^- \rightarrow jjj$ .

<sup>11</sup>So technically, this object may not be called a "jet" as it does not fulfill the energy and angle requirements imposed on the main jets by the jet definition criteria.

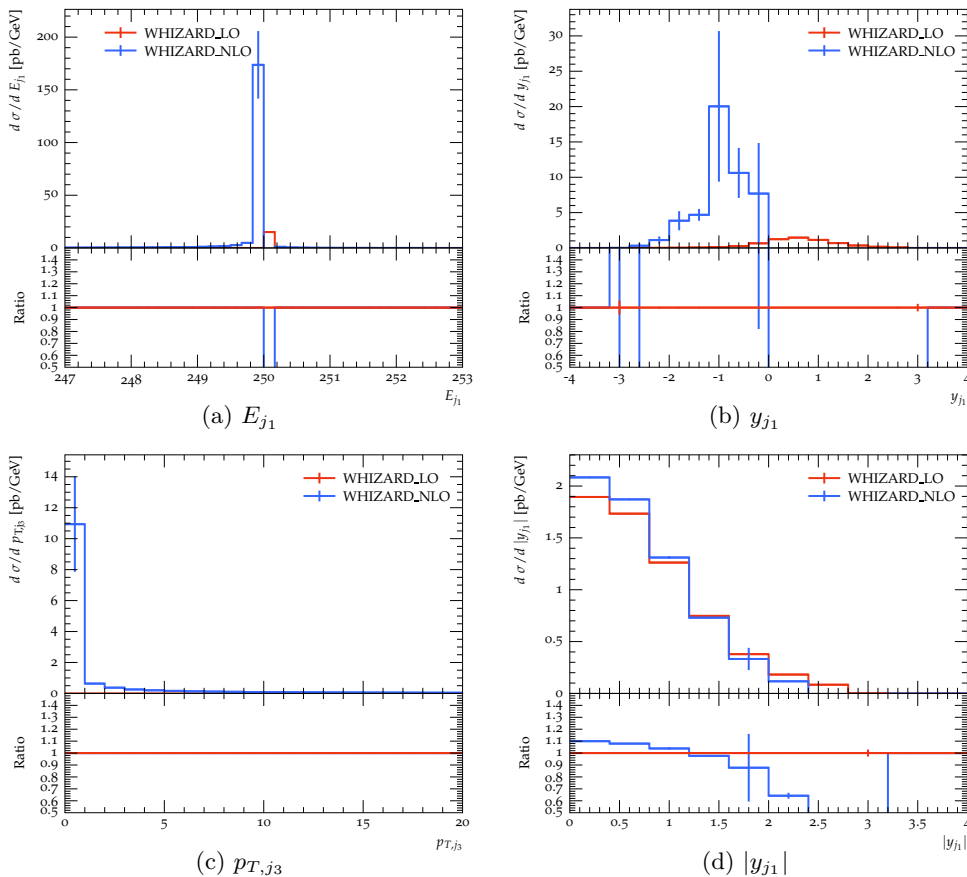


Fig. 2.7: Showcase of issues with fNLO histogramming on the example of the energy of the hardest jet, its rapidity and the transverse momentum of the radiated jet for LO (red) and fNLO (blue) events. The process is  $e^+e^- \rightarrow jj$  at  $\sqrt{s} = 500$  GeV with a scale of  $\mu = H_T/2 = \frac{1}{2} \sum_i \sqrt{p_{T,i}^2 + m_i^2}$  where the sum over  $i$  runs over all final-state partons. Additionally, we require at least 2 jets clustered using the anti- $k_T$  algorithm with  $R = 0.5$  fulfilling  $p_T > 30$  GeV and  $|\eta| < 4$ . The error bands represent the statistical uncertainties of 1M event groups.

The second issue when dealing with NLO events is to determine the correct uncertainty for each bin. Even if we have defined observables so that the cancellation of real-like and counter-events is not spoiled, we are still filling potentially very large negative counterweights from Born-like subevents and very large positive weights from soft or collinear real-like subevents into the same bin. When doing so naively, this huge variation in the weights leads to artificially large uncertainties not resembling the actual uncertainty of the predictions. In order to get realistic uncertainties, the entire event group has to be statistically treated like a single event, meaning that all event weights of an event group are added up beforehand for each bin and only their sum is filled into each histogram as a single entry. As not all subevents have to end up in the same bin, this requires the notion of a fractional fill. This is implemented in an NLO add-on to Rivet 2 [93] called NLOHisto1D available as part of the Rivet contrib repository [95] and natively included in Rivet 3 [94]. The problems discussed in this section only apply to fixed-order NLO events. In the next section, we will discuss the matching of NLO calculations to parton showers at the level of events. This approach will retain full NLO accuracy in the high-energetic regions while remedying the issues of misbinning and determining the correct uncertainties without the need for event groups and subevents. The POWHEG method discussed in sec. 3 will even reduce the number of negative weights.

### 3 The POWHEG matching scheme

So far, we have limited our discussions to calculations at fixed perturbative orders, including computing cross sections as well as simulating events. In order to provide realistic predictions for any experiment, however, we need to do better than that.

The problem with fixed-order results is that they always only describe a limited number of well-separated final-state particles, while in realistic experiments, the number of observed particles grows indefinitely with the experiment's resolution. This goes hand in hand with the second downside of fixed-order approaches, i.e., they are always IR divergent in soft and/or collinear phase-space regions, so they cannot describe the entire phase space without the use of sufficiently inclusive observables or a well-defined resummation scheme. While there are process-specific methods to perform this resummation analytically [96], it is far more practical to employ SMC generators for this purpose. The three most commonly used SMCs are PYTHIA [52], HERWIG [53] and Sherpa [50].

Building on a fixed-order computation, these SMCs perform the leading logarithmic (LL) resummation by applying a *parton shower* algorithm to the events and thereby produce exclusive multi-parton events, not subject to a limit in the number of describable particles. This is done by performing a cascade of predominantly soft or collinear splittings with the present set of partons to lower and lower energies.

QCD confinement dictates that colored states can never be observed directly and will always form colorless bound states, hadrons. So at some point, when the parton shower reaches a low scale, a transition from isolated colored partons to colorless hadrons will occur. This process is called *hadronization*. In a SMC, hadronization is described by a phenomenological model, which cannot be derived from first principles but is instead based on modeling driven by experimental data for hadronic production yields. In this section, we will assume that the hadronization is dealt with externally by one of the above-mentioned SMCs. This is technically possible by handing over an intermediate stage of the events from one program to the next by writing the files to disk or using internal interfaces. We will not go into more detail at this point.

As both steps, the parton shower and the hadronization involve numeric modeling with a non-small number of adjustable parameters, they need to be tuned using experimental data to have a consistent description. These selected sets of parameters are thus called *tunes*.

This section will discuss the basic ideas of parton showers and illuminate how to improve not only LO but also NLO predictions with parton showers without double counting radiations or spoiling the NLO accuracy. As WHIZARD currently strongly relies on the POWHEG-matching method, this section will put a strong focus on POWHEG matching.

#### 3.1 Parton showers and the Sudakov form factor

When matching parton showers with matrix-element calculations, a thorough understanding of how parton showers work and how to manipulate them is crucial, especially beyond leading order. For this reason, we will discuss the basics of how a parton shower is generated in this subsection.

The original idea goes back to G. Fox and S. Wolfram [97] and is inspired by observations of QCD radiation patterns in  $e^+e^-$  collisions for either very soft or very collinear radiation. It relies on the idea that interferences of amplitudes of successive emissions can be neglected, meaning that subsequent splittings can be described independently.

Based on this idea, we model the parton shower by performing a series of subsequent splittings to final-state partons up to some minimum scale  $t_{\min}$  dictated by the detector resolution.

In the standard case, these splittings are governed by splitting probabilities. As explained in, e.g., ref. [98] the inclusive splitting probability of a parton  $i$  to split into the two partons  $j$  and  $k$  can be expressed in

terms of the Altarelli-Parisi splitting functions [81] (c.f. app. A) as

$$d\mathcal{P}_{i \rightarrow jk}(t, z) = \frac{\alpha_S}{2\pi} \hat{P}_{i \rightarrow jk}(z) dt dz \quad , \quad (3.1)$$

where we have integrated over the azimuthal angle,  $z$  represents the energy sharing between the partons  $j$  and  $k$  and  $t = \log\left(\frac{p_T^2}{\Lambda_{\text{QCD}}^2}\right)$  is the ordering parameter of the shower chosen to be the transverse momentum. Another common choice for the scale  $t$  would be some function of the emission angle which results in an angular-ordered shower, known to improve the color coherence [99, 100] of the generated events. However, POWHEG matching to angular-ordered showers requires an additional veto step to respect the hardness criterion defined in the matching procedure. Thus, we will focus on transverse-momentum ordered showers in this work, i.e., showers in which each emission features a lower transverse momentum than the previous one with a transverse-momentum dependent emission scale  $t$ .

The exclusive probability for the first emission is then given by the probability of an emission at scale  $t$  times the probability that there is no emission at any higher scale

$$d\mathcal{P}_{i \rightarrow jk}^{\text{first}}(t, z) = \frac{\alpha_S}{2\pi} \hat{P}_{i \rightarrow jk}(z) \times \Delta(t_{\text{max}}, t) dt dz \quad , \quad (3.2)$$

where  $\Delta(t_{\text{max}}, t)$  is the no-emission probability between some maximum starting scale  $t_{\text{max}}$  and the splitting scale  $t$ . It is also called the *Sudakov form factor* which according to eq. (3.2) is given by

$$\Delta(t_1, t_2) = \exp\left(-\int_{t_2}^{t_1} \int \frac{\alpha_S}{2\pi} \hat{P}_{i \rightarrow jk}(z) dt dz\right) \quad . \quad (3.3)$$

We use a shorthand notation in case the upper scale is the starting scale  $t_{\text{max}}$ :

$$\Delta(t) := \Delta(t_{\text{max}}, t) \quad . \quad (3.4)$$

Although an analytic computation of the Sudakov form factor would be possible, it is more often computed numerically using a series of overestimations and subsequent veto steps called the *Sudakov veto algorithm* [98, 101] to avoid having to compute the integral in eq. (3.3) analytically. We will come back to this strategy in sec. 3.5.1f.

After generating the first emission in this way, we continue the evolution by setting  $t_{\text{max}} = t$  and repeat the process. This guarantees that each subsequent emission is generated at a lower scale  $t$  creating a transverse-momentum ordered shower.

The total cross section will finally contain terms with multiple numbers of splittings [71]:

$$d\sigma^{\text{shower}} = d\sigma^{\text{LO}} \left\{ \Delta(t_{\text{min}}) + dt \hat{P}(t) \Delta(t) \left[ \Delta(t, t_{\text{min}}) + dt' \hat{P}(t') \Delta(t, t') (\Delta(t', t_{\text{min}}) + \dots) \right] \right\} \quad . \quad (3.5)$$

In eq. (3.5), the first term represents the case of no emission, i.e., the Born term, and the second term represents the case of a single emission approximating the real emission. The third term represents the case of exactly two emissions and so on. By applying the Markovian property of the Sudakov

$$\Delta(t_{\text{min}}) = \Delta(t_{\text{max}}, t_{\text{min}}) = \Delta(t_{\text{max}}, t) \Delta(t, t') \Delta(t', t_{\text{min}}) \quad , \quad (3.6)$$

we find, e.g., for the exclusive probability of two splittings

$$d\sigma^{\text{shower}} = d\sigma^{\text{LO}} \Delta(t_{\min}) \hat{P}(t) \hat{P}(t') dt dt' \quad . \quad (3.7)$$

By integrating out all scales in eq. (3.5), we see that the whole shower cascade integrates to one, eventually leaving the total cross section unaltered. Thus, the parton shower is a unitary procedure<sup>12</sup>.

## 3.2 Improving the parton shower – merging and matching

Due to the parton shower’s nature of describing all radiations with splitting functions, it is a very good description of the phase-space regions governed by soft and collinear splittings. In regions governed by hard emissions, however, it fails to accurately describe the radiation pattern without extensive tuning of the shower parameters.

To enhance the parton shower, it is possible to use process-dependent matrix elements instead of universal splitting functions without spoiling the shower unitarity, given by eq. (3.5). The matrix elements better describe hard regions in the phase space but often fail to be accurate in the soft regions. It is thus important to put both approaches together in a well-defined way.

Originally, parton showers were enhanced using LO matrix elements only. In this approach, events are simulated based on matrix elements describing different processes featuring a range of jet multiplicities. Today, it is possible to *merge* computations based on NLO matrix elements of processes with different jet multiplicities, too. Whenever event samples inherently describing different Born processes are combined, this procedure is referred to as *merging*.

In contrast, if only matrix elements describing the same process at different orders, i.e., the Born and the real matrix element in an NLO computation, are taken into account, this method is called *matching*.

Summarizing, while both *merging* and *matching* enhance the parton-shower description with matrix elements of different jet multiplicities, when *merging*, these matrix elements describe different processes, whereas *matching* deals with higher-order corrections to the same process.

### 3.2.1 Merging

The original approach of merging parton showers with matrix elements was first employed in 1987 [102] to describe PETRA and PEP data using *JetSet* [103], a predecessor of *PYTHIA*. Back then, it was only possible to correct the first emission using a single LO matrix element. It was later generalized by Giele, Kosower and Skands and coined as the *unitary matching method* [104]<sup>13</sup>.

Prior to their work, the generalization of parton-shower merging to multiple emissions was achieved by two different methods. On the one hand, there is MLM matching [105, 106] named after M. L. Mangano, and on the other hand, there is CKKW matching [107] coined by Catani, Krauss, Kuhn and Webber.

The main problem that merging algorithms have to solve is the problem of *double counting* jet multiplicities. It arises as both the parton shower and the matrix elements generate additional radiations. This is depicted in fig. 3.1. We can see that the parton shower as well as the matrix elements include a process with two initial-state emissions.

A general solution to this problem is to define disjunct regions according to some jet parameter in which one approach is preferred over the other. Methods based on this idea are called *slicing* merging schemes, as

<sup>12</sup> The parton shower does, however, affect the event kinematics, e.g., the jets’ hardness, so in the presence of cuts, applying a parton shower may indeed affect the fiducial cross section.

<sup>13</sup>For historical reasons, some of the *merging* methods still carry the term "matching" in their names. They are *merging* methods nonetheless.

the idea is to slice the phase space.

The simplest possible choice here is to define a transverse-momentum cut-off for the jet,  $p_{T,\min}$ , below which lies the parton shower domain and above which we prefer the description by the matrix element, thus ensuring that the matrix element is used to describe the hard radiation.

Also, the MLM and the CKKW matching procedures belong to this category of slicing merging schemes. Besides slicing merging schemes, there are also approaches to merging based on subtracting the double-counted parts, referred to as *subtraction* merging schemes.

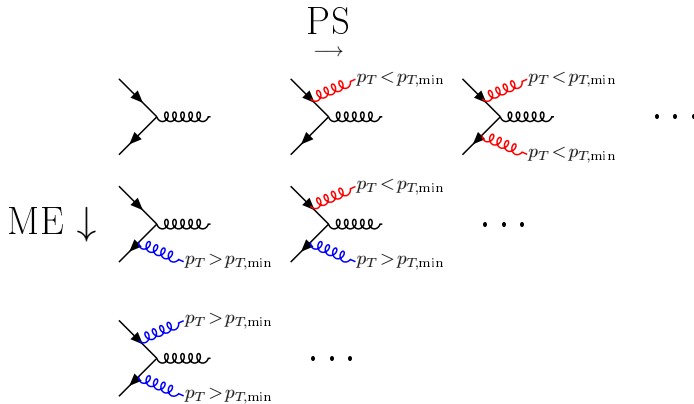


Fig. 3.1: Illustration of double counting when *merging* parton showers with LO matrix-element calculations. Radiations generated by the parton shower are shown in red while radiations described by matrix elements are depicted in blue.

Many elaborate merging schemes introduce an interdependence between the Monte-Carlo program generating the partonic events and the parton-shower program, sometimes up to a point necessitating both tasks to be performed by the same monolithic program. In a modular framework like WHIZARD, this is undesirable. We thus prefer merging schemes that can be implemented independently on the internal details of the subsequent shower. The MLM scheme is one such merging scheme. It has been implemented in WHIZARD in the course of a Ph.D. thesis [71].

### 3.2.2 Matching

The intention of matching is to enhance the predictive quality of the parton shower with hard matrix elements computed at a higher fixed order in such a way that NLO accuracy is achieved for inclusive observables while at the same time maintaining the leading logarithmic accuracy of the parton-shower approach.

Just as different LO matrix elements may describe processes with different numbers of radiated particles, higher-order real matrix elements also feature additional radiated real emissions. For this reason, the basic problem that matching has to solve is the same as before: the goal is to avoid double counting contributions describing the same number of radiated particles. Similar to fig. 3.1, the case of matching is depicted in fig. 3.2.

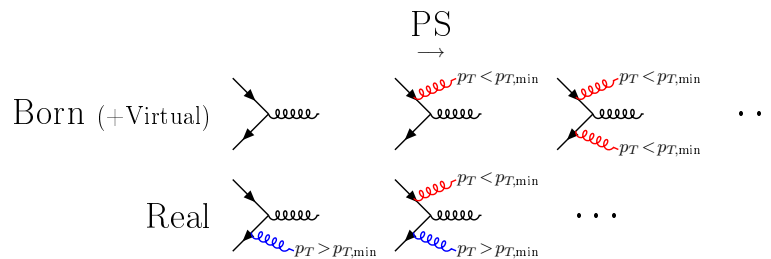


Fig. 3.2: Illustration of double counting when *matching* parton showers with higher-order matrix-element calculations. The Born contribution is depicted in black. Virtual diagrams contribute in the first row, although they are not shown explicitly. Radiations generated by the parton shower are shown in red, while the real radiation is depicted in blue.

More precisely, we follow ref. [108] and understand as *double counting* during matching if the resulting prediction for any observable at the first order beyond the Born approximation in the expansion of the coupling constant does not coincide with the NLO prediction. In the soft and collinear regions of phase space, it is sufficient to prefer the parton-shower description using the Born cross section times a splitting kernel to describe the radiations as, in this case, both predictions agree up to the first emission in the leading terms. In the hard regions of the phase space, the NLO prediction for the first emission is more accurate, so it is possible to avoid double counting by preferring the NLO description of the radiation.

Especially the soft regions of phase space are crucial for the proper cancellation of divergences between the different NLO contributions. The main challenge for any matching algorithm is to solve the problem of double counting without spoiling the NLO subtraction.

The matching of NLO computations with parton showers has been pioneered by Frixione and Webber with MC@NLO matching [108]. It relies on a modified subtraction method adapted to the parton shower. Due to the nature of being based on a subtraction method, the MC@NLO matching scheme produces negatively weighted events across the entire phase space. This can become a significant performance problem for the subsequent processing of the events we will come back to in sec. 3.6.9 at the end of this section. Although the MC@NLO method is still in active use today, mostly via its implementation in MG5\_aMC [45], the explicit dependence on the parton shower and the amount of generated negative weights render this method unfavorable for the projects pursued in this project.

The most famous matching scheme solving this problem of negatively weighted events in such a way that they are suppressed in all perturbatively stable regions of the phase space is POWHEG matching. The basic idea has been proposed [46], implemented [56] and explained in great detail [47] by P. Nason. It is dubbed POWHEG for **P**ositive **W**eighted **H**ardest **E**mission **G**enerator underlining this fact.

The lower rate of negative weights is achieved by relying on slicing instead of a subtraction method for the matching. The original approach uses the emission’s transverse momentum  $p_T$  as a slicing parameter to divide the phase space in a domain governed by the SMC and a domain where the NLO description is governing the first emission. As long as the applied shower algorithm respects the hardest emission generated by the matching algorithm, the matching itself is independent of the subsequent shower. Furthermore, we will see that POWHEG matching fits neatly to the structure of the FKS subtraction mechanism making it the ideal matching algorithm to be implemented in WHIZARD. For these reasons, it is the POWHEG matching that we chose to focus on in this thesis.

Besides MC@NLO and POWHEG matching, there is also the possibility to enhance a SMC with NLO matrix elements based on a dedicated MC factorization scheme and a redefinition of the PDFs. This approach has

been suggested by a Polish group and is dubbed `KrkNLO` [109].

It is also possible to combine matching and merging, i.e., to merge matched NLO samples. In this way, NLO calculations for different Born processes can be combined, further improving the accuracy although formally staying accurate to the NLO. Some of the well-established NLO merging methods are `FxFx` merging [110], `UNLOPS` and `NL3` merging [111] as well as `MINLO` merging [112].

### 3.3 POWHEG matching – the concept

The general idea behind the POWHEG matching is to generate the hardest emission for each event with full NLO accuracy and making sure that each subsequently generated emission is softer than the previous one, guaranteeing that the showering does not spoil the NLO accuracy of infrared finite observables, affecting them at most at the NNLO. This criterion allows to strictly separate the generation of the hardest emission from the shower, making it possible to split the matching into two disjunct stages.

The first stage will generate the hard kinematics describing the hard process and up to one single emission. We will call the generated collection of particle momenta associated with a weight a *POWHEG event*. These POWHEG events can be written to disk in standard event formats like `HepMC` [113, 114] and `LHEF` [55] and can even be analyzed and histogrammed. We want to stress, however, that this is just useful for technical comparisons as their kinematic distributions will not be an accurate description of measured data as long as they lack showering.

Only in the second stage the generated POWHEG events will undergo the parton showering, enhancing the logarithmic accuracy in the soft and collinear regions of phase space and generating the desired distribution of events with NLO accuracy in the hard and logarithmic accuracy in the soft and collinear regions of phase space. This separation of both stages allows us to focus on the first stage throughout this section, leaving the details of the parton shower to the SMC.

In order to preserve the total cross section during this procedure, we should respect the full NLO integrand, gathered from eq. (2.123), (2.167) and (2.172) for the Born, the virtual and the DGLAP remnant contribution, respectively, absorbing the jet measurement functions and explicit symmetry factors present in these equations as well as eq. (2.124) for the real contribution including the subtraction terms derived in that section. It is given by

$$\bar{\mathcal{B}}(\Phi_n) = \mathcal{B}(\Phi_n) + \mathcal{V}(\Phi_n) + \int [\mathcal{R}(\Phi_n, \Phi_{\text{rad}}) - \mathcal{S}(\Phi_n, \Phi_{\text{rad}})] d\Phi_{\text{rad}} + \int [\mathcal{G}_{\text{fin}}^{(\text{in}, \oplus)}(\Phi_n, z) + \mathcal{G}_{\text{fin}}^{(\text{in}, \ominus)}(\Phi_n, z)] \frac{dz}{z} \quad (3.8)$$

denoted as  $\bar{\mathcal{B}}$  similar to eq. (3.2) of ref. [47]. It is this function that we integrate to compute the NLO cross section using MC sampling.

In the first step, we generate  $n$ -particle events with weights according to eq. (3.8). In the next step, we add the real emission to this Born-like seed kinematic. The crucial point is that we resum this emission to LL order in  $p_T$  using a *modified* Sudakov form factor

$$\Delta(\Phi_n, p_T) = \exp \left[ - \int \frac{\mathcal{R}(\Phi_{n+1})}{\mathcal{B}(\Phi_n)} \theta(k_T(\Phi_{n+1}) - p_T) d\Phi_{\text{rad}} \right] , \quad (3.9)$$

where  $k_T(\Phi_{n+1})$  is of the order of the transverse momentum of the radiated parton relative to the emitter before the emission in the CM system of the colliding partons. We see that the fraction  $\mathcal{R}/\mathcal{B}$  takes the place of the splitting function in this Sudakov form factor. In this way, the splitting function is process-specific as opposed to the traditional universal splitting functions (c.f. app. A) and not only accurate in the soft and

collinear regions. Additionally, this matrix-element-based splitting function will include interference effects, e.g., due to color dipoles that are usually beyond the description with  $1 \rightarrow 2$  splitting functions.

Based on this Sudakov form factor, we apply the shower algorithm discussed in sec. 3.1 to generate the first emission only. We already showed in eq. (3.5) that this conserves the total cross section, i.e.

$$d\sigma_{\text{NLO}} = \bar{\mathcal{B}}(\Phi_n) \left( \Delta(p_{T,\text{min}}) + \Delta(k_T(\Phi_{n+1})) \frac{\mathcal{R}(\Phi_{n+1})}{\mathcal{B}(\Phi_n)} d\Phi_{\text{rad}} \right) d\Phi_n. \quad (3.10)$$

Here, the term  $\Delta(p_{T,\text{min}})$  hints at the fact that there is a possibility that no radiation occurs down to  $p_{T,\text{min}}$ , which is typically chosen at  $\mathcal{O}(1 \text{ GeV})$  to avoid reaching unphysical regions of the PDFs or non-perturbative regions of  $\alpha_S$ . In this case, no first emission is generated by the matrix elements, and a Born-like event will be given to the SMC. All subsequent emissions will then be generated at a lower scale by the traditional parton shower.

Cross sections and differential distributions computed based on this construction will have the following properties:

1. At large  $p_T$  predictions coincide with the NLO predictions up to NNLO terms.
2. Infrared safe observables will be accurate to NLO, and this behavior is not spoiled by subsequent showering.
3. The behavior at small  $p_T$  will be no worse than that of the standard SMC.

The second property is probably the least obvious. A detailed proof can be found in sec. 4.3 in the detailed description of the POWHEG method given in ref. [47]. Based on these properties, the POWHEG matching fulfills all the requirements to solve the problem of double counting described in the previous subsection 3.2.

For the shower to conserve properties 1 and 2, it is important that the parton shower does not generate any radiation harder than the first emission. If the applied parton shower is ordered in  $p_T$ , it is sufficient to require that the shower starts at an upper scale equal to the  $p_T$  of the POWHEG event. This should be possible for all SMCs that are compatible with the LHIUP [54, 55].

If the SMC uses a different, e.g., angular ordering, we need to suppress emissions with larger  $p_T$  from the shower. This is possible using *vetoed truncated showers* [46] compensating the fact that the hardest emission of an angular-ordered shower may not always be the first. For simplicity, we will assume  $p_T$ -ordered radiation generation in the following.

The POWHEG-matching scheme has first been implemented in the semi-automated MC event generator named thereafter as the POWHEG-BOX [48]. The POWHEG-BOX framework made matched NLO predictions for numerous processes publicly available [115], in many cases pioneering the utilization of NLO predictions in experimental studies. Its approach, however, is process-specific. The main part containing the implementation of FKS subtraction and the POWHEG matching is automated. However, the matrix elements and the phase-space construction are performed on a process-by-process basis requiring substantial theoretical effort for each new process.

The MC generators **Sherpa** [116] and **HERWIG** [117] also feature their own implementation of POWHEG matching in an automated way, both showing that POWHEG matching is also compatible with CS dipole subtraction.

A preliminary proof-of-concept implementation of POWHEG matching has also become available in the MC event generator **WHIZARD 2.2.7** and was applied to  $t\bar{t}$  production at a future lepton collider [118]. It was substantially generalized to arbitrary processes at hadron- and lepton colliders throughout this thesis and is available for public use from **WHIZARD 3.1.0** on.

### 3.4 Prerequisites

The prerequisites to generate POWHEG events are similar to the requirements we discussed in sec. 2.5 for FKS. We require a Born phase space well-defined by radiation-proof cuts and a separation of the real phase space in singular regions as explained in sec. 2.3.

For a consistent matching, the generated additional radiation must be softer than the transverse momenta of the underlying Born kinematics [47]. This is achieved by separating  $\mathcal{R}$  into singular regions only with an appropriate choice of  $S$ -functions such as the one we chose in sec. 2.3.3.

In general, the requirement on radiation-proof cuts for the Born configuration can be lifted by introducing a separation of the real contribution similar to the real partition (c.f. sec. 2.6.3). Alternatively, a weight can be added to the Born term suppressing the singular Born configurations as described in ref. [47]. Given that we require radiation-proof cuts already for the FKS subtraction, we will not follow these approaches.

#### 3.4.1 Generation of the underlying Born configuration and event weights

The generation of radiation and the matching both act on Born-like events<sup>14</sup>. For each PSP we require a given Born configuration, i.e., a PSP in  $\Phi_n$ , associated with a weight  $w$  and a flavor structure  $f_{\mathcal{B}}$ . This flavor structure should be chosen in such a way that the sum of weights for each flavor structure is proportional to  $\overline{\mathcal{B}}^{f_{\mathcal{B}}}(\Phi_n) d\Phi_n$ , where similar to eq. (3.8) but this time itemized per Born flavor structure,  $\overline{\mathcal{B}}^{f_{\mathcal{B}}}(\Phi_n)$  is given by

$$\begin{aligned} \overline{\mathcal{B}}^{f_{\mathcal{B}}}(\Phi_n) = & \mathcal{B}^{f_{\mathcal{B}}}(\Phi_n) + \mathcal{V}^{f_{\mathcal{B}}}(\Phi_n) + \sum_{\alpha_r \in \{\alpha_r | f_{\mathcal{B}}\}} \int \mathcal{R}_{\alpha_r}(\Phi_n, \Phi_{\text{rad}}) - \mathcal{S}_{\alpha_r}(\Phi_n, \Phi_{\text{rad}}) d\Phi_{\text{rad}} \\ & + \sum_{\alpha_{\oplus} \in \{\alpha_{\oplus} | f_{\mathcal{B}}\}} \int \mathcal{G}_{\alpha_{\oplus}, \text{fin}}^{(\text{in}, \oplus)}(\Phi_n, z) \frac{dz}{z} + \sum_{\alpha_{\ominus} \in \{\alpha_{\ominus} | f_{\mathcal{B}}\}} \int \mathcal{G}_{\alpha_{\ominus}, \text{fin}}^{(\text{in}, \ominus)}(\Phi_n, z) \frac{dz}{z}. \end{aligned} \quad (3.11)$$

where the sums run over all ALRs sharing the same Born flavor structure  $f_{\mathcal{B}}$  and featuring ISR in the case of  $\alpha_{\oplus}$ .

There are two ways to achieve this. Just as for ordinary LO events, it is possible to implement the probability of each flavor structure via the weight's value in weighted events or via the probability density of each flavor structure in unweighted events. In the first case, we directly use eq. (3.11) evaluated at a specific PSP  $\Phi_n$  multiplied by the appropriate phase space factors as weight  $w$  for each event generating *weighted events*. The POWHEG procedure to generate radiation described in the following will only alter the event kinematics keeping the event weights unchanged. This means that in this case, we will also generate weighted POWHEG events, which will still be weighted after showering. These are perfectly fine for technical comparisons and quick plotting as they will reproduce the correct differential distributions when histogrammed and can be generated much faster. However, one needs to make sure that the weights are not lost during subsequent event processing. Some programs, e.g., PYTHIA, assume a weight of unity by default.

One more technical downside is that weighted events generated using an adaptive phase-space mapping (c.f. sec. 4) tend to bear rare kinematic configurations more often, albeit with a small weight. These overly abundant rare configurations increase the probability of errors and warnings when showered.

The same is true for events with a weight identical to zero. These are events that failed the phase-space cuts but are kept nevertheless to allow a consistent counting of events. Keeping the events which failed the phase-space cuts has the advantage that the events carry the information of how many events have passed and failed the cuts, making, e.g., the normalization of histograms easier. However, the downside is

<sup>14</sup>Event in the sense described at the beginning of sec. 2.8.

that computational effort is wasted on events with zero weight, and they also may have rare or even invalid kinematic configurations increasing the number of warnings and errors in subsequent processing.

In the second case, we perform an *unweighting* step on the weighted events such that each event survives only with a probability proportional to its weight

$$\mathcal{P}_{\text{surv},i} = \frac{|w_i|}{w_{\text{max}}} \quad \text{where} \quad w_{\text{max}} = \max_i (|w_i|) \quad . \quad (3.12)$$

After this selection, we assign a weight equal to  $\text{sgn}(w_i)$  to each event producing a sample of *unweighted events*.

A weight determined by eq. (3.11) does not need to be positive. NLO PDFs can take negative values in phase-space regions outside the perturbative region, and also, the subtracted real and virtual components may take negative values. This means that the procedure described above will generate a sample of *indefinite unweighted* events, i.e., a sample of events where each event carries a weight  $w \in \{-1, 1\}$ .

We note that eq. (3.11) contains the only terms influenced by the virtual and the DGLAP NLO contribution in the POWHEG matching. Thus, they influence solely the event weights and flavor abundances of the generated events but not the kinematics.

### 3.5 The generation of radiation – the veto procedure

Given the Born configuration  $(\Phi_n, w, f_B)$ , the next step is to generate the hardest radiation from the Sudakov form factor in eq. (3.9). For the efficient generation of the hardest radiation from the Sudakov form factor, we apply the *POWHEG veto procedure*, an iterative algorithm to efficiently find a valid kinematic configuration for the radiated momentum. For illustrative purposes, we will discuss the veto procedure in general before discussing its application to POWHEG matching in sec. 3.5.2.

#### 3.5.1 The veto procedure in general

Inspired by Nason and Ridolfi (ref. [56], app. C), this section discusses the general technique of how to generate kinematic variables from random numbers with a veto procedure using an upper bounding function (UBF). We will also include a proof of the veto procedure in this section.

#### Generating a kinematic variable from the Sudakov form factor

The basic problem we are facing when generating POWHEG events is that we want to generate positive definite variables  $p(x) > 0$  from a set of (not necessarily uniform) random numbers  $x$  describing an event based on a probability distribution

$$\mathcal{P}_p(x) = R(x) \exp \left[ - \int R(x') \theta(p(x') - p(x)) d^d x' \right] \quad , \quad (3.13)$$

where we assume  $R(x)$  to be positive semi-definite<sup>15</sup> and the full integral over  $R(x)$  to be divergent. To get some more intuition, let us mention that in the application of this procedure later on, the three FKS variables  $(\xi, y, \phi)$  will substitute  $x$  while  $R(x)$  will be proportional to the ratio of matrix elements  $\mathcal{R}_{\alpha_r/B_{f_B}}$ . Using  $\mathcal{P}_p(x)$ , we can infer the probability for a given variable  $p$  by integrating and notice that it is an exact

<sup>15</sup>We have already mentioned that this will not always be the case. We will come back to this issue in sec. 3.5.4.

differential

$$\begin{aligned} \mathcal{P}(p(x) = p) &= \int \mathcal{P}_p(x) \delta(p(x) - p) d^d x = \int R(x) \delta(p(x) - p) \exp \left[ - \int R(x') \theta(p(x') - p) d^d x' \right] d^d x \\ &= \frac{d}{dp} \Delta(p) \quad , \end{aligned} \quad (3.14)$$

where

$$\Delta(p) = \exp \left[ - \int R(x') \theta(p(x') - p) d^d x' \right] \quad (3.15)$$

is the corresponding potential form, which happens to be the Sudakov form factor. As  $R(x)$  is assumed to be non-negative, it is  $0 \leq \Delta(p) \leq 1$ . From this we can also see that the probability distribution  $\mathcal{P}_p(x)$  is correctly normalized to 1:

$$\int \mathcal{P}_p(x) d^d x = \int_0^\infty \int \mathcal{P}_p(x) \delta(p(x) - p) d^d x dp = \Delta(\infty) - \Delta(0) = 1 - \exp \left[ - \int R(x') d^d x' \right] = 1 - e^{-\infty} = 1 \quad . \quad (3.16)$$

The exponent vanishes as  $p \rightarrow +\infty$  due to the  $\theta$  function and diverges as  $p \rightarrow 0$ , based on our assumptions for  $R(x)$ .

In principle, this makes the generation of events based on  $p(x)$  according to a probability distribution  $\mathcal{P}_p(x)$  straightforward using inverse transform sampling (ITS) (c.f. app. B.2 for details):

1. Take a uniform random number  $r$  between 0 and 1.
2. Solve  $\Delta(p) = r$  for  $p$ .
3. Generate the event  $x$  with a distribution proportional to  $R(x) \delta(p(x) - p)$  such that  $p(x) = p$  .

So knowledge of the Sudakov form factor immediately allows us to generate kinematic variables like radiation momenta. This is the basic procedure applied when generating a parton shower.

### The veto procedure

So in principle, our problem is solved, and we can assign momenta to our events based on generated uniform random numbers. However, the problem is the performance of step 2: solving  $\Delta(p) = r$  for  $p$ . This relation has to be solved numerically, which can quickly become very time-consuming. To overcome this issue, we apply the following *veto procedure* inspired by the rejection sampling method<sup>16</sup>, c.f. app. B.3.

We assume that there is an UBF  $U(x)$  such that  $U(x) \geq R(x) \forall x$  and such that

$$\Delta^U(p) = \exp \left[ - \int d^d x' U(x') \theta(p(x') - p) \right] \quad (3.17)$$

is "simple" in the sense that the equation  $\Delta^U(p) = r$  can easily be solved for  $p$ . In practice, we apply a numerical bisection root-finding method to solve eq. (3.17). We then use  $U(x)$  for the generation of  $p$ , and in the end, veto some events to correct for the overestimation. In detail, the steps performed are:

1. We initially set  $p_{\max} = \infty$ .
2. We take a uniform random number  $0 < r_i < 1$  to determine  $p$
3. We solve  $\Delta^U(p) = r_i \Delta^U(p_{\max})$  for  $p$ . A solution  $0 < p < p_{\max}$  always exists for  $0 < r_i < 1$ .

---

<sup>16</sup>ignoring the normalization condition

4. We generate  $x$  according to  $U(x)\delta(p(x) - p)$
5. We take a new uniform random number  $r'$  for the veto.
6. Then, if  $r' < R(x)/U(x)$ , we keep the configuration, successfully generating an event. Otherwise, we set  $p_{\max} = p$  and repeat the process starting with step 3.

In the first attempt, it is  $\Delta^U(p_{\max}) = 1$ . For an event vetoed in the first attempt, we find  $r_1 = \Delta^U(p)$ . So that after setting  $p_{\max} = p$ , we have to solve  $\log(\Delta^U(p)) = \log(r_1) + \log(r_2)$  for  $p$  in the second attempt. For the  $N$ th attempt, we have to solve  $\log(\Delta^U(p)) = \sum_{i=1}^N \log(r_i)$  for  $p$ . The resulting events will then be distributed according to eq. (3.13).

### Proof of the veto procedure

We now want to prove the previous statement and thus, the validity of the veto procedure. When all events have been generated according to the veto procedure, all their distributions will be the sum of the distributions filled with events that got accepted without any veto, that got accepted after the first veto, after the second veto and so on.

We want to investigate this series, starting with the first term given by

$$\mathcal{P}^{(0)}(x) = \int_0^{p_{\max}} \underbrace{\frac{\Delta^U(p_1)}{\Delta^U(p_{\max})}}_{\text{step 3}} \underbrace{U(x)\delta(p(x) - p_1)}_{\text{step 4}} \underbrace{\frac{R(x)}{U(x)}}_{\text{step 6}} dp_1 = R(x)\Delta^U(p(x)) \quad . \quad (3.18)$$

Here, the first fraction in the integrand comes from step 3 and, when integrated over all possible values for  $p_1$ , accounts for all the possible corresponding random numbers  $r_i$ . The second factor arises from step 4 and connects the generated kinematic values  $p(x)$  with the kinematic seed  $x$ . Lastly, the fraction  $\frac{R(x)}{U(x)}$  accounts for the survival probability in step 6. For simplification, we used the fact that  $\Delta^U(p_{\max}) = \Delta^U(\infty) = 1$  and evaluated the integral using the  $\delta$  distribution.

The events which fail the first but survive the second veto will be distributed according to

$$\begin{aligned} \mathcal{P}^{(1)}(x) &= \int_0^{p_{\max}} \frac{\Delta^U(p_1)}{\Delta^U(p_{\max})} \int U(x_1) \delta(p(x_1) - p_1) \left(1 - \frac{R(x_1)}{U(x_1)}\right) \\ &\quad \int_0^{p_1} \frac{\Delta^U(p_2)}{\Delta^U(p_1)} U(x) \delta(p(x) - p_2) \frac{R(x)}{U(x)} dp_2 d^d x_1 dp_1 \\ &= R(x)\Delta^U(p(x)) \int_{p(x)}^{\infty} u(p_1) dp_1 \quad , \end{aligned} \quad (3.19)$$

where we have introduced the short-hand notation

$$u(p) = \int U(x) \delta(p(x) - p) \left(1 - \frac{R(x)}{U(x)}\right) d^d x \quad . \quad (3.20)$$

This time, we have inserted a factor of  $\left(1 - \frac{R(x_1)}{U(x_1)}\right)$  to account for the rejection probability. Due to the  $\delta$  distribution in the second factor, the result will only be non-zero for  $p_1 \geq p(x)$ , so we can use  $p(x)$  as the lower limit of the remaining integral. We also replaced  $p_{\max}$  with its initial value  $\infty$ .

To continue one more step, for the events that only survive the third veto step, we find

$$\begin{aligned}
\mathcal{P}^{(2)}(x) &= \int_0^{p_{\max}} \frac{\Delta^U(p_1)}{\Delta^U(p_{\max})} u(p_1) \int_0^{p_1} \frac{\Delta^U(p_2)}{\Delta^U(p_1)} u(p_2) \\
&\quad \int_0^{p_2} \frac{\Delta^U(p_3)}{\Delta^U(p_2)} U(x) \delta(p(x) - p_3) \frac{R(x)}{U(x)} dp_3 dp_2 dp_1 \\
&= \int_0^{p_{\max}} u(p_1) \int_0^{p_1} u(p_2) \int_0^{p_2} \Delta^U(p_3) \delta(p(x) - p_3) R(x) dp_3 dp_2 dp_1 \\
&= \int_{p(x)}^{p_{\max}} u(p_1) \int_{p(x)}^{p_1} u(p_2) dp_2 dp_1 \Delta^U(p(x)) R(x) \\
&= \frac{1}{2} \int_{p(x)}^{p_{\max}} u(p_1) dp_1 \int_{p(x)}^{p_{\max}} u(p_2) dp_2 \Delta^U(p(x)) R(x) \\
&= R(x) \Delta^U(p(x)) \frac{1}{2} \left[ \int_{p(x)}^{\infty} dp u(p) \right]^2, \tag{3.21}
\end{aligned}$$

canceling the fractions of  $\Delta^U$  terms, using the  $\delta$  distributions to raise the lower integration limit, and making use of the fact that integrating over  $p_2$  from  $p(x)$  to  $p_1$  for every value of  $p_1$  is equivalent to always integrating to  $p_{\max}$  and dividing by 2.

We can now infer the generic term by induction and get

$$\mathcal{P}^{(n)}(x) = \Delta^U(p(x)) R(x) \frac{1}{n!} \left[ \int_{p(x)}^{\infty} u(p) dp \right]^n, \tag{3.22}$$

which, if summed over, yields the desired exponential

$$\begin{aligned}
\sum_{n=0}^{\infty} \mathcal{P}^{(n)}(x) &= R(x) \Delta^U(p(x)) \exp \left[ \int_{p(x)}^{\infty} u(p) dp \right] \\
&= R(x) \Delta^U(p(x)) \exp \left[ \int [U(x') - R(x')] \theta(p(x') - p(x)) d^d x' \right] \\
&= R(x) \exp \left[ - \int R(x') \theta(p(x') - p(x)) d^d x' \right], \tag{3.23}
\end{aligned}$$

concluding the proof by putting in the definitions of  $u(p)$  and  $\Delta^U(p(x))$ . We see that the dependence on the UBF entirely vanishes provided it fulfills the assumed criteria, i.e., that it always is an upper bound for  $R(x)$  even though  $R(x)$  may be divergent in some regions.

### 3.5.2 Dividing and conquering the Sudakov form factor

Now that we have understood the veto procedure in general, we can take a look at how it is applied during the POWHEG matching to generate the real radiation kinematics. This is also explained in detail in sec. 7.1 of ref. [48] and sec. 4.3 of ref. [47] intertwined with technical descriptions of the routines inside the POWHEG code.

At this point, one may wonder why it is necessary to discuss the generation of the real kinematics here again, considering we already thoroughly discussed how to generate the FKS variables and from them the real momenta in sec. 2.4. The reason is that for the POWHEG matching, we want to generate only real events featuring radiation with a transverse momentum above a given threshold  $p_{T,\min}$ . Radiation with a lower transverse momentum should better be generated by the parton shower to avoid unphysical regions of the

PDFs or non-perturbative regions of  $\alpha_S$ . We achieve this by generating a Born-like event in the case that the radiation’s transverse momentum would be smaller than  $p_{T,\min}$ . By default, this parameter is  $p_{T,\min} = 1$  GeV, but the value can be changed with the parameter `powheg_pt_min` in WHIZARD. In order to speed up the event generation, we want to abort generating the radiation of an event below this threshold as early as possible. For this reason, we generate the event’s transverse momentum first, then decide whether to keep or dismiss it, and, if we keep it, generate the rest of the event kinematics based on the generated  $p_T$ .

We start this discussion after having generated an underlying Born configuration as described in sec. 3.4.1 so that the Born kinematics and also the Born flavor structure  $f_B$  are known.

When generating the radiation, we make use of the phase-space segmentation already established in the framework of FKS, i.e., we decompose the Sudakov form factor into a product over ALRs

$$\Delta^{f_B}(\Phi_n, p_T) = \prod_{\alpha_r \in \{\alpha_r | f_B\}} \Delta_{\alpha_r}^{f_B}(\Phi_n, p_T) \quad , \quad (3.24)$$

where  $f_B$  denotes a specific Born flavor structure and  $\alpha_r$  a specific ALR so that the product takes into account all ALRs that share the same underlying Born flavor structure. The Sudakov form factor for a single ALR is then given by

$$\Delta_{\alpha_r}^{f_B}(p_T) \equiv \Delta_{\alpha_r}^{f_B}(\Phi_n, p_T) = \exp \left[ - \int d\Phi_{\text{rad}} \frac{\mathcal{R}_{\text{sin}}(\Phi_{n+1})}{\mathcal{B}^{f_B}(\Phi_n)} \theta(k_T(\Phi_{n+1}) - p_T) \right]_{\alpha_r}^{\overline{\Phi}_n^{\alpha_r} = \Phi_n} . \quad (3.25)$$

The lower label,  $\alpha_r$ , of the square bracket indicates that the quantities inside the bracket should be evaluated for a specific ALR, while the upper label  $\overline{\Phi}_n^{\alpha_r} = \Phi_n$  denotes that the real radiation phase space  $\Phi_{n+1}$  is given by the underlying Born phase space  $\overline{\Phi}_n^{\alpha_r}$  at the point  $\Phi_n$  and the radiation variables  $\Phi_{\text{rad}}$ . We will drop the explicit dependence of the Sudakov form factor on the Born phase space  $\Phi_n$  in our notation from here on.

As we see in eq. (3.25), we only take into account the *singular* part of the real contribution for the generation of radiation. We can include the *finite* part of the real contribution in our events by generating events and treating it as an ordinary finite tree-level contribution (c.f. sec. 2.6.3). By doing so, we remedy the problem of *Born zeroes* we will elaborate on in sec. 3.6.3, which could otherwise become problematic. If no real partition is used, the total real matrix element  $\mathcal{R}$  takes the place of  $\mathcal{R}_{\text{sin}}$  in eq. (3.25).

Eq. (3.25) also makes it clear why POWHEG matching works especially well in conjunction with FKS subtraction. The generation of radiation builds on a Born configuration and the Sudakov splits into a product of Sudakovs over ALR. To achieve something similar based on CS subtraction requires an additional projection similar to FKS itself [119].

At this point, we have assigned one Sudakov form factor to each ALR. We follow app. B of ref. [47] and use a version of the *highest-bid algorithm*, to choose the ALR and thereby the real configuration including the flavor structure of the generated event, For each ALR, we generate a transverse momentum value  $p_T$  with a probability distribution given by

$$\mathcal{P}_{\alpha_r}^{f_B}(p_T) = \frac{\partial}{\partial p_T} \Delta_{\alpha_r}^{f_B}(p_T) \quad , \quad (3.26)$$

which we will discuss in more detail in sec. 3.5.3. We then keep only the highest generated  $p_T$  value and the corresponding ALR.

To see why this is a valid approach, suppose that  $k$  labels the chosen ALR. The probability that the ALR  $k$

has the largest  $p_T$  is given by the product of its probability to be generated

$$\mathcal{P}_k^{f_{\mathcal{B}}}(p_T) = \frac{\partial}{\partial p_T} \Delta_k^{f_{\mathcal{B}}}(p_T) = \frac{\mathcal{R}_{\text{sin}}^{f_{\mathcal{B}},\alpha_r}(\Phi_{n+1}(p_T))}{\mathcal{B}^{f_{\mathcal{B}}}(\Phi_n)} \Delta_k^{f_{\mathcal{B}}}(p_T) \quad (3.27)$$

and the probability that all  $p_T$  in other ALRs are smaller than the chosen  $p_T$ . We remember from sec. 3.1 that the Sudakov form factor  $\Delta(p_T)$  can be interpreted as the non-splitting probability with transverse momenta larger than  $p_T$  to see that this probability is given by

$$\prod_{i \neq k} \Delta_i^{f_{\mathcal{B}}}(p_T) \quad , \quad (3.28)$$

so that the product of both reproduces the full Sudakov given in eq. (3.24).

### 3.5.3 The upper bounding function

As discussed in sec. 3.5.1, to generate the transverse momentum according to eq. (3.26), we need to solve  $\Delta^U(p_T) = r$  for  $p_T$  using a smart choice for the UBF.

We need to find an UBF that overestimates the integrand of the modified Sudakov form factor given by eq. (3.9). We first make the dependence on the phase space explicit to find a suitable overestimation. We parametrize the radiation phase space using the three radiation variables  $\xi$ ,  $y$  and  $\phi$  as

$$d\Phi_{\text{rad}} = \mathcal{J}^{\alpha_r} d\xi dy d\phi \quad , \quad (3.29)$$

where  $\mathcal{J}^{\alpha_r}$  is the Jacobian of the real phase space whose explicit form depends on the emitter of the ALR. This is equivalent to eq. (2.16). The different Jacobians are discussed in sec. 2.4.

To simplify the Sudakov form factor, we choose an upper bounding function  $N U^{\alpha_r}(\xi, y)$  where  $U^{\alpha_r}(\xi, y)$  determines its functional form and  $N$  is a normalization factor we will specify further in sec. 3.5.4, chosen in such a way that the UBF satisfies

$$\frac{\mathcal{J}^{\alpha_r} \mathcal{R}_{\text{sin}}^{f_{\mathcal{B}},\alpha_r}(\Phi_{n+1})}{\mathcal{B}^{f_{\mathcal{B}}}(\Phi_n)} \leq N U^{\alpha_r}(\xi, y) \quad (3.30)$$

across the entire phase space, thus earning its name. For this to hold, the explicit form of  $U^{\alpha_r}(\xi, y)$  has to be adjusted to the ALR's singularities and thus its splitting type. We will discuss four different of such types in sec. 3.5.5ff.

We then generate a  $p_T$  value according to the probability distribution

$$\mathcal{P}_{\alpha_r}^U(p_T) = \frac{\partial}{\partial p_T} \Delta_{\alpha_r}^U(p_T) \quad (3.31)$$

with

$$\Delta_{\alpha_r}^U(p_T) = \exp \left[ - \int N U^{\alpha_r}(\xi, y) \theta(k_T(\Phi_{n+1}) - p_T) d\xi dy d\phi \right] \quad (3.32)$$

by solving  $r = \Delta_{\alpha_r}^U(p_T)$  numerically.

Finally, we perform a veto step to correct for the overestimation of eq. (3.30), i.e., we accept each event generated with a survival probability

$$\mathcal{P}_{\text{surv}} = \frac{1}{N U^{\alpha_r}(\xi, y)} \frac{\mathcal{J}^{\alpha_r} \mathcal{R}_{\text{sin}}^{f_{\mathcal{B}},\alpha_r}(\Phi_{n+1})}{\mathcal{B}^{f_{\mathcal{B}}}(\Phi_n)} \quad (3.33)$$

and else generate a new  $p_T'$  smaller than before and repeat the process.

Fig. 3.3 is a flow chart depicting the highest-bid algorithm for a process with 3 ALRs. For each ALR, we generate a value  $p_T \in [p_{T,\min}, \infty)$  using the procedure described in this section. When all values have been generated, we generate an event based on the largest  $p_T$  and the corresponding ALR. This approach has the benefit of being parallelizable over the ALRs as all ALRs are treated independently.

For a single core, however, this leaves room for optimization. Fig. 3.4 shows an optimized version of the highest-bid algorithm. Here, we sacrificed the ALRs' independence for performance, based on the idea that if we want to keep only the largest  $p_T$  value in the end, we can stop the veto procedure to generate  $p_T$  in an ALR as soon as the current value is smaller than the largest previously generated  $p_T$  value. In this way, the performance of the highest-bid procedure scales like  $\sum_{i=1}^{N_\alpha} \frac{i}{N_\alpha} = \frac{N_\alpha+1}{2}$  even with a single core, assuming that the  $p_T$  distributions of all ALRs are the same, so the second approach is roughly a factor of 2 faster.

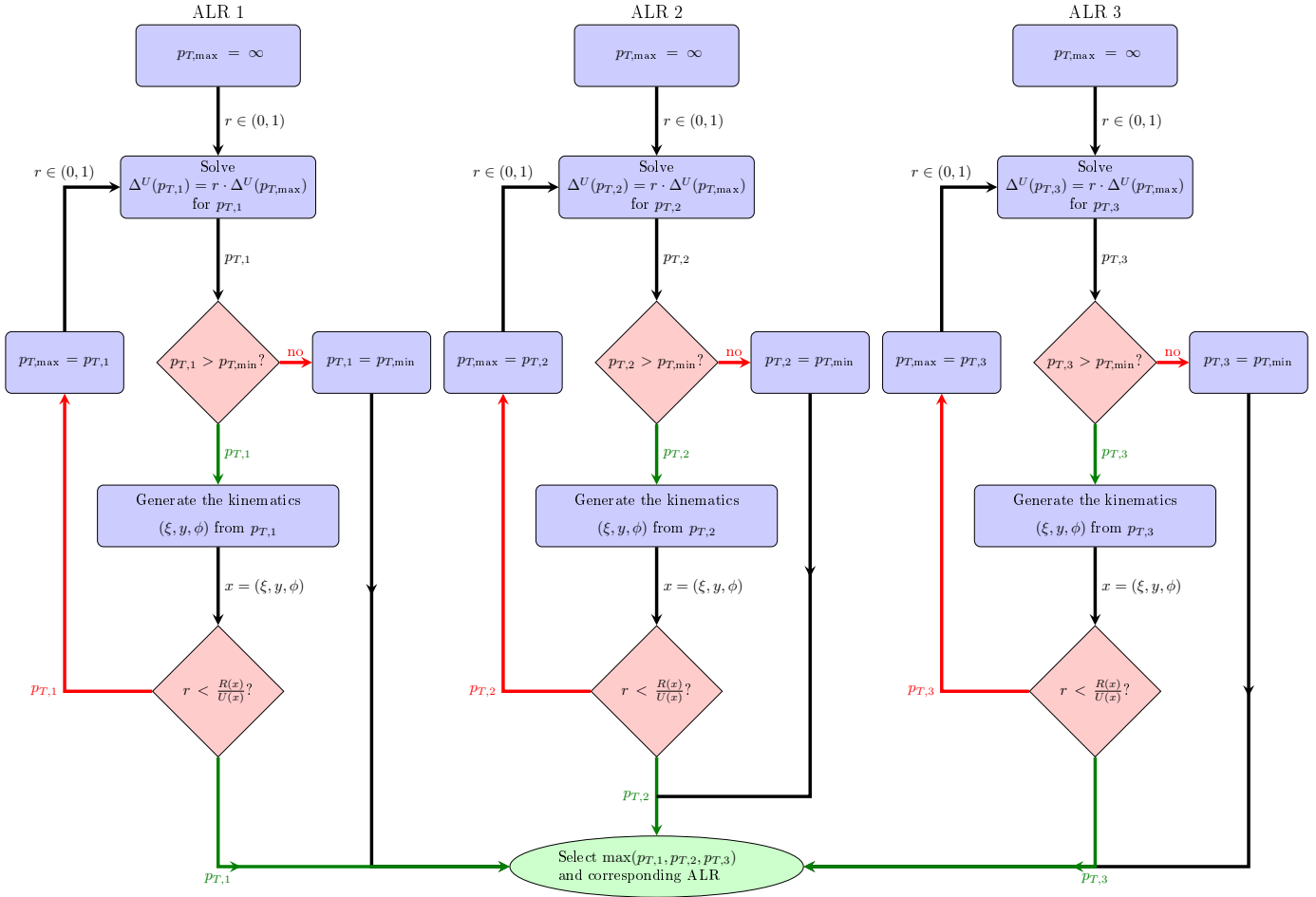


Fig. 3.3: Flow chart depicting the parallelizable highest-bid algorithm with 3 ALRs. A transverse momentum value  $p_T$  is generated in each ALR and the ALR with maximum  $p_T$  determines the event. If in all ALRs,  $p_T = p_{T,\min}$ , a Born event is generated instead. Each  $r$  in this figure denotes a newly generated uniform random number  $r \in (0, 1)$  from the sequence.

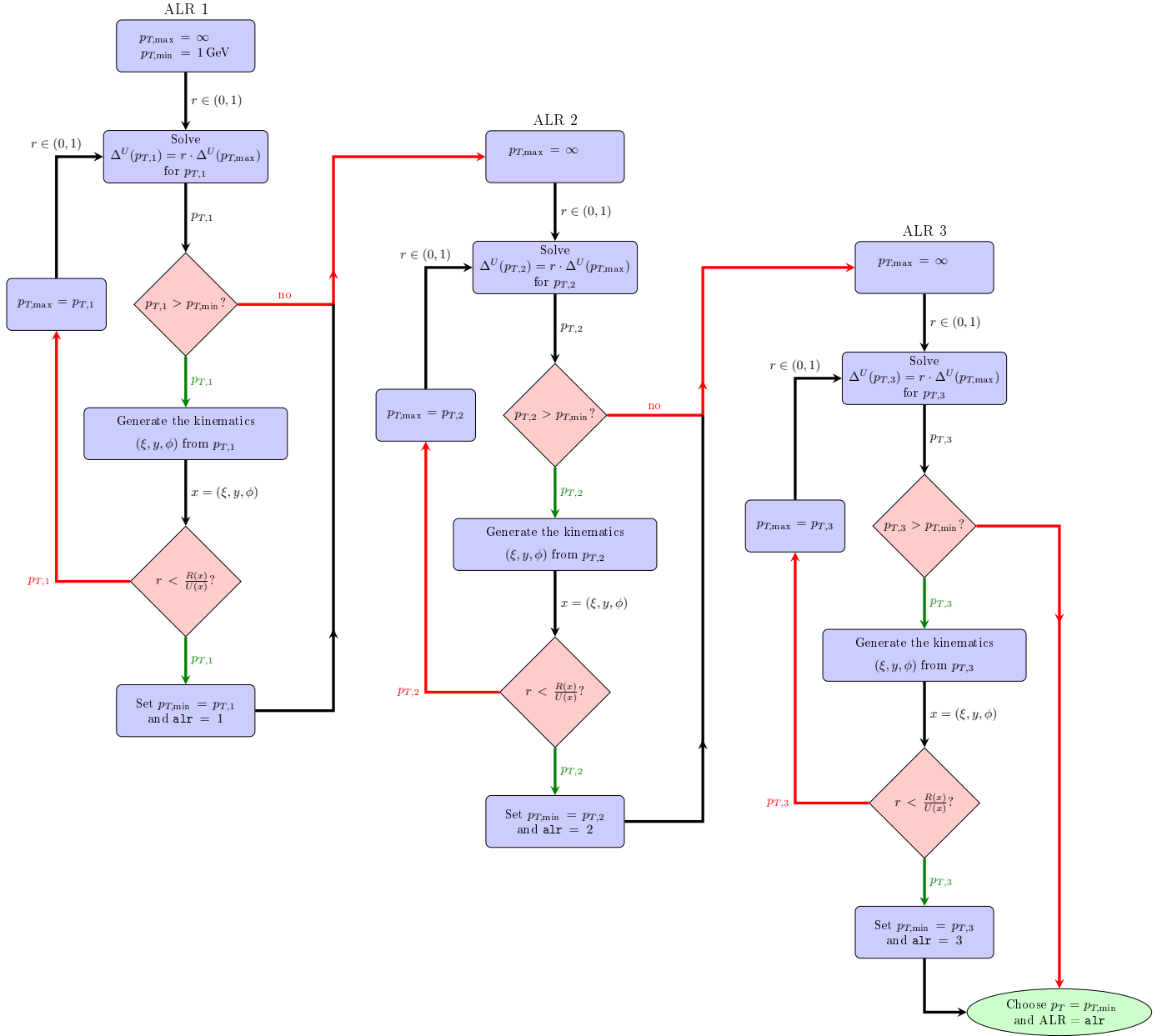


Fig. 3.4: Flow chart depicting the optimized highest-bid algorithm with 3 ALRs. Previously generated  $p_T$  are stored by increasing  $p_{T,\min}$  in subsequent ALRs. If the chosen value for  $p_T$  is still equivalent to the initial  $p_{T,\min}$ , a Born event is generated instead. Each  $r$  in this figure denotes a newly generated uniform random number  $r \in (0, 1)$  from the sequence.

### Multiple UBFs – the stepwise POWHEG veto procedure

Let there be an intermediate upper bounding function  $\mathbb{U}(\Phi_{\text{rad}})$  such that

$$\frac{\mathcal{J}^{\alpha_r} \mathcal{R}_{\text{sin}}^{f_B, \alpha_r}(\Phi_{n+1})}{\mathcal{B}f_B(\Phi_n)} \leq \mathbb{U}(\Phi_{\text{rad}}) \leq N U^{\alpha_r}(\xi, y) \quad . \quad (3.34)$$

We can then split the veto we previously performed in a single step into two steps by first accepting the generated events with a probability

$$\mathcal{P}_{\text{surv}} = \frac{\mathbb{U}(\Phi_{\text{rad}})}{N U^{\alpha_r}(\xi, y)} \quad \text{and then with a probability} \quad \mathcal{P}_{\text{surv}} = \frac{1}{\mathbb{U}(\Phi_{\text{rad}})} \frac{\mathcal{J}^{\alpha_r} \mathcal{R}_{\text{sin}}^{f_{\mathcal{B}}, \alpha_r}(\Phi_{n+1})}{\mathcal{B}^{f_{\mathcal{B}}}(\Phi_n)} . \quad (3.35)$$

which is equivalent to accepting them with the probability given in eq. (3.33). The benefit, however, is that we do not need to evaluate the Born and real matrix elements for all the events that already fail the first veto step. As these computations are the bottleneck of this procedure's performance, we can achieve a significant speedup by performing the veto procedure stepwise. We will take this even further and perform a series of overestimations and veto steps ordered by increasing performance cost to do computations less often the more costly they are.

We summarize all possible veto steps performed in sec. 3.5.9 after we discussed the possible UBF choices. These choices differ in the functional form of the UBF, which depends on the nature of the real emission. We will discuss four different classes:

1. FSR emissions off a massless emitter
2. FSR emissions with a massless recoil system
3. ISR emissions off a massless emitter
4. FSR emissions off a massive emitter.

Before discussing these classes, we will elaborate on a veto step all UBF choices have in common.

### 3.5.4 Normalizing the upper bounding function – the POWHEG grid

Inspired by sec. 7.1 of ref. [48], one of the veto steps is used to optimize the normalization of the UBF. For this, we introduce the *POWHEG grid*  $N_{\#}^{\alpha_r}(\xi, y)$ , which is a stepwise function in  $\xi$  and  $y$ , i.e., a 2D histogram with bins  $([\xi_i, \xi_{i+1}], [y_j, y_{j+1}])$ , where  $\xi_i$  and  $y_i$  are monotonous functions of  $\xi$  and  $y$  respectively, in such a way that it always overestimates the minimal required normalization  $N^{\alpha_r}(\xi, y)$ :

$$\frac{\mathcal{J}^{\alpha_r} \mathcal{R}_{\text{sin}}^{f_{\mathcal{B}}, \alpha_r}(\Phi_{n+1})}{\mathcal{B}^{f_{\mathcal{B}}}(\Phi_n)} = N^{\alpha_r}(\xi, y) U^{\alpha_r}(\xi, y) \leq N_{\#}^{\alpha_r}(\xi, y) U^{\alpha_r}(\xi, y) \leq N_{\text{max}}^{\alpha_r} U^{\alpha_r}(\xi, y) . \quad (3.36)$$

Here,  $\mathcal{J}^{\alpha_r}$  implicitly depends on the phase-space point and we have defined  $N_{\text{max}}^{\alpha_r}$  to be the global maximum of the POWHEG grid

$$N_{\text{max}}^{\alpha_r} = \max_{(\xi, y)} \left( N_{\#}^{\alpha_r}(\xi, y) \right) . \quad (3.37)$$

This second overestimation has the benefit that the normalization factor  $N_{\text{max}}^{\alpha_r}$  does not depend on the specific phase-space point anymore, which allows us to take the normalization out of the integral in eq. (3.32), so that we only have to solve the integral once for each type of UBF.

The veto step to correct for the overestimation performed in eq. (3.36) will be more efficient the smaller the grid values  $N_{\#}^{\alpha_r}(\xi, y)$  are. We thus determine  $N_{\#}^{\alpha_r}(\xi, y)$  as the maximum of what it is supposed to overestimate in each bin,

$$N_{\#}^{\alpha_r}(\xi, y) = \max_{\substack{\xi|\xi_i < \xi \leq \xi_{i+1} \\ y|y_j < y \leq y_{j+1}}} \left( N^{\alpha_r}(\xi, y) \right) = \max_{\substack{\xi|\xi_i < \xi \leq \xi_{i+1} \\ y|y_j < y \leq y_{j+1}}} \left( \frac{\mathcal{J}^{\alpha_r} \mathcal{R}_{\text{sin}}^{f_{\mathcal{B}}, \alpha_r}(\Phi_{n+1})}{\mathcal{B}^{f_{\mathcal{B}}}(\Phi_n)} U^{\alpha_r}(\xi, y) \right) . \quad (3.38)$$

There are two overestimations performed in eq. (3.36). We correct for the first one in the so-called *norm-veto step* by accepting events with a probability

$$\mathcal{P}_{\text{surv}} = N_{\#}^{\alpha r}(\xi, y) / N_{\text{max}}^{\alpha r} \quad , \quad (3.39)$$

followed by a second veto accepting events with probability

$$\mathcal{P}_{\text{surv}} = N^{\alpha r}(\xi, y) / N_{\#}^{\alpha r}(\xi, y) \quad . \quad (3.40)$$

This step requires the computation of the squared matrix elements  $\mathcal{R}_{\text{sin}}$  and  $\mathcal{B}$ , so it is dubbed *matrix-element-veto step*. In this veto step, the dependence on the grid cancels almost entirely.

The only exception to this statement are *grid excess events*: events for which the computed  $N^{\alpha r}(\xi, y)$  is larger than the maximal value encountered when creating the grid. The survival probabilities for these events are formally larger than 100%. We keep these events, but if this happens too often, this indicates that the grid is not an accurate overestimate, so that the generated event sample may be invalid. The issue here is similar to excess events in event unweighting (c.f. eq. (3.12)). We roughly tolerate an excess event fraction of less than 1%. If too many excess events occur, more calls should be spend when filling the grid to improve its estimate. Alternatively, a safety factor larger than 1 can be applied to each bin in the grid to minimize the probability of excess events.

In WHIZARD, the integration and the simulation of events are performed in two separate steps. We can benefit from this approach here by determining the grid values for each bin already when sampling the phase space for the integration. Thus when integrating, we keep track of the maximal encountered values  $N_{\#}^{\alpha r}(\xi, y)$  for each ALR and write them to a file to be read in again when generating events. In this way, the POWHEG grid file can be reused to generate events from a previous integration run similar to the VAMP grids (c.f. app. D.1). There is some freedom in the technical details of the grid. So far, we did not specify the monotonous functions mapping  $(\xi, y)$  to the grid bins. WHIZARD uses a generic grid implementation so that each axis of the grid ranges from 0 to 1. Therefore we have to map the values  $(\xi, y)$  to the unit square  $[0, 1]^2$  to target the bins.

We experimented with different functional forms of the mappings. For  $y$ , we compared a simple linear mapping  $y \mapsto \frac{1+y}{2}$ , taking the absolute value  $y \mapsto |y|$  and the inverse of what we use to sample  $y$  from the initial set of random numbers during the integration step with the intent to profit from the importance sampling in eq. (2.40).

As  $\xi$  is already within  $[0, 1]$ , the simplest possible mapping for  $\xi$  is the identity. We compared this approach to the rescaled version  $\xi \mapsto \xi / \xi_{\text{max}}$  and also included logarithmic, exponential as well as hyperbolic mappings in our comparisons.

The different mappings showed different fractions of events being vetoed in the norm veto step, but we did not observe any significant influence on the overall performance. The more events this step vetoes, the more event kinematics we have to generate. The fewer events are vetoed in this step, the more events will fail the subsequent veto steps. Both effects seem to compensate each other. This means that there is no significant correlation between the grid mappings and the structure of the matrix-element ratio divided by the functional form of the UBF  $\frac{\mathcal{J}^{\alpha r} \mathcal{R}_{\text{sin}}^{f_{\mathcal{B}}, \alpha r}(\Phi_{n+1})}{\mathcal{B}^{f_{\mathcal{B}}}(\Phi_n) U^{\alpha r}(\xi, y)}$  remaining to be exploited for optimizations.

In the end, we decided to keep the mappings

$$\xi \mapsto \frac{\log(1 - \xi)}{\log(1 - \xi_{\text{max}})} \quad \text{and} \quad y \mapsto |y| \quad . \quad (3.41)$$

We capped  $\xi_{\max}$  and  $\xi$  at a value slightly smaller than 1 to ensure the numerical validity of the expression. Of course, it is important to apply the same mappings during integration when writing the grids and during event generation when retrieving the values to ensure that we access the same bin of the grid for the same values  $(\xi, y)$  in both cases.

Also regarding the bin density, there is a certain choice left for the user. Some processes require a finer grid, while a coarse grid is sufficient for others. The grid dimensions can be set using the integer variables `powheg_grid_size_xi` and `powheg_grid_size_y`. Ideally, they are chosen in such a way that the performance for the current process and setup is optimal while keeping the fraction of grid excess events small. A high performance is characterized by a large ratio of the grid's average value over its maximum. If this ratio is too small, lots of events will be vetoed in the first norm veto step, eq. (3.39). In practice, the number of bins in each dimension should be between 1 and 100, and in most cases, a  $10 \times 10$  grid is a good balance between performance and accuracy. More complicated processes and setups might require a finer-grained grid.

To illustrate how such a grid looks like, fig. 3.5 shows the POWHEG grids for the three ALRs of the partonic process  $d\bar{d} \rightarrow e^+e^-$  with 10 bins for each axis. The axes are scaled according to the mappings of eq. (3.41). The bin heights correspond to the values of  $N_{\#}^{\alpha r}(\xi, y)$  in each bin, which are additionally color-coded.

We see that the grid's overall structure is the same in ALR 2 and ALR 3. The peak values of the grid are reached at low values of  $\xi$ . This is a remainder of the real matrix elements' divergence in this region that survived the cancellation with  $U^{\alpha r}(\xi, y)$ . However, in ALR 1, this behavior seems to be entirely canceled with the UBF. Overall, ALR 2 has the highest bin values, followed by ALR 3. This can be estimated from the ratio of PDFs involved in the Born and the real matrix element. In ALR 2, this ratio is given by  $g(x_{\mathcal{R}})/\bar{d}(x_{\mathcal{B}})$ , while in ALR 3 it is  $g(x_{\mathcal{R}})/d(x_{\mathcal{B}})$  so the real enhancement from the gluon PDF seems to explain the larger grid entries here. Thanks to the non-linear mapping of  $\xi$ , the bin heights are much more evenly distributed compared to a linear mapping. This improves the ratios of the mean value over the maximum for each grid which in this case are between 0.40 for ALR 3 and 0.44 for ALR 2.

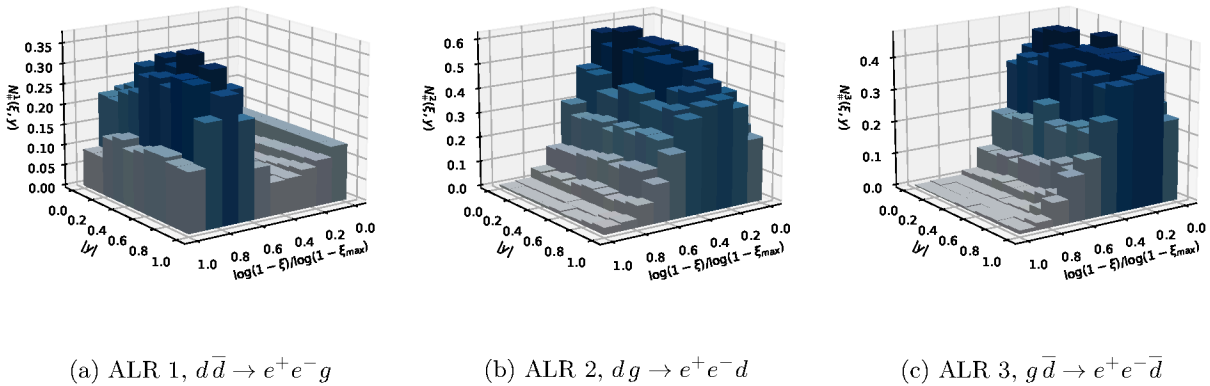


Fig. 3.5: POWHEG grids for the three ALRs of the process  $d\bar{d} \rightarrow e^+e^-$ . The figure design was inspired by fig. B.2 of ref. [71].

### More technical details when generating the POWHEG grid

There are a few more technical issues regarding the generation of the POWHEG grid. Most of them come from the fact that when determining the bin values by eq. (3.38) we have to compute the fraction  $\frac{\mathcal{R}_{\text{sin}}^{f_{\mathcal{B}}, \alpha r}(\Phi_{n+1})}{\mathcal{B}^{f_{\mathcal{B}}}(\Phi_n)}$ . In an NLO computation, none of the squared matrix elements  $\mathcal{R}_{\text{sin}}$  and  $\mathcal{B}$  has to be positive definite as

$\mathcal{R}_{\text{sin}}$  contains potentially large subtraction terms and both include PDF factors that may also take negative values in non-perturbative regions beyond LO. If just one of both values is negative, they will not contribute to the maximum computed in eq. (3.38). If both are simultaneously negative, however, they could. We skip the PSP in both cases when filling the grid to avoid contributions from unphysical regions.

We do the same if at least one of both equals zero. This may happen either for physical reasons such as helicity arguments, which we will discuss in more detail in sec. 3.6.3 or if any of both phase-space points  $\Phi_n$  or  $\Phi_{n+1}$  failed the kinematic cuts. Doing so should not pose a problem as we apply the same kinematic cuts when generating the events, so we should not have to probe the grid at these phase-space points.

Finally, we also skip phase-space points where the PDF values are exceedingly small. In this case, computing the ratio  $\frac{\mathcal{R}_{\text{sin}}^{f_{\mathcal{B}},\alpha_r}(\Phi_{n+1})}{\mathcal{B}^{f_{\mathcal{B}}}(\Phi_n)}$  may become numerically instable. Based on ref. [47] we skip a phase-space point if any of the conditions

1.  $s < 2 \text{ GeV}^2$
2.  $\max(x_{\mathcal{B},\oplus}, x_{\mathcal{B},\ominus}) > 0.9$
3.  $x_{\mathcal{B}}(1 - x_{\mathcal{B}})g(x_{\mathcal{B}}) > 30q(x_{\mathcal{B}})$  for any initial-state quark
4.  $x_{\mathcal{B}}(1 - x_{\mathcal{B}})\sum_{f \in \{q,\bar{q}\}} f(x_{\mathcal{B}}) > 30g(x_{\mathcal{B}})$  for any initial-state gluon

is met. We choose a criterion independent of the actual emitter to not artificially favor specific ALRs.

Skipping some PSPs here increases the numerical stability of the grid and also greatly increases the veto performance by excluding those points that would lead to peaks in the grid much higher than the average value. This is, however, an approximation, possibly increasing the fraction of occurring excess events later in the procedure. It is for this reason that we monitor the fraction of excess events, making sure that they have no significant impact.

One more remark: the POWHEG grid here is used as an overestimator for the probed function. One could get rid of binning and possibly also peak effects by replacing the grid with an analytic function fitted to the probed grid values using machine learning techniques. This could be a well-defined interesting and concise future project.

### 3.5.5 The POWHEG veto procedure – the massless FSR case

In this section, we will focus on probably the most common case of final-state radiation off massless emitters first discussed in sec. 7.1.3 of ref. [48]. The other cases will be discussed in subsequent sections.

In order to satisfy the upper bounding condition eq. (3.30), it is essential that the UBF catches all the divergences of the real matrix element. For final-state radiation off massless emitters, these divergent phase-space regions are reached if  $\xi \rightarrow 0$  as well as  $y \rightarrow 1$ . Therefore, the simplest possible choice is an UBF of the form

$$\boxed{N_{\text{max}}^{\alpha_r} U^{\alpha_r}(\xi, y) = N_{\text{max}}^{\alpha_r} \frac{\alpha_S^{\text{rad}}(p_T)}{\xi(1-y)}} \quad (3.42)$$

exhibiting the same behavior. Other choices with a more complicated functional dependence are possible but do not seem to provide a significant efficiency gain.

#### The $\alpha_S$ veto

All upper bounding functions except the one for massive emitters are explicitly proportional to the strong coupling constant  $\alpha_S$  just as the matrix-element ratio  $\frac{\mathcal{R}_{\text{sin}}^{f_{\mathcal{B}},\alpha_r}(\Phi_{n+1})}{\mathcal{B}^{f_{\mathcal{B}}}(\Phi_n)}$  in the Sudakov exponent. In the

generation of the transverse momentum from the Sudakov, we will first use an overestimated value  $\alpha_S^{\text{rad}}$  and correct this overestimation in another veto step later. It is defined by

$$\alpha_S(\mu) \leq \alpha_S^{\text{rad}}(\mu) := \frac{1}{b_0^{\text{rad}} \log\left(\frac{\mu^2}{\Lambda_{\text{rad}}^2}\right)} \quad . \quad (3.43)$$

inspired by the LO running of  $\alpha_S$ , where we choose to further overestimate  $\alpha_S$  using the LO coefficient of the QCD  $\beta$ -function

$$b_0^{\text{rad}} = \frac{33 - 2 \cdot n_f}{12\pi} \quad \text{with} \quad n_f = 5 \quad . \quad (3.44)$$

Although, in general, when evolving  $\alpha_S$ ,  $n_f$  will be equal to the number of active quark flavors with masses below the scale of  $\alpha_S$ . The exact choice for  $\Lambda_{\text{rad}}$  is to some extent arbitrary as it cancels out in the  $\alpha_S$  veto step. We determine  $\Lambda_{\text{rad}}$  such that the overestimated  $\alpha_S$  agrees with the actual one at the scale  $\mu_0$ , i.e.,  $\alpha_S(\mu_0) = \alpha_S^{\text{rad}}(\mu_0)$ , to be

$$\Lambda_{\text{rad}}^2 = \mu_0^2 \exp\left[-\frac{1}{b_0^{\text{rad}} \alpha_S(\mu_0)}\right] \quad . \quad (3.45)$$

In this way, eq. (3.43) holds for all  $\mu \geq \mu_0$ .  $\frac{\mu_0}{2}$  can be set by the user via the parameter `powheg_lambda` in `WHIZARD`. By default, we determine this parameter via the QCD Landau pole as  $\frac{\mu_0}{2} = \Lambda_{\overline{\text{MS}}}^{n_f=5}$ . Another sensible choice is  $\mu_0 = p_{T,\text{min}}$  such that eq. (3.43) holds for all  $p_T \geq p_{T,\text{min}}$

We then use the UBF given by eq. (3.42) for the generation of the transverse momentum  $p_T$  by solving

$$\Delta_{\alpha_r}^U(p_T) = r \quad (3.46)$$

for  $p_T$ . To do this numerically, we need to solve the integral in the Sudakov exponent. Thanks to the overestimations, this is efficiently possible. The solution is given by eq. (3.51), which we will derive in the following.

In the first actual veto step thereafter, the  $\alpha_S$  *veto*, we correct for the overestimation of  $\alpha_S$  in eq. (3.43) by accepting events with a probability

$$\mathcal{P}_{\text{surv}} = \frac{\alpha_S(p_T)}{\alpha_S^{\text{rad}}(p_T)} \quad . \quad (3.47)$$

### Generation of the radiation kinematics

For all subsequent steps, we need to know the explicit event kinematics, i.e.,  $p_T$  and the FKS variables. Following app. C of ref. [48], we proceed to compute  $\xi$  and  $y$  (and also  $\phi$ ) from the generated  $p_T$ . We derived the allowed ranges of the three FKS variables in sec. 2.3.2. They are given by

$$0 < \xi < \xi_{\text{max}} := \frac{s - M_{\text{rec}}^2}{s} \quad , \quad -1 < y < 1 \quad , \quad 0 < \phi < 2\pi \quad , \quad (3.48)$$

where  $M_{\text{rec}}$  is the mass of the recoil system determined by summing all four-momenta excluding the emitter and the radiated final-state particle

$$M_{\text{rec}}^2 := \left(\sum_{i=1}^{n-1} p_i\right)^2 \quad . \quad (3.49)$$

For FSR, we define the transverse momentum as the orthogonal component of  $\vec{k}_i$  or equivalently  $\vec{k}_j$  w.r.t. their sum  $\vec{k}_i + \vec{k}_j$ . From the definitions of  $\xi$ , and  $y$  (c.f. eqs. (2.18) and (2.20)), we can thus choose a

parametrization for  $p_T$  given by

$$p_T^2 = \frac{s}{2}\xi^2(1-y) \quad \Leftrightarrow \quad y = 1 - \frac{2p_T^2}{s\xi^2} . \quad (3.50)$$

In this context,  $p_T$  has to be understood as a hardness scale, which does not necessarily coincide with the physical transverse momentum, so it does not represent the physical relation between the transverse momentum and  $y$ . We can choose any form for this hardness scale as long as it is of the order of the transverse momentum in the collinear limit and that it coincides with the physical transverse momentum in the soft-collinear limit [47].

With these definitions, we can transform the Sudakov form factor of eq. (3.32) according to

$$\begin{aligned} -\log(\Delta_{\alpha_r}^U(p_T)) &= 2\pi N_{\max}^{\alpha_r} \int_0^{\xi_{\max}} \frac{d\xi}{\xi} \int_{p_T^2}^{\xi^2 s} \alpha_S(k_T) \frac{dk_T^2}{k_T^2} \\ &= \frac{\pi N_{\max}^{\alpha_r}}{b_0^{\text{rad}}} \int_0^{\xi_{\max}^2} \frac{d\xi^2}{\xi^2} \int_{p_T^2/\Lambda_{\text{rad}}^2}^{\xi^2 s/\Lambda_{\text{rad}}^2} \frac{dx}{x \log[x]} \\ &= \frac{\pi N_{\max}^{\alpha_r}}{b_0^{\text{rad}}} \int_0^{\xi_{\max}^2} \frac{d\xi^2}{\xi^2} \theta(\xi_{\max}^2 - p_T^2/s) \log\left[\frac{\log(\xi_{\max}^2 s/\Lambda_{\text{rad}}^2)}{\log(p_T^2/\Lambda_{\text{rad}}^2)}\right] \\ &= \frac{\pi N_{\max}^{\alpha_r}}{b_0^{\text{rad}}} \log\left[\frac{p_T^2}{\Lambda_{\text{rad}}^2}\right] \int_1^{\frac{\log[\xi_{\max}^2 s/\Lambda_{\text{rad}}^2]}{\log[p_T^2/\Lambda_{\text{rad}}^2]}} \theta(\xi_{\max}^2 - p_T^2/s) \log[u] du \\ &= \frac{\pi N_{\max}^{\alpha_r}}{b_0^{\text{rad}}} \theta(\xi_{\max}^2 - p_T^2/s) \left\{ \log\left[\frac{\xi_{\max}^2 s}{\Lambda_{\text{rad}}^2}\right] \log\left[\frac{\log(\xi_{\max}^2 s/\Lambda_{\text{rad}}^2)}{\log(p_T^2/\Lambda_{\text{rad}}^2)}\right] - \log\left[\frac{\xi_{\max}^2 s}{p_T^2}\right] \right\} . \quad (3.51) \end{aligned}$$

In the first step, we overestimated  $\alpha_S$  using eq. (3.43) and changed the integrations from  $\xi$  to  $\xi^2$  and from  $k_T^2$  to  $x := k_T^2/\Lambda_{\text{rad}}^2$ . The theta function we introduced in the third line makes sure that the range of the last integral in the second line is counted just once. In this case, it is  $p_{T,\max} = s\xi_{\max}^2$ . Larger values are forbidden by eq. (3.50) and the range of  $y$ . In the fourth step, we changed integration variables again from  $\xi^2$  to  $u := \frac{\log[\xi^2 s/\Lambda_{\text{rad}}^2]}{\log[p_T^2/\Lambda_{\text{rad}}^2]}$  to solve the remaining integral.

We infer from the  $\xi$  integral in the first line that we have to generate  $\xi$  uniformly in  $\log(\xi)$  between  $p_T/\sqrt{s}$  and  $\xi_{\max}$ . Explicitly, this means

$$\xi = \exp\left[(1-r_\xi)\log\left(\frac{p_T}{\sqrt{s}}\right) + r_\xi\log(\xi_{\max})\right] = \left(\frac{p_T}{\sqrt{s}}\right)^{1-r_\xi} \xi_{\max}^{r_\xi} \quad (3.52)$$

with a uniform random number  $r_\xi \in (0, 1)$ .

Once we have solved eq. (3.46) numerically for  $p_T$  and generated  $\xi$  according to eq. (3.52) we can compute  $y$  from the RHS of eq. (3.50). Finally,  $\phi$  is generated uniformly in its allowed range. To check the consistency of the kinematic construction, we can close the circle afterwards by computing the full four-momenta of the real PSP and making sure that the transverse momentum of the radiated parton w.r.t. the emitter before the radiation indeed matches the  $p_T$  we initially generated. This finalizes the generation of the FKS kinematics.

We note that the procedure to generate  $(\xi, y, \phi)$  here is different from the one described in sec. 2.4.1 for the integration as here we required to have  $p_T$  as one of the primary degrees of freedom.

### The Norm veto

Now knowing  $\xi$  and  $y$ , the second veto we perform is the *norm veto* already mentioned in sec. 3.5.4. We

correct for the overestimation of the normalization by keeping events with a probability

$$\mathcal{P}_{\text{surv}} = \frac{N_{\#}^{\alpha_r}(\xi, y)}{N_{\text{max}}^{\alpha_r}}. \quad (3.53)$$

At the end of this step, we have generated  $\xi$  and  $y$  according to a probability distribution

$$\frac{d\Delta_{\alpha_r}^U}{dp_T} = 2\pi N_{\#}^{\alpha_r}(\xi, y) U^{\alpha_r}(\xi, y) \exp \left[ - \int N_{\#}^{\alpha_r}(\xi', y') U^{\alpha_r}(\xi', y') \theta(k_T(\xi', y') - p_T) d\xi' dy' d\phi \right] d\xi dy \quad (3.54)$$

### The matrix-element veto

Finally, we accept events with a probability

$$\mathcal{P}_{\text{surv}} = \frac{\mathcal{J}^{\alpha_r}(\xi, y) \mathcal{R}_{\text{sin}}^{\alpha_r}(\Phi_{n+1})}{\mathcal{B}^{f_{\mathcal{B}}}(\Phi_n) N_{\#}^{\alpha_r}(\xi, y) U^{\alpha_r}(\xi, y)} \quad (3.55)$$

to correct for not using the actual matrix elements in the first place. This step is equivalent to eq. (3.40). Computing the matrix element values is the most time-consuming step, especially for more complicated processes. By postponing it to the very end, we make sure to only spend this time on events that are most likely to survive the whole veto procedure, thus speeding up the entire event generation.

All events surviving this last veto step will have a valid real kinematic and a  $p_T$  distribution according to the non-overestimated Sudakov form factor.

### 3.5.6 The POWHEG veto procedure – massless recoil systems

We can use the procedure described in the previous section for all processes with FSR off massless emitters with one exception. This exception are processes in which the recoil system is massless, i.e.,  $M_{\text{rec}} = 0$  as, in this case, it is possible for the radiation to take the maximal energy, i.e.,  $\xi = 1$  (c.f. eq. (3.48)). We will illuminate this problem as well as its solution on the example of 2-jet production at a lepton collider in this section. In this case, the recoil system is just a single massless quark. The same holds for FSR in e.g.  $pp \rightarrow jj$ .

### The 3-body Jacobian

Tab. 2 shows the FKS table for the process  $e^+e^- \rightarrow q\bar{q}$  restricted to just one quark flavor and NLO QCD corrections. In this case, there are two potential emitters and thus two ALRs in total.

$\alpha_r$	$f_{\mathcal{R}}$	$i_{\mathcal{R}}$	em	$\mathcal{P}_{\text{FKS}}$	$f_{\mathcal{B}}$	$i_{\mathcal{B}}$
1	[11, -11, 1, -1, 21]	1	3	{(3, 5), (4, 5)}	[11, -11, 1, -1]	1
2	[11, -11, 1, -1, 21]	1	4	{(3, 5), (4, 5)}	[11, -11, 1, -1]	1

Tab. 2: FKS table for the process  $e^+e^- \rightarrow d\bar{d}$ . The index  $\alpha_r$  labels the ALRs as described in sec. 2.3.1,  $f_{\mathcal{B}}$  and  $f_{\mathcal{R}}$  are the Born and the real flavor structure labeled by  $i_{\mathcal{B}}$  and  $i_{\mathcal{R}}$ , respectively.  $\mathcal{P}_{\text{FKS}}$  denotes the ALRs set of FKS pairs and the index **em** refers to the real flavor structure defining the emitter relevant in this ALR.

The real correction to  $e^+e^- \rightarrow q\bar{q}$  is a 3-body process. Its phase space is constructed from the 2-body-phase space plus a gluon emission. The two phase-space elements for ALR 1, in which the FKS pair consists of a quark and the radiated gluon, are given by [47]

$$d\Phi_3^1 = \mathcal{J}^1 d\xi dy d\phi d\Phi_2 \quad \text{and} \quad d\Phi_2 = \frac{1}{32\pi^2} d\cos(\theta_1) d\phi_1. \quad (3.56)$$

The analog equations hold for the other FKS region. In this case, as derived in sec. 2.4.1, eq. (2.77), the Jacobian is given by

$$\mathcal{J}^1 = \frac{q^2}{(4\pi)^3} \frac{\xi(1-\xi)}{\left[1 - \frac{\xi}{2}(1-y)\right]^2} . \quad (3.57)$$

From this, we can see that the Jacobian has a divergence for  $(\xi, y) \rightarrow (1, -1)$ . Such a limit corresponds to the configuration in which the emitted gluon takes all the available energy  $E_{\text{rad}} = q^0/2$ . In this scenario, the emitting quark is soft and can thus be collinear to the second quark. Such a configuration is artificial and so the corresponding divergence is integrable, however, not by naive MC techniques. This integrable singularity is only hit because of the simple kinematic construction we chose in the POWHEG matching.

### The UBF for the case of massless recoil systems

To improve the numerical behavior, we can adjust the UBF for  $e^+e^- \rightarrow q\bar{q}$  in order to fulfill the UBF condition eq. (3.30) for all regions of the phase space. Specifically, we add a factor of  $\frac{1}{1+y}$  to the UBF for FSR off massless emitters given in eq. (3.42) to find

$$\boxed{N_{\text{max}}^{\alpha_r} U^{\alpha_r}(\xi, y) = N_{\text{max}}^{\alpha_r} \frac{\alpha_S^{\text{rad}}(p_T)}{\xi(1-y^2)}} , \quad (3.58)$$

which is also singular for  $y \rightarrow -1$ .

Using this UBF, we first want to generate the transverse momentum  $p_T$  according to

$$\Delta_{\alpha_r}^U(p_T) = \exp \left[ - \int N_{\text{max}}^{\alpha_r} U^{\alpha_r}(\xi, y) \theta(k_T(\xi, y) - p_T) d\phi d\xi dy \right] , \quad (3.59)$$

where we choose the scale  $k_T$  to be given by

$$k_T = \frac{q^0}{2} \xi \sqrt{1-y^2} . \quad (3.60)$$

For the integral in the exponent, we find [47]

$$\int \frac{N_{\text{max}}^{\alpha_r} \alpha_S^{\text{rad}}(k_T)}{\xi(1-y^2)} \theta(k_T(\xi, y) - p_T) d\phi d\xi dy = 2\pi N_{\text{max}}^{\alpha_r} \int_{p_T}^{k_{T,\text{max}}} \alpha_S^{\text{rad}}(k_T) \log \left[ \frac{1 + \sqrt{1 - (k_T/k_{T,\text{max}})^2}}{1 - \sqrt{1 - (k_T/k_{T,\text{max}})^2}} \right] \frac{dk_T}{k_T} \quad (3.61)$$

with

$$k_{T,\text{max}} := \max_{\xi, y} (k_T(\xi, y)) = \frac{q^0}{2} \quad (3.62)$$

as the maximum allowed transverse momentum of the radiated gluon in the case of a massless recoil system. To further break this integral down, we again use the veto method by overestimating

$$\log \left[ \frac{1 + \sqrt{1 - (k_T/k_{T,\text{max}})^2}}{1 - \sqrt{1 - (k_T/k_{T,\text{max}})^2}} \right] = \log \left[ \frac{(1 + \sqrt{1 - (k_T/k_{T,\text{max}})^2})^2}{(k_T/k_{T,\text{max}})^2} \right] \leq \log \left[ \frac{4k_{T,\text{max}}^2}{k_T^2} \right] . \quad (3.63)$$

This is effectively another overestimation of the UBF. We rename the UBF to  $\tilde{U}$  from here on to remember this fact. We finally generate  $p_T$  according to

$$\begin{aligned} \Delta_{\alpha_r}^{\tilde{U}}(p_T) &= \exp \left[ -2\pi N_{\max}^{\alpha_r} \int_{p_T}^{k_{T,\max}} \alpha_S^{\text{rad}}(k_T) \log \left[ \frac{4k_{T,\max}^2}{k_T^2} \right] \frac{dk_T}{k_T} \right] \\ &= \exp \left[ -\frac{\pi N_{\max}^{\alpha_r}}{b_0^{\text{rad}}} \left( \log \left[ \frac{4k_{T,\max}^2}{\Lambda_{\text{rad}}^2} \right] \log \left[ \frac{\log(k_{T,\max}^2/\Lambda_{\text{rad}}^2)}{\log(p_T^2/\Lambda_{\text{rad}}^2)} \right] - \log \left[ \frac{k_{T,\max}^2}{p_T^2} \right] \right) \right] . \end{aligned} \quad (3.64)$$

We see that for these logarithms to be well defined, it has to be  $p_{T,\min} > \Lambda_{\text{rad}}$ , which indeed holds for the recommended choice  $\mu_0 = p_{T,\min}$  according to eq. (3.45). Using this UBF we can solve  $\Delta_{\alpha_r}^{\tilde{U}}(p_T) = r$  with uniform  $r \in (0, 1)$  to generate  $p_T$ .

Similar to the massless FSR case, we first perform the veto steps independent of the rest of the kinematics. In addition to the veto step for overestimating  $\alpha_S$ , which is the same as described in sec. 3.5.5, we have to insert a veto step for the overestimation in eq. (3.63). We call this veto step simply *the UBF veto step*. This veto step is survived with a probability

$$\mathcal{P}_{\text{surv}} = \frac{\log \left[ \frac{1 + \sqrt{1 - (k_T/k_{T,\max})^2}}{1 - \sqrt{1 - (k_T/k_{T,\max})^2}} \right]}{\log \left[ \frac{4k_{T,\max}^2}{k_T^2} \right]} . \quad (3.65)$$

Technically, these two vetos are performed in the same step. We keep them separate in the discussion for pedagogical reasons.

### Generating the radiation kinematics

Now knowing  $p_T$  and thus  $\alpha_S^{\text{rad}}(p_T)$ , we can infer from the LHS of eq. (3.61) that the radiation variables should be sampled (c.f. app. B.2) according to

$$\frac{1}{\xi(1-y^2)} \delta(k_T(\xi, y) - p_T) d\phi d\xi dy . \quad (3.66)$$

We use eq. (3.60) to find

$$\xi = \frac{2p_T}{q^0 \sqrt{1-y^2}} \quad (3.67)$$

from integrating in  $\xi$  over the  $\delta$  distribution. In order to fulfill  $\xi \leq 1$  we need to have  $\sqrt{1-y^2} \geq \frac{p_T}{k_{T,\max}}$ .  $\phi$  is unconstrained and will thus be distributed uniformly between 0 and  $2\pi$ . Absorbing the integral over  $y$  in the differential, we see that  $y$  will be distributed with a probability proportional to

$$\theta \left( \sqrt{1-y^2} - \frac{p_T}{k_{T,\max}} \right) d \log \left[ \frac{1+y}{1-y} \right] . \quad (3.68)$$

So to generate  $y$ , we take a random number uniform in the range allowed by the  $\theta$  function

$$-\log \left[ \frac{1 + \sqrt{1 - (p_T/k_{T,\max})^2}}{1 - \sqrt{1 - (p_T/k_{T,\max})^2}} \right] < r_y < \log \left[ \frac{1 + \sqrt{1 - (p_T/k_{T,\max})^2}}{1 - \sqrt{1 - (p_T/k_{T,\max})^2}} \right] \quad (3.69)$$

and solve  $r_y = \log \left[ \frac{1+y}{1-y} \right]$  for  $y$  to get

$$y = \frac{e^{r_y} - 1}{e^{r_y} + 1} . \quad (3.70)$$

Finally, we generate  $\xi(y, p_T)$  according to eq. (3.67) from the now known  $y$  and  $p_T$ .

We note here that the sequence of computing  $y$  and  $\xi$  is different in this case compared to the simple and the massive FSR case. Here, we first compute  $y(r_y, p_T)$  and then  $\xi(y, p_T)$  while in the other cases, we first compute  $\xi(r_\xi, p_T)$  and from this  $y(\xi, p_T)$ .

Once the event kinematic is determined, we proceed with the norm veto and the matrix-element veto as described before for the massless FSR UBF in sec. 3.5.4 to generate a valid  $p_T$  value for the highest-bid algorithm.

### 3.5.7 The POWHEG veto procedure – the massless ISR case

In the case of radiation off the initial state, the real matrix element diverges as  $x \rightarrow 1$  or  $y \rightarrow \pm 1$ . We thus need to use another upper bounding function for ISR than we used for FSR to catch all the divergent regions. In fact, we can use the same UBF that we used for massless recoil systems, as the divergence structures are equivalent. In our notation, however, we change  $\xi \rightarrow 1 - x$  and the definitions of  $k_T$  and  $k_{T,\max}$  have to be adjusted to be clear also in the case when the Born and the real center-of-mass energy differ. This case has first been discussed by Nason and Ridolfi [56] but is also mentioned in later publications by Nason et al. [47, 48]. A simple possible choice is

$$\boxed{N_{\max}^{\alpha_r} U^{\alpha_r}(x, y) = N_{\max}^{\alpha_r} \frac{\alpha_S^{\text{rad}}(k_T)}{(1-x)(1-y^2)}} \quad (3.71)$$

with

$$k_T^2 = \frac{s_{\mathcal{B}}}{4x} (1-x)^2 (1-y^2) \quad . \quad (3.72)$$

Both are equivalent to the case of massless recoil systems in the previous subsection with  $\xi \rightarrow 1 - x$  and  $q^0 = \sqrt{s} \rightarrow \sqrt{s_{\mathcal{R}}} = \sqrt{s_{\mathcal{B}}/x}$  (c.f. eq. (3.58) and eq. (3.60)). We defined  $k_T$  as the transverse momentum w.r.t. to the beam axis here.

The ranges of  $x$  and  $k_T^2$  are chosen so that  $U^{\alpha_r}(x, y)$  covers the relevant range of radiation variables:

$$1 \geq x \geq \rho := \frac{s_{\mathcal{B}}}{S} = x_{\mathcal{B},\oplus} x_{\mathcal{B},\ominus} \quad \text{and} \quad k_T^2 \leq k_{T,\max}^2 := s_{\mathcal{B}} \frac{(1-x_{\mathcal{B},\oplus}^2)(1-x_{\mathcal{B},\ominus}^2)}{(x_{\mathcal{B},\oplus} + x_{\mathcal{B},\ominus})^2} \quad (3.73)$$

where  $\sqrt{S}$  is the hadronic center-of-mass energy. If we retranslate  $x \rightarrow 1 - \xi$ , we see that  $1 - \rho$  serves as an upper limit for  $\xi$ . Intuitively, this is the case because the energy available for the ISR is limited by the difference between the real and the Born center-of-mass energies  $\sqrt{s_{\mathcal{R}}} - \sqrt{s_{\mathcal{B}}}$ , where the former has the hadronic center-of-mass energy as the upper limit. This is a crude overestimation of the kinematically correct  $\xi_{\max}$  we computed in eq. (2.118). We cannot use the actual  $\xi_{\max}$  at this point already as it depends on  $y$ , which we can only generate after we have a value for  $\xi$ . We solve this problem by first using this extended  $\xi_{\max}^{\text{ext}}$  to generate  $\xi$  and  $y$  and later veto those values of  $\xi > \xi_{\max}$  to not generate values of  $\xi$  which lead to  $x_{\mathcal{B},\oplus} > 1$ . We call this veto step the  $\xi_{\max}$  veto step and execute it right after completing the generation of the kinematics.

In order to generate  $p_T$  uniformly in

$$\Delta_{\alpha_r}^U(p_T) = \exp \left[ - \int \frac{N_{\max}^{\alpha_r} \alpha_S^{\text{rad}}(k_T)}{(1-x)(1-y^2)} \theta(k_T(\xi, y) - p_T) d\phi d\xi dy \right] \quad (3.74)$$

we change integration variables from  $y$  to  $k_T$  inverting eq. (3.72) to find

$$|y| = \sqrt{1 - \frac{4x}{(1-x)^2} \frac{k_T^2}{s_B}} \quad \text{and thus} \quad \frac{1}{(1-x)(1-y^2)} \frac{dy}{dk_T^2} dk_T^2 = -\frac{1}{2} \frac{1}{\sqrt{(1-x)^2 - 4x \frac{k_T^2}{s_B}}} \frac{dk_T^2}{k_T^2}. \quad (3.75)$$

At this point, we supply an additional factor of 2 to account for the fact that each value of  $k_T^2$  corresponds to two possible values of  $y$ . We also switch the integration limits to absorb the prefactor and use  $0 \leq \phi < 2\pi$  to arrive at

$$\int \frac{N_{\max}^{\alpha_r} \alpha_S^{\text{rad}}(k_T)}{(1-x)(1-y^2)} \theta(k_T(\xi, y) - p_T) d\phi d\xi dy = 2\pi N_{\max}^{\alpha_r} \int_{\rho}^{x_-} \int_{p_T^2}^{k_{T,\max}^2} \frac{\alpha_S^{\text{rad}}(k_T)}{\sqrt{(x_+ - x)(x_- - x)}} \frac{dk_T^2}{k_T^2} dx, \quad (3.76)$$

where we have defined the zeroes of the denominator to be

$$x_{\pm} := \left( \sqrt{1 + \frac{k_T^2}{s_B}} \pm \frac{k_T}{\sqrt{s_B}} \right)^2. \quad (3.77)$$

We can perform the  $x$  integration using the identities

$$\frac{d}{dx} \sinh^{-1}(x) = \frac{1}{\sqrt{x^2 + 1}} \quad \text{and} \quad \sinh^{-1}(x) = \log\left(\sqrt{1 + x^2} + x\right) \quad (3.78)$$

for the hyperbolic sine to continue to

$$= 2\pi N_{\max}^{\alpha_r} \int_{p_T^2}^{k_{T,\max}^2} \alpha_S^{\text{rad}}(k_T) \log \left[ \frac{\sqrt{x_+ - \rho} + \sqrt{x_- - \rho}}{\sqrt{x_+ - \rho} - \sqrt{x_- - \rho}} \right] \frac{dk_T^2}{k_T^2}. \quad (3.79)$$

In order to simplify this integral, we overestimate the integrand similar to what we did to solve the integral of the UBF for massless recoil systems in eq. (3.63) using

$$\log \left[ \frac{\sqrt{x_+ - \rho} + \sqrt{x_- - \rho}}{\sqrt{x_+ - \rho} - \sqrt{x_- - \rho}} \right] \leq \log \left[ \frac{\sqrt{x_+} + \sqrt{x_-}}{\sqrt{x_+} - \sqrt{x_-}} \right] \leq \frac{1}{2} \log \left[ \frac{k_T^2 + s_B}{k_T^2} \right] \leq \frac{1}{2} \log \left[ \frac{k_{T,\max}^2 + s_B}{k_T^2} \right]. \quad (3.80)$$

This again necessitates an *UBF veto step* after generating  $p_T$ . Now using the additionally overestimated UBF  $\tilde{U}$ , we can finally generate  $p_T^2$  using the Sudakov factor

$$\Delta_{\alpha_r}^{\tilde{U}}(p_T) = \exp \left( -\frac{\pi N_{\max}^{\alpha_r}}{b_0^{\text{rad}}} \left[ \log \left[ \frac{k_{T,\max}^2 + s_B}{\Lambda^2} \right] \log \left[ \frac{\log(k_{T,\max}^2/\Lambda^2)}{\log(p_T^2/\Lambda^2)} \right] - \log \left[ \frac{k_{T,\max}^2}{p_T^2} \right] \right] \right). \quad (3.81)$$

As an alternative variant [48], it is possible to continue the overestimation in eq. (3.80) dividing it into cases as

$$\frac{1}{2} \log \left[ \frac{k_{T,\max}^2 + s_B}{k_T^2} \right] \leq \frac{1}{2} \begin{cases} \log \left[ \frac{2s_B}{k_T^2} \right] & \text{for } k_T^2 < s_B \\ \log(2) & \text{for } k_T^2 \geq s_B \end{cases}. \quad (3.82)$$

Using this overestimation, we arrive at the more complicated form of the Sudakov form factor

$$\log(\Delta_{\alpha_r}^{\tilde{U}}(p_T)) = -\frac{\pi N_{\max}^{\alpha_r}}{b_0^{\text{rad}}} \begin{cases} \log\left[\frac{2s_{\mathcal{B}}}{\Lambda_{\text{rad}}^2}\right] \log\left[\frac{\log(s_{\mathcal{B}}/\Lambda_{\text{rad}}^2)}{\log(p_T^2/\Lambda_{\text{rad}}^2)}\right] - \log\left[\frac{s_{\mathcal{B}}}{p_T^2}\right] + \log(2) \log\left[\frac{\log(k_{T,\max}^2/\Lambda_{\text{rad}}^2)}{\log(s_{\mathcal{B}}/\Lambda_{\text{rad}}^2)}\right] & \text{for } p_T^2 < s_{\mathcal{B}} < k_{T,\max}^2 \\ \log\left[\frac{2s_{\mathcal{B}}}{\Lambda_{\text{rad}}^2}\right] \log\left[\frac{\log(k_{T,\max}^2/\Lambda_{\text{rad}}^2)}{\log(p_T^2/\Lambda_{\text{rad}}^2)}\right] - \log\left[\frac{k_{T,\max}^2}{p_T^2}\right] & \text{for } p_T^2 < k_{T,\max}^2 \leq s_{\mathcal{B}} \\ \log(2) \log\left[\frac{\log(k_{T,\max}^2/\Lambda_{\text{rad}}^2)}{\log(p_T^2/\Lambda_{\text{rad}}^2)}\right] & \text{for } p_T^2 \geq s_{\mathcal{B}} \end{cases} . \quad (3.83)$$

Both variants are implemented and can be used in WHIZARD. This one here is used by default. We have validated that both lead to statistically equivalent results.

We still need to generate the rest of the event kinematics, starting by generating  $x(p_T, r_x)$ . There are two possible ways to achieve this: inverse transform sampling (ITS) (c.f. app. B.2) and rejection sampling (RS) (c.f. app. B.3).

### Generating the radiation kinematics via inverse transform sampling

According to eq. (3.76), we want to generate  $x$  with unnormalized probability density function

$$f(x) = \frac{1}{\sqrt{(x_+ - x)(x_- - x)}} \quad \text{with } \rho \leq x \leq x_- . \quad (3.84)$$

Using eq. (3.78) again, we find for the distribution function

$$F(x) = \int f(x) dx = \int \frac{1}{\sqrt{(x_+ - x)(x_- - x)}} dx = 2 \sinh^{-1} \left( \sqrt{\frac{x_- - x}{x_+ - x_-}} \right) = 2 \cosh^{-1} \left( \sqrt{\frac{x_+ - x}{x_+ - x_-}} \right), \quad (3.85)$$

where in the last step we also used  $\sinh^{-1}(x) = \text{sgn}(x) \cosh^{-1}(\sqrt{x^2 + 1})$ . Inverting this we find that in order to generate  $x$  uniform in  $F(x)$ , we need to generate

$$x = x_- - (x_+ - x_-) \sinh^2(r_x/2) = x_- - (x_+ - x_-) \left[ \frac{1}{2} \left( e^{r_x/2} - e^{-r_x/2} \right) \right]^2, \quad (3.86)$$

with  $r_x \in \text{Unif}[F(x_-), F(\rho)] = \text{Unif}\left[0, 2 \sinh^{-1} \left( \sqrt{\frac{x_- - \rho}{x_+ - x_-}} \right)\right]$  and  $\text{Unif}[a, b]$  denotes the set of uniform random numbers between  $a$  and  $b$ .

### Generating the radiation kinematics via rejection sampling

Alternatively, it is possible to avoid solving the integral explicitly by using rejection sampling. To see this, we substitute

$$\chi := \sqrt{x_- - x} \Leftrightarrow x = x_- - \chi^2 \quad \text{and} \quad dx = -2\sqrt{x_- - x} d\chi \quad (3.87)$$

to find

$$\int_{\rho}^{x_-} \frac{dx}{\sqrt{(x_+ - x)(x_- - x)}} = 2 \int_0^{\sqrt{x_- - \rho}} \frac{d\chi}{\sqrt{x_+ - x(\chi)}} . \quad (3.88)$$

We could now straightforwardly solve this integral, but instead, we crudely overestimate the integrand with a constant:

$$\frac{1}{\sqrt{x_+ - x}} \leq \frac{1}{\sqrt{x_+ - x_-}} \quad (3.89)$$

to get

$$2 \int_0^{\sqrt{x_- - \rho}} \frac{d\chi}{\sqrt{x_+ - x(\chi)}} \leq \frac{2}{\sqrt{x_+ - x_-}} \int_0^{\sqrt{x_- - \rho}} d\chi \quad . \quad (3.90)$$

In this case, the probability density function is constant, so the Cumulative Distribution Function (CDF) is an identity

$$f(\chi) = 1 \implies F(\chi) = \chi \Leftrightarrow F^{-1}(\chi) = \chi \quad (3.91)$$

We thus generate  $\chi \in \text{Unif}[0, \sqrt{x_- - \rho}]$ , from which we infer

$$x = x_- - (x_- - \rho) \cdot r_x^2 \quad (3.92)$$

with  $r_x \in \text{Unif}[0, 1]$ . Having generated  $x$  we correct for the overestimation of eq. (3.89) by keeping values only with a probability

$$\mathcal{P}_{\text{surv}} = \frac{\frac{1}{\sqrt{x_+ - x}}}{\frac{1}{\sqrt{x_+ - x_-}}} = \sqrt{\frac{x_+ - x_-}{x_+ - x}} \quad . \quad (3.93)$$

Both variants are implemented in WHIZARD. Fig. 3.6 exemplary shows the probability densities of the sampled  $x$  distributions in both cases for the Drell-Yan process. These values are sampled in an intermediate step of the veto procedure. Thus, they do not represent a physically interpretable distribution yet. Also, the functional form does not exactly follow eq. (3.84), as  $x_+$  and  $x_-$  depend on the  $p_T$  value sampled in the step before. Nevertheless, we can see that both ways of sampling  $x$  yield the same distributions. Additionally, we checked that computational effort of both methods shows no significant difference. The solution using ITS is used by default.

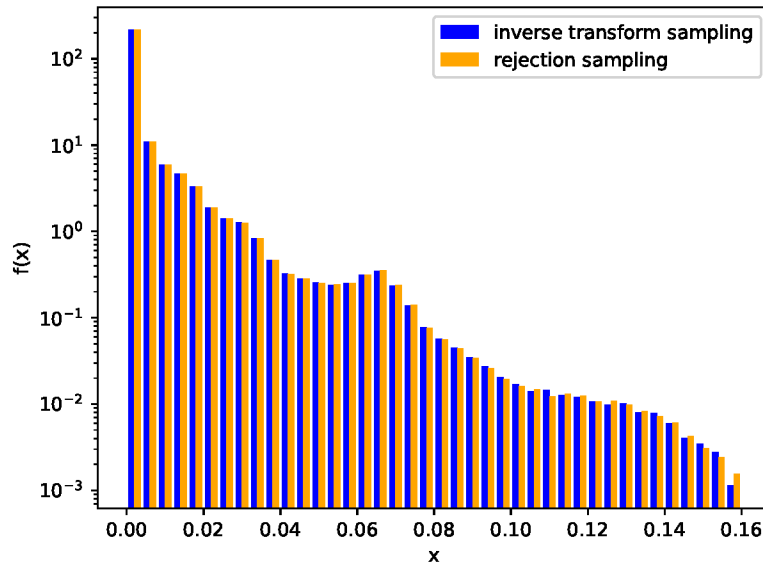


Fig. 3.6: Probability density of  $x$  values sampled using ITS (blue) and RS (orange). 12M  $x$  values have been sampled with each of both methods, while generating POWHEG events for the Drell-Yan process,  $pp \rightarrow e^+e^-$ .

Having generated  $p_T$  and  $x$ , we can compute  $y(p_T, x)$  according to eq. (3.75). We then determine the sign randomly with equal probability as there is no preferred direction for ISR.

To complete the corresponding kinematics, we generate  $\phi$  as always such that it is uniform in  $(0, 2\pi)$ .

### 3.5.8 The POWHEG veto procedure – the massive FSR case

We also need to reconsider our choice of UBF in the case of real emissions off massive partons in the final state as the divergence structure of  $\mathcal{R}/\mathcal{B}$  is different from the case of emissions off massless partons. As was first explained in app. A.3 of ref. [77], we can best see this by using an eikonal approximation to the real amplitude  $A_{\mathcal{R}}$ .

$$A_{\mathcal{R}}^{\mu} = A_{\mathcal{B}} \left( \frac{p^{\mu}}{p \cdot k} - \frac{r^{\mu}}{r \cdot k} + \dots \right). \quad (3.94)$$

To simplify the notation in this context, we use  $p \leftarrow k_{n+2}$  and  $k \leftarrow k_{n+3}$  for the momenta of the emitting and the radiated parton, respectively.  $r$  denotes another massive momentum, e.g., the anti-top in  $pp \rightarrow t\bar{t}$ . For the squared amplitude, we thus get

$$A_{\mathcal{R}}^2 = A_{\mathcal{B}}^2 \left( -\frac{m^2}{(p \cdot k)^2} + \frac{2p \cdot r}{(p \cdot k)(r \cdot k)} + \dots \right). \quad (3.95)$$

by squaring eq. (3.94) and taking into account a  $-g_{\mu\nu}$  from the spin projection. We know that the total squared amplitude must be positive, so the first negative term quadratic in  $m$  cannot dominate. We approximate the second term in the case of  $\vec{p}$  collinear to  $\vec{k}$  by

$$\frac{p \cdot r}{(p \cdot k)(k \cdot r)} \approx \frac{1}{p \cdot k} \frac{p^0}{k^0} \sim \frac{1}{p \cdot k} \frac{q}{2k^0} = \frac{1}{\xi^2 q^2 (1-z)} \quad (3.96)$$

where  $z$  is defined as the slope of the Dalitz plot, c.f. eq. (2.81) in sec. 2.4.2. We do not need to care about constant factors as the UBF will be normalized later anyways. In the last step, we used the energy conservation, eq. (2.44), and the Dalitz parametrization, eq. (2.81), to find

$$p \cdot k = q(\bar{k}_{\text{rec}} - k_{\text{rec}}) = q^0(\bar{E}_{\text{rec}} - E_{\text{rec}}) = q^0((q^0 - \bar{E}_{n+2}) - (q^0 - E_{n+2} - E_{n+3})) = q^0 E_{n+3}(1-z) = \xi \frac{q^2}{2}(1-z) \quad (3.97)$$

To take the phase space into account, we remember the real Jacobian for massive final-state emitter from eq. (2.70)

$$\mathcal{J}_{\mathcal{R}, \text{massive}} = \frac{q^2}{(2\pi)^3} \frac{k^0}{4|\vec{p}_{\mathcal{B}}|} \quad (3.98)$$

Furthermore we observe that by definition of  $\xi$  (c.f. eq. (2.18))

$$k^0 = \frac{\xi q}{2} < \xi q \quad (3.99)$$

So we can substitute  $k^0 \rightarrow \xi q$  in the UBF and we still contain the whole relevant phase-space region.

Putting this together with eq. (3.96) and eq. (3.98), we find a suitable UBF in the case of a massive emitter to be

$$\boxed{N_{\text{max}}^{\alpha_r} U^{\alpha_r}(\xi, z) = N_{\text{max}}^{\alpha_r} \frac{q}{|\vec{p}_{\mathcal{B}}|} \frac{1}{\xi(1-z)}} \quad (3.100)$$

To proceed with the generation of radiation from this UBF, we need an appropriate scale choice for the massive case. As stated in ref. [77], an appropriate choice is

$$k_T^2 = \frac{\xi^2 q^3 (1-z)}{2p_{\mathcal{B}}^0 - z\xi q} \quad (3.101)$$

In contrast to all the other UBFs, the UBF for massive emitters is not proportional to the strong coupling

constant  $\alpha_S$ . This is not necessary because with the scale choice of eq. (3.101)  $\alpha_S$  only diverges for  $\xi \rightarrow 0$ , which the UBF of eq. (3.100) already accounts for. Further divergent regions for, e.g.,  $z \rightarrow 1$  are excluded by non-zero masses in the scale choice.

When integrating this UBF for the Sudakov according to eq. (3.32), we have to solve the integral

$$-\frac{1}{N_{\max}^{\alpha_r}} \log(\Delta_{\alpha_r}^U(p_T)) = \int_0^{2\pi} \int_0^{\xi_{\max}^{\text{ext}}} \int_{z_1}^{z_2} \frac{q}{|\vec{p}_B|} \frac{1}{\xi(1-z)} \theta(k_T(\Phi_{n+1}) - p_T) dz d\xi d\phi \quad . \quad (3.102)$$

Its solution is given by [77]

$$\begin{aligned} -\frac{1}{N_{\max}^{\alpha_r}} \log(\Delta_{\alpha_r}^U(p_T)) &= 2\pi \frac{q}{|\vec{p}_B|} \left[ \log(\xi) \log \left[ (1-z_2) \frac{q}{p_T^2} \right] + \frac{1}{2} \log^2(\xi) + G(-t, q^2, \xi) - G(2|\vec{p}_B|^0, -q, \xi) \right]_{\xi_{\min}(p_T^2)}^{\xi_{\max}(p_T^2)} \\ &+ \frac{q}{|\vec{p}_B|} \theta(\xi_{\max}^{\text{ext}} - \xi_1(p_T^2)) \log \left[ \frac{\xi_{\max}^{\text{ext}}}{\xi_1(p_T^2)} \right] \log \left[ \frac{1-z_2}{1-z_1} \right] \quad , \end{aligned} \quad (3.103)$$

where  $\xi_{\min}$  is the minimal value of  $\xi$  at given  $k_T$

$$\xi_{\min}(k_T^2) := \frac{\sqrt{k_T^2(k_T^2 z_2^2 + 8p_B^0 q(1-z_2))} - k_T^2 z_2}{2q^2(1-z_2)} \quad (3.104)$$

It is derived by solving eq. (3.101) for  $\xi$ , finding that it is a monotonous function of  $z$  and thus using the lower value of  $z$ ,  $z_2$ , which we derived in eq. (2.88). Similarly, we define

$$\xi_{\text{m}}(p_T^2) := \min\left(\xi_1(p_T^2), \xi_{\max}^{\text{ext}}\right) \quad , \quad (3.105)$$

where

$$\xi_1(k_T^2) := \frac{\sqrt{k_T^2(k_T^2 z_1^2 + 8p_B^0 q(1-z_1))} - k_T^2 z_1}{2q^2(1-z_1)} \quad (3.106)$$

as the potential maximum value for  $\xi$  we get from this consideration. Similar to the case of ISR, the actual  $\xi_{\max}$  explicitly depends on  $z$  (c.f. eq. (2.87)) so we cannot determine it prior to generating the kinematics. Instead, we use an extended version

$$\xi_{\max}^{\text{ext}} := 1 - \frac{(m_{\text{em}} + M_{\text{rec}})^2}{q^2} \quad (3.107)$$

in the Sudakov factor and add an additional veto step vetoing events with  $\xi > \xi_{\max}$  to compensate this.

The function  $G$  denotes the primitive of a logarithm defined as

$$G(a, b, \xi) := \int \log(a + b\xi) \frac{d\xi}{\xi} = \begin{cases} \log(a + b\xi) \log\left(1 - \frac{a+b\xi}{a}\right) + \text{Li}_2\left(\frac{a+b\xi}{a}\right) & \text{for } a < 0 \\ \log\left|\frac{b\xi}{a}\right| \log(a) - \text{Li}_2\left(-\frac{b\xi}{a}\right) + \frac{\pi^2}{6} & \text{for } a > 0 \end{cases} \quad (3.108)$$

From the initial integral, eq. (3.102), and the definition of  $k_T$ , we can see that  $\xi$  and  $z$  will be distributed according to

$$\delta\left(\frac{\xi^2 q^3 (1-z)}{2p_B^0 - z\xi q} - p_T^2\right) \frac{d\xi dz}{\xi(1-z)} = \frac{q^2}{p_T^2(\xi q^2 - p_T^2)} d\xi \quad (3.109)$$

where we performed the integration over  $z$ .

So we first generate  $\xi$  uniformly in  $\log(\xi q^2 - p_T^2)$  between  $\xi_{\min}$  and  $\xi_m$

$$\xi = \frac{1}{q^2} \left\{ \exp \left[ \log \left[ q^2 \xi_{\min}(p_T^2) - p_T^2 \right] + r \log \left[ \frac{q^2 \xi_m(p_T^2) - p_T^2}{q^2 \xi_{\min}(p_T^2) - p_T^2} \right] \right] + p_T^2 \right\} \quad (3.110)$$

and then solve the  $\delta$  distribution for  $z$  to find

$$z = \frac{2 p_B^0 p_T^2 - \xi^2 q^3}{\xi q p_T^2 - \xi^2 q^3} \quad . \quad (3.111)$$

Afterwards, we generate  $\phi$  as usual, concluding the generation of the radiation kinematics.

### 3.5.9 The POWHEG veto steps – summary

When generating POWHEG events, we frequently use the veto technique to speed up the event generation. In the previous subsections, we discussed several different cases of UBFs, each requiring potentially different veto steps. For the highest-bid algorithm, we need to generate the radiation kinematics for all possible emitters. Therefore, all cases need to be implemented to be able to deal with different kinds of emitters, possibly even in the same elementary process.

We summarize all the veto steps we perform during the event generation in this section. Veto steps that do not apply to a certain UBF choice will just always be passed.

1. The *UBF veto* corrects for an overestimation of the integrand when computing  $-\frac{1}{N_{\max}^{\alpha_r}} \log(\Delta_{\alpha_r}^{\tilde{U}}(p_T))$ . It is necessary only in the case of ISR or a massless recoil system.
2. The  $\alpha_S$  veto corrects for an overestimation of  $\alpha_S$  with  $\alpha_S^{\text{rad}}$  so the survival probability of this step is given by

$$\mathcal{P}_{\text{surv}} = \frac{\alpha_S(p_T)}{\alpha_S^{\text{rad}}(p_T)} \quad . \quad (3.112)$$

It is executed for all kinds of UBFs except for the one for massive emitters. More details have been given in sec. 3.5.5.

3. The  $\xi_{\max}$  veto corrects for using an extended region for  $\xi_{\max}$ ,  $\xi_{\max}^{\text{ext}}$ , when generating the transverse momentum from the Sudakov form factor to be able to do this prior to having generated  $y$  or  $z$ . This veto step is not probability based. We veto if the generated value of  $\xi$  exceeds the allowed range, i.e., if  $\xi > \xi_{\max}$ . It is only non-trivial in the case of an ISR emitter or a massive FSR emitter.
4. The *Norm veto* corrects for using just the global maximum of the POWHEG grid when first generating  $p_T$  from the Sudakov. So the survival probability associated with this veto step is

$$\mathcal{P}_{\text{surv}} = N_{\#}^{\alpha_r}(\xi, y) / N_{\max}^{\alpha_r} \quad . \quad (3.113)$$

This is discussed in detail in sec. 3.5.4.

5. The *matrix-element veto* is the most time-consuming veto step as it requires computing both the Born and the real matrix element. This is intentionally the last veto step and thus the least often executed one. It corrects for using the POWHEG grid values instead of the matrix element values in the Sudakov when first generating  $p_T$ . Thus, the survival probability is given by

$$\mathcal{P}_{\text{surv}} = \frac{\mathcal{R}(\xi, y) \cdot \mathcal{J}(\xi, y)}{\mathcal{B} \cdot U(\xi, y)} / N_{\#}^{\alpha_r}(\xi, y) \quad . \quad (3.114)$$

If any of these veto steps fails, we set  $p_{T,\max} = p_T$ , generate a new value  $p_T$ , which now has to be smaller than before and repeat the veto procedure.

The flow chart in fig. 3.7 diagrammatically depicts this sequential veto procedure. It includes all potential veto steps; the optional ones are drawn dashed. In comparison to fig. 3.4, it shows more detail on the veto steps but is reduced to a single ALR.

Additional figures and tables illustrating the veto procedure with an emphasis on the technical point of view are gathered in app. C.

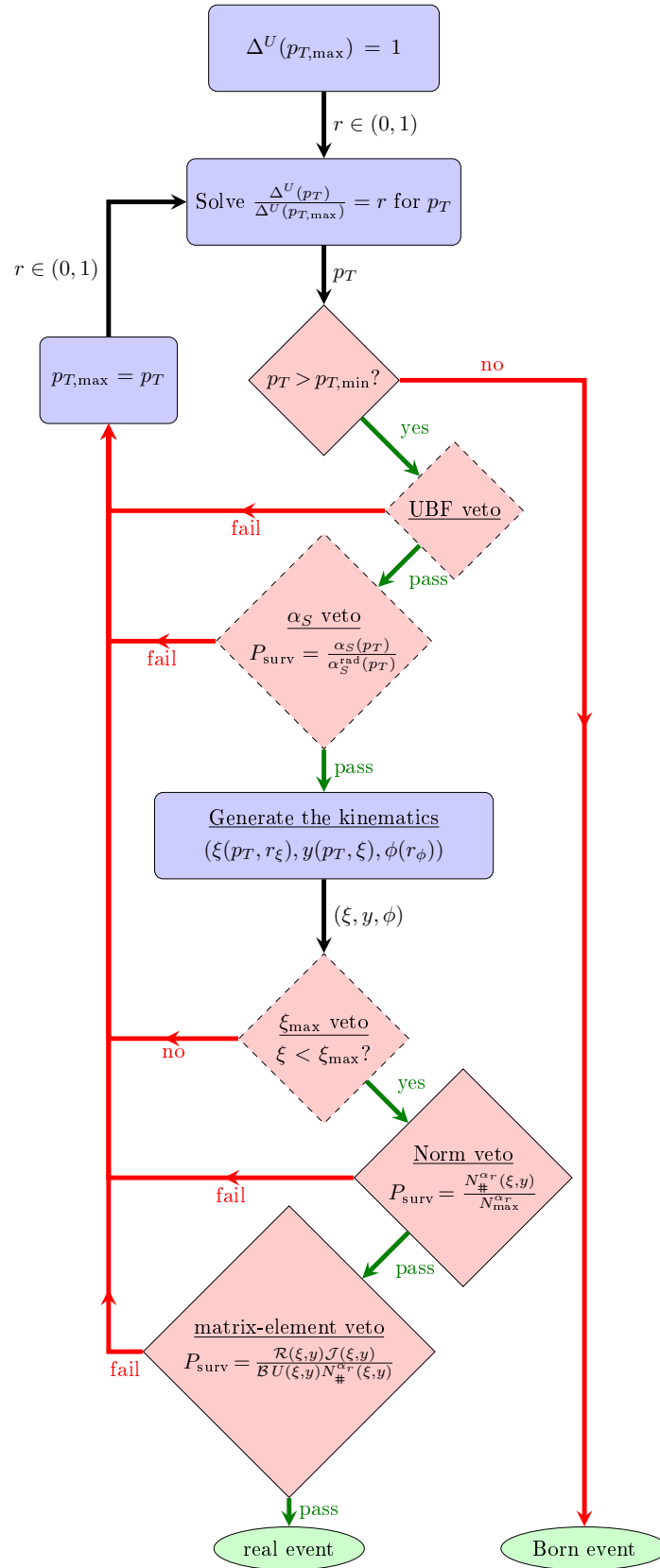


Fig. 3.7: Flow chart of the POWHEG veto procedure showing all potential veto steps. Adapted from ref. [72], fig. E.1. Decisions are depicted in red rhombi, settings and calculations in blue blocks and results in green ellipses. Optional steps are drawn dashed.

### 3.6 Refinements and optimizations

In this section, we will discuss a list of refinements and optimizations to improve both the accuracy of the results as well as their performance. Some general improvements are already implemented in WHIZARD; other suggestions should be investigated in the future.

#### 3.6.1 Performance optimizations in the Sudakov factorization

In sec. 3.5.2, we stated that the Sudakov form factor factorizes into a product over ALRs. We used this fact to perform the veto procedure only once for each ALR and employed the highest-bid algorithm to pick the ALR with the highest generated transverse momentum. As already mentioned in ref. [48], it may be more efficient to group ALRs sharing the same radiation kinematics to reduce the number of transverse momenta to be generated. So instead of splitting the Sudakov form factor into a product over ALRs, we can split it into a product over kinematically different radiation regions. Each radiation region, labeled by  $rr$ , then combines all ALRs that share the same kinematics<sup>17</sup>. E.g., the kinematics for initial-state radiation is the same for Emitters 0, 1 and 2 as the emission angle does not depend on the emitter in the case of ISR. So to reduce the number of Sudakov form factors we can as well write

$$\Delta^{f_{\mathcal{B}}}(p_T) = \prod_{rr \in \{rr|f_{\mathcal{B}}\}} \Delta_{rr}^{f_{\mathcal{B}}}(p_T) \quad (3.115)$$

with

$$\Delta_{rr}^{f_{\mathcal{B}}}(p_T) = \exp \left\{ - \sum_{\alpha_r \in \{\alpha_r|f_{\mathcal{B}},rr\}} \left[ \int d\Phi_{\text{rad}} \frac{\mathcal{R}_{\text{sin}}(\Phi_{n+1})}{\mathcal{B}_{f_{\mathcal{B}}}(\Phi_n)} \theta(k_T(\Phi_{n+1}) - p_T) \right]_{\alpha_r}^{\bar{\Phi}_n^{\alpha_r} = \Phi_n} \right\}, \quad (3.116)$$

where the sum runs over all ALRs that share the same Born flavor structure  $f_{\mathcal{B}}$  and radiation region  $rr$ . In the summands in the exponent, only the real matrix element depends on the ALR. We can thus simplify the expression by summing up all real matrix elements that share the same Born flavor structure and radiation region in the definition

$$\mathcal{R}_{\text{sin}}^{f_{\mathcal{B}},rr}(\Phi_{n+1}) := \sum_{\alpha_r \in \{\alpha_r|rr,f_{\mathcal{B}}\}} \mathcal{R}_{\text{sin}}^{\alpha_r}(\Phi_{n+1}) \quad . \quad (3.117)$$

We then find as the expression for the Sudakov form factors we need to compute per radiation region

$$\Delta_{rr}^{f_{\mathcal{B}}}(p_T) = \exp \left\{ - \left[ \int d\Phi_{\text{rad}} \frac{\mathcal{R}_{\text{sin}}^{f_{\mathcal{B}},rr}(\Phi_{n+1})}{\mathcal{B}_{f_{\mathcal{B}}}(\Phi_n)} \theta(k_T(\Phi_{n+1}) - p_T) \right]_{\alpha_r}^{\bar{\Phi}_n^{\alpha_r} = \Phi_n} \right\} \quad . \quad (3.118)$$

To solve the ambiguity we created when grouping ALRs, we can then select one ALR of all ALRs sharing the same radiation region and Born flavor structure with a probability proportional to the corresponding matrix element value  $\mathcal{R}_{\text{sin}}^{\alpha_r}$ . This effectively determines the real flavor structure.

While this optimization is promising for processes where a large fraction of the ALRs share the same kinematics, i.e., processes in which ALRs featuring ISR dominate, we have already seen in our discussion of the POWHEG grids in sec. 3.5.4 that even though all ALRs in the example process  $d\bar{d} \rightarrow e^+e^-$  share the same ISR kinematic, the POWHEG grids are different. Grouping them, we would have to fill a single POWHEG grid for the sum of the three ALRs. The adaption of the generated grid to the actual matrix-element behavior would thus be less efficient, decreasing the performance again. Additionally, the optimized version of the

<sup>17</sup>In WHIZARD, they are labeled by `i_phs`, an index for different phase spaces.

highest-bid algorithm we depicted in fig. 3.4 already increases the performance of the highest-bid algorithm employed. For these reasons, we refrained from implementing the alternative version of the highest-bid algorithm factorized over radiation regions explained in this section. It is a potential future project.

### 3.6.2 Optimizations of the Sudakov competition in the highest-bid algorithm

In sec. 3.5.3, we presented the highest-bid algorithm in its traditional, parallelizable form and in addition, we showed a slightly optimized version. The task of sampling emission scales from a given Sudakov form factor using the veto procedure is very common in the context of parton showers. Often, the veto procedure is performed in multiple competing emission channels, in our case, the ALRs. In the end, only one channel will be selected, winning the competition.

The traditional algorithm is referred to as *the competition algorithm* in the literature [98, 120], due to its common application or as *Veto-Max* algorithm, emphasizing that in this version, the veto procedures are performed first for each competing channel, selecting the maximum afterwards. It often includes the optimization we depicted in fig. 3.4.

As investigated in ref. [121], more efficient algorithms can be designed, still generating the same distributions. More specifically, the authors suggest to use an algorithm they call the *Generate-Select* algorithm or a slightly modified variant, the *Select-Generate* algorithm. These algorithms first use universal, overestimated scales, selecting the channel using roulette-wheel selection [122] afterwards. In the former, the actual scales are generated before the channel selection, while the latter eliminates the scale dependence of the channel-selection probabilities to be able to generate the scales only after the channel selection.

It would be interesting to study the application of these improved algorithms in the POWHEG-matching procedure in a future project.

### 3.6.3 Born zeroes

In this subsection, we want to elaborate on a problem we have ignored so far. It is also discussed in, e.g., sec. 3.3 of ref. [86]. In the exponent of the Sudakov form factor, e.g., eq. (3.9), we compute the ratio of matrix elements  $\mathcal{R}/\mathcal{B}$ . For many processes, there are phase-space regions in which the Born contribution becomes very small. If this happens, very large ratios occur in the Sudakov exponent. This makes it very hard to determine a reasonable upper bound and moreover, large upper bounding functions render the veto procedure inefficient.

One practical illustrative example is the case of  $W^+$  production depicted diagrammatically in fig. 3.8, including the spin orientations of the particles. Its angular distribution follows  $|M|^2 \sim (1 - \cos(\theta_l))^2$ . The configuration in which the antilepton becomes parallel to the incoming quark, i.e.,  $\theta_l \rightarrow 0$ , is helicity suppressed as the fully parallel configuration would require a spin-flip. The real correction, even to this underlying Born configuration, can very well be non-zero as a hard initial-state emission changes this picture.

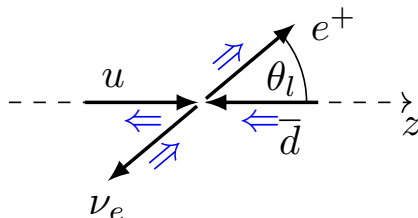


Fig. 3.8: Diagram of the spin configuration in  $u\bar{d} \rightarrow W^+ \rightarrow e^+\nu_e$ . Particle directions are depicted with black arrows and their spin orientation with blue arrows.

The solution to this problem has already been mentioned in sec. 2.6.3. We can overcome this problem by separating the finite part of the real cross section  $\mathcal{R}_{\text{fin}}$  from the singular part  $\mathcal{R}_{\text{sin}}$  and only use the singular part for the ratio in the Sudakov factor. The phase-space configurations in which the real cross section becomes singular are exactly the ones in which the real momenta become Born-like. It follows that the singular real contribution vanishes just as the Born contribution in the problematic PSPs, keeping the ratio of both finite.

Which part of the real cross section enters the POWHEG-matching algorithm in the form of  $\mathcal{R}_{\text{sin}}$  does not affect the cross section of fNLO events but will have an impact on the matched events. The freedom associated with the scale choice dividing both real contributions can be seen as a theoretical uncertainty of the matching scheme.

### 3.6.4 The POWHEG damping factor

In the previous sec. 3.6.3, we solved the problem of the fraction  $\mathcal{R}/\mathcal{B}$  in the Sudakov exponent becoming large. The opposite behavior can be problematic as well. Suppose that in some region of the phase space, the Born matrix element becomes very large, e.g., due to some resonance. According to the requirements we set on the phase-space restrictions in sec. 2.5, it may not diverge, however. Due to the large denominator in the fraction of matrix elements, real radiation would be suppressed in these regions. Although this effect is formerly of higher order, it may still have sizeable effects and is thus worth treating.

The POWHEG-BOX introduces an additional real-partition function to remedy this problem. It is given by

$$F_{\text{damp}}(\Phi_{n+1}) = \frac{h_{\text{damp}}^2}{h_{\text{damp}}^2 + p_T^2} \quad (3.119)$$

and is applied to split the real matrix element according to eq. (2.157f). This introduces another parameter,  $h_{\text{damp}}$ , which can be used to control the strength of the partition. In total, the real-partition function,  $F(\Phi_{n+1})$ , is then given by the product of two functions,

$$F(\Phi_{n+1}) = F_{\text{damp}}(\Phi_{n+1}) \cdot F_{\text{bornzero}}(\Phi_{n+1}) \quad . \quad (3.120)$$

Here, we relabeled the real-partition function we previously referred to as just  $F(\Phi_{n+1})$  as  $F_{\text{bornzero}}(\Phi_{n+1})$ , following the notation of ref. [123] and stressing the fact that it was introduced to remedy the problem of Born zeroes discussed in sec. 3.6.3. In the POWHEG-BOX,  $F_{\text{bornzero}}(\Phi_{n+1})$  is given by eq. (2.163).

In this way,  $F_{\text{damp}}(\Phi_{n+1})$  becomes small for hard emissions, enhancing the finite real contribution. As events resembling the finite real contribution are simulated separately from the POWHEG matching, it is guaranteed that hard emissions can still be generated, even in phase-space regions where  $\mathcal{B}$  takes large values.

In WHIZARD, the implementation of  $F(\Phi_{n+1})$  according to eq. (2.161) performs similar to  $F_{\text{damp}}(\Phi_{n+1})$  in the sense that  $F(\Phi_{n+1}) = 1$  for soft or collinear emissions, i.e., emissions with low transverse momentum. The additional real-partition function  $F_{\text{damp}}(\Phi_{n+1})$  thus did not need to be implemented so far. It could, however, be added to ease technical comparisons with the POWHEG-BOX. In the current state, the parameters  $h_F$  in WHIZARD and  $h_{\text{damp}}$  in the POWHEG-BOX are not directly comparable.

### 3.6.5 Scale choice for the events

During the integration step, the user can set a single `scale` to be used for  $\alpha_S$  and the PDFs in the input file steering the computation. Alternatively, the `factorization_scale` and the `renormalization_scale` can be set separately to any value determined on an event-by-event basis.

When generating events, this scale choice can be optimized. To compute the event weights, we use the same scale definition as in the integration step to not alter the total cross section. In the Sudakov exponent, however, we can improve the accuracy by choosing a different scale. As shown in refs. [47, 56], we can even improve the accuracy of the first emission up to next-to-leading logarithmic (NLL) accuracy by choosing all scales in the Sudakov exponent such that they are at the order of  $p_T$  in the soft or the collinear limit and equal to  $p_T$  in the soft-collinear limit. This scale can but does not have to coincide with the physical transverse momentum itself. In the sections discussing the different UBF types, we have typically denoted this scale as  $k_T$ .

There is one more scale to be determined for the POWHEG events. It is the **SCALUP** variable of the LHIUP [54, 55], the event format typically used to communicate the event properties to the SMC. For the SMC, this scale determines the scale of the hardest emissions generated by the parton shower. As discussed in the beginning of this section, in sec. 3.3, this scale should be the transverse momentum  $p_T$  of the generated emission for  $p_T$ -ordered parton showers in order to avoid double counting.

While it is straightforward to set the **SCALUP** variable to the  $p_T$  of the generated emission for the events generated with the POWHEG veto procedure, the definition of the scale is not so clear for the events generated for the finite real contribution (c.f. sec. 3.5.2), as there is no notion of the "emitting" or the "radiated" parton here. In this case, we set the **SCALUP** variable to the lowest transverse momentum of any of the jets w.r.t. the beam axis. It may be possible to improve the behavior of the parton shower by further optimizing this scale choice, e.g., by letting the user choose a process-specific scale definition to be used for the **SCALUP** variable in this case.

### 3.6.6 Improving the NLL accuracy of $\alpha_S$

As initially stated in sec. 3.3, the accuracy we aimed to achieve with the POWHEG method is to reach NLO accuracy for hard and IR safe observables and LL accuracy for the behavior at small  $p_T$ . These requirements are accomplished with the POWHEG method discussed so far, but we can do even better.

In the hard regime, we are limited to NLO accuracy due to the matrix elements in the Sudakov exponent. In the soft regime, we are eventually limited by the properties of the applied SMC. However, we have control over the first emission. As explained in sec. 4.4 of ref. [47] building on Sudakov resummation techniques, specifically ref. [124], it is possible to increase the logarithmic accuracy of the first emission to NLL with a few minor adjustments. In fact, by replacing the strong coupling constant

$$\alpha_S \rightarrow \left( 1 + \frac{\alpha_S}{2\pi} \left[ \left( \frac{67}{18} - \frac{\pi^2}{6} \right) C_A - \frac{5}{9} n_f \right] \right) \cdot \alpha_S \quad (3.121)$$

everywhere in the Sudakov exponent using the  $\overline{\text{MS}}$  1-loop expression for  $\alpha_S$ , we can achieve NLL accuracy for the first emission in all processes that do not have more than 3 colored Born legs, provided that the scale argument of  $\alpha_S$  as well as the PDFs are chosen as discussed in the previous sec. 3.6.5. This especially improves the accuracy of events featuring a soft first emission at a scale close to  $p_{T,\text{min}}$  which can be of the order of 1 GeV.

For processes involving more than 3 colored partons, this procedure is not sufficient. However, by using color-exclusive Born and real matrix elements in the Sudakov exponent, it is possible to recover the NLL accuracy for these processes, at least for the dominant terms in the large- $N_c$  limit [47].

The factor applied to  $\alpha_S$  in eq. (3.121) is positive for typical values of  $N_c$  and  $n_f$  so this procedure increases

$\alpha_S$ . For very small scales it may happen that  $\alpha_S$  surpasses  $\alpha_S^{\text{rad}}$  in this way, violating eq. (3.43).

We take a few precautions to diminish the effects of this circumstance. One measure is the overestimation of  $\alpha_S^{\text{rad}}$  via  $b_0^{\text{rad}}$  in eq. 4.45 using  $n_f = 5$ . Additionally, we group the  $\alpha_S$  veto step together with the UBF veto step if both are non-trivial. In this way, in the now joined veto step, probabilities larger than 1 are even less likely, further reducing this effect. If this turns out to be a significant problem at some point, one could also apply the correction factor of eq. (3.121) to  $\alpha_S^{\text{rad}}$  too.

### 3.6.7 Color flow of POWHEG events

So far, we have generated the event kinematics using the POWHEG procedure. For an SMC to determine the correct shower pattern, we need to fill the LHIUP with colors for all colored particles. It is thus necessary to determine the color of each final-state particle when generating POWHEG events, although this is not directly part of the POWHEG procedure itself.

The most general way to determine the color structure of the event is to compute the corresponding (squared) matrix elements exclusive in color and choose a color structure randomly with probability proportional to the color structure's contribution to the total squared matrix element of the given flavor structure. This works for all Born-like and all real-like events, but it requires access to all color-exclusive matrix elements. For events with less than four colored partons, there is a simpler possibility to determine the event color without the need to compute all color-exclusive real matrix elements, which is still valid in the collinear regions, based on color planarity proposed in sec. 4.5.1 of ref. [47] and sec. 8 of ref. [48]. For each generated real-like event, the POWHEG-matching procedure has also determined an ALR, specifying the Born and real flavor structure as well as the emitting parton. Together with the Born color structure, these three pieces of information fix the real color structure under the assumption that the emitted parton is planar color-connected to the emitter. So given the Born color structure, we can determine the real color structure without requiring color-exclusive real matrix elements.

The color flows for the three possible final-state and the four possible initial-state splittings are depicted in fig. 3.9 and fig. 3.10. To denote the splittings, we use the notation introduced in sec. 2.6, where the "emitted" particle is mentioned last. For this reason, there is one more type of initial-state splittings than there are final-state splittings, depicted in fig. 3.10b. The one minor exception to the uniqueness of the real color structure is the three-gluon vertex (fig. 3.9c and 3.10d). In these cases, two color assignments are possible. As one is just as probable as the other, we randomly pick one of the two color structures.

In the case of gluon emission from the initial state, there is one more thing to consider. As discussed in sec. 2.3.3, we assign emitter 0 to an ALR combining two regions in which a gluon has been radiated off either initial-state parton. So in this region, we lost the information about the actual emitting parton. To properly determine the real color structure, we need to dissect this region and assign either emitter 1 or emitter 2 to it. As this color assignment procedure is most valid for collinear splittings, we prefer the more collinear option, i.e., we assign emitter 1 if  $y > 0$  and emitter 2 otherwise to determine the splitting that has taken place.

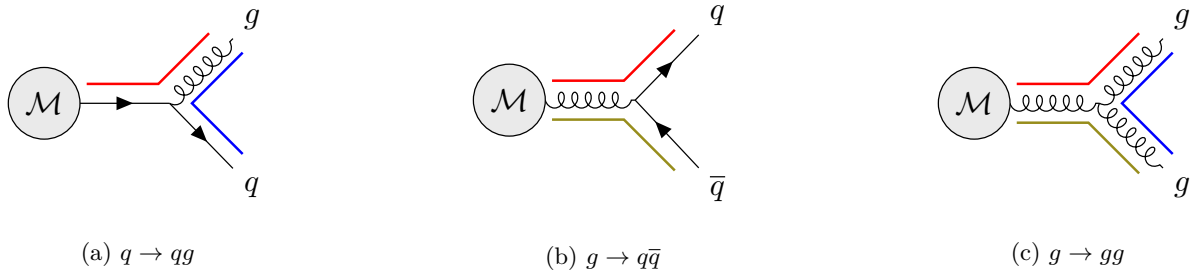


Fig. 3.9: Color flows for all possible final-state splittings.

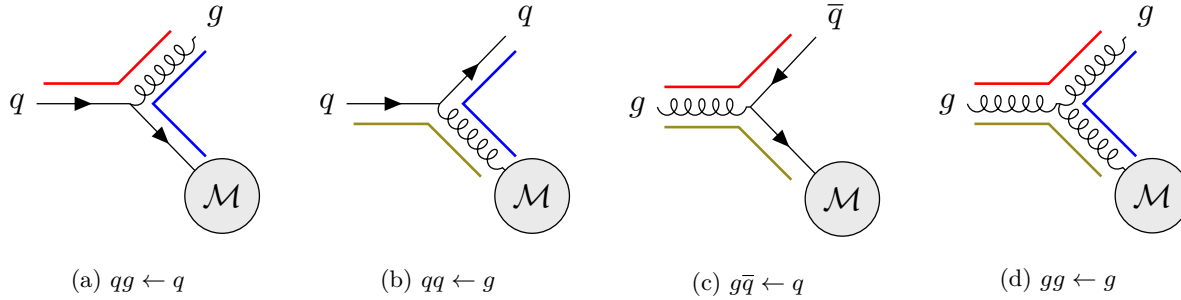


Fig. 3.10: Color flows for all possible initial-state splittings.

### 3.6.8 Resonance history insertion

So far, our entire discussion on the generation of the POWHEG event kinematics focussed on the partonic initial and final-state momenta. But the parton shower needs more information about the process. It needs knowledge about intermediate resonances, whose invariant masses have to be preserved by the parton shower, to reproduce the correct radiation patterns.

A typical example is the process  $e^+e^- \rightarrow u\bar{u}d\bar{d}$  which receives contributions from the two subprocesses  $e^+e^- \rightarrow W^+W^- \rightarrow (u\bar{d})(\bar{u}d)$  and  $e^+e^- \rightarrow ZZ \rightarrow (u\bar{u})(d\bar{d})$ . Without any resonance in the event record, the parton shower would generate a radiation pattern consistent with the continuum production of four quarks. If resonance information is present, the parton shower can generate radiation by taking the energy scale of the vector boson mass and also their finite widths into account. This will lead to a more accurate description involving fewer radiated hadrons after hadronization. The above example also makes it clear that a single process can have multiple distinct *resonance histories* on top of a *background* process;  $e^+e^- \rightarrow \gamma\gamma \rightarrow (u\bar{u})(d\bar{d})$  in this example.

The effect of resonances on the shower pattern is generally more important at lepton colliders due to the dominance of emissions from massive resonances and their products compared to events at the LHC, where ISR dominates the emission pattern. WHIZARD thus puts a lot of effort into accurately describing the involved resonances.

The resonances are inserted in the event record after the basic event kinematics has been generated. When generating POWHEG events, this means that the resonances are inserted in the Born particle set. Luckily, further QCD or QED splittings will not introduce new resonances in the process, so we just need to adjust the momenta of the Born resonances to determine the resonances of the real particle set.

As described in the WHIZARD manual [91], resonance histories are activated by setting `?resonance_history = true` when generating events. WHIZARD then determines a set of potentially resonant contributions for

each event and treats the ratio of their respective squared matrix element over the full squared matrix element as the probability for the resonance insertion.

There are three parameters further adjusting the resonance insertion: The `resonance_on_shell_limit` is a real number that determines how far away from the resonance mass in units of the resonance width an invariant mass may still be part of the set of potentially resonant processes. It is also possible to enable a Gaussian suppression of the resonance insertion probability by  $1/e$  each `resonance_on_shell_turnoff` units of the width away from the resonance mass. Lastly, the parameter `resonance_background_factor` allows to reduce the background contribution within the resonance range. Setting this to zero will always result in a resonance insertion within the allowed resonance range.

Due to the necessity to compute the full squared matrix element as well as all potentially resonant contributions, the resonance insertion is computationally expensive and thus disabled by default.

### 3.6.9 Reducing the number of negative weights

We mentioned in sec. 3.2.2 that many matching procedures at NLO and beyond produce event samples including negatively weighted events. The reason is that, especially in subtraction-based approaches, the total NLO cross section does not need to be locally positive definite across the phase space. For this reason, we restricted our efforts to generating indefinite unweighted event samples including weights  $w \in \{+1, -1\}$  in sec. 3.4.1.

While the generation of indefinite weighted samples is not a fundamental problem as they still allow to predict differential distributions precisely, they lead to inefficiencies in the MC tool chains producing simulated event samples. Especially for upcoming experimental setups with a huge expected increase in the luminosities like the High-Luminosity LHC, this poses one of the major computational challenges [37]. Roughly speaking, for every event contributing with a negative weight, multiple events with positive weights need to be generated to compensate for the negative weights. More precisely, if a fraction  $f_-$  negative events are generated, the statistical uncertainty of the generated sample increases by a factor of  $(1 - 2f_-)^{-1}$  so the number of events that are to be generated for the same precision increases by a factor of  $(1 - 2f_-)^{-2}$  [125]. For example, this implies that for  $f_- = 25\%$  (40%), a factor of 4 (25) more events need to be generated and processed in all subsequent analysis steps.

This problem is most severe for subtraction-based matching procedures like MC@NLO matching. There are ideas, however, to reduce the fraction of generated negative weights also for MC@NLO-type matching procedures [125, 126]. Furthermore, more general approaches to reducing the fraction of generated negative weights by modifying the parton-shower algorithm [127] or the phase-space mapping using importance sampling methods and normalizing flows [128–130] are under investigation. A second category of approaches is based on *resampling*, i.e., picking a subset of the events with preferably positive weights without altering any observables at the cost of introducing correlations between different events [131–134].

The fraction of generated negative weights is typically smaller for matching methods like KrkNLO [109] and POWHEG matching, as these matching procedures are not based on a subtraction approach. The NLO computation itself, however, is based on a subtraction scheme, so that also these methods are not completely free of negative weights and it is still worthwhile to investigate how to reduce the fraction of negative weights also in the matching procedure we focussed on in this thesis.

The weights of the generated POWHEG events are determined from  $\bar{\mathcal{B}}$ , given by eq. (3.8). In this expression, we sum up all NLO contributions locally in the phase space so that potential negative terms are often compensated by the inherently positive Born and the unsubtracted real contribution. This picture changes if we use the real partition. Using a strong real partition, given by small values of the real-partition scale

$h_F$ , we separate the positive contribution of  $\mathcal{R}_{\text{fin}}$  to  $\bar{\mathcal{B}}$  into a separate event sample leading to an increased fraction of negative weights in the sample of events generated using the POWHEG procedure.

This is quantified in fig. 3.11. It shows the fraction of negative weights in event samples generated for the Drell-Yan process,  $pp \rightarrow e^+e^-$ , at  $\sqrt{S_{\text{had}}} = 1 \text{ TeV}$  and top-pair production in association with a jet at a future lepton collider,  $e^+e^- \rightarrow t\bar{t}j$ , at  $\sqrt{S_{\text{had}}} = 500 \text{ GeV}$ . Both setups are described more precisely in sec. 6.1.1 and sec. 6.3.1, respectively, but are of no further concern at this point.

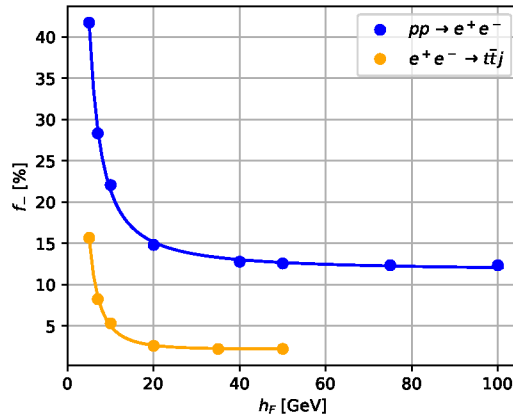


Fig. 3.11: Fractions of negative weights generated for the processes  $pp \rightarrow e^+e^-$  and  $e^+e^- \rightarrow t\bar{t}j$  with varying real-partition scale  $h_F$ . The data points, depicted as dots, have been overlaid by a Laurent polynomial with powers 0, -1, -2 and fitted coefficients. Negative weights of Born-like, as well as real-like events, have been taken into account. The events for the processes  $pp \rightarrow e^+e^-$  and  $e^+e^- \rightarrow t\bar{t}j$  have been generated in the setup described in sec. 6.1.1 and sec. 6.3.1, respectively.

We can clearly see that the fraction of negative weights drastically increases in both cases for small values of the real-partition scale  $h_F$ . At the same time, it is roughly constant in the region above about half its maximum value  $h_F^{\text{max}}$ , determined from the condition that  $\mathcal{R}_{\text{fin}} = 0 \quad \forall h_F \geq h_F^{\text{max}}$ . In the cases shown here, we find  $h_F^{\text{max}} \approx 100 \text{ GeV}$  for  $pp \rightarrow e^+e^-$  and  $h_F^{\text{max}} \approx 50 \text{ GeV}$  for  $e^+e^- \rightarrow t\bar{t}j$ . This observation suggests to avoid values  $h_F < \frac{1}{2}h_F^{\text{max}}$  in larger applications involving parton showering, detector simulations and more elaborate analysis procedures to make efficient use of the available computational capabilities.

## 4 The Monte Carlo event generator WHIZARD

WHIZARD [51] is a general-purpose Monte Carlo event generator to simulate hadron and lepton-collider physics. Using WHIZARD, it is possible to compute all parts of a particle-physics simulation; from determining a physics model to computing total cross sections and generating unweighted event samples.

Historically, WHIZARD 1 was developed as a tool to simulate heavy-boson processes to aid the technical design of TESLA [135, 136], a proposed lepton collider at a CM energy of 800 GeV. This purpose coined its original name, "WHiZarD", for "**W**, **H**iggs, **Z** and respective **D**ecays". The program was rereleased in 2010 as WHIZARD 2, uniting the previously only loosely connected internal packages into a single, monolithic framework, driven by the physics demands of the LHC.

One of these packages is `O'Mega` [137–139], the in-house tree-level matrix-element generator, whose name stands for **O**ptimized **M**onte Carlo event generation **a**mplitudes. `O'Mega` is written in `O'Caml` and generates `Fortran` code or byte-code instructions [140] for the matrix elements by recursively computing helicity amplitudes.

To integrate said matrix elements, WHIZARD employs an amplified version of the VEGAS algorithm [141, 142] called `VAMP` [143] (**V**EGAS **a**mplified). The original package `VAMP`, written in `Fortran95`, was recently superseded by `VAMP2`, a complete re-implementation of the random-number sampling and adaptive multi-channel-integration algorithm, written in `Fortran2008`, using a thread-safe random number generator (RNG) [144] and the message passing interface (MPI). This allows for an efficient parallelization of the integration and event generation on up to  $\mathcal{O}(100)$  CPU cores [145, 146]. For this reason, all results presented in this thesis have been computed using `VAMP2`.

True to its origin, WHIZARD is predominantly used for physics simulations at lepton colliders [32, 35, 147–149]. For this purpose, it is able to take into account lepton-collider beam spectra using the `CIRCE1` [150] and `CIRCE2` [151, 152] subpackages. Both packages fit the beam-energy spectrum obtained from `GuineaPig` [153–155], generating collider-specific files, which contain the fitted spectrum. For a large number of frequently studied collider setups, these beam-spectrum files are available on the WHIZARD `HepForge` webpage [156].

In its core parts, WHIZARD glues together the different internal and external packages and takes over the bookkeeping of flavor structures and matrix elements as well as the phase-space generation.

To describe the proton content in hadron collisions, WHIZARD ships with a number of built-in PDFs. A larger variety of PDFs is provided via an interface to `LHAPDF` [157].

WHIZARD and all its subpackages are steered using the command language `SINDARIN`, a **S**cripting language for **I**Ntegration, **D**ata **A**nalysis, **R**esults display and **I**Nterfaces. All settings are typically written into a single steering file called the `SINDARIN` file. Using `SINDARIN`, the physics model can be selected from a variety of built-in models or any model available via `FeynRules` [158] in the Universal FeynRules Output (UFO) format [159]. Also, the `SINDARIN` language allows to declare physics processes, including the process definition, phase-space cuts, analysis routines and all accompanying technical settings with huge flexibility. This flexibility allows to specify arbitrary phase-space cuts without having to interact with or recompile the code. This includes available features like jet clustering using an interface to `FastJet` [80], jet-flavor tagging and Frixione photon isolation [160].

As a result of a typical application, WHIZARD allows to generate weighted and unweighted events in many different formats, including `HepMC2` [113] and `HepMC3` [114] as well as `LHE` [55].

### 4.1 The Monte Carlo event generator WHIZARD at NLO QCD

#### The evolution of NLO corrections in WHIZARD

With the release of WHIZARD 3.0.0 in 2021, WHIZARD officially supports the computation of cross sections and

differential distributions at the next-to-leading order in QCD in full generality. The advancement towards NLO corrections in WHIZARD started more than a decade ago with hand-tailored NLO EW corrections to chargino production at the ILC [161, 162] and NLO QCD corrections to the production of bottom-quark pairs at the LHC [163, 164].

The work on process-independent NLO QCD corrections began with ref. [72]. In the course of that thesis, general NLO QCD corrections for processes at lepton colliders with up to two final-state jets could be incorporated in WHIZARD 2.4.0. The limitations regarding the jet multiplicities and the initial state could be lifted in the course of ref. [73] and this thesis, extending the availability of NLO QCD corrections in WHIZARD to jet multiplicities of up to 6 jets as presented in refs. [3, 73] and also to hadronic initial states. To cement this achievement, we extended WHIZARD’s extensive functional-test suite with a large number of tests making sure that no future change to the program introduces any regression.

Beyond fixed-order cross sections, we completed the feature to simulate fixed-order NLO event groups according to the procedure described in sec. 2.8. They are required to generate differential distributions with fNLO accuracy.

The NLO QCD corrections in WHIZARD have been implemented in a modular and generally applicable way. Especially, the implementation of QCD corrections for hadronic initial states, including the construction of kinematics for real emissions from the initial state and the infrastructure for the initial state subtraction terms, could be used in the same way in the computation of NLO EW corrections, which greatly facilitated their development in the course of ref. [76].

### Loop matrix elements

NLO computations of any kind include virtual corrections and thus require loop-matrix elements. Moreover, the construction of subtraction terms for some processes requires explicit spin- or color-correlation-matrix elements (c.f. sec. 2.6.1). In the near future, the internal matrix-element generator `O’Mega` will be able to provide these correlated matrix elements. In the current state, however, the correlated matrix elements and the loop-matrix elements are provided via interfaces to external matrix-element generators, so-called *one-loop providers*. For all NLO calculations presented in this thesis, we relied on `OpenLoops 2` [165, 166] for this purpose. `OpenLoops` is an automated generator for tree-level and one-loop amplitudes based on open-loop recursion. From the user perspective, however, it works as a library that provides pre-generated matrix elements for a set number of processes.

Another approach is followed by `Reco1a` [167, 168]. `Reco1a` provides methods for **recursive computations of one-loop amplitudes**, allowing to generate the requested matrix elements on-the-fly.

### The FKS subtraction scheme in WHIZARD

The divergences in the loop-matrix elements cancel with divergent regions in the real matrix elements, allowing to construct subtraction terms. WHIZARD handles this subtraction within the FKS subtraction scheme [62–64, 88] which we reviewed in sec. 2. We will not go into the technical details of its implementation in WHIZARD here. Just like any scientific software framework, WHIZARD is in constant development to adjust to the advances and needs of the experimental side. For this reason, any detailed technical documentation here would sooner or later be outdated.

The WHIZARD source code<sup>18</sup>, on the other hand, is documented using the literate programming tool `noweb` [170], allowing to disentangle source code and documentation, compiling the documentation into a typeset file in portable document format. The documentation is written in  $\text{\LaTeX}$  and contains the

<sup>18</sup>The source code of the latest release is available via the public GitLab [169] or via HepForge [156] as a tarball and also in a single typeset file.

corresponding typeset formulae. Especially the documentation of the FKS phase-space construction, the construction of the subtraction terms and the routines for the event generation of fixed-order as well as POWHEG events, has greatly been extended in the course of this thesis. After studying sec. 2 and the main references mentioned therein, it should be possible to relate the mathematical documentation here and the technical documentation in the source code, should the reader wish to gain a deeper understanding.

### Steering WHIZARD at NLO

How to run and use the NLO capabilities of WHIZARD is documented in the manual [91]. Nevertheless, we will mention the parts specifically relevant for NLO computations here, leaving the general parts like the model and parameter choice as well as the technical settings for later. The syntax stated here refers to WHIZARD version 3.1.0.

For NLO calculations, a matrix-element provider different from the default, `O'Mega`, has to be set for at least the `$loop_me_method` and the `$correlation_me_method`. Alternatively, all matrix elements can be taken from the same matrix-element-provider, in our case `OpenLoops`, by setting

```
1 $method = "openloops"
```

By default, the `$nlo_correction_type` is already set to "QCD", so we do not need to adjust it in this case. Finally, we simply set `nlo_calculation = full` to tell WHIZARD that we want to compute the total NLO QCD cross section. This can be set process-specific, as in

```
2 process eejj_lo = e1, E1 => jet, jet
3 process eejj_nlo = e1, E1 => jet, jet { nlo_calculation = full }
```

In this case, WHIZARD computes the Born, the real, the virtual and for hadron-collisions also the DGLAP remnant component one after another, using their sum to determine the total NLO cross section in the end. This approach has the benefit that the number of generated PSPs and matrix-element calls can be adjusted individually to the complexity of each component. Evaluating the virtual matrix elements is often the most time-consuming task, while the real component has the most complex phase space. For this reason, we often set multiplicative factors for the number of calls to the matrix elements for each of both components with

```
4 mult_call_real = 2
5 mult_call_virt = 0.5
```

Increasing the number of matrix-element calls for just the real component is thus a useful tool to optimize the precision without significantly increasing the time required for the total computation. The same principle holds for the simulation of events, where we can vary the number of generated events for each component. This behavior can be changed by additionally setting

```
6 ?combined_nlo_integration = true
```

In this case, the sum of all components will be integrated simultaneously, using identical PSPs for the underlying Born phase space in each component. This is useful for simple processes as it provides a cleaner output and is also mandatory for, e.g., POWHEG matching. However, it comes at the cost of losing the freedom to generate more PSPs for a specific component.

If everything is set, the integration can be invoked by adding the line

```
7 integrate (eejj_nlo) { iterations = 5:100000:"gw", 4:100000 }
```

, which will lead WHIZARD to integrate the total NLO cross section for the process defined as `eejj_nlo` with 5 stages of 100000 calls each to adapt the integration grids and associated weights, mapping the phase space, followed by 4 stages with 100000 calls each to compute the total cross section.

## 4.2 Parton shower, merging and matching in WHIZARD

As a multi-purpose MC event generator, WHIZARD offers several possibilities to process the generated partonic events further, enhancing them with a parton shower and hadronization. As the most basic approach, WHIZARD implements the Les Houches event accord interface [54, 55], allowing to process the generated events with external parton-shower tools such as PYTHIA [52, 101] or HERWIG [53, 171]. Moreover, WHIZARD ships including the final version of PYTHIA6 [101] and an internal interface to it and also offers a dedicated interface to PYTHIA8 [52]. Additionally, an internal analytic parton shower [172] is available as well as the infrastructure for the *MLM matching* merging procedure (c.f. sec. 3.2.1).

Concerning the matching of NLO events to a parton shower, WHIZARD relies on the POWHEG matching. An experimental implementation of the POWHEG-matching algorithm was developed to describe  $t\bar{t}$  production at a lepton collider, with and without an associated Higgs boson [118], in the course of ref. [71]. This first version included most of the relevant infrastructure for the matching required to generate POWHEG events. However, the generated events lacked information essential for the parton shower, such as the correct scales, information about the resonance structure and the correct flavor- as well as color distributions. It also lacked the flexibility to be applicable to other processes featuring multiple Born or real flavor structures, real emissions from the initial state or requiring any phase-space cuts.

All these limitations could be overcome only in the present work. We extended the flexibility of the implementation towards arbitrary processes at lepton and hadron colliders, including processes with flavor sums, multiple flavor structures and phase-space restrictions. We generalized the real partition (c.f. sec. 2.6.3) such that it can also be used for  $pp$  processes and in conjunction with the POWHEG matching and ensured that all parts of the MC integration and event generation correctly handle samples including negative weights. Furthermore, we optimized the implemented matching algorithm in terms of accuracy, by implementing the scale choices and NLL corrections described in sec. 3.6.5 and 3.6.6, respectively. The performance optimizations included the use of the optimized veto procedure described in sec. 3.5.3 and using the possibility to fill the POWHEG grid already during the integration step, before generating POWHEG events, instead of in an additional, independent step.

We will postpone the technical discussion of how to use and steer the POWHEG matching in WHIZARD to app. D, where we will go through the specific example of generating POWHEG events for the Drell-Yan process in detail.

Part II

## Part 2 – Applications of fixed-order and matched Simulations

## 5 Validation of fixed-order NLO cross sections

Part I of this thesis explains the mathematical and technical background of NLO cross-section calculation and event simulation. In the second part, we will focus on a selection of applications instead.

Before discussing actual predictions, however, it is a crucial task to ensure the validity of the calculations and their implementation. In this section, we will mention a few relations and connections that we can use for self-consistency checks to confirm our confidence in the calculations. After that, we move from self-consistency checks to cross-checks with other MC generators and perform a thorough comparison of a multitude of fNLO QCD total cross sections with the MC generator `MG5_aMC`.

### 5.1 Consistency checks

#### Validation of the $S$ functions

In sec. 2.3.3, we have discussed the subdivision of the real phase space by  $S$  functions. Specifically, we have stated in eq. (2.23) that they have to be a partition of unity, i.e.

$$\sum_{(i,j) \in \mathcal{P}_{\text{FKS}}^{\alpha_r}} S_{ij}^{\alpha_r} = 1 \quad . \quad (5.1)$$

We can use this fact to test the implementation of the  $S$  functions and ALRs, including, to some extent, also the kinematic constructions.

As obvious as eq. (5.1) seems, it is not straightforwardly validated. Suppose we sum all  $S$  functions for a specific set of  $(\xi, y, \phi)$ , determining a PSP, as they are used in the calculation over all ALRs. In that case, they will not sum up to unity for the reason that different emitters may be associated with the considered ALRs, influencing the meaning of especially  $y$ , such that the actual phase-space points  $\Phi_{n+1}^{(\alpha_r)}$  do not coincide. We can see this in the example of the process  $e^+e^- \rightarrow jj$ . We have already seen the FKS table describing the two ALRs in the case of a single jet flavor in tab. 2. Let us consider the case of a collinear emission,  $y \approx 1$ . In this case, eq. (2.26) dictates  $S_{35}^1 \approx 1 \approx S_{45}^2$ , so they clearly do not sum up to unity. This is not a problem as the radiated gluon moves in the exact opposite direction in both cases. Instead, we need to check that  $S_{35}^1 + S_{45}^1 \approx 1 \approx S_{35}^2 + S_{45}^2$  where  $S_{45}^1$  and  $S_{35}^2$  are two  $S$  functions that would normally not contribute to the rest of the computation.

In `WHIZARD`, this self-check has been implemented as a debug routine in the course of this thesis to be able to perform this self-test automatically.

We explicitly chose the functional form of the  $S$  functions in sec. 2.3.3. There is some freedom related to this choice. For example, instead of choosing the phase-space weights  $d_{ij}$  according to eq. (2.31) for FSR and eq. (2.33) for ISR, we can use this opportunity to introduce two free parameters,  $a_S$  and  $b_S$ , and choose

$$d_{ij} := 2^{a_S} \left( \frac{E_i E_j}{E_i + E_j} \right)^{2a_S} (1 - y)^{a_S} \quad \text{for FSR and} \quad (5.2)$$

$$d_{ij} := 2^{b_S} E_j^{2b_S} (1 + (-1)^i y_j)^{b_S} \quad \text{for } i \in \{1, 2\} \quad \text{for ISR} \quad (5.3)$$

instead, similar to what is suggested in ref. [47]. This choice still fulfills all requirements for the  $S$  functions we imposed in sec. 2.3.3 for all positive real values of  $a_S$  and  $b_S$ . We can use the associated freedom to vary both parameters in a sensible range. This will shift contributions between the ALRs, keeping the total cross section constant. In `WHIZARD`, both parameters are referred to `fk_s_dij_exp1` and `fk_s_dij_exp2` and can be varied from the `SINDARIN` file steering `WHIZARD`.

### Variation of slicing parameters

There are some more free parameters in the FKS subtraction scheme. To find the subtraction terms for the real contribution, we used *modified plus distributions* in eq. (2.129f). With these, we introduced three free parameters,  $\xi_{\text{cut}}$ ,  $\delta_O$  and  $\delta_I$ . They act as phase-space-slicing parameters, shifting contributions between the subtracted real contribution and the integrated subtraction terms. While  $\xi_{\text{cut}}$  does so for the soft contributions,  $\delta_O$  and  $\delta_I$  affect the collinear contributions for FSR and ISR, respectively. Varying these parameters within their ranges,  $0 < \xi_{\text{cut}} \leq 1$  and  $0 < \delta_{O/I} \leq 2$ , will affect the partial cross section of the real component as well as the virtual and the DGLAP remnant component but their sum, i.e., the total cross section should be independent of the individual values.

While the explicit dependence on  $\xi_{\text{cut}}$  was implemented in the course of ref. [73], the implementation of  $\delta_O$  and  $\delta_I$  and the automated validation of the total cross section's independence on these parameters have been achieved in the course of this thesis. Furthermore, it has become part of the regularly executed test suite of WHIZARD.

In tab. 3 and tab. 4, we list the partial cross sections of the real component and the virtual or the DGLAP remnant component as well as their sum for different values of  $\xi_{\text{cut}}$  and  $\delta_I$ , respectively. As exemplary processes, we choose  $e^+e^- \rightarrow jjj$  in the first and  $pp \rightarrow e^+e^-$  in the latter case. We can clearly observe that the sum of both affected components is constant for all parameter variations, although the individual cross sections vary significantly. We want to stress again that the independence of the total cross section on the three slicing parameters has been validated for many other processes as well. A similar cross section table for the variation of  $\delta_O$  in the process  $e^+e^- \rightarrow jjjj$  is, e.g., included in ref. [73].

$\xi_{\text{cut}}$	$\sigma^{\mathcal{R}}$ [fb]	$\sigma^{\mathcal{V}}$ [fb]	$\sigma^{\mathcal{R}} + \sigma^{\mathcal{V}}$ [fb]
0.25	-54.65(73)	32.42(16)	-22.22(74)
0.50	- 2.02(69)	-19.17(20)	-21.18(72)
0.75	27.75(68)	-49.33(30)	-21.58(74)
1.00	49.26(84)	-70.37(36)	-21.10(92)

Tab. 3: Partial cross sections for the real and the virtual component of the process  $e^+e^- \rightarrow jjj$  at NLO QCD for different values of  $\xi_{\text{cut}}$ . In this setup, we chose  $\sqrt{S_{\text{had}}} = 1$  TeV, a scale  $\mu = \frac{1}{2}H_T$  and required  $p_T > 30$  GeV and  $|\eta| < 4$  for at least 3 jets clustered with the anti- $k_T$  algorithm with  $R = 0.5$ .

$\delta_I$	$\sigma^{\mathcal{R}}$ [pb]	$\sigma^{\mathcal{G}}$ [pb]	$\sigma^{\mathcal{R}} + \sigma^{\mathcal{G}}$ [pb]
0.50	23.69(31)	168.77(117)	192.46(121)
1.00	38.92(27)	153.25(105)	192.17(108)
1.50	48.01(23)	144.10( 98)	192.11(101)
2.00	54.50(21)	137.62( 93)	192.12( 95)

Tab. 4: Partial cross sections for the real and the DGLAP remnant component of the process  $pp \rightarrow e^+e^-$  at NLO QCD for different values of  $\delta_I$ . In this setup, we chose  $\sqrt{S_{\text{had}}} = 8$  TeV, a scale  $\mu = m_Z$  and required an invariant mass of at least  $m_{e^+e^-} > 50$  GeV for the lepton pair.

### Limit checks

Besides exploiting free parameters in the implementation, we can also explicitly verify that the FKS subtraction terms are constructed so that they cancel the divergences of the unsubtracted real squared amplitude. To do this, we can explicitly evaluate the unsubtracted real squared amplitude,  $\mathcal{R}_{\alpha_r}$ , as well as the subtraction terms,  $\mathcal{S}_{\alpha_r}$ , in the soft, collinear or soft-collinear limit and compare them numerically. If the subtraction

terms are implemented correctly, both terms should coincide up to the sign in these regions. This limit check is particularly helpful should the integration of the subtracted real component for some process have problems to converge on a finite result, as it helps to figure out precisely which terms in which limits are misaligned.

Of course, in our attempt to investigate the behavior of the subtraction terms in the soft or collinear limit, it is numerically impossible just to set  $\xi = 0$  and  $y = \pm 1$ . Instead, we choose values close to the limit and introduce a tolerance for the agreement between the unsubtracted real and the subtraction terms. To probe the cancellation for NLO QCD corrections, we set  $\xi = 10^{-5}$  to test the soft limit and  $y = \pm(1 - 10^{-7})$  to test the (anti) collinear limit. We set both cases' second, yet unconstrained, parameter to the value 0.5. To test the soft-collinear limit, we choose the same extremal values for both  $\xi$  and  $y$ .

Empirically, it turns out that requiring

$$\frac{|\mathcal{R}_{\alpha_r}(\xi, y) - \mathcal{S}_{\alpha_r}(\xi, y)|}{\max(|\mathcal{R}_{\alpha_r}(\xi, y)|, |\mathcal{S}_{\alpha_r}(\xi, y)|)} \stackrel{!}{<} 0.01 \quad (5.4)$$

for a successful limit check yields 90% – 100% of the PSPs successfully passing the limit checks for a large number of processes. This rate drops to minimally 80% for some ALRs of more complicated processes at NLO QCD, so this seems to be a reasonable choice.

For more complicated processes and especially to apply these limit checks to NLO EW corrections, the choice of  $y = \pm(1 - 10^{-7})$  seems to be not collinear enough for the real and the subtraction term to fulfill eq. (5.4) considerably likely. In this case, the values can be manually adjusted so that  $\xi$  takes values closer to 0 or  $y$  takes values closer to 1. Choosing  $y = \pm(1 - 10^{-8})$  is an appropriate tradeoff between having a larger ratio of successful limit checks and numerical stability.

In WHIZARD, this specific choice of PSPs close to the soft or collinear limit can be activated by setting either `?test_soft_limit` and/or `?test_coll_limit` or `?test_anti_coll_limit` to `true`. To perform the actual self-check and print the output, WHIZARD has to have been configured with the flag `--enable-fc-debug` and the command-line flag `--debug subtraction` has to be given additionally to `whizard` when calling the program. Furthermore, these settings should be used in conjunction with the setting `$select_alpha_regions` to probe one ALR at a time.

While the general idea of the limit checks has already been partially implemented in the course of ref. [72], it has been generalized and automatized in the course of this thesis. Among the discussed self-tests, this check facilitated the implementation and validation of the NLO EW subtraction terms WHIZARD in the course of ref. [76] most, as it allows to validate the subtraction terms individually.

### Closure tests

The limit check allows us to specifically probe the FKS subtraction terms and the phase space in the singular limits. As these checks are performed for a constrained set of PSPs, they do not probe the real phase space outside the divergent limits. To some extent, the closure tests constitute the complementary approach, allowing to test the construction of the real phase space and  $S$  functions outside the extreme regions.

The closure test is based on the idea that the unsubtracted real correction to a process with  $n$  jets in the final state should coincide with the Born cross section of the process with  $n + 1$  jets. In order to perform this test, we have to disable the subtraction terms for the real component by setting `?disable_subtraction = true` in the SINDARIN file steering WHIZARD and most importantly, we have to require  $(n + 1)$  well-separated jets in both calculations, also for the real contribution to the  $n$  body process. In this way, we explicitly cut away the singular regions from the real phase space. In a standard NLO computation, this would lead to a divergent integration as we tried to integrate the subtraction terms solely without the real counterparts in

the divergent regions.

The closure test was a valuable tool in the final validation of the implementation of the FKS subtraction scheme at NLO QCD in WHIZARD in the course of ref. [73] and the present work. We applied the closure test to a multitude of processes, validating the FKS phase-space construction, the  $S$  functions and especially the set of FKS pairs,  $\mathcal{P}_{\text{FKS}}$ , associated with each ALR.

Ref. [73] includes results for the closure test of the processes  $e^+e^- \rightarrow jjj$  and  $pp \rightarrow Zj$ . We shall perform the closure test on the example of the process  $e^+e^- \rightarrow t\bar{t}j$  at  $\sqrt{S_{\text{had}}} = 500$  GeV, exemplary. More details of the setup will be given in sec. 6.3.1 but are of no further concern at this point. In this setup, we find for the unsubtracted real cross section of the process  $e^+e^- \rightarrow t\bar{t}j$  as well as for the Born cross section of the process  $e^+e^- \rightarrow t\bar{t}jj$  requiring four well-separated top-jets in both cases

$$\begin{aligned}\sigma_{e^+e^- \rightarrow t\bar{t}j}^{\mathcal{R}} &= (3.156 \pm 0.006) \text{ fb} \\ \sigma_{e^+e^- \rightarrow t\bar{t}jj}^{\mathcal{B}} &= (3.153 \pm 0.004) \text{ fb} \quad .\end{aligned}\tag{5.5}$$

## 5.2 Comparison of fixed-order cross sections at NLO QCD

Self-consistency checks are one way to gain confidence in the implementation of the FKS subtraction scheme in the MC generator WHIZARD. Direct comparisons of computed cross sections with existing multi-purpose MC event generators, developed by other groups, is another approach. MADGRAPH [173] and its NLO extension dubbed MG5\_aMC [45] is one such multi-purpose MC event generator. Just as WHIZARD, it has been developed by multiple scientists over several decades. It is in active use by experimental collaborations, especially at the LHC and can thus be considered to be well validated. Ref. [45] includes an extensive list of total cross sections for hadron as well as lepton-collider processes computed at NLO QCD in a uniform setup, marking the beginning of fully automated multi-purpose calculations at NLO QCD. We will use this available collection of cross sections for a thorough comparison of our results with those computed in ref. [45].

The endeavor of this comparison started with ref. [72], in which the validation of many processes with top quarks, vector bosons and up to two jets in the final state could be achieved. This limitation could be lifted in a collaborative effort, which led to ref. [73] and the present work. In ref. [3], we published a larger selection of processes, including the production of up to 3 jets at a hadron collider and up to 6 jets at an  $e^+e^-$  collider. Finally, ref. [73] contains the comparison of almost all processes shown in ref. [45], which we will also discuss in the following.

### 5.2.1 Process setup

We choose to perform this large-scale comparison of fixed-order cross sections in a uniform setup for all processes with slight modifications for hadron- and lepton-collision processes. The setup described here is equivalent to the one described in ref. [45], complemented with settings included in the run- and parameter cards, employed by MG5\_aMC, which can be found in ref. [174]. All settings therein have been translated to SINDARIN for the purpose of this comparison.

We choose typical CM energies of  $\sqrt{S_{\text{had}}} = 1$  TeV for the lepton-collider processes and  $\sqrt{S_{\text{had}}} = 13$  TeV for the hadron-collider processes. All quarks and leptons except the heaviest, the top quark and the tau lepton, are considered massless by default. For the exceptions, the masses are set to

$$m_t = 173.2 \text{ GeV} \quad \text{and} \quad m_\tau = 1.777 \text{ GeV} \quad .\tag{5.6}$$

Furthermore, we assume a diagonal CKM matrix for the quarks. We consider the heavy bosons to take the mass values

$$m_W = 80.419002 \text{ GeV}, \quad m_Z = 91.188 \text{ GeV} \quad \text{and} \quad m_H = 125 \text{ GeV} \quad (5.7)$$

and set their width to zero. In the present comparison, they are considered to be stable. As EW scheme, we employ in the  $G_F - m_W - m_Z$  input scheme with

$$G_\mu = 1.16639 \cdot 10^{-5} \text{ GeV}^{-2} \quad .$$

Both renormalization and factorization scales are set to

$$\mu = \mu_r = \mu_F = \frac{1}{2} H_T \quad \text{with} \quad H_T := \sum_i \sqrt{p_{T,i}^2 + m_i^2} \quad , \quad (5.8)$$

where we sum over all partons in the final state<sup>19</sup>. For the lepton-collision processes, we set a strong coupling constant of

$$\alpha_S(m_Z) = 0.118 \quad , \quad (5.9)$$

taking into account the running of  $\alpha_S$  at NNLO. For hadron-collision processes we take the value for  $\alpha_S$  from the MSTW2008nlo68c1 [175] PDF which we employ. In processes with at least two  $W$  bosons in the final state, we choose the four-flavor scheme to avoid resonant top contributions. For all other processes, we use the five-flavor scheme.

In processes containing jets, we employ the anti- $k_T$  jet-clustering algorithm [176] with  $R = 0.5$  on all massless QCD partons in the final state. From the resulting objects, we define as jets those fulfilling the selection criteria

$$p_{T,j} > 30 \text{ GeV} \quad \text{and} \quad |\eta_j| < 4 \quad . \quad (5.10)$$

We require at least as many jets as present in the Born process for each process. The requirement on the transverse jet momentum is tightened for hadron-collider processes with only jets in the final state, where we require  $p_{T,j} > 80 \text{ GeV}$  from all jets present at the Born level and at least one jet with  $p_{T,j} > 100 \text{ GeV}$ . We should spend some words on the matrix elements present in the calculation. This entire comparison of cross sections focusses on pure NLO QCD corrections. For each process, we thus always refer to the highest, non-zero order in the strong coupling,  $\alpha_S$ , such that in terms of fig. 2.1, the Born process is of the order  $\mathcal{O}(\alpha_S^N \alpha^m)$  and the corresponding NLO correction is at the order  $\mathcal{O}(\alpha_S^{N+1} \alpha^m)$ . In WHIZARD, we employ `OpenLoops 2` [166] as matrix-element generator for all matrix elements, while `MG5_aMC` always uses its in-house matrix-element provider `MadLoop` [177].

### 5.2.2 Results for the cross sections

In this section, we will present the results. We compared the vast majority of cross sections given in ref. [45], with a few minor exceptions. We excluded processes with explicit  $b$  jets or photons in the final state. They require  $b$ -jet tagging or photon isolation, respectively. Although both features are available in WHIZARD, it is the FKS implementation we aim to validate here and from this point of view, testing the implementation of  $b$ -jet tagging and photon isolation would unnecessarily complicate the comparison. Moreover, we excluded the processes  $pp \rightarrow W^+W^-W^+W^-$ ,  $pp \rightarrow ZZZZ$  and  $pp \rightarrow t\bar{t}W^\pm Z$  from the comparison as there were no matrix-element libraries available from `OpenLoops`. This limitation could be overcome by using `Recola` as

<sup>19</sup>In most cases, defining a scale from partonic objects that did not undergo a clustering into jets, from which we can construct IR finite observables, is dangerous. In the definition of  $H_T$ , however, we sum over *all* final-state partons so that soft and collinear emissions are automatically included.

a matrix-element provider for these processes, but we preferred to stick to a clean setup. We do not show the cross sections for all processes with Higgs bosons contained in ref. [45]. There is nothing special about processes with Higgs bosons regarding the NLO subtraction scheme or phase space, so we include solely the process  $pp \rightarrow HZ$  representatively in this comparison.

Unfortunately, the version of `MG5_aMC` used to compute the cross sections contained in ref. [45] contained a bug affecting all processes with identical QCD particles in the Born final state, which was present up to version 2.6.2. For this reason, only some of the LO cross sections could directly be taken from ref. [45] and all of the NLO cross sections had to be recomputed using `MG5_aMC 2.7.3`.

For `WHIZARD`, the two consecutive versions 2.8.3 and 3.0.0 $\beta$  shortly before the release of `WHIZARD 3.0.0` have been employed to compute most of the cross sections. The only exceptions are the processes  $pp \rightarrow ZZW^\pm j$  and  $pp \rightarrow W^+W^-ZZ$ , which have been recomputed with `WHIZARD 3.0.3` and increased precision, as they showed the largest hints on deviations between both programs initially.

`MG5_aMC` and `WHIZARD` are both MC generators relying on random numbers for their computations. Even if the implementations of the calculations in both programs were identical, their results would not agree numerically. To quantify the significance of the deviation between both results, we list  $\sigma^{\text{sig}}$ , determined by

$$\sigma^{\text{sig}} := \frac{|\sigma^{\text{WZ}} - \sigma^{\text{MG}}|}{\sqrt{(\Delta_{\sigma^{\text{WZ}}}^{\text{stat}})^2 + (\Delta_{\sigma^{\text{MG}}}^{\text{stat}})^2}} \quad (5.11)$$

for the NLO cross sections in the last column, where  $\sigma^{\text{WZ}}$  and  $\Delta_{\sigma^{\text{WZ}}}^{\text{stat}}$  are the total cross section and the respective statistical uncertainty computed with `WHIZARD`;  $\sigma^{\text{MG}}$  and  $\Delta_{\sigma^{\text{MG}}}^{\text{stat}}$  are the analog for `MG5_aMC`. In general, values  $\sigma^{\text{sig}} < 3$  can be regarded as an agreement, values  $3 < \sigma^{\text{sig}} < 5$  may hint on a deviation while values  $\sigma^{\text{sig}} > 5$  are a clear sign of a significant difference.

In the tables presented below, we also show the total  $K$  factor defined by

$$K := \frac{\sigma_{\text{NLO}}}{\sigma_{\text{LO}}} \quad (5.12)$$

to quantify the importance of the NLO corrections for each program separately.

In tab. 5, we show all total cross sections for processes at lepton colliders with pure QCD final state. This includes multi-jet and top-quark production. For all cross sections, we can observe a very good agreement between `MG5_aMC` and `WHIZARD` with  $\sigma^{\text{sig}} < 2$ . Especially processes like  $e^+e^- \rightarrow jjjjj$  and  $e^+e^- \rightarrow t\bar{t}jjj$  require flavor combinatorics, color correlations and the correct treatment of all FKS pairs in full complexity, so this constitutes a thorough test of the NLO subtraction mechanism for massless and massive final-state emitters.

Cross sections for processes involving the production of top quarks and heavy bosons at a lepton collider are listed in tab. 6. The excellent agreement across all processes in this category further increases our confidence in the subtraction mechanism for FSR as well as the phase-space construction for massive emitters and with massive recoil systems.

We will discuss processes at a hadron collider next to test the phase-space construction and the subtraction mechanism for ISR. In tab. 7, we show three different types of processes at a hadron collider. We list the cross sections for the production of up to three jets, the production of a top-quark pair in association with up to two light jets or a second  $t\bar{t}$  pair and the production of a top-quark pair together with heavy bosons and up to a single light jet. Lastly, we include the process  $pp \rightarrow HZ$  as representative of processes involving the production of Higgs bosons at a hadron collider.

In many cases, we also noticed a change in the LO cross sections between those given in ref. [45] and the ones computed with `MG5_aMC 2.7.3`. In these cases, we listed the recomputed values and marked them with an asterisk. All the recomputed LO cross sections are in excellent agreement with the values computed using `WHIZARD`.

Tab. 8 includes all processes at a hadron collider involving one or two weak bosons. All NLO cross sections of processes with a single weak boson on the LHS have been computed with `MG5_aMC 2.7.3`, except for the process  $pp \rightarrow W^\pm jjj$ . Here, we noticed technical difficulties, so instead, we computed the given cross section with `MG5_aMC 2.9.12`. All these cross sections agree better than  $\sigma^{\text{sig}} < 2$ .

Of all processes featuring two weak bosons,  $pp \rightarrow W^+W^- jj$  and  $pp \rightarrow W^+W^+ jj$  show the largest deviations of  $\sigma^{\text{sig}} > 2$ . The cross sections for all other processes, including the very similar process  $pp \rightarrow W^-W^- jj$ , however, agree very well with  $\sigma^{\text{sig}} < 2$ .

In the following table, tab. 9, we list the cross sections for processes with three or four weak bosons in the final state. The most significant deviations among these processes can be observed for  $pp \rightarrow ZZW^\pm$  with  $\sigma^{\text{sig}} = 2.33$  and  $pp \rightarrow W^+W^- ZZ$  with  $\sigma^{\text{sig}} = 3.45$ . The cause for the large discrepancy, especially for the latter process, could not be determined so far. We recomputed both values several times, also with newer versions of `MG5_aMC` up to 2.9.12, to exclude bad seeds causing statistical fluctuations. The differences remain, however. Possible reasons could be differences in the phase-space mappings of both programs affecting unrestricted phase spaces with  $\geq 3$  massive particles in the final state or potential discrepancies in the employed OLPs for this process. On the other hand, considering the scale uncertainties, the cross section computed with `MG5_aMC` is given by  $0.7100 \pm 0.0013$  (stat) $_{-0.0404}^{+0.0497}$  (scale), while for `WHIZARD` we find  $0.7151 \pm 0.0007$  (stat) $_{-0.0407}^{+0.0504}$  (scale). So even for the process  $pp \rightarrow W^+W^- ZZ$  both results agree with  $\sigma_{\text{NLO}}^{\text{sig}} = 0.08$  within the scale uncertainties. implying that the difference is of no relevance for any application. For this reason, we do not consider these individual differences to invalidate the comparison as a whole.

Process	MG5_aMC			WHIZARD			$\sigma_{\text{NLO}}^{\text{sig}}$
	$\sigma_{\text{LO}}[\text{fb}]$	$\sigma_{\text{NLO}}[\text{fb}]$	$K$	$\sigma_{\text{LO}}[\text{fb}]$	$\sigma_{\text{NLO}}[\text{fb}]$	$K$	
$e^+e^- \rightarrow jj$	622.70(5)	639.30(12)	1.03	622.737(8)	639.39(5)	1.03	0.69
$e^+e^- \rightarrow jjj$	340.4(7)	317.3(8)	0.93	340.6(5)	317.8(5)	0.93	0.53
$e^+e^- \rightarrow jjjj$	104.09(20)	103.67(26)	1.00	105.0(3)	104.2(4)	0.99	1.11
$e^+e^- \rightarrow jjjjj$	22.35(5)	24.65(4)	1.10	22.33(5)	24.57(7)	1.10	0.99
$e^+e^- \rightarrow t\bar{t}$	166.32(11)	174.5(3)	1.05	166.37(12)	174.55(20)	1.05	0.14
$e^+e^- \rightarrow t\bar{t}j$	47.95(9)	53.336(10)	1.11	48.12(5)	53.41(7)	1.11	1.05
$e^+e^- \rightarrow t\bar{t}jj$	8.608(18)	10.515(19)	1.22	8.592(19)	10.526(21)	1.23	0.39
$e^+e^- \rightarrow t\bar{t}jjj$	1.0371(21)	1.415(4)	1.36	1.035(4)	1.405(5)	1.36	1.56
$e^+e^- \rightarrow t\bar{t}t\bar{t}$	$0.6385(12) \cdot 10^{-3}$	$1.1941(20) \cdot 10^{-3}$	1.87	$0.6388(8) \cdot 10^{-3}$	$1.1922(11) \cdot 10^{-3}$	1.87	0.83
$e^+e^- \rightarrow t\bar{t}t\bar{t}j$	$2.662(4) \cdot 10^{-5}$	$5.264(9) \cdot 10^{-5}$	1.98	$2.673(7) \cdot 10^{-5}$	$5.251(11) \cdot 10^{-5}$	1.96	0.91

Tab. 5: Comparison of total fixed-order cross sections at LO and NLO QCD for light-jet production and top-quark production in association with light jets between `MG5_aMC` and `WHIZARD`. Results are shown for a 1 TeV  $e^+e^-$  collider, with settings and cuts as explained in sec. 5.2.1. Statistical errors of the integration and the individual  $K$ -factor for each program are shown. For better comparison, we provide the significance  $\sigma_{\text{NLO}}^{\text{sig}}$  of the deviation between the NLO results in the last column. Both LO and NLO `MG5_aMC` results have been recalculated.

Process	MG5_aMC			WHIZARD			
	$\sigma_{\text{LO}}[\text{fb}]$	$\sigma_{\text{NLO}}[\text{fb}]$	$K$	$\sigma_{\text{LO}}[\text{fb}]$	$\sigma_{\text{NLO}}[\text{fb}]$	$K$	$\sigma_{\text{NLO}}^{\text{sig}}$
$e^+e^- \rightarrow t\bar{t}H$	2.021(4)	1.909(3)	0.94	2.020(3)	1.912(3)	0.95	0.71
$e^+e^- \rightarrow t\bar{t}Hj$	$2.545(5) \cdot 10^{-1}$	$2.665(6) \cdot 10^{-1}$	1.05	$2.536(4) \cdot 10^{-1}$	$2.657(4) \cdot 10^{-1}$	1.05	1.11
$e^+e^- \rightarrow t\bar{t}Hjj$	$2.665(5) \cdot 10^{-2}$	$3.141(9) \cdot 10^{-2}$	1.18	$2.646(8) \cdot 10^{-2}$	$3.123(9) \cdot 10^{-2}$	1.18	1.41
$e^+e^- \rightarrow t\bar{t}Z$	4.630(8)	4.942(11)	1.07	4.638(3)	4.937(3)	1.06	0.44
$e^+e^- \rightarrow t\bar{t}Zj$	$6.043(10) \cdot 10^{-1}$	$6.917(24) \cdot 10^{-1}$	1.14	$6.027(9) \cdot 10^{-1}$	$6.921(11) \cdot 10^{-1}$	1.15	0.15
$e^+e^- \rightarrow t\bar{t}Zjj$	$6.426(16) \cdot 10^{-2}$	$8.181(21) \cdot 10^{-2}$	1.27	$6.436(21) \cdot 10^{-2}$	$8.241(29) \cdot 10^{-2}$	1.28	1.68
$e^+e^- \rightarrow t\bar{t}W^\pm jj$	$2.372(5) \cdot 10^{-4}$	$3.714(8) \cdot 10^{-4}$	1.57	$2.387(8) \cdot 10^{-4}$	$3.716(10) \cdot 10^{-4}$	1.56	0.16
$e^+e^- \rightarrow t\bar{t}HZ$	$3.611(7) \cdot 10^{-2}$	$3.592(7) \cdot 10^{-2}$	0.99	$3.623(19) \cdot 10^{-2}$	$3.584(19) \cdot 10^{-2}$	0.99	0.40
$e^+e^- \rightarrow t\bar{t}ZZ$	$3.774(7) \cdot 10^{-2}$	$4.027(8) \cdot 10^{-2}$	1.07	$3.788(6) \cdot 10^{-2}$	$4.032(7) \cdot 10^{-2}$	1.06	0.47
$e^+e^- \rightarrow t\bar{t}HH$	$1.3635(25) \cdot 10^{-2}$	$1.2140(24) \cdot 10^{-2}$	0.89	$1.3650(15) \cdot 10^{-2}$	$1.2168(16) \cdot 10^{-2}$	0.89	0.97
$e^+e^- \rightarrow t\bar{t}W^+W^-$	$1.3632(22) \cdot 10^{-1}$	$1.5350(25) \cdot 10^{-1}$	1.13	$1.3672(21) \cdot 10^{-1}$	$1.5385(22) \cdot 10^{-1}$	1.13	1.05

Tab. 6: Comparison of total fixed-order cross sections at LO and NLO QCD for top-quark production in association with heavy bosons between MG5\_aMC and WHIZARD. Results are shown for a 1 TeV  $e^+e^-$  collider, with settings and cuts as explained in sec. 5.2.1. Statistical errors of the integration and the individual  $K$ -factor for each program are shown. For better comparison, we provide the significance  $\sigma_{\text{NLO}}^{\text{sig}}$  of the deviation between the NLO results in the last column. Both LO and NLO MG5\_aMC results have been recalculated. All processes have been computed in the 5-flavor scheme.

Process	MG5_aMC			WHIZARD			
	$\sigma_{\text{LO}}[\text{fb}]$	$\sigma_{\text{NLO}}[\text{fb}]$	$K$	$\sigma_{\text{LO}}[\text{fb}]$	$\sigma_{\text{NLO}}[\text{fb}]$	$K$	$\sigma_{\text{NLO}}^{\text{sig}}$
$pp \rightarrow jj^*$	$1.1593(23) \cdot 10^9$	$1.6040(29) \cdot 10^9$	1.38	$1.162(4) \cdot 10^9$	$1.601(5) \cdot 10^9$	1.38	0.10
$pp \rightarrow jjj$	$8.940(21) \cdot 10^7$	$7.619(19) \cdot 10^7$	0.85	$9.01(4) \cdot 10^7$	$7.46(9) \cdot 10^7$	0.83	1.73
$pp \rightarrow t\bar{t}$	$4.584(3) \cdot 10^5$	$6.746(14) \cdot 10^5$	1.47	$4.589(9) \cdot 10^5$	$6.740(10) \cdot 10^5$	1.47	0.35
$pp \rightarrow t\bar{t}j^*$	$3.133(5) \cdot 10^5$	$4.095(8) \cdot 10^5$	1.31	$3.123(6) \cdot 10^5$	$4.087(9) \cdot 10^5$	1.31	0.66
$pp \rightarrow t\bar{t}jj^*$	$1.363(3) \cdot 10^5$	$1.784(3) \cdot 10^5$	1.31	$1.360(4) \cdot 10^5$	$1.775(7) \cdot 10^5$	1.31	1.18
$pp \rightarrow t\bar{t}t$	4.505(5)	9.076(13)	2.01	4.485(6)	9.070(9)	2.02	0.38
$pp \rightarrow t\bar{t}W^\pm$	$3.777(3) \cdot 10^2$	$5.668(18) \cdot 10^2$	1.50	$3.775(5) \cdot 10^2$	$5.674(5) \cdot 10^2$	1.50	0.32
$pp \rightarrow t\bar{t}W^\pm j^*$	$2.352(3) \cdot 10^2$	$3.434(8) \cdot 10^2$	1.46	$2.356(7) \cdot 10^2$	$3.427(8) \cdot 10^2$	1.45	0.62
$pp \rightarrow t\bar{t}Z$	$5.273(4) \cdot 10^2$	$7.652(25) \cdot 10^2$	1.45	$5.260(7) \cdot 10^2$	$7.639(9) \cdot 10^2$	1.45	0.49
$pp \rightarrow t\bar{t}Zj$	$3.953(4) \cdot 10^2$	$5.079(14) \cdot 10^2$	1.28	$3.943(14) \cdot 10^2$	$5.069(17) \cdot 10^2$	1.29	0.45
$pp \rightarrow t\bar{t}W^+W^-$	6.675(6)	9.934(19)	1.49	6.679(9)	9.943(11)	1.49	0.41
$pp \rightarrow t\bar{t}ZZ$	1.349(14)	1.843(4)	1.37	1.3590(29)	1.842(3)	1.36	0.20
$pp \rightarrow HZ$	$6.468(8) \cdot 10^2$	$7.693(19) \cdot 10^2$	1.19	$6.474(11) \cdot 10^2$	$7.679(12) \cdot 10^2$	1.19	0.62

Tab. 7: Comparison of total fixed-order cross sections at LO and NLO QCD for the production of top quarks and/or light jets in association with heavy gauge bosons between MG5\_aMC and WHIZARD. Results are shown for a 13 TeV  $pp$  collider, with settings and cuts as explained in sec. 5.2.1. Statistical errors of the integration and the individual  $K$ -factor for each program are shown. For better comparison, we provide the significance  $\sigma_{\text{NLO}}^{\text{sig}}$  of the deviation between the NLO results in the last column. LO MG5\_aMC results are mostly taken from ref. [45]. An asterisk marks the recalculated LO values. NLO results are always recalculated. For the processes with pure multi-jet final state, we impose stricter jet cuts requiring at least  $p_{T,j} > 80$  GeV from all jets present at Born level and at least one jet with  $p_{T,j} > 100$  GeV. Processes with at least two opposite-sign  $W$  bosons are calculated in the four-flavor scheme.

Process	MG5_aMC			WHIZARD			$\sigma_{\text{NLO}}^{\text{sig}}$
	$\sigma_{\text{LO}}[\text{fb}]$	$\sigma_{\text{NLO}}[\text{fb}]$	$K$	$\sigma_{\text{LO}}[\text{fb}]$	$\sigma_{\text{NLO}}[\text{fb}]$	$K$	
$pp \rightarrow W^\pm *$	$1.370(3) \cdot 10^8$	$1.765(5) \cdot 10^8$	1.29	$1.3749(8) \cdot 10^8$	$1.7696(10) \cdot 10^8$	1.29	0.90
$pp \rightarrow W^\pm j *$	$2.045(4) \cdot 10^7$	$2.839(9) \cdot 10^7$	1.39	$2.046(3) \cdot 10^7$	$2.854(5) \cdot 10^7$	1.39	1.46
$pp \rightarrow W^\pm jj$	$6.805(15) \cdot 10^6$	$7.780(13) \cdot 10^6$	1.14	$6.856(12) \cdot 10^6$	$7.814(27) \cdot 10^6$	1.14	1.13
$pp \rightarrow W^\pm jjj$	$1.821(2) \cdot 10^6$	$1.962(4) \cdot 10^6$	1.08	$1.840(5) \cdot 10^6$	$1.978(7) \cdot 10^6$	1.07	1.98
$pp \rightarrow Z$	$4.248(5) \cdot 10^7$	$5.415(16) \cdot 10^7$	1.27	$4.2541(3) \cdot 10^7$	$5.4086(16) \cdot 10^7$	1.27	0.40
$pp \rightarrow Zj$	$7.209(5) \cdot 10^6$	$9.75(3) \cdot 10^6$	1.35	$7.215(4) \cdot 10^6$	$9.733(10) \cdot 10^6$	1.35	0.54
$pp \rightarrow Zjj$	$2.348(6) \cdot 10^6$	$2.684(5) \cdot 10^6$	1.14	$2.364(5) \cdot 10^6$	$2.676(7) \cdot 10^6$	1.13	0.93
$pp \rightarrow Zjjj$	$6.344(8) \cdot 10^5$	$6.897(22) \cdot 10^5$	1.09	$6.381(23) \cdot 10^5$	$6.85(3) \cdot 10^5$	1.07	1.26
$pp \rightarrow W^+W^-$	$7.355(5) \cdot 10^4$	$10.296(28) \cdot 10^4$	1.40	$7.352(10) \cdot 10^4$	$10.268(11) \cdot 10^4$	1.40	0.93
$pp \rightarrow W^+W^-j$	$2.865(3) \cdot 10^4$	$3.716(10) \cdot 10^4$	1.30	$2.853(7) \cdot 10^4$	$3.733(7) \cdot 10^4$	1.31	1.39
$pp \rightarrow W^+W^-jj *$	$1.1480(24) \cdot 10^4$	$1.3866(24) \cdot 10^4$	1.21	$1.150(5) \cdot 10^4$	$1.372(6) \cdot 10^4$	1.19	2.26
$pp \rightarrow W^+W^+jj *$	$1.5011(19) \cdot 10^2$	$2.252(4) \cdot 10^2$	1.50	$1.506(5) \cdot 10^2$	$2.235(7) \cdot 10^2$	1.48	2.11
$pp \rightarrow W^-W^-jj$	$6.752(7) \cdot 10^1$	$9.994(14) \cdot 10^1$	1.48	$6.772(24) \cdot 10^1$	$9.982(28) \cdot 10^1$	1.47	0.38
$pp \rightarrow ZW^\pm$	$2.777(3) \cdot 10^4$	$4.485(12) \cdot 10^4$	1.62	$2.780(5) \cdot 10^4$	$4.488(4) \cdot 10^4$	1.61	0.24
$pp \rightarrow ZW^\pm j$	$1.605(5) \cdot 10^4$	$2.100(5) \cdot 10^4$	1.31	$1.609(4) \cdot 10^4$	$2.0940(28) \cdot 10^4$	1.30	1.05
$pp \rightarrow ZW^\pm jj$	$8.038(9) \cdot 10^3$	$9.05(2) \cdot 10^3$	1.13	$8.06(3) \cdot 10^3$	$9.02(4) \cdot 10^3$	1.12	0.67
$pp \rightarrow ZZ *$	$1.0971(20) \cdot 10^4$	$1.4185(25) \cdot 10^4$	1.29	$1.0969(10) \cdot 10^4$	$1.4183(11) \cdot 10^4$	1.29	0.07
$pp \rightarrow ZZj$	$3.662(3) \cdot 10^3$	$4.817(16) \cdot 10^3$	1.32	$3.667(9) \cdot 10^3$	$4.807(8) \cdot 10^3$	1.31	0.56
$pp \rightarrow ZZjj *$	$1.3454(24) \cdot 10^3$	$1.678(3) \cdot 10^3$	1.25	$1.356(6) \cdot 10^3$	$1.684(8) \cdot 10^3$	1.24	0.70

Tab. 8: Comparison of total fixed-order cross sections at LO and NLO QCD for heavy vector boson (pair) production in association with light jets between MG5\_aMC and WHIZARD. Results are shown for a 13 TeV  $pp$  collider, with settings and cuts as explained in sec. 5.2.1. Statistical errors of the integration and the individual  $K$ -factor for each program are shown. For better comparison, we provide the significance  $\sigma_{\text{NLO}}^{\text{sig}}$  of the deviation between the NLO results in the last column. LO MG5\_aMC results are mostly taken from ref. [45]. An asterisk marks the recalculated LO values. All NLO results have been recalculated. Processes with at least two opposite-sign  $W$  bosons are calculated in the four-flavor scheme.

Process	MG5_aMC			WHIZARD			$\sigma_{\text{NLO}}^{\text{sig}}$
	$\sigma_{\text{LO}}[\text{fb}]$	$\sigma_{\text{NLO}}[\text{fb}]$	$K$	$\sigma_{\text{LO}}[\text{fb}]$	$\sigma_{\text{NLO}}[\text{fb}]$	$K$	
$pp \rightarrow W^+W^-W^\pm$	$1.307(3) \cdot 10^2$	$2.111(4) \cdot 10^2$	1.62	$1.3033(21) \cdot 10^2$	$2.1170(22) \cdot 10^2$	1.62	1.31
$pp \rightarrow W^+W^-W^\pm j$	$9.167(10) \cdot 10^1$	$12.00(4) \cdot 10^1$	1.31	$9.149(26) \cdot 10^1$	$11.985(29) \cdot 10^1$	1.31	0.30
$pp \rightarrow ZW^+W^-$	$9.658(65) \cdot 10^1$	$16.751(27) \cdot 10^1$	1.73	$9.742(15) \cdot 10^1$	$16.824(16) \cdot 10^1$	1.73	2.33
$pp \rightarrow ZW^+W^- j$	$8.340(10) \cdot 10^1$	$10.590(17) \cdot 10^1$	1.27	$8.325(23) \cdot 10^1$	$10.600(26) \cdot 10^1$	1.27	0.32
$pp \rightarrow ZZW^\pm *$	$3.073(6) \cdot 10^1$	$5.630(12) \cdot 10^1$	1.83	$3.062(6) \cdot 10^1$	$5.615(6) \cdot 10^1$	1.83	1.12
$pp \rightarrow ZZW^\pm j$	$2.810(4) \cdot 10^1$	$3.652(7) \cdot 10^1$	1.30	$2.816(8) \cdot 10^1$	$3.673(9) \cdot 10^1$	1.30	1.84
$pp \rightarrow ZZZ *$	$1.0833(18) \cdot 10^1$	$1.431(5) \cdot 10^1$	1.32	$1.0842(16) \cdot 10^1$	$1.4295(16) \cdot 10^1$	1.32	0.29
$pp \rightarrow ZZZ j$	4.823(11)	6.386(23)	1.32	4.845(16)	6.391(18)	1.32	0.17
$pp \rightarrow W^+W^-W^\pm Z *$	0.6575(12)	1.233(3)	1.88	0.6604(18)	1.2404(20)	1.88	2.05
$pp \rightarrow W^+W^-ZZ$	0.4320(13)	0.7100(13)	1.64	0.4316(7)	0.7151(7)	1.66	3.45
$pp \rightarrow W^\pm ZZZ$	0.05862(10)	0.12446(26)	2.12	0.05869(8)	0.12468(13)	2.12	0.76

Tab. 9: Comparison of total fixed-order cross sections at LO and NLO QCD for the production of three to four heavy vector bosons in association with light jets between MG5\_aMC and WHIZARD. Results are shown for a 13 TeV  $pp$  collider, with settings and cuts as explained in sec. 5.2.1. Statistical errors of the integration and the individual  $K$ -factor for each program are shown. For better comparison, we provide the significance  $\sigma_{\text{NLO}}^{\text{sig}}$  of the deviation between the NLO results in the last column. LO MG5\_aMC results are mostly taken from ref. [45]. An asterisk marks the recalculated LO values. NLO results are always recalculated. Processes with at least two opposite-sign  $W$  bosons are calculated in the four-flavor scheme.

### 5.3 Validation of the real partition

In sec. 2.6.3, we discussed the possibility of partitioning the real contribution to the NLO cross section into a finite and a singular part. To validate also this approach, we recompute the total real cross sections of a selection of processes from each category in the same setup used in the previous section. We compare the real cross sections computed in the standard approach, without using the real partition, with the sum of both contributions the real partition yields. In the latter approach, we choose a small real-partition scale of  $h_F = 10 \text{ GeV}$  to amplify the potential differences of both approaches.

The results are listed in tab. 10. It contains the real cross sections and the significance measure of their deviation,  $\sigma^{\text{sig}}$ , for three different  $e^+e^-$  and three different  $pp$  processes. The almost same absolute value of the three  $e^+e^-$  cross sections is a coincidence. The real cross sections alone barely have any physical meaning as their value may depend on details of the subtraction scheme (c.f. tab. 3 and 4). For all processes, we observe a large cancellation between the real finite and the real singular contribution owing to the low value of  $h_F$  chosen. For this reason, the uncertainty of the total real cross section is larger when using the real partition in this case. The real singular contribution takes negative values here since all the subtraction terms are included in the real singular part, regardless of the chosen real-partition scale. All cross sections computed using the real partition agree better than  $\sigma^{\text{sig}} < 1$  with the corresponding value computed without the real partition. This makes us confident that the implementation of the real partition is correct.

process	no partition		with partition				$\sigma^{\text{sig}}$		
	$\sigma^{\mathcal{R}}$		$\sigma^{\mathcal{R}_{\text{sin}}}$	$\sigma^{\mathcal{R}_{\text{fin}}}$	$\sigma^{\mathcal{R}_{\text{sin}}} + \sigma^{\mathcal{R}_{\text{fin}}}$				
$e^+e^- \rightarrow jj$	37.30(2)	fb	-1805.0(4)	fb	1841.9(4)	fb	36.9(5)	fb	0.77
$e^+e^- \rightarrow jjj$	38.4(3)	fb	- 961.6(2)	fb	999.5(6)	fb	37.9(6)	fb	0.68
$e^+e^- \rightarrow t\bar{t}$	-39.61(3)	fb	- 134.87(13)	fb	95.27(6)	fb	-39.60(14)	fb	0.04
$pp \rightarrow jj$	80.2(1.1)	nb	-6492.0(1.1)	nb	6572.4(3)	nb	80(3)	nb	0.03
$pp \rightarrow t\bar{t}j$	-117.2(5)	pb	- 933.7(5)	pb	816.5(4)	pb	-117.2(7)	pb	0.03
$pp \rightarrow t\bar{t}W^\pm$	89.32(11)	fb	- 519.1(2)	fb	608.5(2)	fb	89.4(3)	fb	0.39

Tab. 10: Comparison of cross sections computed with and without using the real partition.  $\sigma^{\mathcal{R}}$  is the total real cross section,  $\sigma^{\mathcal{R}_{\text{sin}}}$  and  $\sigma^{\mathcal{R}_{\text{fin}}}$  denote the cross section of the real singular and the real finite cross section, respectively. In the last column, we indicate the agreement of the real cross section and the sum of both real components when using the real partition as  $\sigma^{\text{sig}}$  in analogy to eq. (5.11). All computations have been performed in the setup described in sec. 5.2.1. We chose a real-partition scale of  $h_F = 10 \text{ GeV}$  for the processes computed using the real partition.

## 6 Applications of POWHEG matching

So far, we have focussed on validating and predicting total cross sections. In this section, we will turn our attention to differential distributions of fNLO events, whose simulation we explained in sec. 2.8 and POWHEG events as well as events fully matched to a parton shower using the POWHEG-matching procedure we discussed in detail in sec. 3.

Our discussion in these two sections is fully general and applies to all processes at hadron and lepton colliders. The same holds for our implementations of both procedures in the MC generator WHIZARD, which was carried out in the course of this thesis. Nevertheless, we can only discuss a limited number of examples.

Our choice is twofold: On the one hand, we choose one of the simplest yet most thoroughly studied processes at the LHC, the production of two opposite-sign leptons,  $pp \rightarrow e^+e^-$ , coined (neutral-current) *Drell-Yan* process [178]. It is simple enough to understand and validate the effects of the POWHEG-matching method while still featuring all the challenges of processes with hadronic initial state and ISR.

At first, we will perform an in-depth comparison of our predictions with calculations from the POWHEG-BOX in a simplified setup and then proceed to a much more realistic setup in a comparison with actual measured data from the LHC Run 2 taken in 2016 with the CMS detector.

On the other hand, we pick top-quark pair production in association with a jet,  $e^+e^- \rightarrow t\bar{t}j$ , as representative of processes at lepton colliders. It is an interesting process in top-quark measurements and also the optimal candidate to probe the real partition in the context of POWHEG matching on a process featuring FSR off massive and massless emitters without the complication of additional initial-state radiation.

### 6.1 The Drell-Yan process $pp \rightarrow e^+e^-$ compared to the POWHEG-BOX

In the first step, we validate our implementation of the POWHEG-matching procedure for the example of the Drell-Yan process with the POWHEG-BOX. Examples of the contributing Feynman diagrams to this process at LO and NLO are depicted in fig. 6.1.

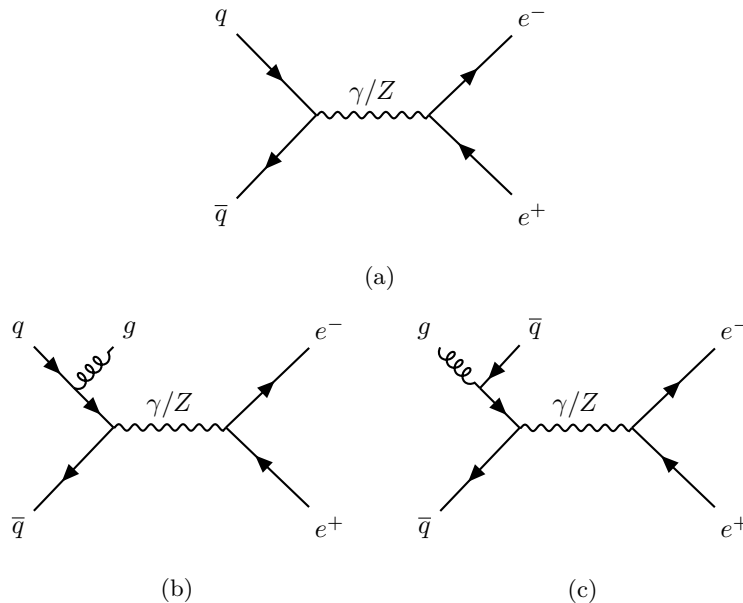


Fig. 6.1: Feynman diagrams contributing to the Drell-Yan process  $pp \rightarrow e^+e^-$  at LO (upper row) and to the NLO real correction (lower row). Contributing virtual loop diagrams are omitted.

This process is the optimal candidate for this comparison, as it is simple yet already displays many non-trivial features, such as the presence of a non-trivial initial state, requiring the involvement of PDFs, the requirement of phase-space cuts already at Born level, as the process for massless electrons would be IR singular and multiple Born as well as real flavor structures, due to the rich content of the proton, including flavor-changing initial-state splittings. Especially the latter require a careful assignment of the PDFs and also gluon radiation from the initial state for which we grouped together ALRs assigned a single emitter 0. Additionally, it is the cleanest possible validation of the POWHEG matching implementation using the ISR UBF we discussed in sec. 3.5.7.

### 6.1.1 Process setup and event selection

We choose a comparatively simple setting in our comparison of calculated cross sections and differential distributions for  $pp \rightarrow e^+e^-$  with the POWHEG-BOX. For this computation, we employ the SM in the  $G_F - m_W - m_Z$  input scheme with numerical input parameters given by

$$G_\mu = 1.16639 \cdot 10^{-5} \text{ GeV}^{-2},$$

$$m_e = m_d = m_u = m_s = m_c = m_b = 0 \text{ eV} \quad \text{and} \quad m_t = 173.2 \text{ GeV},$$

$$\begin{aligned} m_W &= 80.419 \text{ GeV} & \Gamma_W &= 2.049 \text{ GeV} \\ m_Z &= 91.188 \text{ GeV} & \Gamma_Z &= 2.443 \text{ GeV} \\ m_H &= 125.0 \text{ GeV} & \Gamma_H &= 4.143 \text{ MeV}, \end{aligned}$$

where the masses and widths refer to the pole values for the gauge bosons. They are used for the results at LO and NLO alike for better comparability. The electromagnetic coupling is determined from the above input parameters to take the fixed value

$$\alpha = \frac{\sqrt{2}}{\pi} G_\mu m_W^2 \left( 1 - \frac{m_W^2}{m_Z^2} \right) = 0.00754677 \quad \text{and} \quad \alpha_S(m_Z) = 0.120179 \quad (6.1)$$

is the value we use for the strong coupling constant, determined by the MSTW2008nlo68c1 PDF [175], employed by LHAPDF 6.3.0. It is graphically shown in fig. 6.2.

We take the matrix elements for the Born process  $pp \rightarrow e^+e^-$  at the order  $\mathcal{O}(\alpha_S^0 \alpha^2)$  from 0'Mega and all other matrix elements from OpenLoops. We choose a CM energy of  $\sqrt{S_{\text{had}}} = 14 \text{ TeV}$  with symmetric proton-beam setup and fixed factorization and renormalization scale given by

$$\mu_F = \mu_R = m_Z \quad . \quad (6.2)$$

As this process features just two leptons in the final state at the Born level, choosing a lower bound on the invariant lepton mass of

$$m_{e^+e^-} > 10 \text{ GeV} \quad (6.3)$$

is sufficient to exclude the phase-space divergence at low  $\sqrt{s}$  but still leaves the low-energy region in which the details of the matching scheme are most important.

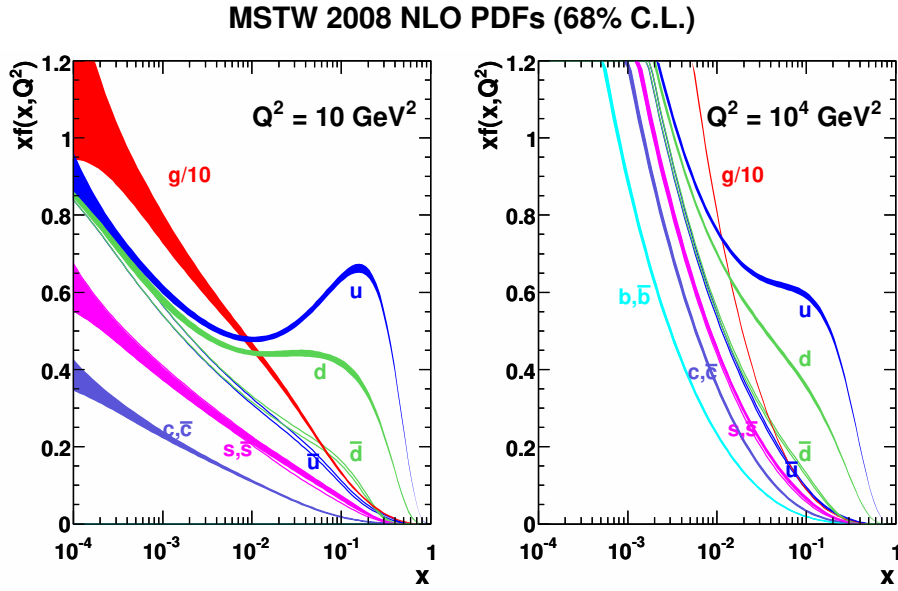


Fig. 6.2: MSTW 2008 NLO PDFs at  $\mu_F^2 = Q^2 = 10 \text{ GeV}^2$  and  $\mu_F^2 = Q^2 = 10^4 \text{ GeV}^2$  including the  $1\sigma = 68\%$  confidence level uncertainty bands [175].

In order to simplify the event simulation, we use the combined integration mode for all NLO components. The fNLO events are generated weighted according to the procedure described in sec. 2.8. We generate unweighted events for the POWHEG events and those matched to a parton shower. This avoids the problem that kinematical edge cases causing technical problems in the shower or the analysis routines are more likely to occur in weighted events associated with very low weights. For the POWHEG matching, we choose a  $10 \times 10$  POWHEG grid (c.f. sec. 3.5.4) and a low value of  $p_{T,\text{min}} = 1 \text{ GeV}$  as our focus in this comparison lies on the matching procedure rather than on the behavior of the employed parton shower. Furthermore, we perform a resonance insertion (c.f. sec. 3.6.8) for the parton shower to preserve the resonances in such a way that a resonant  $Z$  boson is inserted in every generated event, equivalent to the behavior of the POWHEG-BOX.

### 6.1.2 Total cross sections

Tab. 11 lists the total cross sections in this setting at LO and NLO computed with WHIZARD as well as the POWHEG-BOX. It includes the statistical uncertainties determined from the MC integration uncertainty as well as the scale uncertainties determined by varying the scale choice of eq. (6.2) by a factor of 2 up and down<sup>20</sup>.

program	order	cross section	$\pm$ stat. unc.	$\pm$ scale unc.	$\sigma^{\text{sig}}$
WHIZARD	LO	13620.93	$\pm 1.92$	+ 2956 (21.7%) - 2842 (20.9%)	1.48
POWHEG		13625.83	$\pm 2.70$	+ 2953 (21.7%) - 2843 (20.9%)	
WHIZARD	NLO	9649.46	$\pm 1.89$	+ 308 (3.19%) - 390 (4.04%)	0.52
POWHEG		9650.83	$\pm 1.87$	+ 306 (3.17%) - 393 (4.07%)	

Tab. 11: Table of LO and NLO cross sections in pb for the process  $pp \rightarrow e^+e^-$  computed with the POWHEG-BOX and WHIZARD. Statistical uncertainties, i.e., the MC integration uncertainties and scale uncertainties are shown separately.

<sup>20</sup>We refrain from an independent variation of the renormalization and the factorization scale here. We also neglect PDF uncertainties.

The last column quantifies the significance of the deviation of both results from WHIZARD and the POWHEG-BOX in terms of

$$\sigma^{\text{sig}} := \frac{|\sigma^{\text{WZ}} - \sigma^{\text{PG}}|}{\sqrt{(\Delta_{\sigma^{\text{WZ}}}^{\text{stat}})^2 + (\Delta_{\sigma^{\text{PG}}}^{\text{stat}})^2}} \quad , \quad (6.4)$$

defined in full analogy to eq. (5.11). With values far below 2, we find excellent agreement between both programs for the results at LO as well as NLO.

We should also interpret the cross-section values. We see that from LO to NLO, the scale uncertainties decrease by about 90% thanks to the higher-order perturbative terms taken into account. The total cross section also decreases significantly at NLO. When discussing the effect of NLO corrections, it is useful to define the  $K$ -factor

$$K := \frac{\sigma_{\text{NLO}}}{\sigma_{\text{LO}}} \quad \text{and} \quad \delta_{\text{NLO}} := \frac{\sigma_{\text{NLO}} - \sigma_{\text{LO}}}{\sigma_{\text{LO}}} = K - 1 \quad (6.5)$$

as the *NLO correction*. In this case, we find  $K = 0.708$ , which amounts to an NLO correction of  $\delta_{\text{NLO}} \approx -30\%$ . At first glance, this is unexpected as the Drell-Yan process is known [179–182] to receive large and positive NLO QCD corrections, mostly due to the fact that only the NLO corrections open up gluonic production channels not present at LO (fig. 6.1c). These channels are enhanced by typically large gluon PDFs at the LHC, which we can also see in fig. 6.2. In this case, however, this effect is overcompensated by another effect. While it is true that the NLO corrections in the high-energy regime are positive, the majority of the cross section comes from the lower end of the phase-space region allowed by eq. (6.3). We can verify this by computing the cross section at higher invariant lepton masses. The results are shown in tab. 12. We clearly see that at higher energies, the total cross section decreases drastically, while the NLO correction increases by up to roughly +20%.

At lower CM energies, we typically find lower values of  $x$  (c.f. eq. (2.10)). In our construction of the FKS phase space, we learned that we construct the real phase space from the Born phase space in such a way that the mass of the recoil system, which in our case equals  $m_{e^+e^-}$ , stays unaltered. This also holds for ISR where this implies  $x_{\mathcal{R}} \geq x_{\mathcal{B}}$  (c.f. eq. (2.114)). From the RHS of fig. 6.2, we see that the PDFs decrease with this change, especially at  $\mu_R^2 = m_Z^2 \approx 10^4 \text{ GeV}^2$ , explaining our observation.

	$m_{e^+e^-} > 10 \text{ GeV}$	$m_{e^+e^-} > 50 \text{ GeV}$	$m_{e^+e^-} > 100 \text{ GeV}$
LO	$13620.93 \pm 1.92$	$1892.30 \pm 0.14$	$72.635 \pm 0.005$
NLO	$9649.46 \pm 1.89$	$2151.79 \pm 0.17$	$85.500 \pm 0.007$
K	0.71	1.14	1.18

Tab. 12: Table of cross sections for the process  $pp \rightarrow e^+e^-$  with increasing selection cut on the invariant lepton mass. The cross sections have been computed with WHIZARD and are given in pb.

In sec. 2.6.3, we discussed the possibility of splitting the real contribution into a singular and a remaining finite part. We validated the real partition at the level of cross sections already in sec. 5.3 for a number of processes. Additionally, we want to study the impact of different real-partition scales on the partial cross sections of the Drell-Yan process in this section.

Tab. 13 shows the Drell-Yan cross sections computed with the real partition in the setup mentioned in sec. 6.1.1 for three different values of the real-partition scale,  $h_F$ . The cross section labeled "finite" refers to the cross section of the finite real component only, while the cross section labeled "combined" combines the cross section contributions of all other components, including the singular real component. We clearly see that also in this case, the sum of both parts is constant and statistically compatible with the total NLO cross section reported in tab. 11. Although the same amount of iterations and calls have been performed in

the integrations, the result with the lowest real-partition scale  $h_F$  is the least precise as, in this case, we are integrating the unsubtracted real cross section almost separately from the subtraction terms.

	$h_F$	combined	finite	sum
WHIZARD	5 GeV	$1719.25 \pm 2.92$	$7937.52 \pm 2.61$	$9656.77 \pm 3.92$
WHIZARD	50 GeV	$9369.71 \pm 1.66$	$280.69 \pm 0.23$	$9650.40 \pm 1.68$
WHIZARD	100 GeV	$9595.36 \pm 1.76$	$55.34 \pm 0.05$	$9650.70 \pm 1.76$

Tab. 13: Table of cross sections for the process  $pp \rightarrow e^+e^-$  computed with WHIZARD for different real-partition scales,  $h_F$ . The "combined" cross section is determined from the sum of the Born, the virtual, the DGLAP remnant and the singular real NLO component, while the "finite" cross section belongs to just the finite real part. All cross sections are given in pb. The stated uncertainties are MC integration uncertainties only.

### 6.1.3 POWHEG events

We will dedicate this section to a detailed comparison of differential distributions generated using POWHEG events simulated by WHIZARD and the POWHEG-BOX. At this stage, up to a single emission has been generated using the POWHEG-matching prescription discussed in sec. 3, and no parton shower has been applied yet, meaning that we are inspecting an intermediate step to the fully showered distributions still at parton level. The generated events are analyzed and plotted using Rivet 3.1.4 [94]. We show the results in fig. 6.3. The differential distributions therein set the NLO distributions of the POWHEG-BOX's and WHIZARD's generated POWHEG events labeled "POWHEG NLO" and "WHIZARD NLO", respectively, in comparison with the LO and the fNLO distribution of events simulated with WHIZARD<sup>21</sup>.

Fig. 6.3a shows the differential distribution of the invariant dilepton mass  $m_{e^+e^-} := \sqrt{(p_{e^+} + p_{e^-})^2}$ . In the upper part of the plot, we see the absolute value of the observables per bin in pb/GeV. In contrast, the lower part shows the ratio over the distribution of the POWHEG events, generated with WHIZARD, for which the scale uncertainty is shown as a light blue band. In the general shape, we can clearly see the  $Z$ -pole at  $m_{e^+e^-} = m_Z$  as well as the photon-propagator divergence at low  $m_{e^+e^-}$ , cut off at 10 GeV.

In the ratio plot, we observe excellent agreement between all NLO distributions over the full range of  $m_{e^+e^-}$  shown. Even the fixed-order distribution agrees well with both distributions of POWHEG events because the invariant dilepton mass is equal to the radiation recoil mass, which is preserved in the construction of the NLO phase space. This is also the reason for the comparatively few bins with uncertainty spikes in the fNLO distribution, as the counter-events end up in the same bin as the corresponding subevents with positive weights. We can now also graphically understand the negative total NLO corrections we investigated using total cross sections in the previous section. We can clearly see that the NLO corrections are negative only in the range of  $m_{e^+e^-} < m_Z/2$ , where the photon propagator dominates.

In the middle row on the LHS in fig. 6.3b, we compare the distributions of the electron transverse momentum  $p_{T,e^-} := \sqrt{p_{x,e^-}^2 + p_{y,e^-}^2}$ . We see a pronounced maximum at about  $p_{T,e^-} \approx 5$  GeV, which is the result of the huge number of events at a low dilepton mass cutoff at 10 GeV.

We can observe a second, less pronounced peak at  $p_{T,e^-} = m_Z/2$ . For the LO events, it is followed by a clear cutoff. This feature is known as the *Jacobian peak*, which is often used for vector-boson-mass measurements. It can be explained as the consequence of a variable transformation to  $p_T$ . If the  $Z$  boson would decay at

<sup>21</sup>The term "POWHEG events" refers to the events generated using the POWHEG-matching prescription. They are partonic events, not including the effects of parton showering and hadronization.

rest, we had  $p_{T,e^-} = \frac{m_Z}{2} \sin(\theta)$  so that we get

$$\frac{d\sigma}{dp_{T,e^-}} = \frac{d\sigma}{d\cos(\theta)} \frac{d\cos(\theta)}{dp_{T,e^-}} = \frac{d\sigma}{d\cos(\theta)} \frac{2p_{T,e^-}}{m_Z \sqrt{\left(\frac{m_Z}{2}\right)^2 - p_{T,e^-}^2}}, \quad (6.6)$$

describing the said sharp peak and cutoff. Now the  $Z$  boson is typically not produced at rest. It is more likely to be boosted, especially if it originates from a  $q\bar{q}$  pair in which one of the quarks is a valence quark. As this boost is along the  $z$  axis, it does not disturb this picture. With additional ISR, the  $Z$  boson momentum may also have a transverse component so that we can observe electron transverse momenta larger than  $m_Z/2$  beyond LO.

Comparing the NLO distributions, we again find agreement between both distributions of POWHEG events. While also the fNLO distribution agrees with both predictions in the range  $p_{T,e^-} < m_Z/2$ , it deviates beyond that. This is a general feature that goes back to two of the main principles of the matching. The matching is designed to suppress the soft regions prior to the showering. Requiring a conservation of the total cross section at the same time implies an enhancement at large radiation energies, which is what we see in fig. 6.3b beyond  $p_{T,e^-} \approx m_Z/2$ .

At this critical point, we can also see one of the typical issues of fixed-order NLO events we discovered in sec. 2.8.1: events with very soft real radiation typically require a large cancellation of positive and negative weights. The additional radiation, however, tends to cause a slightly larger transverse momentum for the real subevents than for the Born-like counterevents. This circumstance separates the two contributions in the neighboring bins in the center of the plot, causing the odd behavior of a very small entry followed by a drastic increase in the next bin.

The electron rapidity is depicted on the RHS in fig. 6.3c. Here, the agreement between all NLO predictions is remarkable across the entire range. The LO distribution, however, is much more central as the LO simulation is missing the intrinsic  $p_T$  of the  $Z$  boson. Our observations concerning the agreement between fixed-order and POWHEG events as well as misbinning effects of fNLO events also hold in this case as rapidity differences are invariant under the boost of the recoil system from the Born to real phase space.

Both previously discussed distributions for the positrons are omitted. They are equivalent to the electron distributions, as there is no preferred charge.

Fig. 6.3d and 6.3e in the lower row show the transverse momentum and rapidity distribution of the radiated parton, respectively. Both histograms can only be filled by events featuring real radiation. For this reason, no LO distribution is shown. This also implies that the distributions are not NLO-accurate themselves but rather resemble the LO description of the process  $pp \rightarrow e^+e^- j$ .

In these distributions, we see a clear peak of the fNLO distributions in the central rapidity region and the region of low  $p_{T,j_1}$ . Technically, the leftmost bin in the  $p_{T,j_1}$  distribution of the fNLO events is not well-defined as it contains arbitrarily soft radiations. Without any requirements on the jet energy, the transverse momentum is not an IR safe observable even if we applied a jet-clustering algorithm (which is an identity operation at parton level, in this case, anyways). We thus exclude all events with  $p_{T,j_1} < 2 \text{ GeV}$  in both histograms to only show finite results. The remaining events at low  $p_{T,j_1}$  lead to an overshoot in the central region of the rapidity distribution nonetheless. The lower fNLO prediction for larger jet transverse momenta fits to the fNLO prediction of the lepton transverse momentum at high  $p_T$ .

Comparing the fNLO distributions with the POWHEG events, we see that the latter generally show a much less severe behavior, taming the divergence towards low values of  $p_{T,j_1}$ , which is one of the main goals of the matching prescription. The LL resummation performed by the parton-shower radiation is curing the fNLO deficiencies. Between both distributions of POWHEG events, we again see a very good agreement across

the vast majority of both radiation distributions. This is remarkable as the kinematic description of the radiation is most sensitive to the details of the matching algorithm. Taking a closer look at the regions of very low transverse momenta and angles to the beam axis, however, we can spot some deviations of up to 3%. At the low-energy end of the distributions, this can be caused by minor technical differences such as the choice of  $\xi_{\min}$  (c.f. eq. (2.39)) or internal process-independent technical cuts on energies and momenta to avoid numerically instable regions in the matrix-element calculations. In less technical applications, however, these different choices do not pose a problem since the low-energy region is typically simulated by the SMC rather than the fixed-order description by choosing a value for  $p_{T,\min}$  larger than the 1 GeV chosen here. Furthermore, this very soft region is often cut out of the fiducial phase space in experimental analyses.

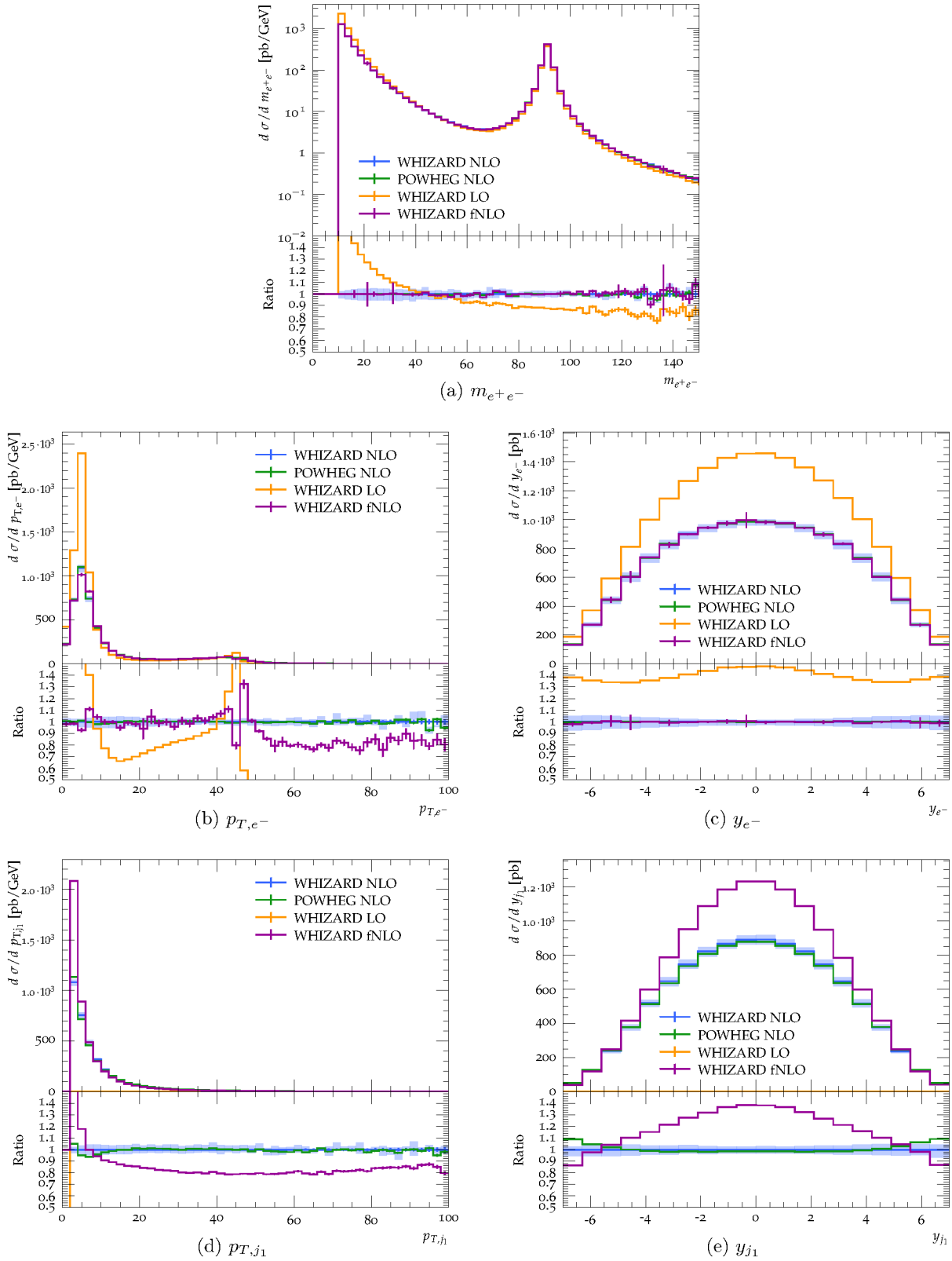


Fig. 6.3: Comparison of LO, fNLO and NLO distributions for  $pp \rightarrow e^+e^-$  from WHIZARD and the POWHEG-BOX. The error bars depict the statistical uncertainty, while the light blue band indicates the scale uncertainty of the WHIZARD NLO event distribution. We simulated 50M weighted POWHEG events with WHIZARD and 50M unweighted POWHEG events with the POWHEG-BOX and additionally 10M unweighted LO events and 10M weighted fNLO event groups with WHIZARD. No real partition was used and no parton shower has been applied yet.

All distributions discussed so far have been generated without the use of the real partition, although in sec. 3.6.3, we emphasized the benefits of the real partition in conjunction with the POWHEG-matching scheme. The neutral Drell-Yan process at tree level is remarkably simple. So simple that the Born matrix element in the denominator of the Sudakov form factor (c.f. eq. (3.9)) has no zeroes making it possible to find a suitable UBF also without partitioning the real matrix element as we have seen in fig. 6.3.

We still want to use this opportunity to understand the effects of the real partition. For this purpose, fig. 6.4 shows differential distributions of POWHEG events for the same observables as discussed before generated with the real partition for both MC generators WHIZARD and the POWHEG-BOX.

WHIZARD employs the real partition criterion given by eq. (2.161), which depends on the real-partition scale  $h_F$ . As explained in sec. 2.6.3, this scale determines which portion of the real matrix element is considered to be part of the finite contribution and can thus be generated separately from the POWHEG-matching procedure. A large real-partition scale leads to a small finite part such that  $h_F = \sqrt{S_{\text{had}}}$  reproduces the case of no applied partition at all. The POWHEG-BOX on the other hand, uses eq. (2.163) as real-partition criterion and, as described in sec. 3.6.4, an additional criterion inspired by eq. (2.164), with a real partition function given by

$$F = \frac{h_{\text{damp}}^2 m_Z^2}{h_{\text{damp}}^2 m_Z^2 + p_{T,Z}^2} \quad . \quad (6.7)$$

It has the same edge behavior as WHIZARD's approach for small  $p_T$ . This partition function is equivalent to eq. (3.119) but here, the dimensionful quantity  $m_Z$  has been factored out, so that  $h_{\text{damp}}$  is dimensionless in this context. In this case, we have chosen the recommended value of  $h_{\text{damp}} = 0.25$ .

In the distribution of the invariant dilepton mass and the electron rapidity in fig. 6.4a and 6.4c we can barely spot any significant difference between the displayed distributions. This is no surprise as we noticed before that both distributions show a general consensus between the fNLO and POWHEG event distributions.

Fig. 6.4b, on the other hand, is more conclusive. It shows the electron transverse momentum. There are only minor deviations at  $p_{T,e^-} < m_Z/2$ , but beyond that, we can observe a few things. While the agreement between both distributions without real partition is still visible, we see that they also agree with the distribution corresponding to the largest real-partition scale  $h_F = 100$  GeV up to  $p_{T,e^-} \approx 80$  GeV. This nicely confirms the expected behavior described above while at the same time assuring that nothing went wrong during the general procedure of generating events using the real partition (c.f. app. D for the technical details on that). Moreover, we also find a good agreement of both predictions applying a strong real-partition criterion for the events generated with the POWHEG-BOX and WHIZARD, although the chosen real-partition functions are not identical (c.f. eq. (2.161) vs. eq. (2.164)), confirming that both are valid choices. Regarding the distribution with the intermediate real-partition scale of  $h_F = 50$  GeV, we see that it interpolates nicely between the distributions with a strong ( $h_F = 5$  GeV) and no real partition at all. This is also true for further real-partition scale choices, which we do not show explicitly to avoid cluttering the picture. In our discussion of fig. 6.3b, we noticed that the matching causes an enhancement at high transverse momenta. We can see here that the real partition can remedy this problem as for small real-partition scales, the fNLO behavior at large  $p_T$  can be restored. This property is an advantage of the real partition beyond remedying the problem of Born zeroes.

Most of these observations are equally valid for the remaining two distributions describing the radiated parton. The effect of the real partition helping to restore the fNLO behavior is even more pronounced in the transverse-momentum distribution in fig. 6.4d. More precisely, we can see that the distributions with real partition tend to agree with the fixed-order predictions at about  $p_{T,j_1} \approx h_F$ .

In realistic applications, we recommend not choosing a too low value for  $h_F$  to use the benefits of the

real partition while keeping the fNLO accuracy at high  $p_T$ . Also, based on our findings in sec. 3.6.9, very small central values for  $h_F$  should be avoided in order to avoid generating a large fraction of negatively weighted events. To estimate the associated uncertainty, we recommend varying it by a factor of 2, or more conservatively, by a factor of 4.

We can also spot one more effect, namely a difference between both strong partitioning predictions of WHIZARD and the POWHEG-BOX. We can see that WHIZARD predicts up to 20% more events in the region of very low  $p_{T,j_1}$ . The reason is that with a real-partition scale of  $h_F = 5$  GeV, events with a similarly low radiation transverse momentum belong to the finite part of the real partition, which does not include any subtraction terms. We thus observe a behavior similar to that of the fNLO events we saw in fig. 6.3: an excess at low  $p_{T,j_1}$  and central  $y_{j_1}$ . This is another hint that a too-low choice for the real-partition scale will not optimally describe low energy emissions, which, on the other hand, are usually better described by the SMC, anyways.

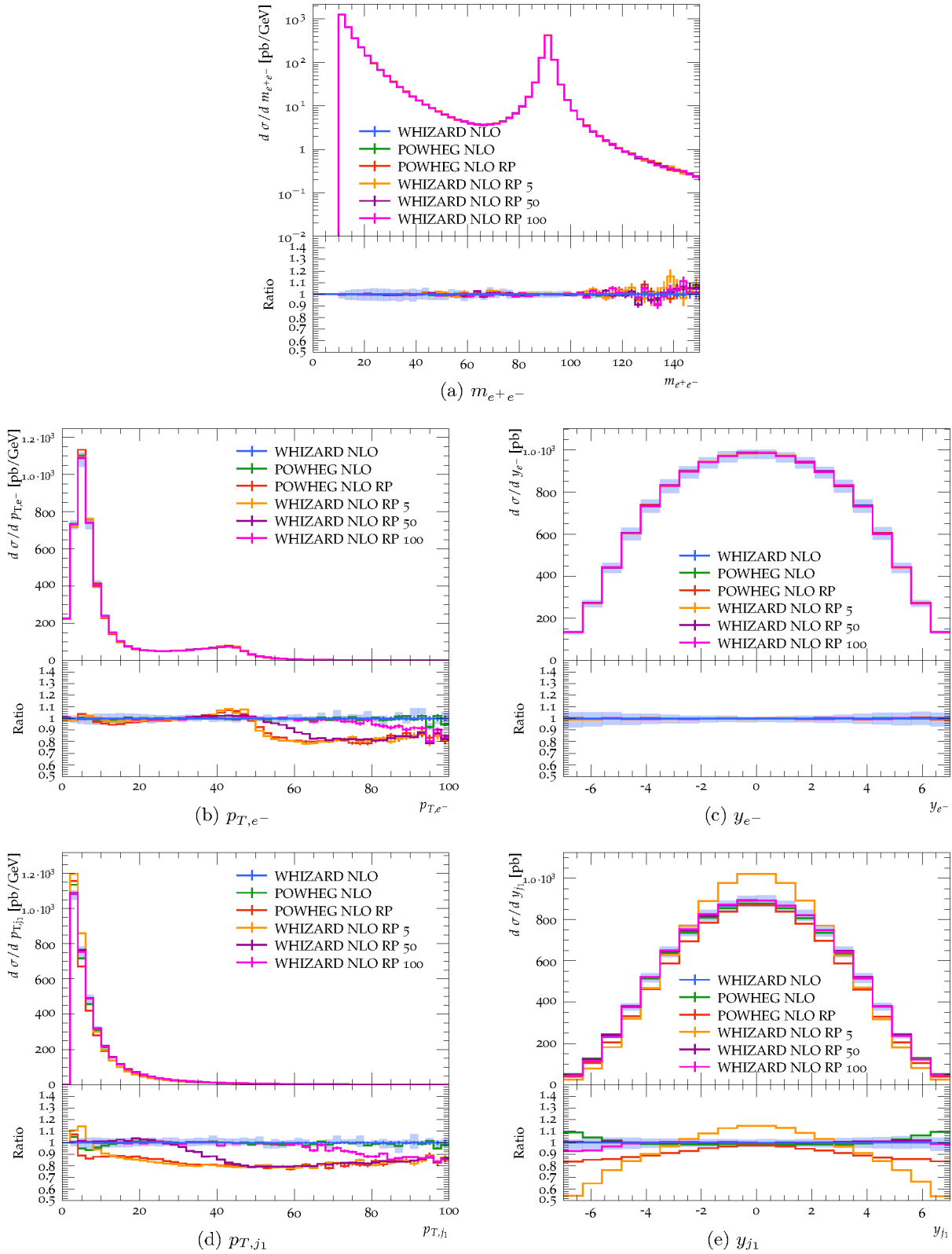


Fig. 6.4: Comparison of NLO distributions for  $pp \rightarrow e^+e^-$  events with real-partition scales of  $h_F \in \{5 \text{ GeV}, 50 \text{ GeV}, 100 \text{ GeV}\}$  for WHIZARD and  $h_{\text{damp}} = 0.25$  for the POWHEG-BOX. The error bars depict the statistical uncertainty, while the light blue band indicates the scale uncertainty of the WHIZARD NLO event distribution. We simulated 50M weighted POWHEG events with WHIZARD and 50M unweighted POWHEG events with the POWHEG-BOX for the distributions without real partition and 10M unweighted events for each component of the distributions with real partition. No parton shower has been applied yet.

### 6.1.4 Effects of the parton shower

In the simulation of the parton level POWHEG events we focussed on so far, we generated just up to a single emission and explicitly excluded emissions at low transverse momentum from our perturbative description. This is, of course, only part of the full picture. To describe physics at all scales, we apply a parton shower to simulate the remaining lower energetic interactions.

#### The shower setup

In this study, we employed PYTHIA 8.307 [183] to simulate parton shower and hadronization. To steer PYTHIA, we used a mixture of the examples `main31` and `main44` shipped together with the main program of PYTHIA. Additionally, we had to explicitly handle the event weight in order to preserve the weight's sign also for negatively weighted events, which are to a reduced but still non-negligible extent still present in the POWHEG events we hand to PYTHIA.

Regarding the shower settings, we mostly stuck to PYTHIA's default choices in this MC level comparison. As we aim to compare WHIZARD and the POWHEG-BOX, we give precedence to the information stored in the input Les Houches Event Files (LHEFs) whenever possible. This includes the settings concerning the beams and lepton masses. However, we explicitly choose the settings managing PYTHIA's behavior according to the POWHEG-matching prescription.

We disable emission vetoing and also vetoing radiations from multi-particle interactions as we employ a transverse-momentum ordered shower. We set the upper transverse momentum for the emissions to the `SCALUP` parameter in the LHEFs, while during event generation, we set this value to the  $p_T$  of the emission generated by the parton level MC and to  $p_{T,\min}$  if no real emission was generated (c.f. also sec. 3.6.5). For this, we choose a  $p_T$  definition with respect to the emitting parton with PYTHIA's definition of the emitter and the  $p_T$  definition of the POWHEG-BOX. Most importantly, we force PYTHIA to always respect this scale choice<sup>22</sup>. We disable the QED shower and also matrix element corrections performed by PYTHIA. Finally, we set the options for the running of  $\alpha_S$  to the same values as chosen in the parton level MC generators. The last mentioned settings are set twice, once for the space-like ISR and once for the time-like FSR shower. In technical terms, these settings are displayed on the right.

```

1 POWHEG:nFinal = 2
2 POWHEG:veto = 0
3 POWHEG:MPIveto = 0
4 POWHEG:pThard = 0
5 POWHEG:pTent = 0
6 POWHEG:emitted = 0
7 POWHEG:pTdef = 1
8 SpaceShower:pTmaxMatch = 1
9 SpaceShower:QEDshowerByL = off
10 SpaceShower:QEDshowerByQ = off
11 SpaceShower:MEcorrections = off
12 SpaceShower:alphaSvalue = 0.120179
13 SpaceShower:alphaSorder = 1
14 TimeShower:pTmaxMatch = 1
15 TimeShower:QEDshowerByL = off
16 TimeShower:QEDshowerByQ = off
17 TimeShower:MEcorrections = off
18 TimeShower:alphaSvalue = 0.120179
19 TimeShower:alphaSorder = 1

```

These settings are documented in the PYTHIA8 manual [184], while ref. [185] specifically discusses the effects of these settings on the POWHEG matching.

With the parton shower applied, the simulated events will contain a large number of final-state particles, including soft particles and those very collinear to each other. To nevertheless be able to define meaningful observables, we cluster the colored final-state particles into jets, using the anti- $k_T$  algorithm [176] as implemented in `FastJet 3.3.4` [186] with  $R = 0.4$ . In the jet definition, we require  $p_{T,j} > 2 \text{ GeV}$  to avoid IR unsafe regions at low transverse momenta. Considering the cuts, we keep eq. (6.3) as before so that the jet definition only affects the jet observables  $p_{T,j_1}$  and  $y_{j_1}$  but does not restrict the radiation for other observables, as this would violate their IR safety.

<sup>22</sup>This is achieved by setting `pTmaxMatch = 1`. What we refer to as  $p_{T,\min}$  from the perspective of the parton level MC generator is referred to as  $p_{T,\max}$  from the perspective of the SMC.

Although applying the parton shower is a unitary procedure if integrated over the entire phase space, the additional radiation generated by the parton shower typically softens the present jets making it harder for the events to pass the jet criteria eventually lowering the fiducial cross section (c.f. sec. 3.1). In our case, however, the NLO corrections as well as additional emissions will not affect the dilepton mass  $m_{e^+e^-}$  on which the cuts solely depend. For this reason, the total cross sections, as mentioned in sec. 6.1.2 keep their value also in this extended setup, including the parton shower.

### Differential distributions

The differential distributions for this setup, predicted by WHIZARD and the POWHEG-BOX in conjunction with PYTHIA, are depicted in fig. 6.5. We compare the predictions from both programs with and without a real partition (RP) for the same observables as before. While for the POWHEG-BOX, we choose  $h_{\text{damp}} = 0.25$  as before, we only show the results for  $h_F = 5$  GeV from WHIZARD to keep the diagrams tidy. Nevertheless, we can conclude from the discussion before that the distributions for real-partition scales  $h_F > 5$  GeV will lie between both distributions presented from WHIZARD.

We do not discuss fNLO predictions from here on as, although applying a parton shower to the generated fNLO events might technically be possible, it will have issues with double counting of emissions, which to avoid was the main motivation for using the matching procedure.

By comparison of fig. 6.5a-c with the corresponding distributions discussed in the previous subsection, shown in fig. 6.3, we see that the kinematic distributions of the leptons are as unaffected by the parton shower. The reason is the same as for the total cross sections: the conservation of the invariant lepton mass.

More insightful are the remaining two jet distributions. Comparing the jet transverse-momentum distributions of fig. 6.5d with the same pre-shower distribution in fig. 6.3d, we see that the jet has become harder, most likely by gathering more energy from secondary ISR. Moreover, the sharp increase towards the lower end has given way to a peak at about  $p_{T,j_1} \approx 10$  GeV as in an event with more than one clustered jet, the hardest one less often has very low energy.

Viewing the different predictions in relation, we see that both distributions from WHIZARD and the POWHEG-BOX also agree remarkably well in their description of the hardest jet angle and momentum. This holds for both distributions, even with applied real partition and most remarkably also in the regime of very soft jets, where we saw a deviation in the prediction with a real-partition scale of  $h_F = 5$  GeV in fig. 6.4d.

This is a non-trivial achievement as in opposition to the comparison at parton level, the parton shower additionally depends on the flavors and colors present in the events, the choice of the parton shower-starting scale as well as the information about resonant subprocesses all of which have been implemented only in the course of this thesis. Only with the correct resonances present in the events generated at parton level the parton shower can take this into account to determine which particle's invariant mass is to be preserved. In the absence of resonances, more soft and longitudinal radiations would be simulated, as parton shower and hadronization are allowed to adjust the momenta of partons.

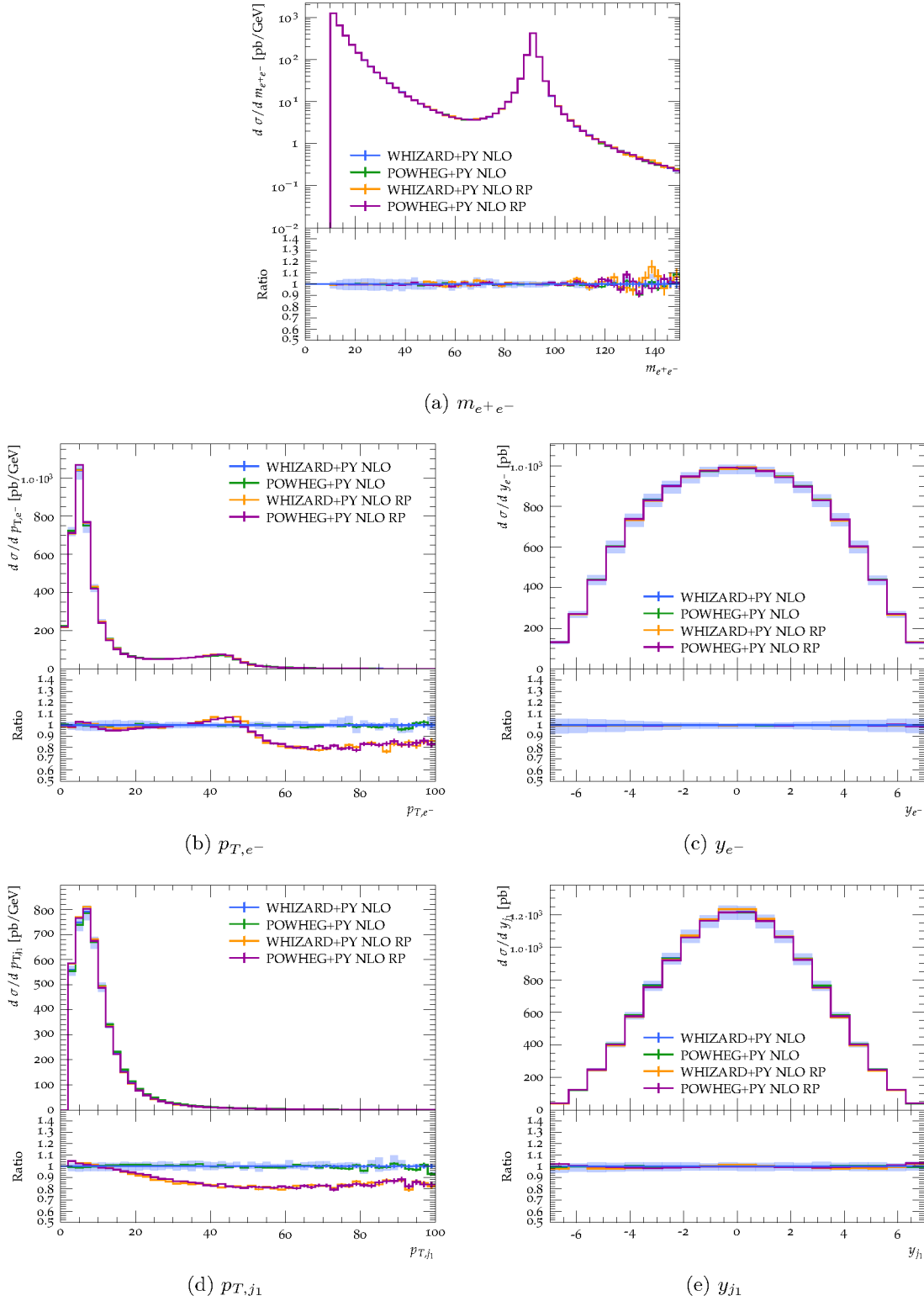


Fig. 6.5: Comparison of NLO distributions for  $pp \rightarrow e^+e^-$  events from the POWHEG-BOX and WHIZARD, including the parton shower simulated by PYTHIA. For the distributions without real partition, we simulated 20M unweighted events with WHIZARD and 30M unweighted events with the POWHEG-BOX. For the distributions with real partition, we simulated 10M unweighted events with a real-partition scale of  $h_F = 5$  GeV for each component of the real partition with WHIZARD and 10M unweighted events in total with a damping parameter of  $h_{\text{damp}} = 0.25$  with the POWHEG-BOX.

## 6.2 The Drell-Yan process $pp \rightarrow e^+e^-$ compared to data

After the successful validation with the well-established implementation of the POWHEG matching in the POWHEG-BOX, we will attempt a more realistic application next. The Drell-Yan process is regularly studied with varying foci by the ATLAS and the CMS experimental collaborations. From the available analyses at  $\sqrt{S_{\text{had}}} = 13 \text{ TeV}$  [187–189], we pick the most recent analysis performed by the CMS collaboration, ref. [189], studying  $Z$  boson angular and transverse-momentum distributions in the resonance region in data collected at  $\sqrt{S_{\text{had}}} = 13 \text{ TeV}$  in 2016 corresponding to an integrated luminosity of  $35.9 \text{ fb}^{-1}$ .

In our comparison, we focus on the electronic decay of the  $Z$  boson. However, from the MC perspective, there is no conceptual difference to the muonic decay.

### 6.2.1 Process setup and event selection

We shall briefly explain the process setup and the event selection here, focusing on the settings relevant for the MC simulation. In app. D, we discuss these settings at the technical level in full detail. For the details concerning the particle detection, reconstruction and background reduction, we refer to the CMS publication [189].

We choose masses and other input parameters according to the Particle Data Group (PDG) Review of Particle Physics [190], neglecting lepton and 5 light quark masses. We employ the PDF set NNPDF30\_nlo\_as\_0118 [191] and choose

$$\mu_F = \mu_R = \sqrt{(p_T^Z)^2 + m_{e^+e^-}^2} \quad (6.8)$$

as the central factorization and renormalization scale. We use Born matrix elements generated by `0'Mega` and NLO matrix elements provided by `OpenLoops`.

At the generator level, we require an invariant lepton mass of

$$m_{e^+e^-} > 50 \text{ GeV} \quad , \quad (6.9)$$

less strict than those we will require in the analysis to avoid discarding PSPs, which would pass the kinematic requirements only after the parton showering, hadronization and subsequent reconstruction. The exact choice here should have no influence on the final results, however.

Concerning the resonance insertion in the generated events, we choose a more elaborate simulation as before by inserting resonant  $Z$  bosons in a range of  $16\Gamma_Z$  centered around  $m_Z$  with a Gaussian suppression of  $1/e$  at  $4\Gamma_Z$  (c.f. sec. 3.6.8).

Considering the matching settings, we fill a  $10 \times 10$  POWHEG grid and choose  $p_{T,\text{min}} = 2.5 \text{ GeV}$  as the central value for the minimum transverse momentum that radiation described by the hard matrix element may have. We will also consider variations of  $p_{T,\text{min}}$  around the central value.

For the parton shower, hadronization and the underlying-event simulation, we employ PYTHIA 8.307 [183] with the tune CUETP8M1 [192, 193] also known as the CMS Tune MonashStar. This determines the QCD and electromagnetic initial-state as well as final-state shower. Regarding the PYTHIA settings for the POWHEG matching, we choose the same values for all the "POWHEG" settings as well as `pTmaxMatch` mentioned in sec. 6.1.4.

For the analysis of the generated events, we employ Rivet 3.1.4 [94]. By virtue of Rivets analysis preservation system, we are able to reuse the CMS analysis prepared in the course of ref. [189]. Within Rivet, it is referred to under the name `CMS_2019_I1753680`. It performs the  $Z$ -boson reconstruction and histogramming.

At the analysis level, we impose stricter cuts than we used for the integration and the simulation of the

partonic events. We require two oppositely charged, same-flavor leptons to fulfill

$$|\eta_\ell| < 2.4 \quad \text{and} \quad p_{T,\ell} > 25 \text{ GeV} \quad (6.10)$$

and a dilepton invariant mass within 15 GeV around  $m_Z = 91.1876 \text{ GeV}$ ,

$$|m_{\ell^+\ell^-} - m_Z| < 15 \text{ GeV} \quad . \quad (6.11)$$

This ensures that the leptons are well within the detector acceptance, optimizes the trigger efficiency and selects well-identifiable  $Z$ -boson candidates. In this setup, the fiducial phase space is much more restricted than in the technical comparison with the POWHEG-BOX we performed before.

Rivets analysis preservation system also provides access to the differential distributions of the unfolded background-subtracted data corrected for detector effects and shown in ref. [189], drastically simplifying the present comparison.

### 6.2.2 Cross sections

Before we compare differential distributions, we will first look at the measured total cross section compared to predictions from different MC generators. In tab. 14, we summarize the total cross sections for the leptonic decay channel, given in ref. [189] and extend them with our own result.

While MG5\_aMC 2.3.3 [45] and WHIZARD employ the NNPDF 3.0 PDF set NNPDF30\_nlo\_as\_0118 [191], FEWZ instead uses the NNPDF 3.1 [194] NNLO PDF set. The given scale uncertainties are estimated by varying both scales,  $\mu_R$  and  $\mu_F$ , independently by a factor of 2 up and down, excluding the extreme variations, with the scale given in eq. (6.8) as the nominal value. As opposed to the approach followed in ref. [189], we omit PDF uncertainties in our predictions and choose not to symmetrize the uncertainties.

	order	$\sigma$ in pb
Data		$712 \pm 10$ (sys) $\pm 18$ (lumi)
FEWZ	NNLO QCD	$719 \pm 8$ (stat+PDF+scale)
MG5_aMC	NLO QCD	$682 \pm 55$ (stat+PDF+scale)
WHIZARD	NLO QCD	$658.56^{+18.13}_{-38.11}$ (stat+scale)
WHIZARD	LO QCD	$630.31^{+83.05}_{-92.43}$ (stat+scale)

Tab. 14: Predicted and measured cross sections for the Drell-Yan process. The measured cross section (data) and those computed with FEWZ and MG5\_aMC are stated as reported in ref. [189]. For the latter two, the given uncertainties include the statistical MC uncertainties as well as PDF and scale uncertainties. The last two rows show the results computed with WHIZARD. Here, the given uncertainties reflect the symmetric statistical and asymmetric scale uncertainties.

Qualitatively, we can see that the highest-order prediction by FEWZ agrees best with the measured cross section, as both values are within their respective uncertainties. Both NLO QCD computations yield results about 5 – 8% lower, from which we can conclude the NNLO QCD correction to be positive. The results computed with MG5\_aMC and WHIZARD at NLO QCD roughly agree within their scale uncertainties, although their central values differ by about 4%. This difference is likely related to different approaches to the parton-shower matching and merging. While WHIZARD employs the POWHEG-matching method, MG5\_aMC relies on MC@NLO matching and additionally performs NLO merging, taking up to two additional partons at Born level in the matrix-element calculations into account, using the FxFx merging scheme [110]. Unfortunately, the total cross section computed with the POWHEG-BOX, which follows an approach more similar to that of

WHIZARD, is not reported.

Considering the LO cross section, we see that both the NLO QCD as well as the NNLO QCD corrections are positive. The reason is that each order enables more processes with a gluonic initial state to contribute, leading to an enhancement of the cross section due to the large gluon PDFs.

### 6.2.3 Differential distributions

Besides total cross sections, we also want to compare differential distributions of measured data and MC predictions. Ref. [189] puts a strong focus on the properties of the reconstructed  $Z$  boson. Following this approach, we will discuss differential distributions of the  $Z$ -boson transverse momentum,  $p_T^Z$ , and its rapidity,  $|y_Z|$ . While  $|y_Z|$  predominantly covers the angular properties of the  $Z$  boson, its transverse momentum also covers the energetic component. It is a property of the  $Z$  boson often studied in the Drell-Yan process. In a naive LO description of the process without any additional radiation, the  $Z$  boson would not have any transverse momentum. Its transverse-momentum distribution is thus the ideal candidate to test the SM description of the intrinsic  $p_T$  of the initial partons and ISR effects probing the strong interaction. Moreover, a precise calibration of the  $p_T$  measurements of weak bosons is crucial for  $W$ -mass measurements at the Tevatron and the LHC.

We generated several differential distributions using WHIZARD, all with NLO accuracy but with different parameters of the shower-starting scale,  $p_{T,\min}$ , and the real-partition scale,  $h_F$ . Both parameters are determined by the parton-level MC generator. They are thus not part of the parton-shower tune, although they do have an influence on the shower behavior. We consider variations to estimate their effect. To avoid confusion, we show variations of  $p_{T,\min}$  in fig. 6.6 separately from the variations of  $h_F$  in fig. 6.7. We will discuss both variations simultaneously, nonetheless.

The rapidity distributions are shown in fig. 6.6b and fig. 6.7b. From the plateau at values  $|y_Z| \lesssim 1$ , we see that  $Z$  bosons central in the detector are favored. In both figures, varying  $p_{T,\min}$  or  $h_F$  barely influences the simulated distributions, as they all agree, most often even within the very small statistical uncertainties. Similarly, we noticed in the previous subsection that the lepton rapidity is barely influenced by the shower-starting scale or the real-partition scale. We can clearly see that the  $|y_Z|$  distribution, normalized to the total cross section, is off by a roughly constant  $-(6-8)\%$ , owing to the slightly lower prediction for the total cross section compared to the experimentally determined value. This effect can be circumvented by choosing the same normalization for all distributions. For this reason, we show the same distributions normalized to unity in fig. 6.6c. Once the distributions are normalized to the same integral, the agreement between prediction and measurement is almost perfect.

In figs. 6.6a and 6.7a we show the  $Z$ -boson transverse momentum. Here, such excellent agreement between simulation and measurement cannot be observed. In both figures, we notice a strong dependence of the distribution on both indirect shower parameters we consider variations of. We can see a deviation between the predictions and the data, especially in two scenarios. For the lowest value of  $p_{T,\min}$ , 1 GeV, we clearly see that the predicted peak of the distribution exceeds the measurement. Taking into account the scale uncertainty, which, for clarity, is displayed only for the  $p_{T,\min} = 2.5$  GeV distribution in blue in fig. 6.6a, we can see that they almost cover the exceeding. Thus, it is not a severe problem but indicates that a larger shower-starting scale yields better predictions. In this case, more of the low- $p_T$  region is populated by the parton shower.

The observation and also the conclusion is similar for the variation of the real-partition scale in fig. 6.7a. We see that the prediction of the  $Z$ -boson transverse momentum is off for  $h_F = 50$  GeV. The behavior is even similar to the distribution for  $p_{T,\min} = 1$  GeV shown in fig. 6.6a. In both cases, the variation of the distributions for different values of  $p_{T,\min}$  and  $h_F$  is almost covered by the scale uncertainties. To be more

conservative about the uncertainties, variations of  $p_{T,\min}$  and  $h_F$  should be included as well.

Overall, the best description is achieved with  $p_{T,\min} = 2.5 \text{ GeV}$  and using the real partition but with a large real-partition scale of  $h_F = 100 \text{ GeV}$ , splitting off only a minor part of the real cross section into the real finite component. It is shown in blue in fig. 6.7a. To get a general description of LHC processes, the optimal choices for  $p_{T,\min}$  and  $h_F$  should be determined together with the parton-shower tune, taking data for multiple processes into account. However, this is a separate project.

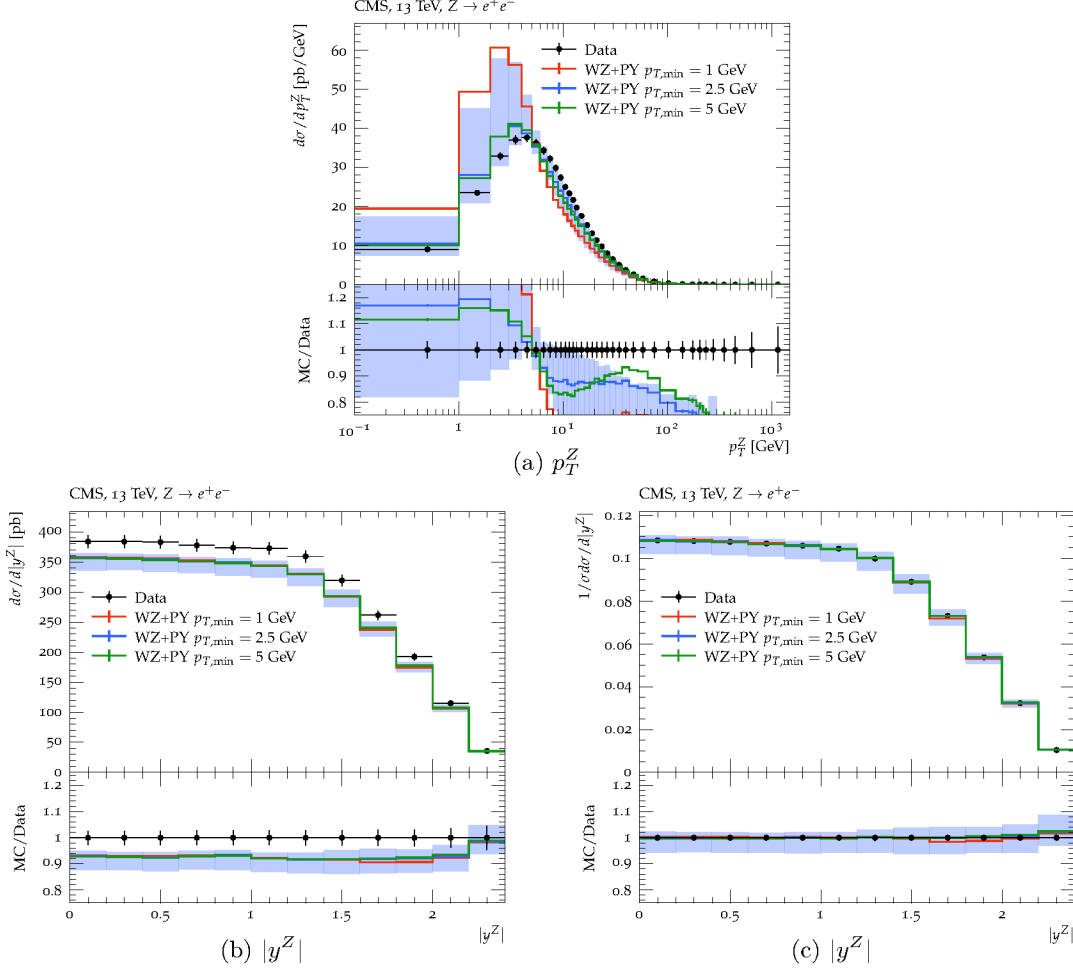


Fig. 6.6: Observable distributions for showered  $pp \rightarrow e^+e^-$  events without real partition for different choices of  $p_{T,\min} \in \{1 \text{ GeV}, 2.5 \text{ GeV}, 5 \text{ GeV}\}$  compared to CMS data reported in ref. [189]. While the distributions in subfig. (a) and (b) are normalized to the total cross section, all distributions in subfig. (c) are normalized to unity. The error bars for the data correspond to the total experimental uncertainty, while the error bars for MC distributions show the statistical uncertainties of 10M unweighted events. The scale uncertainties, determined by varying  $\mu_F$  and  $\mu_R$  independently by a factor of 2 up and down, are displayed as a blue band for the distribution with  $p_{T,\min} = 2.5 \text{ GeV}$ .

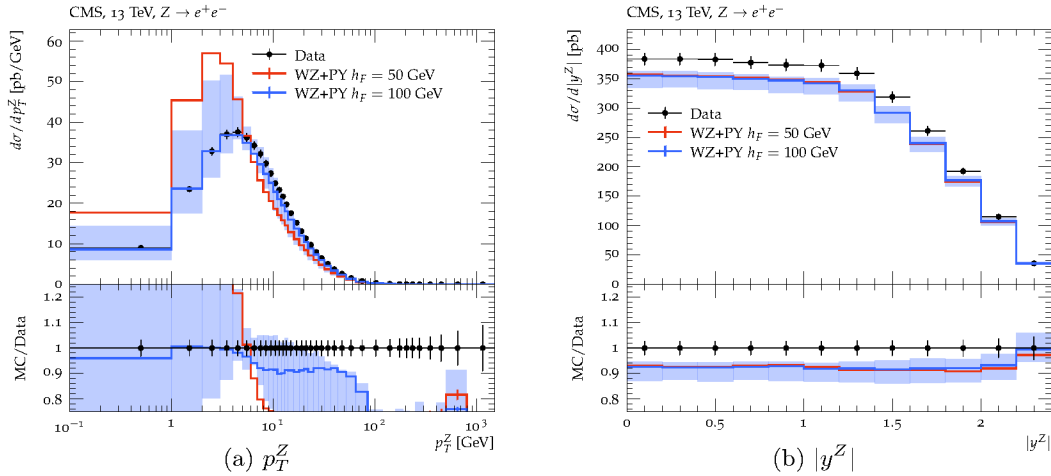


Fig. 6.7: Observable distributions for showered  $pp \rightarrow e^+e^-$  events with  $p_{T,\min} = 2.5$  GeV and different real-partition scales  $h_F \in \{50 \text{ GeV}, 100 \text{ GeV}\}$  compared to CMS data reported in ref. [189]. The error bars for the data correspond to the total experimental uncertainty, while the error bars for MC distributions show the statistical uncertainties of 10M unweighted events for each component of the real partition. The scale uncertainties, determined by varying  $\mu_F$  and  $\mu_R$  independently by a factor of 2 up and down, are displayed as a blue band for the distribution with  $h_F = 100$  GeV.

Ref. [189] also discusses predictions of several MC generators in comparison to the performed measurements. Specifically, the data shown in fig. 6.6 and fig. 6.7 presented here is included in figs. 5 and 6 therein. For reference, they are included here as fig. 6.8 and fig. 6.9.

Fig. 6.8 shows a comparison of the measured rapidity distribution with MC predictions computed with MG5\_aMC, POWHEG and FEWZ. The settings chosen for FEWZ are the same as those used to compute the NNLO cross sections shown in the previous section, including that no parton shower is applied. Just like WHIZARD, MG5\_aMC and POWHEG both employ the NNPDF 3.0 PDF set NNPDF30\_nlo\_as\_0118 [191] and both predictions include parton-shower modeling.

Comparing the  $Z$ -boson rapidity distributions computed with WHIZARD with those in fig. 6.8, we see that overall, the NNLO prediction by FEWZ agrees best with the data, while both NLO predictions by MG5\_aMC and POWHEG show an overall deviation of  $\approx -5\%$ , similar to our prediction.

Lacking the parton-shower modeling, the prediction computed with FEWZ for the  $Z$ -boson transverse momentum is not shown in fig. 6.9. Instead, predictions computed with POWHEG using the MINLO procedure [112] and the NNPDF 3.1 NLO PDF set [194] are included. In the region  $p_T^Z < 10$  GeV, both predictions from MG5\_aMC and POWHEG tend to slightly lower values than the measured data, while the MINLO prediction agrees with the data, especially in the lowest bins but still features a large uncertainty. On the contrary, our prediction tends to overshoot the data in this transverse-momentum range. Especially low transverse momenta are most often governed by the parton shower, so the differences can most likely be accounted to differences in the parton-shower modeling beyond the parton-shower tune like the POWHEG-matching parameters or the treatment of resonances (c.f. sec. 3.6.8).

In the central region,  $10 \text{ GeV} < p_T^Z < 100 \text{ GeV}$ , the overall behavior of a rise in the ratio of predictions over the data can be observed for all programs more or less pronounced. For WHIZARD, this is particularly the case for the distribution using  $p_{T,\min} = 5$  GeV. However, the slightly lower total cross section computed with WHIZARD, which we saw most clearly in the  $|y_Z|$  distribution, leads to a prediction roughly 10% smaller than the data in the central region. At the upper end of the transverse-momentum distribution, the predictions computed with WHIZARD and POWHEG both tend towards lower cross sections compared to the data, while the ones using MG5\_aMC or the MINLO procedure stay in agreement with the data. Comparing the displayed

uncertainties, we see that the behavior of small uncertainties around  $p_T^Z = 10$  GeV, which increase going outwards, is most comparable to the uncertainty behavior displayed in ref. [189] for the MINLO procedure. Summarizing, our predictions using the POWHEG-matching scheme can describe the measured data well at NLO accuracy for some parameter choices and show a behavior similar to the predictions computed in the course of ref. [189] using the POWHEG-BOX. An in-depth analysis of the remaining differences would require a more thorough dive into the technical differences of the employed MC generators.

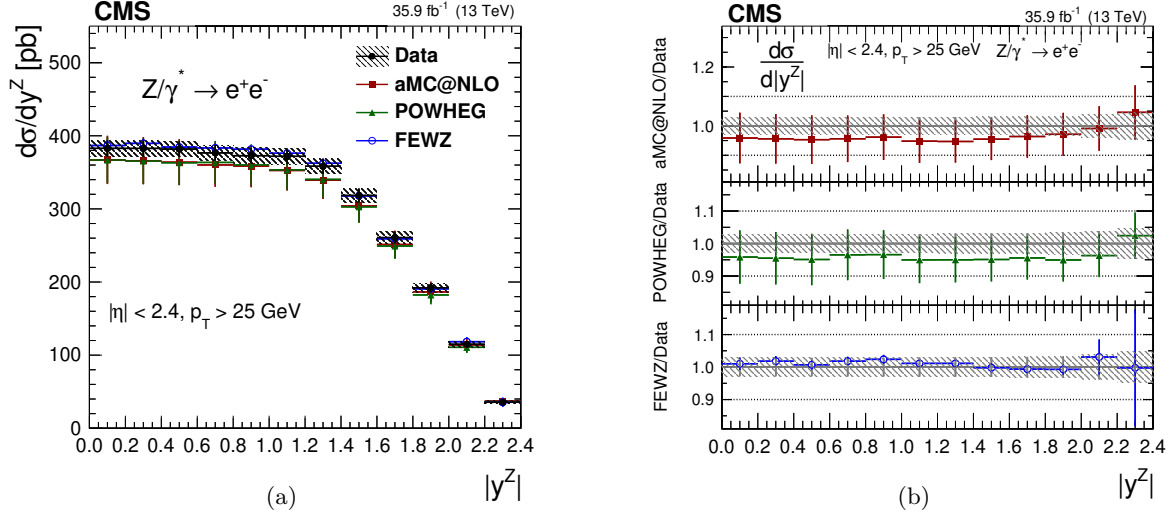


Fig. 6.8: The measured absolute cross sections (left) in bins of  $|y^Z|$  for the dielectron final state. The shaded bands around the data points (black) correspond to the total experimental uncertainty. The measurement is compared to the predictions with MG5\_aMC (square red markers), POWHEG (green triangles) and FEWZ (blue circles). The error bars around the predictions correspond to the combined statistical, PDF and scale uncertainties. This is fig. 5 of ref. [189].

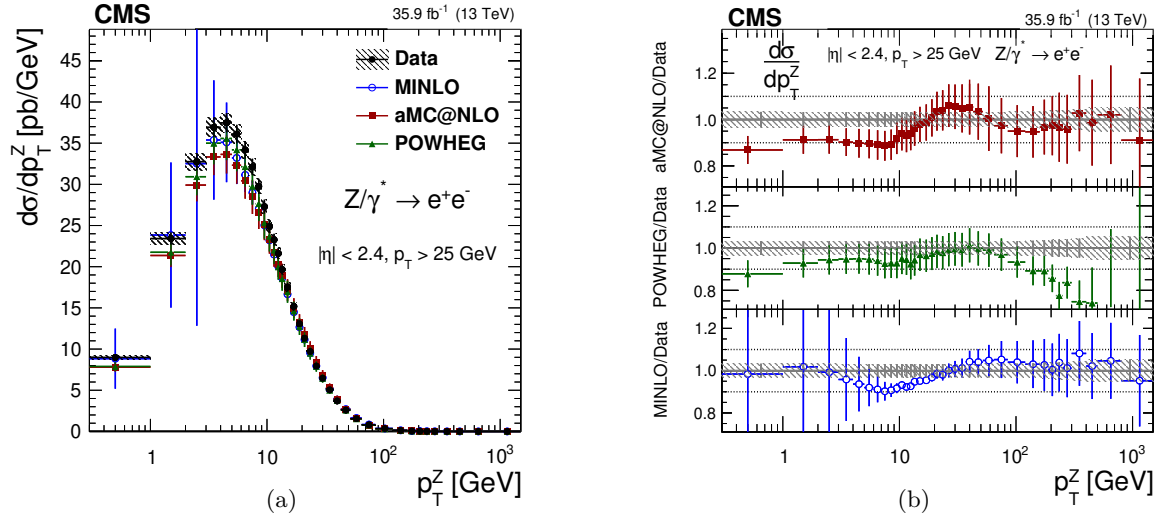


Fig. 6.9: The measured absolute cross sections (left) in bins of  $|p_T^Z|$  for the dielectron final state. The shaded bands around the data points (black) correspond to the total experimental uncertainty. The measurement is compared to the predictions with MG5\_aMC (square red markers), POWHEG (green triangles) and POWHEG-MINLO (blue circles). The error bars around the predictions correspond to the combined statistical, PDF and scale uncertainties. This is fig. 6 of ref. [189].

### 6.3 Predictions for $e^+e^- \rightarrow t\bar{t}j$ measurements at a future lepton collider

A multi-purpose MC generator like WHIZARD allows to make predictions for total and differential distributions about a plethora of different processes. We have implemented the ability to generate fixed-order NLO as well as POWHEG events with the same standard of generality, yet, we have only discussed matched predictions for the Drell-Yan process at the LHC so far. In this section, we switch gears to study the production of a top-quark pair associated with a jet at a future lepton collider.

One of the main prospects of future lepton colliders is to improve the top-mass measurement at the top-pair threshold. For this reason, a center of mass energy of  $\sqrt{S_{\text{had}}} \in [350, 380] \text{ GeV} \gtrsim 2m_t$  is often among the proposed energy stages [32, 33, 147, 195] while later stages usually include larger CM energies like  $\sqrt{S_{\text{had}}} = 500 \text{ GeV}$ , to study the production and interaction of Higgs bosons, e.g., in association with top quarks.

Using the radiative return effect, i.e., additional radiation taking away energy, so that the recoil system gets closer to a resonance mass, it is also possible to study the top threshold at higher CM energies, e.g., by studying the processes  $e^+e^- \rightarrow t\bar{t}\gamma$  [196] for which  $e^+e^- \rightarrow t\bar{t}j$  is a background process. Also from the technical perspective,  $e^+e^- \rightarrow t\bar{t}j$  is ideally suited to complement our previous results. While we previously discussed the Drell-Yan process, featuring ISR exclusively,  $e^+e^- \rightarrow t\bar{t}j$  at NLO QCD features FSR off massless as well as massive emitters. This allows to additionally test the POWHEG matching, including the UBFs derived in sec. 3.5.5 and 3.5.8. Moreover, it is the ideal candidate to apply and study the real partition, as we have already pointed out in sec. 2.6.3.

#### 6.3.1 Process setup and event selection

Although WHIZARD is capable of computing the NLO QCD corrections to the full  $2 \rightarrow 7$  off-shell process, including the decays of both top quarks, we assume the top quarks to be stable in our setup for several reasons. Most of all, decaying top quarks often require more elaborate reconstruction techniques in the analysis, which produce less clear results and are not the focus of this thesis. A hadronic top decay overall complicates the jet combinatorics. This would not be the case for the leptonic decay but this one also would not have much influence on the NLO QCD corrections or the matching either. Even if we assumed stable  $W$  bosons, we would have to take into account threshold effects leading to large  $K$  factors as  $e^+e^- \rightarrow W^+bW^-\bar{b}j$  is subject to radiative return towards the top threshold [197]. Also from the technical side, radiation off top quarks is probably the best opportunity to test the kinematic construction and UBFs in the POWHEG matching for massive emitters.

With the same considerations, we refrain from employing a parton shower to the generated POWHEG events. In a subsequent shower, the top quarks would necessarily decay, leading to the abovementioned problems. At the applied precision level, a full study with a description of the top-quark decay with NLO matrix elements would be necessary.

In this investigation, we thus study the production of two top quarks in association with an additional jet at an  $e^+e^-$  collider with a CM energy of  $\sqrt{S_{\text{had}}} = 500 \text{ GeV}$ . We take the default values for the masses and widths from the 2022 PDG Review of Particle Physics [198]. Differing from that, we obviously have to set  $\Gamma_t = 0$ , and we round the top mass to  $m_t = 172.5 \text{ GeV}$  while considering all other quarks as well as the light leptons to be massless. For  $\alpha_S$ , we thus take the lightest 5 quark flavors into account in the running of  $\alpha_S$  described at NNLO. The renormalization scale is set to

$$\mu_R = H_T/2 \quad \text{with} \quad H_T := \sum_i \sqrt{p_{T,i}^2 + m_i^2} \quad , \quad (6.12)$$

where the sum runs over all final-state partons.

To avoid divergences from soft or collinear jet radiation and to guarantee a well-defined IR finite Born cross section, we employ the anti- $k_T$  algorithm [176] with  $R = 0.5$  as implemented in `FastJet 3.3.4` [186] to cluster light quarks and top quarks into jets. We also equally include top quarks in the clustering to avoid artifacts from hard collinear radiation off the top quarks in the differential distributions. In the following, we require at least 3 of those jets to fulfill the requirements

$$p_T > 15 \text{ GeV} \quad \text{and} \quad |y| < 4.5 \quad (6.13)$$

on their transverse momentum and rapidity, respectively.

Regarding the POWHEG event simulation, we again use a  $10 \times 10$  POWHEG grid and  $p_{T,\min} = 1 \text{ GeV}$  to be able to observe the behavior of the matching in the sensitive soft regions.

All tree-level matrix elements in the computation are generated by the in-house matrix-element generator `O'Mega`, while `OpenLoops` provides the loop matrix elements.

### 6.3.2 Total cross sections

In our first discussion of the real partition in sec. 2.6.3, we already elaborated that the present process,  $e^+e^- \rightarrow t\bar{t}j$ , greatly benefits from the approach of partitioning the real matrix element in a singular and a finite part because some of the real subprocesses, i.e., those featuring a  $g \rightarrow q\bar{q}$  splitting, have finite contributions. Here, we want to use this opportunity to study this claim quantitatively.

To do this, we compute the real cross section with three different real-partition scales, one of them corresponding to not using the real partition at all. In tab. 15, we show the integration histories for the integrations of the singular real component in each case. We also show the cross section computed for the finite real component to be able to compare the results for the full real cross section, too. We do not show the integration history for the real finite as it usually integrates very well, requiring no subtraction terms and thus, no cancellation of contributions. For this reason, it also integrates much faster than the singular real contribution so that we can as well increase the number of iterations and calls for the real finite without much cost, if necessary.

First of all, we can see that the summed results in the last row are in statistical agreement, so the total cross section is unaffected by the real partition as it should be. Comparing the convergence behavior, assessable from the evolution of the absolute as well as relative uncertainties along the iterations, we can see an improvement if we turn on the real partition with  $h_F = 50 \text{ GeV}$ . As the total results for the integral of the singular real contribution differ, the relative uncertainty gives the best hint on the convergence of the integration. We can see that splitting off only a small finite part already improves the integration. The effect is suppressed, however, as the largest contribution to the cross section comes from ALRs featuring gluon radiation.

The last column shows the integration history with  $h_F = 5 \text{ GeV}$ , splitting off a larger finite real part. By choosing a too-small value for  $h_F$ , we are almost integrating the subtraction terms separately from the singular real contribution. This leads to negative partial values for the real singular cross section and a large cancellation between both components, which altogether decreases the convergence. So for the integration,  $h_F$  is optimally chosen in such a way that the total real cross section is roughly split into equal parts and that none of them becomes negative.

It.	$h_F = \infty \text{ GeV}$			$h_F = 50 \text{ GeV}$			$h_F = 5 \text{ GeV}$		
	Int.	Err.	Err. [%]	Int.	Err.	Err. [%]	Int.	Err.	Err. [%]
1	2.80	0.25	8.91%	3.34	0.30	8.85%	-15.18	0.35	2.32%
2	3.45	0.22	6.56%	3.19	0.16	4.86%	-15.40	0.21	1.38%
3	2.95	0.21	7.24%	3.01	0.15	5.02%	-15.17	0.19	1.25%
4	3.06	0.20	6.40%	2.96	0.15	5.17%	-15.41	0.16	1.06%
5	3.25	0.16	5.02%	2.92	0.16	5.61%	-15.52	0.15	1.00%
$\mathcal{R}_{\text{sin}}$	3.12	0.09	2.90%	3.04	0.07	2.47%	-15.38	0.09	0.56%
$\mathcal{R}_{\text{fin}}$				0.09	0.00	0.26%	18.40	0.03	0.18%
$\mathcal{R}_{\text{sin}} + \mathcal{R}_{\text{fin}}$	3.12	0.09	2.90%	3.13	0.07	2.40%	3.02	0.09	3.03%

Tab. 15: Integration histories of the cross-section computation of the process  $e^+e^- \rightarrow t\bar{t}j$ . The cross sections are given in fb. The results are shown for three different real-partition scales, where  $h_F = \infty \text{ GeV}$  is used to denote that no real partition was performed. For the processes with real partition, the results of the different iterations refer to the singular real component only. For the finite real component, we simply state the total result to account for it in the sum of both components depicted in the last row. In all integrations, we performed 5 iterations with 100k matrix-element calls each, adapting both grids and weights in each iteration.

Setting aside the endeavor of optimizing the performance, tab. 16 lists the cross sections, including the Born and virtual contributions for different real-partition scales at NLO as well as LO. Taking the LO cross section into account, we can infer a  $K$  factor of  $K = 1.32$ . For the NLO results, we can see that, while the finite cross section increases with decreasing  $h_F$ , the sum of both parts stays in remarkable agreement for all choices of the real-partition scale. While the real-partition scale has no influence on the total cross sections or fnLO events, it does influence the differential distributions of POWHEG events to which we will turn our attention next.

	order	$h_F$	combined	finite	sum
WHIZARD	LO		$38.79 \pm 0.02$		$38.79 \pm 0.02$
WHIZARD	NLO	$\infty \text{ GeV}$	$51.05 \pm 0.05$		$51.05 \pm 0.05$
WHIZARD	NLO	50 GeV	$51.01 \pm 0.06$	$0.0862 \pm 0.0001$	$51.10 \pm 0.06$
WHIZARD	NLO	20 GeV	$48.47 \pm 0.06$	$2.600 \pm 0.002$	$51.07 \pm 0.06$
WHIZARD	NLO	5 GeV	$32.64 \pm 0.06$	$18.39 \pm 0.02$	$51.03 \pm 0.06$

Tab. 16: Cross section of the process  $e^+e^- \rightarrow t\bar{t}j$  in fb at LO and NLO QCD for different real-partition scales  $h_F$ . The second entry for  $h_F = \infty \text{ GeV}$  corresponds to no applied real partition. Thus, the real finite cross section is left blank. The displayed uncertainties refer to the MC integration. The NLO cross section including scale uncertainties obtained by varying the renormalization scale by a factor of 2 is given by  $\sigma_{\text{NLO}} = 51.05^{+2.04}_{-1.98} \text{ fb}$ .

### 6.3.3 Differential distributions

Generating POWHEG events while using the real partition will produce two separate event samples: One contains the events generated for the real finite component and another for the POWHEG events, which account for all other components, including the singular real component. Before we discuss the differential distributions of POWHEG events generated with different real-partition scales, it is interesting to understand which phase-space regions each event sample populates.

Generally speaking, the employed real-partition function, given by eq. (2.161), ensures that all hard radiations, i.e., those in which the radiation receives a large momentum, belong to the sample of the real finite

contribution. At the same time, all lower energetic emissions are incorporated in the POWHEG-event sample, combining the contributions of the Born, the virtual, the singular real component and the subtraction terms. This behavior can be seen in fig. 6.10. It shows the differential distributions of both samples and their sum separately for the invariant mass of the system of both top jets,  $m_{t\bar{t}}$ , as well as the transverse-momentum distributions of the top jet,  $p_{T,t}$ , and the fourth hardest jet,  $p_{T,j_4}$ , if the jets are ordered by decreasing transverse momentum. In this context, 'top jets' refers to clustered objects containing at least one (anti)top quark. This definition makes use of generator information. Under experimental conditions, a similar definition would involve the proper reconstruction and tagging of the top quarks. For this example, we choose a real-partition scale of  $h_F = 5$  GeV, so that the real finite sample contributes a significant portion to the total cross section.

First discussing the invariant ditop-mass, we see that the distribution starts at twice the top mass,  $2m_t$ , and goes up almost to the available energy of  $\sqrt{S_{\text{had}}} = 500$  GeV leaving just enough room for the one jet we require to fulfill its transverse-momentum requirements. Considering the subsamples for both real partition components, we see that the real finite dominates at low  $m_{t\bar{t}}$ , where the non-top jets take most of the momentum, while it drops to zero at  $m_{t\bar{t}}$  close to the total available energy, where the radiated jet is energetically constrained to be very soft.

Fig. 6.10b shows the transverse-momentum distribution<sup>23</sup> of the top jet. We see a scarce population of the region below  $p_{T,t} = 15$  GeV, as this region may only be populated if the jet containing the top quark is not among the three jets we require to fulfill  $p_T > 15$  GeV. In this case, both jets not containing a top quark are required to be high-energetic, so the region  $p_T < 15$  GeV is dominated by the real finite contribution. The upper end of the distribution is reached at  $p_T \approx 175$  GeV. Such a top jet has to have an energy of at least 244 GeV leaving just enough energy for the second top jet and the third jet to compensate for its transverse momentum. The real finite contribution diminishes even earlier as it has to fulfill eq. (2.161), which dictates that it drops to zero at

$$\sqrt{m_t^2 + 2p_t \cdot p_j} \approx 177.5 \text{ GeV} \quad , \quad (6.14)$$

where  $p_t$  and  $p_j$  are the four-momenta of the top quark and the radiated parton, respectively.

Fig. 6.10c shows the transverse-momentum distribution of the fourth hardest jet, i.e., the jet with the lowest transverse momentum, if existent. The fact that the fourth hardest jet does not exist in Born-like events and events in which two of the final-state partons are clustered together implies that the integral of this distribution does not have to match the total cross section. This is most obvious for the real singular contribution labeled "com" for "combined" in this figure. If the fourth hardest jet exists, it is always just a single parton and does not have to fulfill the jet requirements of eq. (6.13). It is therefore arguable to call it a "jet" at all if we interpret the jet-selection criteria as the jet definition. Nevertheless, we will continue to do so for the sake of consistency in the nomenclature.

In the distribution, we can see that only the lower end of soft  $p_{T,j_4}$  receives contributions from the real singular component, while the real finite constitutes 100% of the total distribution in all regions of hard radiated jets where  $p_{T,j_4} > 10$  GeV.

<sup>23</sup>In our idealized picture of a lepton collider without ISR photon radiation or Beamstrahlung, we could as well consider the absolute value of the particle's momenta as in this case also the momentum component along the beam axis is reconstructible. For comparison with the hadron-collider setup, it is useful to stick to the transverse component only, however.

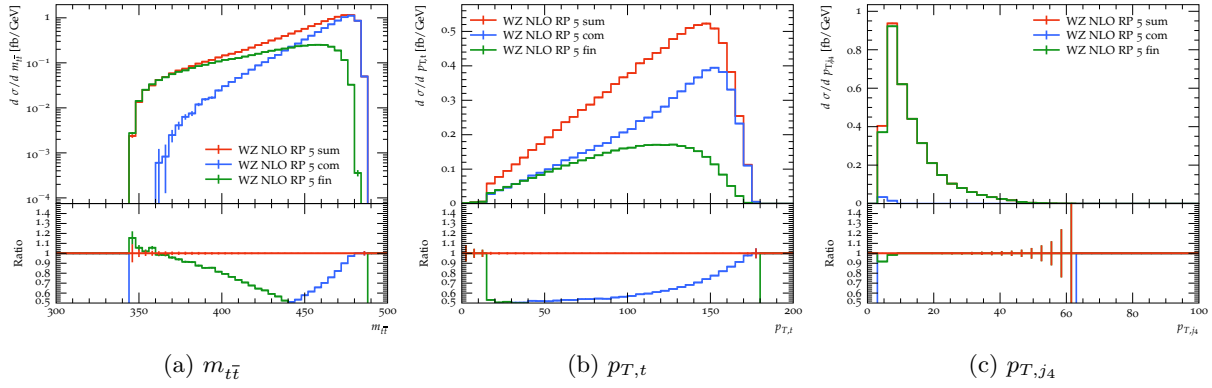


Fig. 6.10: Differential distributions for  $e^+e^- \rightarrow t\bar{t}j$  events with a real-partition scale of  $h_F = 5$  GeV. 1M unweighted events generated from the real finite (fin) contribution and 1M unweighted POWHEG events from the real singular contribution combined with the Born and the virtual contribution (com) are shown separately in relation to the sum (sum) of both parts. No parton shower has been applied.

Moving away from our individual analysis of the real finite and the real singular component, we will compare the complete differential distributions of fixed-order as well as POWHEG events next. In fig. 6.11, we show the differential distributions for a multitude of observables based on simulated POWHEG events without real partition, LO events, POWHEG events generated using the real partition with multiple real-partition scales  $h_F \in \{5 \text{ GeV}, 20 \text{ GeV}, 50 \text{ GeV}\}$  as well as fixed-order NLO events. To generate the fixed-order NLO events, we used the real partition with  $h_F = 50$  GeV, too. We checked that the events generated in this way fully agree with the fixed-order NLO events generated without real partition and omitted the latter.

Fig. 6.11a shows the distribution of the invariant mass of both top jets, equivalent to fig. 6.10a. We can observe full agreement between all NLO distributions within the scale uncertainties in the range  $m_{t\bar{t}} > 400$  GeV, with only mild variations below. This is no surprise as all NLO distributions are normalized to the same total cross section. In the lower half of the distribution, we see that the fNLO distribution predicts slightly larger differential cross sections, while the fNLO prediction is significantly lower in the rightmost bin. The reason is that the negative subtraction terms may be separated from the positive true real terms in the fNLO events. This is not possible for the generated POWHEG events. We see in the distribution of the real finite events, in fig. 6.10a, that the unsubtracted real contribution populates the LHS of the  $m_{t\bar{t}}$  distribution<sup>24</sup>. Thus, we see a positive excess here. However, the counterevents populate the RHS of the distribution, explaining the significantly smaller entry in the highest bin. Both effects also affect neighboring bins for the reason that a single radiated parton is already present at Born level in this process. For  $e^+e^- \rightarrow t\bar{t}$ , both effects would be more pronounced. It is for the same reason that the LO prediction only exceeds the NLO predictions at large  $m_{t\bar{t}}$ . On average, the LO prediction is much lower compared to the NLO prediction just as the total cross sections (c.f. tab. 16).

The behavior of the top jet transverse momentum shown in fig. 6.11b is similar. We find full agreement of all NLO predictions within the scale uncertainties, most often also within the much smaller statistical uncertainties. We discussed the shape already in the example of fig. 6.10b.

In the next figure, fig. 6.11c, we can see the transverse-momentum distribution of the hardest jet. It is similar but not equivalent to fig. 6.11b. The hardest jet, i.e., the jet with the largest transverse momentum, does not always have to include one of the top quarks. Also, opposed to the distribution of  $p_{T,t}$ , the region

<sup>24</sup>The events generated separately for the real finite component when POWHEG matching are very similar to the real-like fNLO events as both are always real-like and contain no subtraction terms. Their singular counterparts, however, are treated differently.

$p_{T,j_1} < 15$  GeV is completely excluded by the applied cuts.

The distribution of the second hardest jet,  $p_{T,j_2}$ , shown in fig. 6.11d follows a less linear pattern compared to  $p_{T,j_1}$  but also in this distribution, we see agreement between all NLO-accurate distributions except at very low  $p_{T,j_2} < 40$  GeV. In this region, it is noticeable that the fixed-order NLO description tends to predict softer jets, even if that would be in the log-enhanced parton-shower regime. Looking at the lower edge, we can also spot that the POWHEG events generated with  $h_F = 5$  GeV predict similarly larger cross sections at low  $p_{T,j_2}$ . The real finite contribution to the total cross section increases the lower the real-partition scale  $h_F$  gets. The events generated from the real finite component do not undergo the POWHEG-matching procedure. They are thus treated more like the fNLO events which explains why they tend to deviate from the remaining NLO predictions in the same direction.

Fig. 6.11e depicts the transverse momentum of the third hardest jet. Often, this is the hardest jet not including a top quark, explaining the radically different pattern compared to the previous two jet- $p_T$  distributions. In this observable, also the differences between the different NLO descriptions start to show more clearly. As already mentioned, the fNLO description predicts the least hard jets followed by the POWHEG events with real-partition scales  $h_F \in \{5 \text{ GeV}, 20 \text{ GeV}, 50 \text{ GeV}\}$ , which interpolate between the fNLO and the POWHEG prediction without real partition. We have seen the same behavior for the Drell-Yan process in fig. 6.3d and fig. 6.4d.

This impression is the same if we jump to the transverse momentum of the fourth jet in fig. 6.11i. In both distributions describing the fourth jet, we excluded all events in the lowest transverse-momentum bin at  $p_{T,j_4} < 2.5$  GeV as we would otherwise include arbitrarily soft partons. Since there can never be a fourth clustered jet in the LO picture, we excluded the LO distributions from both observables as well. Especially for large real-partition scales or no applied real partition, the POWHEG procedure flattens the transverse-momentum distribution towards the lower edge as this is the region to be populated by the SMC in a subsequent step.

Fig. 6.11f-6.11h show the rapidity distributions of the three hardest jets. For all three jets, the bulk of the jets lies within the central region at  $|y| < 1$ , featuring a slight broadening of this region for the softer jets. This behavior is directly implied by the transverse-momentum ordering we imposed to label the jets. For all these rapidity distributions, we can again observe excellent agreement between all NLO distributions in the entire region not suffering from statistical limitations.

Finally, in fig. 6.11j we display the rapidity distribution of the fourth hardest jet. Relating it to the transverse-momentum distribution of said jet, we can directly see that the increased amount of soft jets for lower real-partition scales of the POWHEG events translates to an increased amount of jets in the rapidity distribution, too.

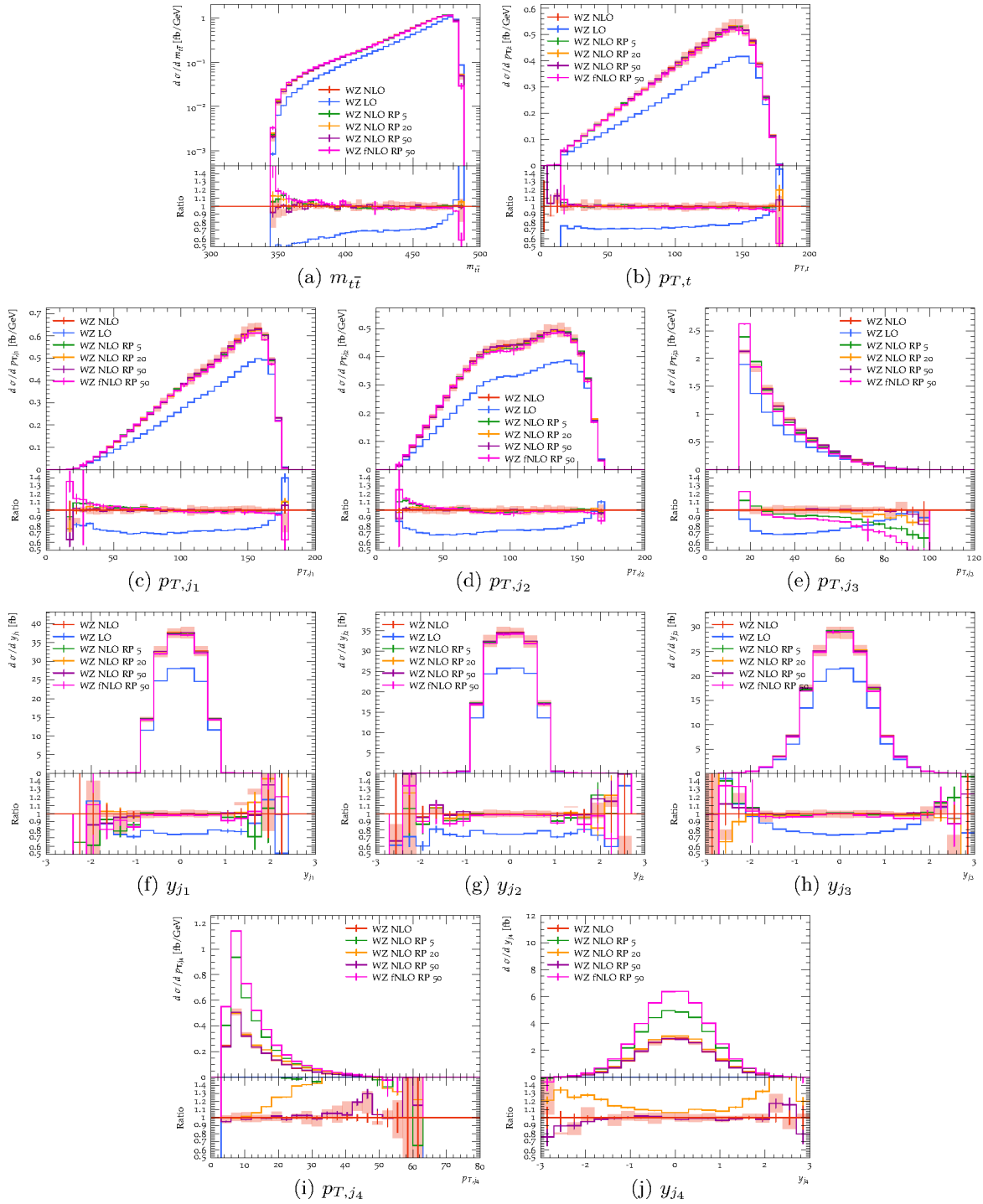


Fig. 6.11: Differential distributions for  $e^+e^- \rightarrow t\bar{t}j$  fixed-order and POWHEG events. We show, in subsequent order, NLO POWHEG events generated without real partition, LO events, NLO POWHEG events with real-partition scales  $h_F \in \{5 \text{ GeV}, 20 \text{ GeV}, 50 \text{ GeV}\}$  and fNLO events also generated using the real partition, respectively. The fNLO events generated without real partition are not shown as they fully agree with the fNLO event distribution already included. The scale uncertainties, indicated by the semi-transparent red band, are computed for the distributions of the NLO POWHEG events without real partition, which function as the baseline, by varying the renormalization scale by a factor of 2 around the central value given by eq. (6.12). In total, we simulated 1M unweighted NLO POWHEG events, 1M weighted LO events, 1M unweighted events for each of the real finite contributions to the POWHEG-event distributions in addition to 1M unweighted POWHEG events for each real-partition scale and 5M weighted events for each component of the fNLO event distribution. Events in the leftmost  $p_{T,j4}$  bin have been excluded from both  $p_{T,j4}$  and  $y_{j4}$  distributions, as it does not constitute an IR safe observable. No parton shower has been applied to the events.

## 6.4 Corollary

In this section, we discussed several applications of POWHEG matching. In the first application, we successfully validated the implemented matching procedure in an in-depth comparison of differential distributions of lepton and jet momenta in the Drell-Yan process with the POWHEG-BOX in a technical setup.

We proceeded to a more realistic setup, in which we compared our simulated predictions for the same process to data taken with the CMS experiment. Here, we found that our prediction roughly agrees with the measured data for some parameter choices, showing similar deviations from the data as predictions computed with other MC generators if we consider the scale uncertainties.

Furthermore, we employed the same matching procedure to an entirely different process, the production of two top quarks and a jet at a lepton collider. These examples demonstrate that the POWHEG matching we implemented can now be applied process-independently, facilitating future studies with NLO accuracy and parton-shower resummation.

On many occasions throughout this thesis, we discussed the dependence of our predictions on the shower-starting scale,  $p_{T,\min}$ , and the real-partition scale,  $h_F$ . The shower-starting scale decides which emissions are generated by the parton shower in terms of an upper limit for the transverse momentum. On the other hand, the real-partition scale is a second scale deciding which part of the real matrix element enters the Sudakov form factor, which is the basis for generating the real emission transverse momentum of the POWHEG events. Both are, in principle, free parameters not determinable from first principles. They are defined in the MC program simulating the parton-level events but ultimately affect the parton shower. Variations of both parameters could be considered to estimate the theoretical uncertainties associated with this freedom. However, we need some heuristics to determine the recommended central value.

$p_{T,\min}$  is typically chosen at the order  $\mathcal{O}(1 \text{ GeV})$ . For larger values, the parton shower populates more of the phase-space regions featuring harder emissions, which becomes a less accurate description, and lower values would use the matrix-element description in soft or collinear regions better described by the parton shower. In our comparison with measured data, a value of  $p_{T,\min} = 2.5 \text{ GeV}$  turned out to fit best to the measured data.

Throughout this thesis, we discussed the effects of the real-partition scale in several contexts. Concerning the integration performance, we showed for both processes we studied in detail, in tab. 13 and tab. 15, that a light real partition with a large real-partition scale may improve the convergence, while a real partition chosen too strong separates the real cross section too much from the subtraction terms and spoils the cancellation of divergences, thereby worsening the convergence of the integration. The results here suggest to determine the real-partition scale in such a way that not more than a minor portion of less than 50% of the real contribution is split off into the real finite component.

In app. C.2, we discuss the veto and survival rates for events in the veto steps of the POWHEG-matching veto procedure. Here, we notice that using the real partition can improve the performance of the event generation, provided that the scale  $h_F$  is not chosen too low.

Furthermore, we studied the effects of the real-partition scale on the number of generated events with negative weights in sec. 3.6.9. For the same reason that affects the integration, we found that the fraction of negative weights drastically increases for very small values of  $h_F$ . In order to generate events with a large fraction of positive weights, we determined that  $h_F$  should be chosen at least half the value at which the partial cross section of the real singular contribution agrees with the total real contribution.

The previous observations are merely technical observations affecting the integration and event processing performance. Eventually, the parameter choice able to describe the experimental results most accurately

should be favored, even at the cost of performance. Regarding the effect of the real-partition scale on differential distributions, we showed in fig. 6.4d that the real-partition scale neatly allows to choose to what extent the simulated POWHEG events resemble the fixed-order description. More precisely, we found that the emission transverse momentum agrees with the fixed-order prediction at  $p_{T,j_1} \gtrsim h_F$ .

Most importantly, in comparison with CMS data, we noticed that a larger real-partition scale of  $h_F = 100$  GeV also yields the prediction agreeing the most with the measured data, as shown in fig. 6.7a.

Summarizing, our results consistently favor a large real-partition scale, which splits off a small portion of the real matrix element into its own component. Depending on the available CM energy and the typical scale of the process, values between  $h_F = 50$  GeV and  $h_F = 100$  GeV seem to be a good starting point for most processes. Variations of  $h_F$  by a factor of 2, or more conservatively, a factor of 4, can be used to estimate the associated uncertainty. A more general, optimal choice of  $h_F$  could be determined by taking multiple processes, potentially at different colliders, into account, similar to the determination of parton-shower tunes. The same holds for the shower-starting scale  $p_{T,\min}$ . In this endeavor, also dynamical scale choices such as  $h_F = \frac{1}{2}H_T$  could be studied.

## 7 Conclusion and outlook

In the present work, we covered the automation of process-independent NLO QCD corrections in the MC generator `WHIZARD`. This applies to both cross sections and differential distributions at fixed-order as well as the matching of NLO computations to parton showers using the `POWHEG` method.

In Part I, we presented the mathematical and technical background, starting with a detailed description of the FKS subtraction scheme in sec. 2, which included the construction of the radiation phase space for all the relevant potential kinds of emitters, the subdivision of the real phase space using  $S$  functions and the construction of the subtraction terms. We concluded this section with a discussion of how to generate events with fixed-order accuracy and potential traps when using these events to fill histograms, representing differential distributions.

The basic infrastructure of the FKS subtraction scheme in `WHIZARD` was already implemented before the beginning of this thesis. However, it was only applicable to processes with up to two jets in the final state and not featuring any emissions from the initial state. We lifted these limitations in the course of the work leading to this thesis and ref. [73]. We fully generalized the implementation to hadron- as well as lepton colliders and an in principle arbitrary number of jets in the final state. This included the phase-space construction for emissions from the initial state, dealing with flavor-changing initial-state splittings, which require to adjust the PDF flavors in addition to rescaling  $x$  and upgrading the combined integration mode, to be able to deal with the additional DGLAP remnant component. The implementation has been applied for the production of up to 6 jets at a lepton collider as presented in refs. [3] and [73].

We also thoroughly validated the process-independent computation of NLO QCD corrections, presented in sec. 5. Firstly, we discussed several internal consistency checks that were either implemented or automatized during this thesis. Among the consistency checks we automated are checking the partition of unity property of the FKS  $S$  functions, the variation of slicing parameters like  $\delta_I$ , and explicitly testing the cancellation of subtraction terms with the real contribution in the soft or collinear limit.

Secondly, we computed a plethora of cross sections at NLO QCD in a standardized setup, comparing them with cross sections computed with `MG5_aMC`, presented in ref. [45]. Of all the 21 cross sections with leptonic initial state we compared, no two results for the same process deviate more than  $\sigma_{\text{NLO}}^{\text{sig}} = 2$ . Given the various processes we compared, this is remarkable evidence for the universal validity of the subtraction mechanism for FSR. We also compared 43 cross sections in an LHC-like setup. Only 5 processes display minor deviations of  $\sigma_{\text{NLO}}^{\text{sig}} > 2$ ; only a single one,  $pp \rightarrow W^+W^- ZZ$ , exceeds  $\sigma_{\text{NLO}}^{\text{sig}} = 3$ . As reason for the remaining minor deviations, we suspect differences in the phase-space setup for massive bosons between the both programs or differences among the employed OLPs. However, the generally outstanding agreement between the predictions of both programs for all other processes makes us confident that the minor deviation we observe here does not invalidate the FKS implementation in general. We included both parts of our validation efforts into the regularly executed functional test suite of `WHIZARD`, thus making sure that the achieved results will still be reproducible with future versions.

As the last point concerning NLO QCD cross sections at fixed order, we generalized the possibility to partition the real matrix element into a finite and a singular part towards  $pp$  collisions, and such that it became possible to generate events for each part separately. This is a prerequisite for using the real partition in conjunction with the `POWHEG` matching.

We dedicated sec. 3 to NLO QCD corrections beyond fixed order. We discussed parton-shower matching of NLO computations using the `POWHEG` method. The `POWHEG` method integrates well with the FKS subtraction scheme and offers a matching prescription, which can be implemented independently of the applied Shower

Monte Carlo (SMC) program. We explained the general idea of using the veto procedure to simulate events based on transverse momenta sampled from a modified Sudakov form factor, taking the NLO real matrix element as an estimation for an emission probability. Moreover, we demonstrated the veto procedure for several types of upper bounding functions (UBFs), covering all cases of potential emitters in the final state as well as massless initial states. This range of UBFs makes our implementation of the POWHEG-matching procedure as a whole general and process-independent.

Before the beginning of this thesis, the POWHEG-matching implementation was far from general. It was merely an experimental process-specific implementation valid for the production of a top-quark pair at a lepton collider. The general applicability to processes at lepton and hadron colliders, processes defined with flavor sums, such as jets, and those requiring a restriction of the phase space to be well-defined could only be achieved in the present work. The same holds for the inclusion of correct information beyond the bare weights and momenta in the generated events. This includes the determination of the color- and the flavor structure of the generated events as well as the inclusion of intermediate resonant particles. Each of these is crucial for a proper operation of the subsequent parton shower and hadronization module. Also, a subsequent detector simulation would otherwise be precluded.

Furthermore, we presented several refinements: with an appropriate choice of scales and  $\alpha_S$ , it is possible to achieve NLL accuracy for most processes in the matching procedure. To improve the usability for large-scale applications, we made a number of performance optimizations by optimizing the highest-bid algorithm and filling the POWHEG grid already parallel to setting up the integration grids instead of in a separate step. The performance of subsequent event processing can be improved by reducing the fraction of generated negative event weights, which we also commented on. The statistically correct treatment of samples of indefinite weights in all parts of the MC event generation could be ensured as a byproduct of this endeavor, too.

In sec. 6, we exemplified three different applications of the matching. We validated our implementation by comparing predictions for the Drell-Yan process with the POWHEG-BOX. In this comparison, we achieved excellent agreement between both programs. This holds for the generated POWHEG events, i.e., partonic events with maximally one extra radiated parton, and the events including parton shower and hadronization. Although the process under consideration is a simple, often studied process, it features ISR, different initial-state flavors and thus multiple color flows and flavor structures for the real emission processes. It thus constitutes a non-trivial candidate for validating the POWHEG matching.

Beyond the validation efforts, we applied the POWHEG matching in a fully realistic setup, matching that of an analysis performed by the CMS collaboration [189]. In this endeavor, we found that our prediction roughly agrees with the data and predictions from other MC generators employed in the course of ref. [189]. The remaining differences can be explained by minor technical differences between the employed programs and different choices in the description of the physics regarding the parton shower, e.g., matching and merging schemes. Although all employed tools used the same SMC, PYTHIA, and the same tune, several parameters influencing the matching procedure in the MC program simulating the hard process, such as the shower-starting scale,  $p_{T,\min}$ , and the real-partition scale,  $h_F$ , as well as the real-partition function itself and the details regarding the treatment of resonances, cannot be determined from first principles and are not included in the definition of the parton-shower tune, either. To have consistent settings for a wide range of applications, these parameters should be determined similar to or in conjunction with the parton-shower tune itself.

Lastly, we applied the POWHEG matching to an entirely different process, the production of a top-quark pair in association with a jet at a lepton collider. This application shows the generality of the matching implementation on the example of a process featuring multiple Born and real flavor structures as well as massless and massive emitters in the final state.

All features presented in this thesis, especially the generalization of the POWHEG matching, are publicly available and ready to be employed in phenomenological studies from WHIZARD version 3.1.0 on.

In the near future, there will be several projects benefiting from the enhanced capabilities at NLO QCD. On the one hand, there are applications at the LHC such as a continuation of the effort to compare predictions from different MC generators for measurements of same-sign vector boson scattering (VBS) up to the technical level in the course of ref. [9]. On the other hand, applications at lepton colliders profit from NLO QCD corrections, too. Here, their availability in WHIZARD comes in especially handy, as in this way, analyses not only profit from the higher-order QCD corrections but also from the lepton-collider specific competence of WHIZARD, including a description of beam spectra and initial-state radiation of photons. Two projects for the foreseen future in this domain are feasibility studies for  $b$ -mass measurements at the ILC [199] as well as top-mass measurements in  $e^+e^- \rightarrow t\bar{t}$  and  $e^+e^- \rightarrow t\bar{t}h$  events at the threshold, including a resummation of soft and collinear radiation via the POWHEG matching.

Besides NLO QCD corrections, the community has put a lot of work in the process-independent computation of NLO EW and mixed QCD+EW corrections in the past decade [200, 201]. Also in WHIZARD, the process-independent implementation of fixed-order NLO EW corrections could be completed in an effort parallel to the present work [76]. The NLO EW and mixed corrections are incorporated in the same FKS framework as the pure NLO QCD corrections. In this way, they reuse many of the features we implemented and discussed in this work, including the ability to simulate fixed-order NLO events and the construction of the ISR phase space and subtraction terms. Moreover, the automated self-consistency checks we discussed in sec. 5.1 greatly facilitated their debugging.

Implementing these features first in the setting of hadron colliders allowed for their stand-alone validation prior to their application in NLO EW corrections. The test suite we created from the validated processes allowed us to work on the NLO EW corrections without having to worry about introducing regressions. Considering applications of the implemented EW corrections, we recently computed predictions for multi-boson processes at a muon collider [1]. Future projects include the short list given at the beginning of this paragraph. Especially VBS receives large EW corrections [202], predominantly in the high-energy tails of the differential distributions and also the accuracy of top-threshold measurements [203–208] could further be improved by taking into account NLO EW corrections.

Another interesting project for the near future is the combination of the two topics we touched, the generalization of the POWHEG matching to also take into account EW corrections, or at least photon radiation, a.k.a. QED corrections. As the POWHEG matching, in our case, is built upon the FKS framework, this generalization is straightforward. The computation of mixed NLO corrections is organized in singular regions, alpha regions (ALRs) such that some ALRs account for the QCD corrections to the Born process, while other ALRs account for the QED corrections. In the POWHEG matching approach, the Sudakov form factor factorizes over the ALRs, so that in the conjunction of both, radiated QCD and QED particles are treated democratically. This means that the highest-bid algorithm will prefer the QCD or QED radiation according to the matrix-element ratios,  $\mathcal{R}/\mathcal{B}$ , in the Sudakov exponent. Thus, events featuring radiated gluons and photons will be generated in the same event sample. The remaining parton shower should then generate additional QCD and QED radiation, taking the appropriate radiation scales into account. From our side, all that is left to do to complete this generalization is to switch to using  $\alpha$  instead of  $\alpha_S$  as a coupling constant and skip the running of the coupling constant as well as the color-flow determination for QED radiation. As both the mixed NLO corrections and the POWHEG matching are already implemented in WHIZARD in a process-independent way, we are close to completing this generalization.

The automation of process-independent NNLO corrections is another active field of research and several NNLO subtraction schemes are discussed at the time [209–216]. One particular scheme, inspired by FKS subtraction, is coined STRIPPER [217, 218]. A more recent application of this method to diphoton plus jet production at the LHC can be found in ref. [219]. For MC generators with FKS-based NLO subtraction schemes, this might be the most promising approach of automatizing NNLO QCD corrections [71, 72]. The NNLO computation is then organized as computing the higher-order correction to the NLO correction, involving real corrections to the NLO real corrections and virtual corrections to the NLO virtual corrections, dubbed double-real and double-virtual contributions, respectively. In addition, virtual corrections to the NLO real and real corrections to the NLO virtual contributions have to be accounted for. Organizing these new types of contributions should be possible by extending the existing component structure in *WHIZARD*. However, the computation requires the availability of all relevant NNLO matrix elements. Especially for the two-loop computations required for the double-virtual contributions, only matrix elements for specific processes are available so far. Defining an algorithm to compute them process-independently is an ongoing effort.

# Appendix

## A The Altarelli-Parisi splitting functions

The Altarelli-Parisi splitting functions [81] are the kernels of the QCD evolution equation for parton distributions in the collinear factorization. They can directly be derived from the QCD vertices and are thus a universal property of the theory. As such, they find applications on many occasions, also throughout this thesis. We will list two different forms here for reference.

### A.1 The spin-dependent case

We will first discuss the more general but less familiar spin-dependent case. In this case, the splitting functions do not only depend on the momentum fraction  $z$  and the transverse momentum  $k_\perp$  defined according to eq. (2.138) but also on the helicity of the splitting particle. In fermion splittings, we will denote their spins as  $s_i, s'_i$ . For gluon splittings, we will use the Lorentz indices  $\mu, \nu$ . In sec. 2.6.1, we commonly denoted both pairs of indices as  $\lambda$ . Moreover, we keep the  $\epsilon$  dependence of the splitting functions in  $d = 4 - 2\epsilon$  dimensions. To derive the splitting functions in 4 dimensions, it is trivial to take the limit  $\epsilon \rightarrow 0$  later on. Following ref. [57], we define

$$\hat{P}_{f_{\mathcal{B}}^i \rightarrow f_{\mathcal{R}}^i f_{\mathcal{R}}^j}^{s_i s'_i}(z, k_\perp; \epsilon) := \langle s_i | P_{f_{\mathcal{B}}^i \rightarrow f_{\mathcal{R}}^i f_{\mathcal{R}}^j}(z, k_\perp; \epsilon) | s'_i \rangle \quad \text{and} \quad (\text{A.1})$$

$$\hat{P}_{f_{\mathcal{B}}^i \rightarrow f_{\mathcal{R}}^i f_{\mathcal{R}}^j}^{\mu\nu}(z, k_\perp; \epsilon) := \langle \mu | P_{f_{\mathcal{B}}^i \rightarrow f_{\mathcal{R}}^i f_{\mathcal{R}}^j}(z, k_\perp; \epsilon) | \nu \rangle \quad . \quad (\text{A.2})$$

We denoted the splitting function's splitting type adjusted to their application throughout this thesis, i.e., as the splitting connecting the Born and the real flavor structure. For our definition<sup>25</sup> of  $z$  and  $k_\perp$ , we find for the spin-dependent splitting functions [48]

$$\hat{P}_{q \rightarrow qg}^{s_i s'_i}(z, k_\perp; \epsilon) = \hat{P}_{\bar{q} \rightarrow \bar{q}g}^{s_i s'_i}(z, k_\perp; \epsilon) := \delta^{s_i s'_i} C_F \left[ \frac{1 + (1-z)^2}{z} - \epsilon z \right] \quad (\text{A.3})$$

$$\hat{P}_{q \rightarrow gq}^{s_i s'_i}(z, k_\perp; \epsilon) = \hat{P}_{\bar{q} \rightarrow g\bar{q}}^{s_i s'_i}(z, k_\perp; \epsilon) := \delta^{s_i s'_i} C_F \left[ \frac{(1+z)^2}{1-z} - \epsilon(1-z) \right] \quad (\text{A.4})$$

$$\hat{P}_{g \rightarrow q\bar{q}}^{\mu\nu}(z, k_\perp; \epsilon) := T_F \left[ -g^{\mu\nu} - 4z(1-z) \frac{k_\perp^\mu k_\perp^\nu}{k_\perp^2} \right] \quad (\text{A.5})$$

$$\hat{P}_{g \rightarrow gg}^{\mu\nu}(z, k_\perp; \epsilon) := C_A \left[ -2 \left( \frac{z}{1-z} + \frac{1-z}{z} \right) g^{\mu\nu} + 4z(1-\epsilon)(1-z) \frac{k_\perp^\mu k_\perp^\nu}{k_\perp^2} \right] \quad (\text{A.6})$$

using the symmetry  $\hat{P}_{q \rightarrow gq}^{s_i s'_i}(z, k_\perp; \epsilon) = \hat{P}_{q \rightarrow qg}^{s_i s'_i}(1-z, k_\perp; \epsilon)$ .

### A.2 The spin-averaged case

After an angular integration over the  $d = 4 - 2\epsilon$  dimensional phase-space element  $d\Omega_{d-2}$ , the spin-dependence will average out, leading to the more familiar form of the splitting functions. While the effect is trivial for the already diagonal fermion-splitting functions, we have to average the  $k_\perp$ -dependent terms in the gluon-splitting functions. Following ref. [220], we use the relation

$$\left\langle \frac{k_\perp^\mu k_\perp^\nu}{k_\perp^2} \right\rangle_\phi = \frac{1}{d-2} \left( -g^{\mu\nu} + \frac{\bar{k}_i^\mu \eta^\nu + \eta^\mu \bar{k}_i^\nu}{\bar{k} \cdot \eta} \right) \quad , \quad (\text{A.7})$$

---

<sup>25</sup>This parametrization is different from the one chosen in ref. [57] leading to an inverted sign of the  $k_\perp^\mu k_\perp^\nu$ -dependent terms.

where  $\bar{k}_i$  is the Born momentum of the emitter and  $\eta$  is defined as in eq. (2.138).

Inserting eq. (A.7) into eq. (A.5) and (A.6) and dropping the second, longitudinal term proportional to  $\bar{k}_i^\mu$  of eq. (A.7) anticipating the Ward identity  $k^\mu \mathcal{M}_\mu = 0$ , we find for the spin-averaged splitting functions

$$\langle \hat{P}_{q \rightarrow qq} \rangle(z, \epsilon) = \langle \hat{P}_{\bar{q} \rightarrow \bar{q}g} \rangle(z, \epsilon) := C_F \left[ \frac{1 + (1-z)^2}{z} - \epsilon z \right] \quad (\text{A.8})$$

$$\langle \hat{P}_{q \rightarrow gq} \rangle(z, \epsilon) = \langle \hat{P}_{\bar{q} \rightarrow g\bar{q}} \rangle(z, \epsilon) := C_F \left[ \frac{(1+z)^2}{1-z} - \epsilon(1-z) \right] \quad (\text{A.9})$$

$$\langle \hat{P}_{g \rightarrow q\bar{q}} \rangle(z, \epsilon) := T_F \left[ 1 - \frac{2z(1-z)}{1-\epsilon} \right] \quad (\text{A.10})$$

$$\langle \hat{P}_{g \rightarrow gg} \rangle(z, \epsilon) := 2C_A \left[ \frac{z}{1-z} + \frac{1-z}{z} + z(1-z) \right] \quad (\text{A.11})$$

## B Basic random number sampling methods

When generating the POWHEG kinematics, we need to generate them according to a given distribution based on uniformly distributed random numbers. Such a problem is very common when applying Monte Carlo strategies. Especially in MC event generators, also the integration and the event simulation rely on the sampling of random numbers in arbitrary distributions generated from a set of initially uniformly distributed random numbers. The numerous ways to deal with this problem are treated in many textbooks, e.g., refs. [221, 222]. For completeness, we will discuss a few basic strategies we applied in the main part of the present work in this appendix.

### B.1 Basic definitions

#### Probability density function (PDF)

A PDF<sup>26</sup> is a continuous function resembling the relative likelihood of a random variable. In such a continuous distribution, the likelihood of any specific value is zero as there is an infinite pool of possibilities to draw from. Rather, we interpret the PDF's integral as the probability of a given random variable  $X$  falling in a certain range,

$$\mathcal{P}(X|X \in [a, b]) = \int_a^b f_X(x) dx \quad \text{with } a, b \in \mathbb{R} \quad \text{and } a < b \quad . \quad (\text{B.1})$$

Mathematically, a PDF  $f_X(x)$  thus has to fulfill

$$f_X(x) \geq 0 \quad \forall x \quad \text{and} \quad \int f_X(x) = 1 \quad (\text{B.2})$$

for all probabilities to be positive and sum up to unity.

#### Cumulative Distribution Function (CDF)

A CDF is a continuous function of a real-valued random variable. Evaluated at position  $x$ , it is the probability of random values  $X$  smaller than or equal to  $x$ , i.e.,  $F_X(x) = \mathcal{P}(X \leq x)$ . For scalar continuous distributions, it is thus the integral of the corresponding PDF,

$$f_X(x) = \frac{dF_X(x)}{dx} \quad \text{and} \quad F_X(x) = \int_{-\infty}^x f_X(t) dt \quad . \quad (\text{B.3})$$

As  $f$  and  $F$  are canonically used to denote the PDF and the CDF, respectively, we use the label  $X$  to indicate that they refer to the same random variable  $X$ .

### B.2 Inverse Transform Sampling (ITS)

One of the simplest sampling strategies is the *inverse transform sampling*. This method allows to generate random variables  $X$  following a given CDF  $F_X$ . Its idea is based on the observation that if  $X$  is a continuous random variable with CDF  $F_X$ , then the variable  $Y = F_X(X)$  is uniformly distributed in the interval  $[0, 1]$ , i.e., it is  $Y \in \text{Unif}[0,1]$ .

To see this, we define a random variable  $Y := F_X(X)$ , i.e.,  $Y$  is generated by evaluating the CDF  $F_X(x)$  at a random value  $X$ , which itself has the CDF  $F_X$ . We find for the CDF  $F_Y$  with any  $y \in [0, 1]$ :

$$F_Y(y) = \mathcal{P}(Y \leq y) = \mathcal{P}(F_X(X) \leq y) = \mathcal{P}(X < F_X^{-1}(y)) = F_X(F_X^{-1}(y)) = y \quad (\text{B.4})$$

---

<sup>26</sup>In this appendix only, "PDF" refers to "probability density function" instead of "parton distribution function".

and if  $F_Y(y) = y$ , then  $f_Y(y) = 1$ . If this holds for all  $y \in [0, 1]$ , the variable  $Y$  is uniformly distributed in the interval  $[0, 1]$ .

The inverse transform sampling is just the inverse of this approach: given a uniformly distributed random variable  $Y \in \text{Unif}[0, 1]$ , we can generate a random variable  $X$  with CDF  $F_X$  using the inverse<sup>27</sup>

$$X = F_X^{-1}(Y) \quad . \quad (\text{B.5})$$

### Truncated distributions

If we want to generate the random variable  $X$  in a specific interval  $(a, b]$ , this can easily be implemented in the inverse transform sampling. We can simply take a uniform random number  $Y$  from the interval  $(F(a), F(b)]$  and the value  $X$  will be distributed according to  $F_X$  in the interval  $(a, b]$ .

### A simple example

Suppose we want to generate a random variable  $X \in [0, 1]$  according to a PDF

$$f_X(t) = 2t \quad . \quad (\text{B.6})$$

We first compute the CDF

$$F_X(x) = \int_0^x f_X(t) dt = x^2 \quad (\text{B.7})$$

and then form the inverse,  $F_X^{-1}(x) = \sqrt{x}$ . So given a uniform random variable  $r \in \text{Unif}[0, 1]$ , we can generate  $X$ , such that it has a PDF  $f_X$ , by taking the square root,

$$X = \sqrt{r} \quad . \quad (\text{B.8})$$

## B.3 Rejection Sampling (RS)

The ITS is only sometimes applicable, as for this method, the CDF needs to exist analytically and be invertible. When dealing with probability distributions, this is rarely the case. To overcome this problem, it can be combined with rejection sampling.

The general idea of rejection sampling is to overestimate the PDF  $f_X(x)$  with a function  $g_X(x)$ , which is integrable and whose primitive function is invertible and to correct this overestimation with a subsequent veto step.

Given a PDF  $f_X(x)$ , we find an overestimated PDF  $g_X(x)$  such that

$$\exists k > 0 \in \mathbb{R} : f_X(x) \leq k \cdot g_X(x) \quad \forall x \in \mathbb{R} \quad . \quad (\text{B.9})$$

Here, introducing the real factor  $k$  is necessary as  $\int f_X(x) dx = \int g_X(x) dx = 1$ , so without  $k$ , a  $g_X(x) \neq f_X(x)$  would not exist. We then proceed to generate the random variable  $X$  according to  $g_X(x)$  by using, e.g., the ITS and afterwards keep it only with probability

$$\mathcal{P}_{\text{surv}}(X) = \frac{f_X(X)}{k \cdot g_X(X)} \quad . \quad (\text{B.10})$$

The random variables surviving this procedure will be distributed according to the PDF  $f_X(x)$ .

---

<sup>27</sup> In this context,  $F_X^{-1}$  denotes the *quantile function* defined by  $F_X^{-1}(y) := \inf\{x \in \mathbb{R} | F_X(x) \geq y\}$ , which is equal to the inverse function of  $F_X$  only if  $F_X$  is strictly monotonically increasing.

## C Technical supplements to the POWHEG veto procedure

This section contains some technical supplements to the POWHEG veto procedure. They may help to get a deeper technical understanding of the procedure.

### C.1 Evolution of the transverse momentum

In sec. 3.5.9, we summarized the veto steps of the POWHEG veto procedure. In total, we explained 5 veto steps: the UBF veto, the  $\alpha_S$  veto, the  $\xi_{\max}$  veto, the norm veto and the matrix-element-veto step. Technically, we combined the first two veto steps, so that we have up to 4 veto steps left. In this section, we want to understand how the value of the generated transverse momentum  $p_T$  evolves while we try to generate a value that survives all veto steps in order to generate an event.

We generated 10 POWHEG events for the Drell-Yan process, in the setup described in sec. 6.1.1, but without real partition and restricted to a single ALR. After each successfully passed veto step, we note the pairs of generated transverse momenta and the value of the Sudakov form factor,  $(p_T, \Delta(p_T))$ . These pairs of values are displayed in a double-logarithmic scatterplot in fig. C.1.

We can see in total 10 tracks of dots. The evolution begins at large transverse momenta, i.e., on the RHS. Here, the Sudakov form factor takes large values, so the emission probabilities are small. In this region, often already the first veto step, the UBF veto, fails. Thus, we see blue entries predominantly on the RHS. Overall, most of the data points are colored yellow. This indicates a tendency for failing norm veto steps. Each track will finally end in a data point colored cyan. These resemble passed matrix-element-veto steps. After each passed matrix-element-veto step, the veto procedure has determined a valid  $p_T$  value to enter the competition with the other ALRs in the highest-bid procedure. In this case, all 10 generated  $p_T$  values are below 17 GeV. After the matrix-element-veto step is passed, the evolution stops. However, an event with the chosen transverse momentum will only be simulated if the generated  $p_T$  is the largest among all ALRs.

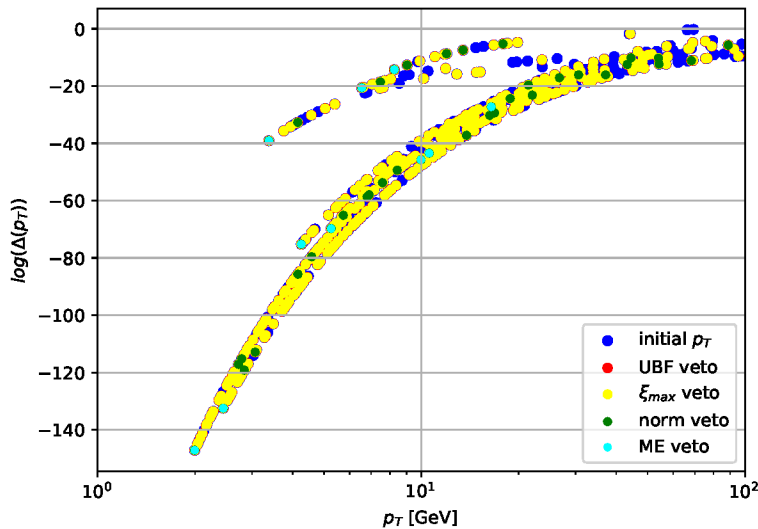


Fig. C.1: Evolution of the transverse momentum during the POWHEG veto procedure. 10 POWHEG events for the Drell-Yan process have been generated in the setup described in sec. 6.1.1. Only transverse momenta generated in ALR 1 are shown. ALR 1 is defined by the Born process  $d\bar{d} \rightarrow e^+e^-$  and gluon radiation. Each passed step in the veto procedure used to generate these events resembles a single dot at  $(p_T, \Delta(p_T))$  in this scatterplot. The last passed veto step for each generated transverse momentum is indicated by color.

## C.2 Veto and survival rates

When generating POWHEG events using the veto procedure, WHIZARD keeps track of how many attempts to generate a valid POWHEG event failed in which steps of the veto procedure. Studying these rates allows to understand which veto steps are only unlikely passed and thus have the potential to be optimized.

To study the veto rates, we first turn to the Drell-Yan process in the setup described in sec. 6.1.1. The veto procedure factorizes over ALRs, and as the Drell-Yan process features only ISR, the UBFs employed in each ALR are the same, i.e., the one we discussed in sec. 3.5.7. We can thus representatively pick a single ALR. We pick ALR 1, which features gluon radiation off either initial-state quark. Furthermore, we compare runs with three different real-partition settings to see how separating the finite part from the real cross section entering the Sudakov form factor influences the veto rates.

The runtimes to generate 200k events, the percentage of grid excesses and the veto rates in this setup are displayed in tab. 17. For the veto rates, we list the local veto rate,  $\mathcal{P}_{\text{veto}}^{\text{loc}}$ , i.e., the fraction of events vetoed in each step and the total survival rate,  $\mathcal{P}_{\text{surv}}^{\text{tot}}$ , i.e., the fraction of the total attempts to generate an event passing the corresponding veto step. For the  $n$ -th veto step, they are connected via  $\mathcal{P}_{\text{surv}}^{\text{tot}} = \prod_{i=1}^n (1 - \mathcal{P}_{\text{veto}, i}^{\text{loc}})$ .

Comparing the different choices for the real partition, we see that they only mildly influence the UBF veto and the  $\xi_{\text{max}}$  veto. The reason is that the real partition affects the real matrix element, which only indirectly affects the  $p_T$  values sampled from the Sudakov factor in the overestimated form via the maximum of the POWHEG grid,  $N_{\text{max}}^{\alpha_r}$ . The individual bin values of the POWHEG grid are not relevant at this point and the analytic overestimation necessitating the UBF veto is also not directly influenced by the real matrix element. Moreover, the veto rates of the first veto steps have a low impact on the total computational cost, as a veto early in the procedure only discards computationally cheap steps. Nevertheless, we see lower veto rates for a stronger separation of the real-partition parts because the grid maximum decreases if we exclude a portion from the real matrix element.

The effect of the real partition becomes most dominantly visible in the norm-veto step. Here, the veto rate is proportional to the ratio of the grid's maximum over its mean value. If we confine the real matrix element to a smaller range, the efficiency of this step improves. At the same time, the real partition alleviates the effects of phase-space regions with very small Born matrix elements, as we discussed in sec. 3.6.3. Due to these effects, the veto rate drops from 91.98% to 16.75% if we activate the real partition with  $h_F = 50$  GeV. As a side note, the huge veto rate of the norm-veto step without real partition explains why yellow is the predominant color in fig. C.1; most often, the  $\xi_{\text{max}}$  veto is the last survived veto step.

With a smaller variation of the matrix-element ratio in the Sudakov form factor, also the UBF is a better overestimate, so that even the veto rate of the matrix-element veto improves. Overall, a factor of approximately 38 fewer event-generation attempts are necessary to generate the same number of events with  $h_F = 50$  GeV compared to not using the real partition. This also explains the decreased runtime.

If the real-partition scale is decreased further to 5 GeV, even more events survive the norm-veto step. However, most of them fail the subsequent and more expensive matrix-element-veto step, overcompensating the positive effects and leading to lower total survival rates and a slight increase in the total runtime.

There are some downsides to using the real partition, too. On the one hand, these improvements come at the cost of increased grid excesses. With a fraction of up to 0.76% at  $h_F = 5$  GeV, however, they are still tolerable. On the other hand, if we use the real partition to generate the POWHEG events, we have to generate events representing the real finite component additionally in a separate run. To optimize the reduction of the statistical uncertainties per invested time, we should generate more events for the real finite component the larger its contribution to the total cross section is. A tiny uncertainty for just a small contribution to most of the distribution will not improve the overall picture much. The same holds for the generated POWHEG events. This implies that, in a realistic comparison, we should measure the additional time required to

generate the events representing the real finite contribution and we should also consider that the simulation of fewer POWHEG events is necessary for small values of  $h_F$ . In the study presented here, we considered the simulation of POWHEG events only.

Summarizing, we can observe that a mild real partition significantly improves the veto procedure's efficiency. However, it remains to be validated that this applies to other processes and emitters requiring other UBFs as well.

$h_F$	$\infty$ GeV		50 GeV		5 GeV	
Runtime events:	9min		6min		7min	
Grid excesses:	0.02%		0.19%		0.76%	
Veto step ↓	$\mathcal{P}_{\text{veto}}^{\text{loc}}$	$\mathcal{P}_{\text{surv}}^{\text{tot}}$	$\mathcal{P}_{\text{veto}}^{\text{loc}}$	$\mathcal{P}_{\text{surv}}^{\text{tot}}$	$\mathcal{P}_{\text{veto}}^{\text{loc}}$	$\mathcal{P}_{\text{surv}}^{\text{tot}}$
UBF veto	30.57%	69.25%	29.43%	70.57%	24.10%	75.90%
$\xi_{\text{max}}$ veto	5.94%	65.14%	5.91%	66.40%	4.16%	72.74%
Norm veto	91.98%	5.22%	16.75%	55.28%	13.40%	62.99%
ME veto	85.36%	0.76%	47.37%	29.09%	77.27%	14.32%
Total	99.24%	0.76%	70.91%	29.09%	85.68%	14.32%

Tab. 17: Veto and survival probabilities of each veto step during the POWHEG veto procedure for the process  $d\bar{d} \rightarrow e^+e^-$ , i.e., the Drell-Yan process restricted to a single proton flavor. The veto probability,  $\mathcal{P}_{\text{veto}}^{\text{loc}}$  is local in the sense that it refers to a single veto only, whereas the survival probability is total, i.e., it takes into account all previous steps. We show three cases of no real partition ( $h_F = \infty$  GeV) and a real partition with real-partition scales of  $h_F = 50$  GeV and  $h_F = 5$  GeV. The runtime refers to the simulation of 200k events on a single core. The same amount of events has been generated to estimate the veto rates. The given veto and survival fractions refer to ALR 1, which features gluon radiation off either initial-state quark. The rates in the other two ALRs are roughly equivalent. We chose a POWHEG grid with dimension 10x10 and  $p_{T,\text{min}} = 1$  GeV.

## D Generating POWHEG events with WHIZARD

This section will exemplify all the technical settings we use to generate POWHEG events with WHIZARD. We typically write all the relevant settings in a single file that can be read in to load the configuration and start the computations. This file is written in the scripting language SINDARIN. It usually consists of subsequent parameter definitions read line-by-line but a more complex syntax to define scales and cuts is possible, too. All the details of SINDARIN, including a description of all parameters, are specified in the WHIZARD manual [91]. The manual is also always the most up-to-date reference for all the settings, should they change in future versions. The settings described in this section refer to WHIZARD version 3.1.0. We will take the setup we used for the comparison of differential distributions with data taken by the CMS experiment in sec. 6.2 as an example to illustrate the general procedure.

### D.1 Steering WHIZARD - The SINDARIN file

At the beginning of each SINDARIN file, we choose the model and set the particle masses and widths. In this case, we choose the  $G_F - m_W - m_Z$  input scheme and set the masses and widths of all bosons to their PDG [190] values. This indirectly fixes the electromagnetic coupling constant  $\alpha$ , which is a derived parameter in this scheme. We neglect the masses of all light leptons and quarks, choosing non-zero masses only for the top quark and the tau lepton.

```

1 model = SM ("GF_MW_MZ")
2 GF = 1.16637E-5
3
4 mW = 80.379
5 mZ = 91.1876
6 mH = 125.0
7 wW = 2.085 GeV
8 wZ = 2.4952 GeV
9 wH = 3.2 GeV
10
11 ms = 0 eV
12 mc = 0 eV
13 mb = 0 eV
14 mtop = 173.2
15
16 me = 0 keV
17 mmu = 0 MeV
18 mtau = 1.777 GeV

```

Secondly, we define abbreviations for flavor sums, that we will later use to define the scale and the phase-space cuts. We include all 5 massless quark flavors in the definition of the proton.

```

19 alias pr = u:U:d:D:s:S:c:C:b:B:gl
20 alias lep = e1:e2
21 alias alep = E1:E2
22 alias leptons = lep:alep

```

Next, we determine the running of  $\alpha_S$ . Although the Born process does not depend on  $\alpha_S$ , it is a proportionality constant for the NLO QCD correction. Here, we take the value of  $\alpha_S$  matching that of the active LHAPDF set and member.

```

23 ?alphas_is_fixed = false
24 ?alphas_from_lhapdf = true

```

We continue with some technical settings. We choose `OpenLoops` as the matrix-element provider for all except the Born matrix elements. This is necessary for two reasons: on the one hand, `0'Mega` does not yet provide spin- and color-correlated matrix elements. On the other hand, the relative probabilities for different color structures, needed for correct parton showering, rely on `0'Mega` Born matrix elements, as, for

the moment, color information from other matrix-element providers is not fully processed. As explained in sec. 3.6.7, this is sufficient to also determine the color information for the events featuring real radiation. For `OpenLoops`, we also have to explicitly set the powers of  $\alpha$  and  $\alpha_S$  matching the desired matrix elements.

```
25 $method = "openloops"
26 $born_me_method = "omega"
27 alpha_power = 2
28 alphas_power = 0
```

To make use of WHIZARD's parallelization capabilities, we switch to the thread-safe RNG `RNGstream` [144] and also to `VAMP2`. Additionally, we disable multi-threading in `O'Mega` to avoid any clash with the MPI parallelization.

```
29 $rng_method = "rng_stream"
30 $integration_method = "vamp2"
31 ?omega_openmp = false
32 openmp_num_threads = 1
```

Coming back to the physics, we determine the CM energy and the beam setup and choose the PDF set.

```
33 sqrts = 13 TeV
34 beams = p, p => lhpdf
35 $lhpdf_file = "NNPDF30_nlo_as_0118"
```

The phase-space cuts at generator-level, requiring the lepton system to be in a mass window around the  $Z$  pole, which are employed in the analysis described in sec. 6.2.1, could be implemented using

```
36 cuts = let subevt @hard_elecs_pt = select if Pt > 25 GeV [leptons] in
37       let subevt @hard_elecs_rap = select if abs(Eta) < 2.4 [@hard_elecs_pt] in
38       let real mee = eval M [lep, alep] in
39       count [@hard_elecs_rap] == 2
40       and abs(mee - mZ) < 15 GeV
```

This, however, is only useful to estimate the total cross section. For a realistic application including a parton shower, we need to loosen the phase-space restrictions to avoid dropping events prior to applying the shower that would pass our requirements afterwards. We choose to require an invariant lepton mass of 50 GeV at this point, but the results of the applied analysis should not be sensitive to the chosen value.

```
36 cuts = all M > 50 GeV [lep, alep]
```

We determine the scale according to eq. (6.8).

```
37 scale = let real mll = eval M [lep, alep] in
38       let real ptz = eval Pt [lep + alep] in
39       sqrt(ptz^2 + mll^2)
```

Next, we set the parameters determining the resonance insertion. We already elaborated on these in sec. 3.6.8. In this application, we insert resonant  $Z$  bosons with invariant masses up to 8 widths away from the resonance with a  $1/e$  Gaussian suppression  $4\Gamma_Z$  away from the  $Z$  mass.

Unfortunately, including resonances in the generated events is currently not possible if WHIZARD is run on many cores in parallel using the MPI implementation. To circumvent this problem, it is possible to split the computation into two separate runs. In the first run, we use the MPI to compute the total cross section in the parallel mode. For this, we do not need resonance information. In the second run, we simulate events, reusing the phase-space mapping and the POWHEG grid determined in the integration step. As the simulated events are independent, this can always be trivially parallelized by starting separate instances of the program. This allows to include the resonance information in the generated events while still using multiple cores for the simulation.

```
40 ?resonance_history = true
41 resonance_on_shell_turnoff = 4
42 resonance_on_shell_limit = 8
```

For the simulation of POWHEG events, we need to compute the contributions from all NLO components at PSPs related to the same underlying Born PSP. This is achieved by activating the combined integration mode. We also activate the real partition. When generating POWHEG events, we want to include the singular part of the real contribution. We choose a real-partition scale of  $h_F = 5$  GeV.

```
43 ?combined_nlo_integration = true
44
45 $real_partition_mode = "singular"
46 real_partition_scale = 5 GeV
```

We define the process as  $pp \rightarrow e^+e^-$  using the previously defined alias for the proton. We also specify that we want to perform an NLO calculation at this opportunity.

```
47 process ppee = pr, pr => e1, E1 { nlo_calculation = full }
```

The POWHEG grid (c.f. sec. 3.5.4) is filled as a byproduct of the integration stage. Thus, most settings relevant for generating POWHEG events have to be set before the `integrate` statement.

We want to generate unweighted POWHEG events to avoid rare kinematic configurations, which might cause errors when applying a parton shower. We choose a  $10 \times 10$  POWHEG grid and set  $p_{T,\min} = 2.5$  GeV.

```
48 ?unweighted = true
49 ?powheg_matching = true
50 powheg_grid_size_xi = 10
51 powheg_grid_size_y = 10
52 powheg_pt_min = 2.5 GeV
```

Finally, we start the integration of the total cross section, adapting the grids and weights with 500k matrix-element calls in 8 iterations, followed by 5 iterations with 500k calls to compute the actual result.

```
53 integrate (ppee) { iterations = 8:500000:"gw", 5:500000 }
```

After the cross section has been computed and the grids have been determined, we turn to the event simulation. We generate 1M events and request a progress report every 20%.

```
54 n_events = 1000000
55 checkpoint = n_events / 5
```

Furthermore, we have to explicitly tolerate negative event weights.

```
56 ?negative_weights = true
```

We choose to write the events in two different formats, `HepMC` for a direct analysis using `Rivet` and `LHEF` to be passed to `PYTHIA`. For the `HepMC` format, we have to explicitly state that the total cross section should be included in the generated event files. For the `LHEF` format, we disable including the explicit matrix-element values in each generated event. This information is only relevant for the matrix-element method, which we will not pursue. Excluding it saves some space if the events are written to disk<sup>28</sup>.

```
57 sample_format = lhef, hepMC
58 ?hepMC_output_cross_section = true
59 ?lhef_write_sqme_prc = false
```

Lastly, we run the simulation by invoking

```
60 simulate (ppee)
```

<sup>28</sup>Having to store all the generated events on disk can be avoided by using FIFO files. These are named pipes in the file system, merely marking a location from which the generated events can be read while they are being written.

### Generating events for the finite real component

The procedure described so far will generate events using the POWHEG-matching prescription. They will feature up to one more parton in the final state than present in the Born process and their weights will be given by the sum of the Born, the virtual, the DGLAP remnant and the singular real component.

To also take into account the finite real contribution, which we split off the real contribution by using the real partition, we need to generate events for this component, too. We do this in a separate run with slightly different settings than before. In this case, we simulate events for the real component only, specifying that we only want to compute the finite part of the real partition. We cannot use the combined integration mode when computing just the real finite part, and also, we have to disable the POWHEG matching. The events representing the finite real contribution will not need to undergo the matching procedure. This will generate a second event sample containing only real-like events.

```
1 nlo_calculation = real
2 $real_partition_mode = finite
3 ?combined_nlo_integration = false
4 ?powheg_matching = false
```

## D.2 Using Rivet

In the next step, both generated event samples should be showered and hadronized by an SMC for realistic applications. We discussed the shower settings steering the POWHEG matching in PYTHIA already in sec. 6.1.4. The SMC will generate event files in the HepMC format. Whether or not the simulated events are showered, we can use Rivet [94] to analyze the generated events.

We will not discuss the details of writing the analysis routines in Rivet here. Many experimental analyses for Rivet are available online, and how to write one from scratch is documented in the Rivet GitLab [223] and the Rivet manual [93]. Instead, we will focus on how to run rivet with an emphasis on how to deal with multiple event samples constituting a single distribution.

The procedure described in sec. D.1 will generate a separate event sample for the finite real component and the POWHEG events taking all other components into account. Analyzing them will yield two separate YODA [224] files containing the resulting histogram information. Due to the processing, that the event samples underwent, and potentially different sample sizes, the sample normalizations might have been altered. To reproduce meaningful differential distributions, each sample must contribute proportionally to the cross section it represents. If any event sample is not normalized to the respective cross section, this can be remedied by invoking the `yodascale` script, available as part of the Rivet 3 distribution. For example, calling

```
1 yodascale.py -c '. * 1.25x' ppee.yoda
```

will scale all histograms contained in the `ppee.yoda` file by a factor of 1.25.

At this point, we have two separate sets of histograms, each properly normalized. We can merge both sets of histograms by invoking another script, `yodamerge`.

```
2 yodamerge -o ppee_sum.yoda --add ppee_comb.yoda ppee_fin.yoda
```

This will additively merge both YODA files. If both samples have been normalized correctly prior to the merging, a histogram with just a single bin should reproduce the total cross section.

Finally, the histogram data stored in the YODA files can be plotted, as usual, using the scripts `rivet-mkhtml` and `make-plots` from the main Rivet distribution.

## References

- [1] P. Bredt, W. Kilian, J. Reuter, and P. Stienemeier. “NLO Electroweak Corrections to Multi-Boson Processes at a Muon Collider” (Aug. 2022). arXiv: [2208.09438](https://arxiv.org/abs/2208.09438).
- [2] P. Bredt, J. Reuter, and P. Stienemeier. “Automated NLO SM corrections for all colliders”. *41st International Conference on High Energy Physics*. Oct. 2022. arXiv: [2210.07157](https://arxiv.org/abs/2210.07157).
- [3] P. Stienemeier et al. “WHIZARD 3.0: Status and News”. *International Workshop on Future Linear Colliders*. Apr. 2021. arXiv: [2104.11141](https://arxiv.org/abs/2104.11141).
- [4] J. Reuter et al. “Status of the WHIZARD generator for linear collider”. *International Workshop on Future Linear Colliders*. Feb. 2020. arXiv: [2002.06122](https://arxiv.org/abs/2002.06122).
- [5] S. Braß et al. “Precision Monte Carlo simulations with WHIZARD”. *CERN Yellow Reports: Monographs* 3 (2020). Ed. by A. Blondel, J. Gluza, S. Jadach, P. Janot, and T. Riemann, pp. 205–210. DOI: [10.23731/CYRM-2020-003.205](https://doi.org/10.23731/CYRM-2020-003.205).
- [6] W. Kilian et al. “New Developments in WHIZARD Version 2.6”. *International Workshop on Future Linear Colliders (LCWS2017) Strasbourg, France, October 23-27, 2017*. 2018. arXiv: [1801.08034](https://arxiv.org/abs/1801.08034).
- [7] S. Braß, P. Bredt, J. Reuter, P. Stienemeier, and V. Rothe. “Automation of NLO SM processes in WHIZARD for hadron and lepton collisions”. 2023. in preparation.
- [8] M. Diehl and P. Stienemeier. “Gluons and sea quarks in the proton at low scales”. *Eur. Phys. J. Plus* 135.2 (2020), p. 211. DOI: [10.1140/epjp/s13360-020-00200-6](https://doi.org/10.1140/epjp/s13360-020-00200-6). arXiv: [1904.10722](https://arxiv.org/abs/1904.10722).
- [9] A. Ballestrero et al. “Precise predictions for same-sign W-boson scattering at the LHC”. *The European Physical Journal C* 78.8 (Aug. 2018), p. 671. ISSN: 1434-6052. DOI: [10.1140/epjc/s10052-018-6136-y](https://doi.org/10.1140/epjc/s10052-018-6136-y). arXiv: [1803.07943](https://arxiv.org/abs/1803.07943).
- [10] C. F. Anders et al. “Vector boson scattering: Recent experimental and theory developments”. *Rev. Phys.* 3 (2018), pp. 44–63. DOI: [10.1016/j.revip.2018.11.001](https://doi.org/10.1016/j.revip.2018.11.001). arXiv: [1801.04203](https://arxiv.org/abs/1801.04203).
- [11] J. Thomson. *Cathode rays*. 1897. DOI: <https://doi.org/10.1038/162098a0>.
- [12] J. Thomson. “XXIV. On the structure of the atom: an investigation of the stability and periods of oscillation of a number of corpuscles arranged at equal intervals around the circumference of a circle; with application of the results to the theory of atomic structure”. *The London, Edinburgh, and Dublin Philosophical Magazine and Journal of Science* 7.39 (1904), pp. 237–265. DOI: [10.1080/14786440409463107](https://doi.org/10.1080/14786440409463107).
- [13] E. Rutherford. *The scattering of alpha and beta particles by matter and the structure of the atom*. 1911.
- [14] N. Bohr. “On the Constitution of Atoms and Molecules”. *Phil. Mag. Ser. 6* 26 (1913), pp. 1–24. DOI: [10.1080/14786441308634955](https://doi.org/10.1080/14786441308634955).
- [15] N. Bohr. “On the Constitution of Atoms and Molecules. 2. Systems containing only a Single Nucleus”. *Phil. Mag. Ser. 6* 26 (1913), p. 476. DOI: [10.1080/14786441308634993](https://doi.org/10.1080/14786441308634993).
- [16] J. R. Rydberg. “XXXIV. On the structure of the line-spectra of the chemical elements”. *Philosophical Magazine Series 1* 29 (1890), pp. 331–337.
- [17] A. Sommerfeld. “Zur Quantentheorie der Spektrallinien”. *Annalen der Physik* 356.17 (1916), pp. 1–94. DOI: <https://doi.org/10.1002/andp.19163561702>.

- [18] E. Schrödinger. “An Undulatory Theory of the Mechanics of Atoms and Molecules”. *Phys. Rev.* 28 (6 Dec. 1926), pp. 1049–1070. DOI: [10.1103/PhysRev.28.1049](https://doi.org/10.1103/PhysRev.28.1049).
- [19] P. A. M. Dirac. “The quantum theory of the electron”. *Proc. Roy. Soc. Lond.* A117 (Feb. 1928), pp. 610–624. DOI: [10.1098/rspa.1928.0023](https://doi.org/10.1098/rspa.1928.0023).
- [20] W. E. Lamb and R. C. Retherford. “Fine Structure of the Hydrogen Atom by a Microwave Method”. *Phys. Rev.* 72 (3 Aug. 1947), pp. 241–243. DOI: [10.1103/PhysRev.72.241](https://doi.org/10.1103/PhysRev.72.241).
- [21] H. A. Bethe. “The Electromagnetic Shift of Energy Levels”. *Phys. Rev.* 72 (4 Aug. 1947), pp. 339–341. DOI: [10.1103/PhysRev.72.339](https://doi.org/10.1103/PhysRev.72.339).
- [22] J. Schwinger. “On Quantum-Electrodynamics and the Magnetic Moment of the Electron”. *Phys. Rev.* 73 (4 Feb. 1948), pp. 416–417. DOI: [10.1103/PhysRev.73.416](https://doi.org/10.1103/PhysRev.73.416).
- [23] P. Kusch and H. M. Foley. “The Magnetic Moment of the Electron”. *Phys. Rev.* 74.3 (1948), p. 250. DOI: [10.1103/PhysRev.74.250](https://doi.org/10.1103/PhysRev.74.250).
- [24] A. Vanhoefer. “Search for lepton-flavour violating decays of the Higgs boson at the LHC”. Universität Hamburg, Diss., 2017. PhD thesis. Universität Hamburg, 2017, p. 355. DOI: [10.3204/PUBDB-2017-02776](https://doi.org/10.3204/PUBDB-2017-02776).
- [25] ATLAS. “Observation of a new particle in the search for the Standard Model Higgs boson with the ATLAS detector at the LHC”. *Phys. Lett.* B716 (2012), pp. 1–29. DOI: [10.1016/j.physletb.2012.08.020](https://doi.org/10.1016/j.physletb.2012.08.020). arXiv: [1207.7214](https://arxiv.org/abs/1207.7214).
- [26] CMS. “Observation of a new boson at a mass of 125 GeV with the CMS experiment at the LHC”. *Phys. Lett.* B716 (2012), pp. 30–61. DOI: [10.1016/j.physletb.2012.08.021](https://doi.org/10.1016/j.physletb.2012.08.021). arXiv: [1207.7235](https://arxiv.org/abs/1207.7235).
- [27] F. Englert and R. Brout. “Broken Symmetry and the Mass of Gauge Vector Mesons”. *Phys. Rev. Lett.* 13 (9 Aug. 1964), pp. 321–323. DOI: [10.1103/PhysRevLett.13.321](https://doi.org/10.1103/PhysRevLett.13.321).
- [28] P. W. Higgs. “Broken Symmetries and the Masses of Gauge Bosons”. *Phys. Rev. Lett.* 13 (16 Oct. 1964), pp. 508–509. DOI: [10.1103/PhysRevLett.13.508](https://doi.org/10.1103/PhysRevLett.13.508).
- [29] G. S. Guralnik, C. R. Hagen, and T. W. B. Kibble. “Global Conservation Laws and Massless Particles”. *Phys. Rev. Lett.* 13 (20 Nov. 1964), pp. 585–587. DOI: [10.1103/PhysRevLett.13.585](https://doi.org/10.1103/PhysRevLett.13.585).
- [30] I. Zurbano Fernandez et al. “High-Luminosity Large Hadron Collider (HL-LHC): Technical design report”. 10/2020 (Dec. 2020). Ed. by I. Béjar Alonso et al. DOI: [10.23731/CYRM-2020-0010](https://doi.org/10.23731/CYRM-2020-0010).
- [31] “The International Linear Collider Technical Design Report - Volume 1: Executive Summary” (June 2013). Ed. by T. Behnke et al. arXiv: [1306.6327](https://arxiv.org/abs/1306.6327).
- [32] “The International Linear Collider Technical Design Report - Volume 2: Physics” (June 2013). Ed. by H. Baer et al. arXiv: [1306.6352](https://arxiv.org/abs/1306.6352).
- [33] J. de Blas et al. “The CLIC Potential for New Physics”. 3/2018 (Dec. 2018). DOI: [10.23731/CYRM-2018-003](https://doi.org/10.23731/CYRM-2018-003). arXiv: [1812.02093](https://arxiv.org/abs/1812.02093).
- [34] A. Abada et al. “FCC Physics Opportunities: Future Circular Collider Conceptual Design Report Volume 1”. *Eur. Phys. J. C* 79.6 (2019), p. 474. DOI: [10.1140/epjc/s10052-019-6904-3](https://doi.org/10.1140/epjc/s10052-019-6904-3).
- [35] A. Abada et al. “FCC-ee: The Lepton Collider: Future Circular Collider Conceptual Design Report Volume 2”. *Eur. Phys. J. ST* 228.2 (2019), pp. 261–623. DOI: [10.1140/epjst/e2019-900045-4](https://doi.org/10.1140/epjst/e2019-900045-4).
- [36] “CEPC Conceptual Design Report: Volume 1 - Accelerator” (Sept. 2018). arXiv: [1809.00285](https://arxiv.org/abs/1809.00285).

- [37] S. Amoroso et al. “Challenges in Monte Carlo Event Generator Software for High-Luminosity LHC”. *Comput. Softw. Big Sci.* 5.1 (2021). Ed. by A. Valassi, E. Yazgan, and J. McFayden, p. 12. DOI: [10.1007/s41781-021-00055-1](https://doi.org/10.1007/s41781-021-00055-1). arXiv: [2004.13687](https://arxiv.org/abs/2004.13687).
- [38] P. Stienemeier. “Precise predictions for same-sign Vector Boson Scattering at the LHC” (2018). Master’s thesis, p. 100. DOI: [10.3204/PUBDB-2018-03516](https://doi.org/10.3204/PUBDB-2018-03516).
- [39] J. Ellis. “TikZ-Feynman: Feynman diagrams with TikZ”. *Comput. Phys. Commun.* 210 (2017), pp. 103–123. DOI: [10.1016/j.cpc.2016.08.019](https://doi.org/10.1016/j.cpc.2016.08.019). arXiv: [1601.05437](https://arxiv.org/abs/1601.05437).
- [40] G. ’t Hooft and M. J. G. Veltman. “Regularization and Renormalization of Gauge Fields”. *Nucl. Phys.* B44 (1972), pp. 189–213. DOI: [10.1016/0550-3213\(72\)90279-9](https://doi.org/10.1016/0550-3213(72)90279-9).
- [41] F. Bloch and A. Nordsieck. “Note on the Radiation Field of the electron”. *Phys. Rev.* 52 (1937), pp. 54–59. DOI: [10.1103/PhysRev.52.54](https://doi.org/10.1103/PhysRev.52.54).
- [42] T. Kinoshita. “Mass singularities of Feynman amplitudes”. *J. Math. Phys.* 3 (1962), pp. 650–677. DOI: [10.1063/1.1724268](https://doi.org/10.1063/1.1724268).
- [43] T. D. Lee and M. Nauenberg. “Degenerate Systems and Mass Singularities”. *Phys. Rev.* 133 (1964). [25(1964)], B1549–B1562. DOI: [10.1103/PhysRev.133.B1549](https://doi.org/10.1103/PhysRev.133.B1549).
- [44] S. Höche. “Introduction to parton-shower event generators”. *Proceedings, Theoretical Advanced Study Institute in Elementary Particle Physics: Journeys Through the Precision Frontier: Amplitudes for Colliders (TASI 2014): Boulder, Colorado, June 2-27, 2014*. 2015, pp. 235–295. DOI: [10.1142/9789814678766\\_0005](https://doi.org/10.1142/9789814678766_0005). arXiv: [1411.4085](https://arxiv.org/abs/1411.4085).
- [45] J. Alwall et al. “The automated computation of tree-level and next-to-leading order differential cross sections, and their matching to parton shower simulations”. *JHEP* 07 (2014), p. 079. DOI: [10.1007/JHEP07\(2014\)079](https://doi.org/10.1007/JHEP07(2014)079). arXiv: [1405.0301](https://arxiv.org/abs/1405.0301).
- [46] P. Nason. “A New method for combining NLO QCD with shower Monte Carlo algorithms”. *JHEP* 11 (2004), p. 040. DOI: [10.1088/1126-6708/2004/11/040](https://doi.org/10.1088/1126-6708/2004/11/040). arXiv: [hep-ph/0409146](https://arxiv.org/abs/hep-ph/0409146).
- [47] S. Frixione, P. Nason, and C. Oleari. “Matching NLO QCD computations with Parton Shower simulations: the POWHEG method”. *JHEP* 11 (2007), p. 070. DOI: [10.1088/1126-6708/2007/11/070](https://doi.org/10.1088/1126-6708/2007/11/070). arXiv: [0709.2092](https://arxiv.org/abs/0709.2092).
- [48] S. Alioli, P. Nason, C. Oleari, and E. Re. “A general framework for implementing NLO calculations in shower Monte Carlo programs: the POWHEG BOX”. *JHEP* 06 (2010), p. 043. DOI: [10.1007/JHEP06\(2010\)043](https://doi.org/10.1007/JHEP06(2010)043). arXiv: [1002.2581](https://arxiv.org/abs/1002.2581).
- [49] T. Gleisberg et al. “Event generation with SHERPA 1.1”. *JHEP* 02 (2009), p. 007. DOI: [10.1088/1126-6708/2009/02/007](https://doi.org/10.1088/1126-6708/2009/02/007). arXiv: [0811.4622](https://arxiv.org/abs/0811.4622).
- [50] E. Bothmann et al. “Event Generation with Sherpa 2.2”. *SciPost Phys.* 7.3 (2019), p. 034. DOI: [10.21468/SciPostPhys.7.3.034](https://doi.org/10.21468/SciPostPhys.7.3.034). arXiv: [1905.09127](https://arxiv.org/abs/1905.09127).
- [51] W. Kilian, T. Ohl, and J. Reuter. “WHIZARD - simulating multi-particle processes at LHC and ILC”. *The European Physical Journal C* 71.9 (Sept. 2011), p. 1742. ISSN: 1434-6044. DOI: [10.1140/epjc/s10052-011-1742-y](https://doi.org/10.1140/epjc/s10052-011-1742-y). arXiv: [0708.4233](https://arxiv.org/abs/0708.4233).
- [52] T. Sjöstrand et al. “An Introduction to PYTHIA 8.2”. *Comput. Phys. Commun.* 191 (2015), pp. 159–177. DOI: [10.1016/j.cpc.2015.01.024](https://doi.org/10.1016/j.cpc.2015.01.024). arXiv: [1410.3012](https://arxiv.org/abs/1410.3012).
- [53] J. Bellm et al. “Herwig 7.2 release note”. *Eur. Phys. J. C* 80.5 (2020), p. 452. DOI: [10.1140/epjc/s10052-020-8011-x](https://doi.org/10.1140/epjc/s10052-020-8011-x). arXiv: [1912.06509](https://arxiv.org/abs/1912.06509).

- [54] E. Boos et al. “Generic user process interface for event generators”. *Physics at TeV colliders. Proceedings, Euro Summer School, Les Houches, France, May 21-June 1, 2001*. 2001. arXiv: [hep-ph/0109068](#).
- [55] J. Alwall et al. “A Standard format for Les Houches event files”. *Comput. Phys. Commun.* 176 (2007), pp. 300–304. DOI: [10.1016/j.cpc.2006.11.010](#). arXiv: [hep-ph/0609017](#).
- [56] P. Nason and G. Ridolfi. “A Positive-weight next-to-leading-order Monte Carlo for Z pair hadroproduction”. *JHEP* 08 (2006), p. 077. DOI: [10.1088/1126-6708/2006/08/077](#). arXiv: [hep-ph/0606275](#).
- [57] S. Catani and M. Seymour. “A general algorithm for calculating jet cross sections in NLO QCD”. *Nuclear Physics B* 485.1-2 (Feb. 1997), pp. 291–419. ISSN: 05503213. DOI: [10.1016/S0550-3213\(96\)00589-5](#). arXiv: [9605323](#).
- [58] S. Catani, S. Dittmaier, M. H. Seymour, and Z. Trocsanyi. “The Dipole formalism for next-to-leading order QCD calculations with massive partons”. *Nucl. Phys. B* 627 (2002), pp. 189–265. DOI: [10.1016/S0550-3213\(02\)00098-6](#). arXiv: [hep-ph/0201036](#).
- [59] D. A. Kosower. “Antenna factorization of gauge theory amplitudes”. *Phys. Rev. D* 57 (1998), pp. 5410–5416. DOI: [10.1103/PhysRevD.57.5410](#). arXiv: [hep-ph/9710213](#).
- [60] J. M. Campbell, M. A. Cullen, and E. W. N. Glover. “Four jet event shapes in electron - positron annihilation”. *Eur. Phys. J. C* 9 (1999), pp. 245–265. DOI: [10.1007/s100529900034](#). arXiv: [hep-ph/9809429](#).
- [61] D. A. Kosower. “Antenna factorization in strongly ordered limits”. *Phys. Rev. D* 71 (2005), p. 045016. DOI: [10.1103/PhysRevD.71.045016](#). arXiv: [hep-ph/0311272](#).
- [62] S. Frixione, Z. Kunszt, and A. Signer. “Three jet cross-sections to next-to-leading order”. *Nucl. Phys. B* 467 (1996), pp. 399–442. DOI: [10.1016/0550-3213\(96\)00110-1](#). arXiv: [hep-ph/9512328](#).
- [63] S. Frixione. “A General approach to jet cross-sections in QCD”. *Nucl. Phys. B* 507 (1997), pp. 295–314. DOI: [10.1016/S0550-3213\(97\)00574-9](#). arXiv: [hep-ph/9706545](#).
- [64] R. Frederix, S. Frixione, F. Maltoni, and T. Stelzer. “Automation of next-to-leading order computations in QCD: the FKS subtraction”. *Journal of High Energy Physics* 2009.10 (Oct. 2009), pp. 003–003. ISSN: 1029-8479. DOI: [10.1088/1126-6708/2009/10/003](#). arXiv: [0908.4272](#).
- [65] T. Robens. “Nagy-Soper Subtraction: A Review”. *Mod. Phys. Lett. A* 28 (2013), p. 1330020. DOI: [10.1142/S0217732313300206](#). arXiv: [1306.1946](#).
- [66] G. Bevilacqua, M. Czakon, M. Kubocz, and M. Worek. “Complete Nagy-Soper subtraction for next-to-leading order calculations in QCD”. *JHEP* 10 (2013), p. 204. DOI: [10.1007/JHEP10\(2013\)204](#). arXiv: [1308.5605](#).
- [67] Z. Nagy and D. E. Soper. “Parton showers with quantum interference”. *JHEP* 09 (2007), p. 114. DOI: [10.1088/1126-6708/2007/09/114](#). arXiv: [0706.0017](#).
- [68] Z. Nagy and D. E. Soper. “Parton showers with quantum interference: Leading color, with spin”. *JHEP* 07 (2008), p. 025. DOI: [10.1088/1126-6708/2008/07/025](#). arXiv: [0805.0216](#).
- [69] Z. Nagy and D. E. Soper. “Parton showers with quantum interference: Leading color, spin averaged”. *JHEP* 03 (2008), p. 030. DOI: [10.1088/1126-6708/2008/03/030](#). arXiv: [0801.1917](#).
- [70] T. Gleisberg and F. Krauss. “Automating dipole subtraction for QCD NLO calculations”. *Eur. Phys. J. C* 53 (2008), pp. 501–523. DOI: [10.1140/epjc/s10052-007-0495-0](#). arXiv: [0709.2881](#).
- [71] B. Chokouf e Nejad. “Scrutinizing the Top Quark at Lepton Colliders with Higher Orders”. PhD thesis. Hamburg: DESY, 2017. DOI: [10.3204/PUBDB-2017-07624](#).

- [72] C. Weiss. “Top quark physics as a prime application of automated higher-order corrections.” PhD thesis. Hamburg: DESY, 2017. DOI: [10.3204/PUBDB-2017-07541](https://doi.org/10.3204/PUBDB-2017-07541).
- [73] V. Rothe. “Automation of NLO QCD Corrections and the Application to  $N$ -Jet Processes at Lepton Colliders”. Dissertation. Universität Hamburg, 2021, p. 229. DOI: [10.3204/PUBDB-2021-03538](https://doi.org/10.3204/PUBDB-2021-03538).
- [74] Particle Data Group. “Review of Particle Physics”. *Progress of Theoretical and Experimental Physics* 2020.8 (Aug. 2020). 083C01, pp. 661–664. ISSN: 2050-3911. DOI: [10.1093/ptep/ptaa104](https://doi.org/10.1093/ptep/ptaa104). eprint: <https://academic.oup.com/ptep/article-pdf/2020/8/083C01/34673722/ptaa104.pdf>.
- [75] S. Frixione, E. Laenen, P. Motylinski, and B. R. Webber. “Single-top production in MC@NLO”. *JHEP* 03 (2006), p. 092. DOI: [10.1088/1126-6708/2006/03/092](https://doi.org/10.1088/1126-6708/2006/03/092). arXiv: [hep-ph/0512250](https://arxiv.org/abs/hep-ph/0512250).
- [76] P. M. Bredt. “Automated NLO EW Corrections to Processes at Hadron and Lepton Colliders”. Dissertation. Universität Hamburg, 2022.
- [77] L. Barze, G. Montagna, P. Nason, O. Nicrosini, and F. Piccinini. “Implementation of electroweak corrections in the POWHEG BOX: single  $W$  production”. *JHEP* 04 (2012), p. 037. DOI: [10.1007/JHEP04\(2012\)037](https://doi.org/10.1007/JHEP04(2012)037). arXiv: [1202.0465](https://arxiv.org/abs/1202.0465).
- [78] R. Dalitz. “CXII. On the analysis of  $\tau$ -meson data and the nature of the  $\tau$ -meson”. *The London, Edinburgh, and Dublin Philosophical Magazine and Journal of Science* 44.357 (1953), pp. 1068–1080. DOI: [10.1080/14786441008520365](https://doi.org/10.1080/14786441008520365).
- [79] R. H. Dalitz. “Decay of  $\tau$  Mesons of Known Charge”. *Phys. Rev.* 94 (4 May 1954), pp. 1046–1051. DOI: [10.1103/PhysRev.94.1046](https://doi.org/10.1103/PhysRev.94.1046).
- [80] M. Cacciari, G. P. Salam, and G. Soyez. “FastJet User Manual”. *Eur. Phys. J. C* 72 (2012), p. 1896. DOI: [10.1140/epjc/s10052-012-1896-2](https://doi.org/10.1140/epjc/s10052-012-1896-2). arXiv: [1111.6097](https://arxiv.org/abs/1111.6097).
- [81] G. Altarelli and G. Parisi. “Asymptotic Freedom in Parton Language”. *Nucl. Phys. B* 126 (1977), pp. 298–318. DOI: [10.1016/0550-3213\(77\)90384-4](https://doi.org/10.1016/0550-3213(77)90384-4).
- [82] S. Catani and M. Grazzini. “The soft gluon current at one loop order”. *Nucl. Phys. B* 591 (2000), pp. 435–454. DOI: [10.1016/S0550-3213\(00\)00572-1](https://doi.org/10.1016/S0550-3213(00)00572-1). arXiv: [hep-ph/0007142](https://arxiv.org/abs/hep-ph/0007142).
- [83] Y. L. Dokshitzer, V. A. Khoze, A. H. Mueller, and S. I. Troian. *Basics of perturbative QCD*. 1991.
- [84] A. Bassetto, M. Ciafaloni, and G. Marchesini. “Jet Structure and Infrared Sensitive Quantities in Perturbative QCD”. *Phys. Rept.* 100 (1983), pp. 201–272. DOI: [10.1016/0370-1573\(83\)90083-2](https://doi.org/10.1016/0370-1573(83)90083-2).
- [85] S. Alioli, P. Nason, C. Oleari, and E. Re. “NLO Higgs boson production via gluon fusion matched with shower in POWHEG”. *JHEP* 04 (2009), p. 002. DOI: [10.1088/1126-6708/2009/04/002](https://doi.org/10.1088/1126-6708/2009/04/002). arXiv: [0812.0578](https://arxiv.org/abs/0812.0578).
- [86] S. Alioli, P. Nason, C. Oleari, and E. Re. “NLO vector-boson production matched with shower in POWHEG”. *JHEP* 07 (2008), p. 060. DOI: [10.1088/1126-6708/2008/07/060](https://doi.org/10.1088/1126-6708/2008/07/060). arXiv: [0805.4802](https://arxiv.org/abs/0805.4802).
- [87] G. Altarelli, R. K. Ellis, and G. Martinelli. “Leptoproduction and Drell-Yan Processes Beyond the Leading Approximation in Chromodynamics”. *Nucl. Phys. B* 143 (1978). [Erratum: *Nucl.Phys.B* 146, 544 (1978)], p. 521. DOI: [10.1016/0550-3213\(78\)90067-6](https://doi.org/10.1016/0550-3213(78)90067-6).
- [88] T. Ježo and P. Nason. “On the Treatment of Resonances in Next-to-Leading Order Calculations Matched to a Parton Shower”. *JHEP* 12 (2015), p. 065. DOI: [10.1007/JHEP12\(2015\)065](https://doi.org/10.1007/JHEP12(2015)065). arXiv: [1509.09071](https://arxiv.org/abs/1509.09071).
- [89] Y. L. Dokshitzer. “Calculation of the Structure Functions for Deep Inelastic Scattering and  $e^+e^-$  Annihilation by Perturbation Theory in Quantum Chromodynamics.” *Sov. Phys. JETP* 46 (1977), pp. 641–653.

- [90] V. N. Gribov and L. N. Lipatov. “Deep inelastic e p scattering in perturbation theory”. *Sov. J. Nucl. Phys.* 15 (1972), pp. 438–450.
- [91] *WHIZARD manual*. URL: <http://whizard.hepforge.org/manual.pdf> (visited on Nov. 3, 2022).
- [92] R. Brun and F. Rademakers. “ROOT: An object oriented data analysis framework”. *Nucl. Instrum. Meth. A* 389 (1997). Ed. by M. Werlen and D. Perret-Gallix, pp. 81–86. DOI: [10.1016/S0168-9002\(97\)00048-X](https://doi.org/10.1016/S0168-9002(97)00048-X).
- [93] A. Buckley et al. “Rivet user manual”. *Comput. Phys. Commun.* 184 (2013), pp. 2803–2819. DOI: [10.1016/j.cpc.2013.05.021](https://doi.org/10.1016/j.cpc.2013.05.021). arXiv: [1003.0694](https://arxiv.org/abs/1003.0694).
- [94] C. Bierlich et al. “Robust Independent Validation of Experiment and Theory: Rivet version 3” (2019). arXiv: [1912.05451](https://arxiv.org/abs/1912.05451).
- [95] C. Bierlich, A. Buckley, C. Gutschow, et al. *Rivet Contrib: Repository with external tools and contributions from and for users of Rivet*. URL: <https://gitlab.com/hepcedar/rivetcontrib> (visited on Nov. 4, 2022).
- [96] R. K. Ellis, W. J. Stirling, and B. R. Webber. “QCD and collider physics”. *Camb. Monogr. Part. Phys. Nucl. Phys. Cosmol.* 8 (1996), pp. 1–435.
- [97] G. C. Fox and S. Wolfram. “A Model for Parton Showers in QCD”. *Nucl. Phys. B* 168 (1980), pp. 285–295. DOI: [10.1016/0550-3213\(80\)90111-X](https://doi.org/10.1016/0550-3213(80)90111-X).
- [98] L. Lönnblad. “Fooling Around with the Sudakov Veto Algorithm”. *Eur. Phys. J. C* 73.3 (2013), p. 2350. DOI: [10.1140/epjc/s10052-013-2350-9](https://doi.org/10.1140/epjc/s10052-013-2350-9). arXiv: [1211.7204](https://arxiv.org/abs/1211.7204).
- [99] M. Akrawy et al. “A study of coherence of soft gluons in hadron jets”. *Physics Letters B* 247.4 (1990), pp. 617–628. ISSN: 0370-2693. DOI: [https://doi.org/10.1016/0370-2693\(90\)91911-T](https://doi.org/10.1016/0370-2693(90)91911-T).
- [100] F. Herren, S. Höche, F. Krauss, D. Reichelt, and M. Schoenherr. “A new approach to color-coherent parton evolution” (Aug. 2022). arXiv: [2208.06057](https://arxiv.org/abs/2208.06057).
- [101] T. Sjöstrand, S. Mrenna, and P. Skands. “PYTHIA 6.4 physics and manual”. *Journal of High Energy Physics* 2006.05 (2006), p. 026.
- [102] M. Bengtsson and T. Sjöstrand. “Coherent parton showers versus matrix elements - implications of PETRA/PEP data”. *Physics Letters B* 185.3 (1987), pp. 435–440. ISSN: 0370-2693. DOI: [https://doi.org/10.1016/0370-2693\(87\)91031-8](https://doi.org/10.1016/0370-2693(87)91031-8).
- [103] T. Sjöstrand and M. Bengtsson. “The Lund Monte Carlo for Jet Fragmentation and e+ e- Physics. Jetset Version 6.3: An Update”. *Comput. Phys. Commun.* 43 (1987), p. 367. DOI: [10.1016/0010-4655\(87\)90054-3](https://doi.org/10.1016/0010-4655(87)90054-3).
- [104] W. T. Giele, D. A. Kosower, and P. Z. Skands. “Higher-Order Corrections to Timelike Jets”. *Phys. Rev. D* 84 (2011), p. 054003. DOI: [10.1103/PhysRevD.84.054003](https://doi.org/10.1103/PhysRevD.84.054003). arXiv: [1102.2126](https://arxiv.org/abs/1102.2126).
- [105] M. L. Mangano, M. Moretti, and R. Pittau. “Multijet matrix elements and shower evolution in hadronic collisions:  $Wb\bar{b} + n$  jets as a case study”. *Nucl. Phys. B* 632 (2002), pp. 343–362. DOI: [10.1016/S0550-3213\(02\)00249-3](https://doi.org/10.1016/S0550-3213(02)00249-3). arXiv: [hep-ph/0108069](https://arxiv.org/abs/hep-ph/0108069).
- [106] M. L. Mangano, M. Moretti, F. Piccinini, and M. Treccani. “Matching matrix elements and shower evolution for top-quark production in hadronic collisions”. *JHEP* 01 (2007), p. 013. DOI: [10.1088/1126-6708/2007/01/013](https://doi.org/10.1088/1126-6708/2007/01/013). arXiv: [hep-ph/0611129](https://arxiv.org/abs/hep-ph/0611129).
- [107] S. Catani, F. Krauss, R. Kuhn, and B. R. Webber. “QCD matrix elements + parton showers”. *JHEP* 11 (2001), p. 063. DOI: [10.1088/1126-6708/2001/11/063](https://doi.org/10.1088/1126-6708/2001/11/063). arXiv: [hep-ph/0109231](https://arxiv.org/abs/hep-ph/0109231).

- [108] S. Frixione and B. R. Webber. “Matching NLO QCD computations and parton shower simulations”. *JHEP* 06 (2002), p. 029. DOI: [10.1088/1126-6708/2002/06/029](https://doi.org/10.1088/1126-6708/2002/06/029). arXiv: [hep-ph/0204244](https://arxiv.org/abs/hep-ph/0204244).
- [109] S. Jadach, W. Płaczek, S. Sapeta, A. Siódmok, and M. Skrzypek. “Matching NLO QCD with parton shower in Monte Carlo scheme — the KrkNLO method”. *JHEP* 10 (2015), p. 052. DOI: [10.1007/JHEP10\(2015\)052](https://doi.org/10.1007/JHEP10(2015)052). arXiv: [1503.06849](https://arxiv.org/abs/1503.06849).
- [110] R. Frederix and S. Frixione. “Merging meets matching in MC@NLO”. *JHEP* 12 (2012), p. 061. DOI: [10.1007/JHEP12\(2012\)061](https://doi.org/10.1007/JHEP12(2012)061). arXiv: [1209.6215](https://arxiv.org/abs/1209.6215).
- [111] L. Lönnblad and S. Prestel. “Merging Multi-leg NLO Matrix Elements with Parton Showers”. *JHEP* 03 (2013), p. 166. DOI: [10.1007/JHEP03\(2013\)166](https://doi.org/10.1007/JHEP03(2013)166). arXiv: [1211.7278](https://arxiv.org/abs/1211.7278).
- [112] K. Hamilton, P. Nason, C. Oleari, and G. Zanderighi. “Merging H/W/Z + 0 and 1 jet at NLO with no merging scale: a path to parton shower + NNLO matching”. *JHEP* 05 (2013), p. 082. DOI: [10.1007/JHEP05\(2013\)082](https://doi.org/10.1007/JHEP05(2013)082). arXiv: [1212.4504](https://arxiv.org/abs/1212.4504).
- [113] M. Dobbs and J. B. Hansen. “The HepMC C++ Monte Carlo event record for High Energy Physics”. *Comput. Phys. Commun.* 134 (2001), pp. 41–46. DOI: [10.1016/S0010-4655\(00\)00189-2](https://doi.org/10.1016/S0010-4655(00)00189-2).
- [114] A. Buckley et al. “The HepMC3 event record library for Monte Carlo event generators”. *Computer Physics Communications* 260 (2021), p. 107310. ISSN: 0010-4655. DOI: <https://doi.org/10.1016/j.cpc.2020.107310>.
- [115] *The POWHEG BOX*. URL: <https://powhegbox.mib.infn.it/> (visited on Nov. 4, 2022).
- [116] S. Höche, F. Krauss, M. Schönherr, and F. Siegert. “Automating the POWHEG method in Sherpa”. *JHEP* 04 (2011), p. 024. DOI: [10.1007/JHEP04\(2011\)024](https://doi.org/10.1007/JHEP04(2011)024). arXiv: [1008.5399](https://arxiv.org/abs/1008.5399).
- [117] S. Plätzer and S. Gieseke. “Dipole Showers and Automated NLO Matching in Herwig++”. *Eur. Phys. J. C* 72 (2012), p. 2187. DOI: [10.1140/epjc/s10052-012-2187-7](https://doi.org/10.1140/epjc/s10052-012-2187-7). arXiv: [1109.6256](https://arxiv.org/abs/1109.6256).
- [118] B. Chokoufí Nejad, W. Kilian, J. Reuter, and C. Weiss. “Matching NLO QCD Corrections in WHIZARD with the POWHEG scheme”. *PoS EPS-HEP2015* (2015), p. 317. arXiv: [1510.02739](https://arxiv.org/abs/1510.02739).
- [119] A. Mück. “Parton-shower matching for electroweak corrections”. *Nuclear and Particle Physics Proceedings* 261-262 (2015). Advances in Computational Particle Physics, pp. 308–310. ISSN: 2405-6014. DOI: <https://doi.org/10.1016/j.nuclphysbps.2015.03.020>.
- [120] S. Plätzer and M. Sjö Dahl. “The Sudakov Veto Algorithm Reloaded”. *Eur. Phys. J. Plus* 127 (2012), p. 26. DOI: [10.1140/epjp/i2012-12026-x](https://doi.org/10.1140/epjp/i2012-12026-x). arXiv: [1108.6180](https://arxiv.org/abs/1108.6180).
- [121] R. Kleiss and R. Verheyen. “Competing Sudakov Veto Algorithms”. *Eur. Phys. J. C* 76.7 (2016), p. 359. DOI: [10.1140/epjc/s10052-016-4231-5](https://doi.org/10.1140/epjc/s10052-016-4231-5). arXiv: [1605.09246](https://arxiv.org/abs/1605.09246).
- [122] A. Lipowski and D. Lipowska. “Roulette-wheel selection via stochastic acceptance”. *Physica A Statistical Mechanics and its Applications* 391.6 (Mar. 2012), pp. 2193–2196. DOI: [10.1016/j.physa.2011.12.004](https://doi.org/10.1016/j.physa.2011.12.004). arXiv: [1109.3627](https://arxiv.org/abs/1109.3627).
- [123] F. Febres Cordero, M. Kraus, and L. Reina. “Top-quark pair production in association with a  $W^\pm$  gauge boson in the POWHEG-BOX”. *Phys. Rev. D* 103.9 (2021), p. 094014. DOI: [10.1103/PhysRevD.103.094014](https://doi.org/10.1103/PhysRevD.103.094014). arXiv: [2101.11808](https://arxiv.org/abs/2101.11808).
- [124] R. Bonciani, S. Catani, M. L. Mangano, and P. Nason. “Sudakov resummation of multiparton QCD cross-sections”. *Phys. Lett. B* 575 (2003), pp. 268–278. DOI: [10.1016/j.physletb.2003.09.068](https://doi.org/10.1016/j.physletb.2003.09.068). arXiv: [hep-ph/0307035](https://arxiv.org/abs/hep-ph/0307035).

- [125] R. Frederix, S. Frixione, S. Prestel, and P. Torrielli. “On the reduction of negative weights in MC@NLO-type matching procedures”. *JHEP* 07 (2020), p. 238. DOI: [10.1007/JHEP07\(2020\)238](https://doi.org/10.1007/JHEP07(2020)238). arXiv: [2002.12716](https://arxiv.org/abs/2002.12716).
- [126] K. Danziger, S. Höche, and F. Siegert. “Reducing negative weights in Monte Carlo event generation with Sherpa” (Oct. 2021). arXiv: [2110.15211](https://arxiv.org/abs/2110.15211).
- [127] J. Olsson, S. Plätzer, and M. Sjö Dahl. “Resampling Algorithms for High Energy Physics Simulations”. *Eur. Phys. J. C* 80.10 (2020), p. 934. DOI: [10.1140/epjc/s10052-020-08500-y](https://doi.org/10.1140/epjc/s10052-020-08500-y). arXiv: [1912.02436](https://arxiv.org/abs/1912.02436).
- [128] C. Gao, J. Isaacson, and C. Krause. “i-flow: High-dimensional Integration and Sampling with Normalizing Flows”. *Mach. Learn. Sci. Tech.* 1.4 (2020), p. 045023. DOI: [10.1088/2632-2153/abab62](https://doi.org/10.1088/2632-2153/abab62). arXiv: [2001.05486](https://arxiv.org/abs/2001.05486).
- [129] E. Bothmann, T. Janßen, M. Knobbe, T. Schmale, and S. Schumann. “Exploring phase space with Neural Importance Sampling”. *SciPost Phys.* 8.4 (2020), p. 069. DOI: [10.21468/SciPostPhys.8.4.069](https://doi.org/10.21468/SciPostPhys.8.4.069). arXiv: [2001.05478](https://arxiv.org/abs/2001.05478).
- [130] C. Gao, S. Höche, J. Isaacson, C. Krause, and H. Schulz. “Event Generation with Normalizing Flows”. *Phys. Rev. D* 101.7 (2020). DOI: [10.1103/PhysRevD.101.076002](https://doi.org/10.1103/PhysRevD.101.076002). arXiv: [2001.10028](https://arxiv.org/abs/2001.10028).
- [131] J. R. Andersen, C. Gütschow, A. Maier, and S. Prestel. “A Positive Resampler for Monte Carlo events with negative weights”. *Eur. Phys. J. C* 80.11 (2020), p. 1007. DOI: [10.1140/epjc/s10052-020-08548-w](https://doi.org/10.1140/epjc/s10052-020-08548-w). arXiv: [2005.09375](https://arxiv.org/abs/2005.09375).
- [132] B. Nachman and J. Thaler. “Neural resampler for Monte Carlo reweighting with preserved uncertainties”. *Phys. Rev. D* 102.7 (2020). DOI: [10.1103/PhysRevD.102.076004](https://doi.org/10.1103/PhysRevD.102.076004). arXiv: [2007.11586](https://arxiv.org/abs/2007.11586).
- [133] B. Stienen and R. Verheyen. “Phase space sampling and inference from weighted events with autoregressive flows”. *SciPost Phys.* 10.2 (2021), p. 038. DOI: [10.21468/SciPostPhys.10.2.038](https://doi.org/10.21468/SciPostPhys.10.2.038). arXiv: [2011.13445](https://arxiv.org/abs/2011.13445).
- [134] J. R. Andersen and A. Maier. “Unbiased elimination of negative weights in Monte Carlo samples”. *Eur. Phys. J. C* 82.5 (2022), p. 433. DOI: [10.1140/epjc/s10052-022-10372-3](https://doi.org/10.1140/epjc/s10052-022-10372-3). arXiv: [2109.07851](https://arxiv.org/abs/2109.07851).
- [135] J. A. Aguilar-Saavedra et al. “TESLA: The Superconducting electron positron linear collider with an integrated x-ray laser laboratory. Technical design report. Part 3. Physics at an e+ e- linear collider” (2001). arXiv: [hep-ph/0106315](https://arxiv.org/abs/hep-ph/0106315).
- [136] R. Chierici, S. Rosati, and M. Kobel. “Strong electroweak symmetry breaking signals in w w scattering at tesla”. *Physics and Experiments with Future Linear e+ e- Colliders: Proceedings, 5th International Linear Collider Workshop (LCWS 2000) Batavia, Illinois, October 24-28, 2000*. 2001, pp. 544–549.
- [137] T. Ohl. “O’mega: An Optimizing matrix element generator”. *AIP Conf. Proc.* 583 (2001). [,173(2000)], pp. 173–175. DOI: [10.1063/1.1405295](https://doi.org/10.1063/1.1405295). arXiv: [hep-ph/0011243](https://arxiv.org/abs/hep-ph/0011243).
- [138] M. Moretti, T. Ohl, and J. Reuter. “O’Mega: An Optimizing Matrix Element Generator. I: Basic Algorithms”. *IKDA-2001-06, LC-TOOL-2001-040* (Feb. 2001), p. 29. arXiv: [hep-ph/0102195](https://arxiv.org/abs/hep-ph/0102195).
- [139] W. Kilian, T. Ohl, J. Reuter, and C. Speckner. “QCD in the Color-Flow Representation”. *JHEP* 10 (2012), p. 022. DOI: [10.1007/JHEP10\(2012\)022](https://doi.org/10.1007/JHEP10(2012)022). arXiv: [1206.3700](https://arxiv.org/abs/1206.3700).
- [140] B. Chokoufè Nejad, T. Ohl, and J. Reuter. “Simple, parallel virtual machines for extreme computations”. *Comput. Phys. Commun.* 196 (2015), pp. 58–69. DOI: [10.1016/j.cpc.2015.05.015](https://doi.org/10.1016/j.cpc.2015.05.015). arXiv: [1411.3834](https://arxiv.org/abs/1411.3834).

- [141] G. P. Lepage. “A new algorithm for adaptive multidimensional integration”. *Journal of Computational Physics* 27.2 (1978), pp. 192–203. ISSN: 0021-9991. DOI: [https://doi.org/10.1016/0021-9991\(78\)90004-9](https://doi.org/10.1016/0021-9991(78)90004-9).
- [142] G. P. Lepage. “VEGAS: An Adaptive Multi-dimensional Integration Program” (Mar. 1980).
- [143] T. Ohl. “Vegas revisited: Adaptive Monte Carlo integration beyond factorization”. *Comput. Phys. Commun.* 120 (1999), pp. 13–19. DOI: [10.1016/S0010-4655\(99\)00209-X](https://doi.org/10.1016/S0010-4655(99)00209-X). arXiv: [hep-ph/9806432](https://arxiv.org/abs/hep-ph/9806432).
- [144] P. L’Ecuyer, R. Simard, E. Chen, and D. Kelton. “An Object-Oriented Random-Number Package With Many Long Streams And Substreams”. *Operations Research* 50 (Dec. 2002), pp. 1073–1075. DOI: [10.1287/opre.50.6.1073.358](https://doi.org/10.1287/opre.50.6.1073.358).
- [145] S. Brass, W. Kilian, and J. Reuter. “Parallel Adaptive Monte Carlo Integration with the Event Generator WHIZARD”. *Eur. Phys. J. C* 79.4 (2019), p. 344. DOI: [10.1140/epjc/s10052-019-6840-2](https://doi.org/10.1140/epjc/s10052-019-6840-2). arXiv: [1811.09711](https://arxiv.org/abs/1811.09711).
- [146] S. Braß. “Parallel adaptive Monte Carlo integration and vector-boson scattering at the Large Hadron Collider”. PhD thesis. Siegen U., 2019.
- [147] K. Fujii et al. “Physics Case for the International Linear Collider” (June 2015). arXiv: [1506.05992](https://arxiv.org/abs/1506.05992).
- [148] H. Abramowicz et al. “The International Linear Collider Technical Design Report - Volume 4: Detectors” (June 2013). Ed. by T. Behnke et al. arXiv: [1306.6329](https://arxiv.org/abs/1306.6329).
- [149] R. Franceschini et al. “The CLIC Potential for New Physics”. 3/2018 (Dec. 2018). Ed. by J. de Blas. DOI: [10.23731/CYRM-2018-003](https://doi.org/10.23731/CYRM-2018-003). arXiv: [1812.02093](https://arxiv.org/abs/1812.02093).
- [150] T. Ohl. “CIRCE version 1.02: Beam spectra for simulating linear collider physics”. *Comput. Phys. Commun.* 101 (1997), pp. 269–288. DOI: [10.1016/S0010-4655\(96\)00167-1](https://doi.org/10.1016/S0010-4655(96)00167-1). arXiv: [hep-ph/9607454](https://arxiv.org/abs/hep-ph/9607454).
- [151] T. Ohl. *CIRCE2: From Guinea-Pig to WHIZARD*. Second International WHIZARD Forum. URL: <https://indico.desy.de/event/10353/contributions/1414/attachments/1013/1143/circe2-handout.pdf> (visited on Nov. 5, 2022).
- [152] T. Ohl. *CIRCE2: Guinea-Pig for the Masses*. ECFA Higgs Factories: 1st Topical Meeting on Generators. URL: <https://indico.cern.ch/event/1078675/contributions/4571682/attachments/2341626/3992871/circe2-handout.pdf> (visited on Nov. 5, 2022).
- [153] D. Schulte. “Beam-beam simulations with GUINEA-PIG” (1999).
- [154] C. Rimbault et al. “GUINEA PIG++ : An Upgraded Version of the Linear Collider Beam Beam Interaction Simulation Code GUINEA PIG”. *Conf. Proc. C* 070625 (2007). Ed. by C. Petit-Jean-Genaz, p. 2728. DOI: [10.1109/PAC.2007.4440556](https://doi.org/10.1109/PAC.2007.4440556).
- [155] D. Schulte. “Study of Electromagnetic and Hadronic Background in the Interaction Region of the TESLA Collider”. PhD thesis. Hamburg U., 1997.
- [156] *WHIZARD HepForge webpage*. URL: <http://whizard.hepforge.org> (visited on Oct. 15, 2022).
- [157] A. Buckley et al. “LHAPDF6: parton density access in the LHC precision era”. *Eur. Phys. J. C* 75 (2015), p. 132. DOI: [10.1140/epjc/s10052-015-3318-8](https://doi.org/10.1140/epjc/s10052-015-3318-8). arXiv: [1412.7420](https://arxiv.org/abs/1412.7420).
- [158] A. Alloul, N. D. Christensen, C. Degrande, C. Duhr, and B. Fuks. “FeynRules 2.0 - A complete toolbox for tree-level phenomenology”. *Comput. Phys. Commun.* 185 (2014), pp. 2250–2300. DOI: [10.1016/j.cpc.2014.04.012](https://doi.org/10.1016/j.cpc.2014.04.012). arXiv: [1310.1921](https://arxiv.org/abs/1310.1921).
- [159] C. Degrande et al. “UFO - The Universal FeynRules Output”. *Comput. Phys. Commun.* 183 (2012), pp. 1201–1214. DOI: [10.1016/j.cpc.2012.01.022](https://doi.org/10.1016/j.cpc.2012.01.022). arXiv: [1108.2040](https://arxiv.org/abs/1108.2040).

- [160] S. Frixione. “Isolated photons in perturbative QCD”. *Phys. Lett.* B429 (1998), pp. 369–374. DOI: [10.1016/S0370-2693\(98\)00454-7](https://doi.org/10.1016/S0370-2693(98)00454-7). arXiv: [hep-ph/9801442](https://arxiv.org/abs/hep-ph/9801442).
- [161] W. Kilian, J. Reuter, and T. Robens. “NLO Event Generation for Chargino Production at the ILC”. *Eur. Phys. J. C* 48 (2006), pp. 389–400. DOI: [10.1140/epjc/s10052-006-0048-y](https://doi.org/10.1140/epjc/s10052-006-0048-y). arXiv: [hep-ph/0607127](https://arxiv.org/abs/hep-ph/0607127).
- [162] T. Robens, J. Kalinowski, K. Rolbiecki, W. Kilian, and J. Reuter. “(N)LO Simulation of Chargino Production and Decay”. *Acta Phys. Polon.* B39 (2008), pp. 1705–1714. arXiv: [0803.4161](https://arxiv.org/abs/0803.4161).
- [163] T. Binoth et al. “Next-to-leading order QCD corrections to  $pp \rightarrow b \text{ anti-}b b \text{ anti-}b + X$  at the LHC: the quark induced case”. *Phys. Lett.* B685 (2010), pp. 293–296. DOI: [10.1016/j.physletb.2010.02.010](https://doi.org/10.1016/j.physletb.2010.02.010). arXiv: [0910.4379](https://arxiv.org/abs/0910.4379).
- [164] N. Greiner, A. Guffanti, T. Reiter, and J. Reuter. “NLO QCD corrections to the production of two bottom-antibottom pairs at the LHC”. *Phys. Rev. Lett.* 107 (2011), p. 102002. DOI: [10.1103/PhysRevLett.107.102002](https://doi.org/10.1103/PhysRevLett.107.102002). arXiv: [1105.3624](https://arxiv.org/abs/1105.3624).
- [165] F. Cascioli, P. Maierhofer, and S. Pozzorini. “Scattering Amplitudes with Open Loops”. *Phys. Rev. Lett.* 108 (2012), p. 111601. DOI: [10.1103/PhysRevLett.108.111601](https://doi.org/10.1103/PhysRevLett.108.111601). arXiv: [1111.5206](https://arxiv.org/abs/1111.5206).
- [166] F. Buccioni et al. “OpenLoops 2”. *Eur. Phys. J. C* 79.10 (2019), p. 866. DOI: [10.1140/epjc/s10052-019-7306-2](https://doi.org/10.1140/epjc/s10052-019-7306-2). arXiv: [1907.13071](https://arxiv.org/abs/1907.13071).
- [167] S. Actis, A. Denner, L. Hofer, A. Scharf, and S. Uccirati. “Recursive generation of one-loop amplitudes in the Standard Model”. *JHEP* 04 (2013), p. 037. DOI: [10.1007/JHEP04\(2013\)037](https://doi.org/10.1007/JHEP04(2013)037). arXiv: [1211.6316](https://arxiv.org/abs/1211.6316).
- [168] S. Actis et al. “RECOLA: REcursive Computation of One-Loop Amplitudes”. *Comput. Phys. Commun.* 214 (2017), pp. 140–173. DOI: [10.1016/j.cpc.2017.01.004](https://doi.org/10.1016/j.cpc.2017.01.004). arXiv: [1605.01090](https://arxiv.org/abs/1605.01090).
- [169] *WHIZARD GitLab webpage*. URL: <https://gitlab.tp.nt.uni-siegen.de/whizard/public> (visited on Oct. 15, 2022).
- [170] N. Ramsey. “Literate programming simplified”. *IEEE Software* 11.5 (1994), pp. 97–105. DOI: [10.1109/52.311070](https://doi.org/10.1109/52.311070).
- [171] J. Bellm et al. “Herwig 7.0/Herwig++ 3.0 release note”. *Eur. Phys. J. C* 76.4 (2016), p. 196. DOI: [10.1140/epjc/s10052-016-4018-8](https://doi.org/10.1140/epjc/s10052-016-4018-8). arXiv: [1512.01178](https://arxiv.org/abs/1512.01178).
- [172] W. Kilian, J. Reuter, S. Schmidt, and D. Wiesler. “An Analytic Initial-State Parton Shower”. *JHEP* 04 (2012), p. 013. DOI: [10.1007/JHEP04\(2012\)013](https://doi.org/10.1007/JHEP04(2012)013). arXiv: [1112.1039](https://arxiv.org/abs/1112.1039).
- [173] F. Maltoni and T. Stelzer. “MadEvent: Automatic event generation with MadGraph”. *JHEP* 02 (2003), p. 027. DOI: [10.1088/1126-6708/2003/02/027](https://doi.org/10.1088/1126-6708/2003/02/027). arXiv: [hep-ph/0208156](https://arxiv.org/abs/hep-ph/0208156).
- [174] J. Alwall et al. *Supplemental run and parameter cards to [45]*. URL: [http://amcatnlo.web.cern.ch/amcatnlo/cards\\_paper.htm](http://amcatnlo.web.cern.ch/amcatnlo/cards_paper.htm) (visited on Nov. 7, 2022).
- [175] A. D. Martin, W. J. Stirling, R. S. Thorne, and G. Watt. “Parton distributions for the LHC”. *Eur. Phys. J. C* 63 (2009), pp. 189–285. DOI: [10.1140/epjc/s10052-009-1072-5](https://doi.org/10.1140/epjc/s10052-009-1072-5). arXiv: [0901.0002](https://arxiv.org/abs/0901.0002).
- [176] M. Cacciari, G. P. Salam, and G. Soyez. “The Anti- $k(t)$  jet clustering algorithm”. *JHEP* 04 (2008), p. 063. DOI: [10.1088/1126-6708/2008/04/063](https://doi.org/10.1088/1126-6708/2008/04/063). arXiv: [0802.1189](https://arxiv.org/abs/0802.1189).
- [177] V. Hirschi et al. “Automation of one-loop QCD corrections”. *JHEP* 05 (2011), p. 044. DOI: [10.1007/JHEP05\(2011\)044](https://doi.org/10.1007/JHEP05(2011)044). arXiv: [1103.0621](https://arxiv.org/abs/1103.0621).
- [178] S. D. Drell and T.-M. Yan. “Massive Lepton-Pair Production in Hadron-Hadron Collisions at High Energies”. *Phys. Rev. Lett.* 25 (5 Aug. 1970), pp. 316–320. DOI: [10.1103/PhysRevLett.25.316](https://doi.org/10.1103/PhysRevLett.25.316).

- [179] G. Altarelli, R. Ellis, and G. Martinelli. “Large perturbative corrections to the Drell-Yan process in QCD”. *Nuclear Physics B* 157.3 (1979), pp. 461–497. ISSN: 0550-3213. DOI: [https://doi.org/10.1016/0550-3213\(79\)90116-0](https://doi.org/10.1016/0550-3213(79)90116-0).
- [180] J. Kubar-Andre and F. E. Paige. “Gluon corrections to the Drell-Yan model”. *Phys. Rev. D* 19 (1 Jan. 1979), pp. 221–229. DOI: [10.1103/PhysRevD.19.221](https://doi.org/10.1103/PhysRevD.19.221).
- [181] K. Harada, T. Kaneko, and N. Sakai. “Hadronic lepton-pair production beyond the leading order in perturbative QCD”. *Nuclear Physics B* 155.1 (1979), pp. 169–188. ISSN: 0550-3213. DOI: [https://doi.org/10.1016/0550-3213\(79\)90361-4](https://doi.org/10.1016/0550-3213(79)90361-4).
- [182] P. Aurenche and J. Lindfors. “QCD corrections to direct lepton production in hadronic collisions”. *Nuclear Physics B* 185.2 (1981), pp. 274–300. ISSN: 0550-3213. DOI: [https://doi.org/10.1016/0550-3213\(81\)90318-7](https://doi.org/10.1016/0550-3213(81)90318-7).
- [183] C. Bierlich et al. “A comprehensive guide to the physics and usage of PYTHIA 8.3” (Mar. 2022). arXiv: [2203.11601](https://arxiv.org/abs/2203.11601).
- [184] *PYTHIA online manual*. URL: <https://www.pythia.org/latest-manual/> (visited on Nov. 8, 2022).
- [185] A. Buckley and D. Bakshi Gupta. “Powheg-Pythia matching scheme effects in NLO simulation of dijet events” (Aug. 2016). arXiv: [1608.03577](https://arxiv.org/abs/1608.03577).
- [186] M. Cacciari, G. P. Salam, and G. Soyez. *FastJet User Manual*. URL: <http://fastjet.fr/repo/fastjet-doc-3.3.4.pdf> (visited on Nov. 5, 2022).
- [187] G. Aad et al. “Measurement of distributions sensitive to the underlying event in inclusive Z-boson production in pp collisions at  $\sqrt{s} = 13$  TeV with the ATLAS detector”. *Eur. Phys. J. C* 79.8 (2019), p. 666. DOI: [10.1140/epjc/s10052-019-7162-0](https://doi.org/10.1140/epjc/s10052-019-7162-0). arXiv: [1905.09752](https://arxiv.org/abs/1905.09752).
- [188] A. M. Sirunyan et al. “Measurement of the differential Drell-Yan cross section in proton-proton collisions at  $\sqrt{s} = 13$  TeV”. *JHEP* 12 (2019), p. 059. DOI: [10.1007/JHEP12\(2019\)059](https://doi.org/10.1007/JHEP12(2019)059). arXiv: [1812.10529](https://arxiv.org/abs/1812.10529).
- [189] A. M. Sirunyan et al. “Measurements of differential Z boson production cross sections in proton-proton collisions at  $\sqrt{s} = 13$  TeV”. *JHEP* 12 (2019), p. 061. DOI: [10.1007/JHEP12\(2019\)061](https://doi.org/10.1007/JHEP12(2019)061). arXiv: [1909.04133](https://arxiv.org/abs/1909.04133).
- [190] Particle Data Group. “Review of Particle Physics”. *Phys. Rev. D* 98, 010001 (2018).
- [191] R. D. Ball et al. “Parton distributions for the LHC Run II”. *JHEP* 04 (2015), p. 040. DOI: [10.1007/JHEP04\(2015\)040](https://doi.org/10.1007/JHEP04(2015)040). arXiv: [1410.8849](https://arxiv.org/abs/1410.8849).
- [192] P. Skands, S. Carrazza, and J. Rojo. “Tuning PYTHIA 8.1: the Monash 2013 Tune”. *Eur. Phys. J. C* 74.8 (2014), p. 3024. DOI: [10.1140/epjc/s10052-014-3024-y](https://doi.org/10.1140/epjc/s10052-014-3024-y). arXiv: [1404.5630](https://arxiv.org/abs/1404.5630).
- [193] V. Khachatryan et al. “Event generator tunes obtained from underlying event and multiparton scattering measurements”. *Eur. Phys. J. C* 76.3 (2016), p. 155. DOI: [10.1140/epjc/s10052-016-3988-x](https://doi.org/10.1140/epjc/s10052-016-3988-x). arXiv: [1512.00815](https://arxiv.org/abs/1512.00815).
- [194] R. D. Ball et al. “Parton distributions from high-precision collider data”. *Eur. Phys. J. C* 77.10 (2017), p. 663. DOI: [10.1140/epjc/s10052-017-5199-5](https://doi.org/10.1140/epjc/s10052-017-5199-5). arXiv: [1706.00428](https://arxiv.org/abs/1706.00428).
- [195] T. Barklow et al. “ILC Operating Scenarios” (June 2015). arXiv: [1506.07830](https://arxiv.org/abs/1506.07830).
- [196] M. Boronat et al. “Top quark mass measurement in radiative events at electron-positron colliders”. *Phys. Lett. B* 804 (2020), p. 135353. DOI: [10.1016/j.physletb.2020.135353](https://doi.org/10.1016/j.physletb.2020.135353). arXiv: [1912.01275](https://arxiv.org/abs/1912.01275).

- [197] B. Chokouf  Nejad et al. “NLO QCD predictions for off-shell  $t\bar{t}$  and  $t\bar{t}H$  production and decay at a linear collider”. *JHEP* 12 (2016), p. 075. DOI: [10.1007/JHEP12\(2016\)075](https://doi.org/10.1007/JHEP12(2016)075). arXiv: [1609.03390](https://arxiv.org/abs/1609.03390).
- [198] R. L. Workman. “Review of Particle Physics”. *PTEP* 2022 (2022). DOI: [10.1093/ptep/ptac097](https://doi.org/10.1093/ptep/ptac097).
- [199] J. Aparisi et al. “Snowmass White Paper: prospects for measurements of the bottom quark mass” (Mar. 2022). arXiv: [2203.16994](https://arxiv.org/abs/2203.16994).
- [200] B. Biedermann et al. “Automation of NLO QCD and EW corrections with Sherpa and Recola”. *Eur. Phys. J. C* 77 (2017), p. 492. DOI: [10.1140/epjc/s10052-017-5054-8](https://doi.org/10.1140/epjc/s10052-017-5054-8). arXiv: [1704.05783](https://arxiv.org/abs/1704.05783).
- [201] R. Frederix et al. “The automation of next-to-leading order electroweak calculations”. *JHEP* 07 (2018), p. 185. DOI: [10.1007/JHEP07\(2018\)185](https://doi.org/10.1007/JHEP07(2018)185). arXiv: [1804.10017](https://arxiv.org/abs/1804.10017).
- [202] B. Biedermann, A. Denner, and M. Pellen. “Large electroweak corrections to vector-boson scattering at the Large Hadron Collider”. *Phys. Rev. Lett.* 118.26 (2017), p. 261801. DOI: [10.1103/PhysRevLett.118.261801](https://doi.org/10.1103/PhysRevLett.118.261801). arXiv: [1611.02951](https://arxiv.org/abs/1611.02951).
- [203] W. Beenakker, S. van der Marck, and W. Hollik. “e+e- annihilation into heavy fermion pairs at high-energy colliders”. *Nuclear Physics B* 365.1 (1991), pp. 24–78. ISSN: 0550-3213. DOI: [https://doi.org/10.1016/0550-3213\(91\)90606-X](https://doi.org/10.1016/0550-3213(91)90606-X).
- [204] J. Fleischer, A. Leike, T. Riemann, and A. Werthenbach. “Electroweak one loop corrections for e+ e- annihilation into t anti-top including hard bremsstrahlung”. *Eur. Phys. J. C* 31 (2003), pp. 37–56. DOI: [10.1140/epjc/s2003-01263-8](https://doi.org/10.1140/epjc/s2003-01263-8). arXiv: [hep-ph/0302259](https://arxiv.org/abs/hep-ph/0302259).
- [205] G. Belanger et al. “Full O(alpha) electroweak and O(alpha(s)) corrections to e+ e- -> t anti-t H”. *Phys. Lett. B* 571 (2003), pp. 163–172. DOI: [10.1016/j.physletb.2003.07.072](https://doi.org/10.1016/j.physletb.2003.07.072). arXiv: [hep-ph/0307029](https://arxiv.org/abs/hep-ph/0307029).
- [206] C. Farrell and A. H. Hoang. “The Large Higgs energy region in Higgs associated top pair production at the linear collider”. *Phys. Rev. D* 72 (2005), p. 014007. DOI: [10.1103/PhysRevD.72.014007](https://doi.org/10.1103/PhysRevD.72.014007). arXiv: [hep-ph/0504220](https://arxiv.org/abs/hep-ph/0504220).
- [207] A. Denner, S. Dittmaier, M. Roth, and M. M. Weber. “Radiative corrections to Higgs boson production in association with top quark pairs at e+ e- colliders”. *Nucl. Phys. B* 680 (2004), pp. 85–116. DOI: [10.1016/j.nuclphysb.2003.12.028](https://doi.org/10.1016/j.nuclphysb.2003.12.028). arXiv: [hep-ph/0309274](https://arxiv.org/abs/hep-ph/0309274).
- [208] Y. You et al. “Electroweak radiative corrections to e+ e- -> t anti-t h at linear colliders”. *Phys. Lett. B* 571 (2003), pp. 85–91. DOI: [10.1016/j.physletb.2003.07.064](https://doi.org/10.1016/j.physletb.2003.07.064). arXiv: [hep-ph/0306036](https://arxiv.org/abs/hep-ph/0306036).
- [209] C. Anastasiou, K. Melnikov, and F. Petriello. “A new method for real radiation at NNLO”. *Phys. Rev. D* 69 (2004), p. 076010. DOI: [10.1103/PhysRevD.69.076010](https://doi.org/10.1103/PhysRevD.69.076010). arXiv: [hep-ph/0311311](https://arxiv.org/abs/hep-ph/0311311).
- [210] S. Catani and M. Grazzini. “An NNLO subtraction formalism in hadron collisions and its application to Higgs boson production at the LHC”. *Phys. Rev. Lett.* 98 (2007), p. 222002. DOI: [10.1103/PhysRevLett.98.222002](https://doi.org/10.1103/PhysRevLett.98.222002). arXiv: [hep-ph/0703012](https://arxiv.org/abs/hep-ph/0703012).
- [211] A. Gehrmann-De Ridder, T. Gehrmann, and E. W. N. Glover. “Antenna subtraction at NNLO”. *JHEP* 09 (2005), p. 056. DOI: [10.1088/1126-6708/2005/09/056](https://doi.org/10.1088/1126-6708/2005/09/056). arXiv: [hep-ph/0505111](https://arxiv.org/abs/hep-ph/0505111).
- [212] J. Currie, E. W. N. Glover, and S. Wells. “Infrared Structure at NNLO Using Antenna Subtraction”. *JHEP* 04 (2013), p. 066. DOI: [10.1007/JHEP04\(2013\)066](https://doi.org/10.1007/JHEP04(2013)066). arXiv: [1301.4693](https://arxiv.org/abs/1301.4693).
- [213] R. Boughezal, X. Liu, and F. Petriello. “N-jettiness soft function at next-to-next-to-leading order”. *Phys. Rev. D* 91.9 (2015), p. 094035. DOI: [10.1103/PhysRevD.91.094035](https://doi.org/10.1103/PhysRevD.91.094035). arXiv: [1504.02540](https://arxiv.org/abs/1504.02540).

- [214] J. Gaunt, M. Stahlhofen, F. J. Tackmann, and J. R. Walsh. “N-jettiness Subtractions for NNLO QCD Calculations”. *JHEP* 09 (2015), p. 058. DOI: [10.1007/JHEP09\(2015\)058](https://doi.org/10.1007/JHEP09(2015)058). arXiv: [1505.04794](https://arxiv.org/abs/1505.04794).
- [215] V. Del Duca et al. “Jet production in the CoLoRFulNNLO method: event shapes in electron-positron collisions”. *Phys. Rev. D* 94.7 (2016), p. 074019. DOI: [10.1103/PhysRevD.94.074019](https://doi.org/10.1103/PhysRevD.94.074019). arXiv: [1606.03453](https://arxiv.org/abs/1606.03453).
- [216] F. Caola, K. Melnikov, and R. Röntsch. “Nested soft-collinear subtractions in NNLO QCD computations”. *EPJC* 77.4 (2017), p. 248. DOI: [10.1140/epjc/s10052-017-4774-0](https://doi.org/10.1140/epjc/s10052-017-4774-0). arXiv: [1702.01352](https://arxiv.org/abs/1702.01352).
- [217] M. Czakon. “A novel subtraction scheme for double-real radiation at NNLO”. *Phys. Lett. B* 693 (2010), pp. 259–268. DOI: [10.1016/j.physletb.2010.08.036](https://doi.org/10.1016/j.physletb.2010.08.036). arXiv: [1005.0274](https://arxiv.org/abs/1005.0274).
- [218] M. Czakon and D. Heymes. “Four-dimensional formulation of the sector-improved residue subtraction scheme”. *Nucl. Phys. B* 890 (2014), pp. 152–227. DOI: [10.1016/j.nuclphysb.2014.11.006](https://doi.org/10.1016/j.nuclphysb.2014.11.006). arXiv: [1408.2500](https://arxiv.org/abs/1408.2500).
- [219] H. A. Chawdhry, M. Czakon, A. Mitov, and R. Poncelet. “NNLO QCD corrections to diphoton production with an additional jet at the LHC”. *JHEP* 09 (2021), p. 093. DOI: [10.1007/JHEP09\(2021\)093](https://doi.org/10.1007/JHEP09(2021)093). arXiv: [2105.06940](https://arxiv.org/abs/2105.06940).
- [220] S. Catani, M. H. Seymour, and Z. Trocsanyi. “Regularization scheme independence and unitarity in QCD cross-sections”. *Phys. Rev. D* 55 (1997), pp. 6819–6829. DOI: [10.1103/PhysRevD.55.6819](https://doi.org/10.1103/PhysRevD.55.6819). arXiv: [hep-ph/9610553](https://arxiv.org/abs/hep-ph/9610553).
- [221] L. Devroye. “Non-Uniform Random Variate Generation”. *Springer NY* 843 (1986). DOI: [10.1007/978-1-4613-8643-8](https://doi.org/10.1007/978-1-4613-8643-8).
- [222] D. E. Knuth. *The Art of Computer Programming, Volume 2: Seminumerical Algorithms*. Third. Addison-Wesley, 1997.
- [223] C. Bierlich, A. Buckley, C. Gutschow, et al. *Rivet GitLab*. URL: <https://gitlab.com/hepcedar/rivet/-/tree/release-3-1-x/doc/tutorials> (visited on Oct. 20, 2022).
- [224] A. Buckley, D. Grellscheid, M. Kawalec, H. Hoeth, C. Gutschow, et al. *YODA — Yet more Objects for Data Analysis*. URL: <https://yoda.hepforge.org/> (visited on Oct. 20, 2022).
- [225] *Eidesstattliche Erklärung für Promotionen im Fachbereich Physik der Universität Hamburg*. URL: <https://www.physik.uni-hamburg.de/dokumente/promotionen/formalien-der-dissertation-eidesstattliche-erklaerung.pdf> (visited on Nov. 6, 2022).

## List of figures

1.1	Fine structure and Lamb shift of the hydrogen atom's energy levels . . . . .	2
1.2	Particle content of the Standard Model of particle physics . . . . .	3
1.3	Diagrammatic representation of the NLO QCD contributions to dijet production . . . . .	4
1.4	Feynman diagram of a quark radiating a gluon. . . . .	4
1.5	Schematic of a hadron-hadron collision indicating different parts of the simulation by color. . . . .	6
2.1	Contributions to the total NLO cross section. . . . .	9
2.2	Exemplary flavor-changing splittings . . . . .	14
2.3	All possible FSR QCD splittings . . . . .	36
2.4	All possible ISR QCD splittings . . . . .	38
2.5	Exemplary Feynman diagrams for the real correction to the process $e^+e^- \rightarrow t\bar{t}j$ . . . . .	42
2.6	Contributions from all components to a figurative histogram showing the number of jets. . . . .	47
2.7	Showcase of issues with fNLO histogramming on the example of $e^+e^- \rightarrow jj$ . . . . .	49
3.1	Illustration of double counting when <i>merging</i> parton showers with matrix-element calculations . . . . .	53
3.2	Illustration of double counting when <i>matching</i> parton showers with higher-order matrix-element calculations . . . . .	54
3.3	Flow chart depicting the parallelizable highest-bid algorithm . . . . .	64
3.4	Flow chart depicting the optimized highest-bid algorithm . . . . .	65
3.5	POWHEG grids for the three ALRs of the process $d\bar{d} \rightarrow e^+e^-$ . . . . .	68
3.6	Probability density of sampled $x$ values. . . . .	78
3.7	Flow chart of the veto procedure showing all potential veto steps . . . . .	83
3.8	Diagram of the spin configuration in $u\bar{d} \rightarrow W^+ \rightarrow e^+\nu_e$ . . . . .	85
3.9	Color flows of all possible FSR splittings . . . . .	89
3.10	Color flows of all possible ISR splittings . . . . .	89
3.11	Fractions of negative weights generated for the processes $pp \rightarrow e^+e^-$ and $e^+e^- \rightarrow t\bar{t}j$ . . . . .	91
6.1	Feynman diagrams contributing to the Drell-Yan process. . . . .	108
6.2	MSTW 2008 NLO PDFs . . . . .	110
6.3	Comparison of LO, fNLO and NLO distributions for $pp \rightarrow e^+e^-$ . . . . .	115
6.4	Comparison of NLO distributions for $pp \rightarrow e^+e^-$ with different real-partition scales. . . . .	118
6.5	Comparison of NLO distributions for $pp \rightarrow e^+e^-$ events from the POWHEG-BOX and WHIZARD, including the parton shower simulated by PYTHIA. . . . .	121
6.6	Observable distributions for showered $pp \rightarrow e^+e^-$ events with different choices of $p_{T,\min}$ compared to CMS data. . . . .	125
6.7	Observable distributions for showered $pp \rightarrow e^+e^-$ events with different real-partition scales compared to CMS data. . . . .	126
6.8	Measured $pp \rightarrow e^+e^-$ cross sections in bins of $ y^Z $ . . . . .	127
6.9	Measured $pp \rightarrow e^+e^-$ cross sections in bins of $ p_T^Z $ . . . . .	127
6.10	Differential distributions for $e^+e^- \rightarrow t\bar{t}j$ events with a real-partition scale of $h_F = 5$ GeV. . . . .	132
6.11	Differential distributions for $e^+e^- \rightarrow t\bar{t}j$ fixed-order and POWHEG events. . . . .	134
C.1	Evolution of the transverse momentum during the POWHEG veto procedure. . . . .	146

## List of tables

1	FKS table for the process $e^+e^- \rightarrow jjj$ . . . . .	15
2	FKS table for the process $e^+e^- \rightarrow d\bar{d}$ . . . . .	72
3	Partial $e^+e^- \rightarrow jjj$ cross sections for the real and the virtual component for different values of $\xi_{\text{cut}}$ . . . . .	98
4	Partial $pp \rightarrow e^+e^-$ cross sections for the real and the DGLAP remnant component for different values of $\delta_T$ . . . . .	98
5	Comparison of f(N)LO cross sections for light-jet production and top-quark production at a lepton collider in association with light jets between MG5_aMC and WHIZARD. . . . .	103
6	Comparison of f(N)LO cross sections for top-quark production at a lepton collider in association with heavy bosons between MG5_aMC and WHIZARD. . . . .	104
7	Comparison of f(N)LO cross sections for the production of top quarks and/or light jets at a hadron collider in association with heavy gauge bosons between MG5_aMC and WHIZARD. . . . .	104
8	Comparison of f(N)LO cross sections for heavy vector boson (pair) production at a hadron collider in association with light jets between MG5_aMC and WHIZARD. . . . .	105
9	Comparison of f(N)LO cross sections for the production of three to four heavy vector bosons at a hadron collider in association with light jets between MG5_aMC and WHIZARD. . . . .	106
10	Comparison of cross sections computed with and without using the real partition. . . . .	107
11	Table of cross sections for the process $pp \rightarrow e^+e^-$ computed with the POWHEG-BOX and WHIZARD. . . . .	110
12	Table of cross sections for the process $pp \rightarrow e^+e^-$ with increasing cut on the invariant lepton mass. . . . .	111
13	Table of cross sections for the process $pp \rightarrow e^+e^-$ computed with WHIZARD for different real-partition scales. . . . .	112
14	Predicted and measured cross sections for the Drell-Yan process. . . . .	123
15	Integration histories of the cross-section computation of the process $e^+e^- \rightarrow t\bar{t}j$ . . . . .	130
16	Cross section of the process $e^+e^- \rightarrow t\bar{t}j$ at LO and NLO QCD for different real-partition scales. . . . .	130
17	Veto and survival probabilities during the POWHEG veto procedure for the process $d\bar{d} \rightarrow e^+e^-$ . . . . .	148

## List of acronyms

<b>ALR</b> alpha region	<b>LL</b> leading logarithmic
<b>ATLAS</b> A Toroidal LHC AparatuS	<b>LO</b> leading order
<b>CDF</b> Cumulative Distribution Function	<b>MC</b> Monte Carlo
<b>CEPC</b> Circular Electron Positron Collider	<b>MLM</b> M. L. Mangano
<b>CKKW</b> Catani, Krauss, Kuhn and Webber	<b>MPI</b> message passing interface
<b>CKM</b> Cabibbo-Kobayashi-Maskawa	<b>NLL</b> next-to-leading logarithmic
<b>CLIC</b> Compact Linear Collider	<b>NLO</b> next-to-leading order
<b>CM</b> center-of-mass	<b>NNLO</b> next-to-next-to-leading order
<b>CMS</b> Compact Muon Solenoid	<b>OLP</b> one-loop provider
<b>CS</b> Catani-Seymour	<b>PDF</b> parton distribution function
<b>DGLAP</b> Dokshitzer–Gribov–Lipatov–Altarelli– Parisi	<b>PDG</b> Particle Data Group
<b>EW</b> electroweak	<b>PEP</b> Positron-Electron Project
<b>FCC</b> Future Circular Collider	<b>PETRA</b> Positron-Elektron-Tandem-Ring-Anlage
<b>FIFO</b> first in first out	<b>PSP</b> phase-space point
<b>FKS</b> Frixione–Kunszt–Signer	<b>QCD</b> quantum chromodynamics
<b>fnLO</b> fixed next-to-leading order	<b>QED</b> quantum electrodynamics
<b>FSR</b> final-state radiation	<b>QFT</b> quantum field theory
<b>ILC</b> International Linear Collider	<b>RHS</b> right hand side
<b>IR</b> infrared	<b>RNG</b> random number generator
<b>ISR</b> initial-state radiation	<b>RS</b> rejection sampling
<b>ITS</b> inverse transform sampling	<b>SM</b> Standard Model of particle physics
<b>KLN</b> Kinoshita–Lee–Nauenberg	<b>SMC</b> Shower Monte Carlo
<b>LHC</b> Large Hadron Collider	<b>UBF</b> upper bounding function
<b>LHEF</b> Les Houches Event File	<b>UFO</b> Universal FeynRules Output
<b>LHIUP</b> Les Houches Interface for User Processes	<b>UV</b> ultraviolet
<b>LHS</b> left hand side	<b>VBS</b> vector boson scattering

## Acknowledgements

Many people guided and accompanied me during my time as a doctoral researcher. This project could not have been completed without their support.

First and foremost, I want to thank my main supervisor, *Jürgen Reuter*, for countless on- and off-topic scientific and technical discussions around the clock. Secondly, I owe thanks to *Gudrid Moortgat-Pick*, the co-supervisor of this thesis, for her spontaneous availability whenever needed. Furthermore, I am very pleased to have *Peter Schleper* and *Markus Diehl* as members of my thesis committee. I owe deep thanks to both for shaping my scientific career. I also thank *Arwen Pearson* for kindly chairing the committee.

I want to thank *DESY* for providing financial support for most of this project and the *DESY Theory Group* for providing an international and open-minded environment. My special thanks goes to its group leader, *Christophe Grojean*, for not forgetting the individual interests even of minor members of the group. It was a pleasure to participate in some of the many local regular and annual seminars and conferences organized at the DESY campus. For organizing those conferences and a mutual exchange of technical and administrative support, I want to thank both secretaries *Julia Herrmann* and *Cristina Guerro*.

The intergroup networking among doctoral students on the DESY campus was greatly facilitated by the doctoral representations *CHAMPP* and *DOIT*. Together, we discussed the concerns and needs of doctoral students during regularly organized lunch breaks and social events. These would not have been possible without the help of the *PIER Helmholtz Graduate School*. I specifically appreciate *Stefanie Tepass* for personally being interested in the well-being of the many doctoral students benefitting from being a member of PIER. Moreover, I sincerely thank the *MIN Graduate Center* for providing me with a short-term scholarship in the final phase of the project.

I am grateful for the company I found in the *WHIZARD collaboration*. My thanks goes to *Wolfgang Kilian* and *Thorsten Ohl* for sharing their insights and for their hospitality during the many regular WHIZARD meetings we had in Hamburg, Siegen and Würzburg and *Simon Brass* for contributing to the success of this thesis by sharing knowledge about debugging and parallelization. Moreover, I owe deep gratitude to my fellow junior WHIZARDS, *Vincent Rothe* and *Pia Bredt*, for the countless hours we spend working together to unravel the mysteries of the WHIZARD source code.

Also beyond the WHIZARD collaboration, I met many colleagues who eventually became friends. This includes my fellow student admins of the Theory Group *Jonas Wittbrodt*, *Marco Hufnagel*, *Henrique Rubira*, *Philine van Vliet* and *Carlo Tasillo* and everyone who participated in the DESY Theory Board Game Evenings we often organized, especially *Philipp Tontsch*, *Frederik Depta*, *Jeremy Mann*, *Lorenzo Quintavalle*, *Cyrille Praz* and many of the aforementioned students. Furthermore, I owe a deep sense of gratitude to my long-term friends *Alicia Wongel*, *Torben Lange* and *Felix Giese* for believing in me when I did not.

Finally, my heartfelt thanks goes to *Celina Toth* for keeping me sane in times of a global pandemic and *my family* for their unlimited, unconditional support.

## Eidesstattliche Versicherung / Declaration on oath

Hiermit versichere ich an Eides statt, die vorliegende Dissertationsschrift selbst verfasst und keine anderen als die angegebenen Hilfsmittel und Quellen benutzt zu haben. [225]

Hamburg, \_\_\_\_\_

Unterschrift: \_\_\_\_\_